Western Graduate&PostdoctoralStudies

Western University
Scholarship@Western

Electronic Thesis and Dissertation Repository

August 2011

X-ray Photoelectron Spectroscopy Studies on the Oxidation Processes of Nickel, Chromium and their Alloys

Bradley P. Payne, *The University of Western Ontario*

Supervisor: Professor N. Stewart McIntyre, *The University of Western Ontario*

A thesis submitted in partial fulfillment of the requirements for the Doctor of Philosophy degree in Chemistry

© Bradley P. Payne 2011

Follow this and additional works at: https://ir.lib.uwo.ca/etd

Part of the Materials Chemistry Commons, and the Physical Chemistry Commons

Recommended Citation

Payne, Bradley P., "X-ray Photoelectron Spectroscopy Studies on the Oxidation Processes of Nickel, Chromium and their Alloys" (2011). *Electronic Thesis and Dissertation Repository*. 201.
https://ir.lib.uwo.ca/etd/201

This Dissertation/Thesis is brought to you for free and open access by Scholarship@Western. It has been accepted for inclusion in Electronic Thesis and Dissertation Repository by an authorized administrator of Scholarship@Western. For more information, please contact wlswadmin@uwo.ca.

X-ray Photoelectron Spectroscopy Studies on the Oxidation Processes of Nickel, Chromium and their Alloys

By

Bradley Philip Payne

Graduate Program

in

Chemistry

Submitted in partial fulfilment

of the requirements for the degree of

Doctor of Philosophy

The School of Graduate and Postdoctoral Studies

The University of Western Ontario

London, Ontario,

August, 2011

© Bradley Philip Payne 2011

THE UNIVERSITY OF WESTERN ONTARIO

FACULTY OF GRADUATE STUDIES

CERTIFICATE OF EXAMINATION

Thesis Supervisor	Examination Board
_____	_____
Professor N. Stewart McIntyre	Professor Oleg Semenikhin
	_____
	Professor J. Clara Wren
	_____
	Professor Hugo de Lasa
	_____
	Professor Serge Kaliaguine

The thesis by

Bradley Philip Payne

entitled

X-ray Photoelectron Spectroscopy Studies on the Oxidation Processes of Nickel, Chromium and their Alloys

is accepted in partial fulfilment of the

requirements for the degree of

Doctor of Philosophy

Date_____ _____

Chair of Examining Board

ABSTRACT

The reaction of polycrystalline Ni metal surfaces with low pressures (~ 130 Pa) of O_2 gas or H_2O vapour produced thin defective nickel oxide films containing both Ni^{2+} and Ni^{3+} species at 25°C and 300°C. Exposure of Ni metal samples to H_2O vapour resulted in a much slower reaction rate when compared to similar doses of O_2 gas. This difference was attributed to a slower place exchange with a surface hydroxyl (OH (ads)) intermediate compared to that of an adsorbed oxygen atom (O (ads)). This OH (ads) species appears only to be stabilized on metallic Ni and termination of oxide growth is believed to occur once all the available surface metal sites have been covered with oxide.

The Cr $2p_{3/2}$ spectra of polycrystalline Cr_2O_3 contain multiplet structures that bear a strong resemblance to those calculated by Gupta and Sen for the free Cr^{3+} ion. The Cr $2p_{3/2}$ spectrum for $Cr(OH)_3$ was isolated from that produced by Cr_2O_3 and the multiplet structure was qualitatively reassembled for that of the hydroxide. Reactions of either O_2 gas or H_2O vapour with metallic Cr both produced thin Cr_2O_3 films that were deficient in Cr^{3+} and, depending on the reactant, showed varying concentrations of hypo-stoichiometric Cr moieties. No such species was observed following the oxidation of a NiCr (20%) (NiCr) alloy surface in an acidic (pH = 5) aqueous solution.

The O/Ni ratios derived from the XPS spectra of a number of well-characterized Ni oxides were calculated and found to correspond well to the expected O/Ni ratios for these oxides. These ratios were then applied to the analysis of oxides that were electrochemically grown on Ni and NiCr alloy surfaces.

The exposure of polycrystalline Ni metal and NiCr alloy surfaces to basic aqueous environments under mildly oxidizing potentials (0.0 V vs. Ag/AgCl) and temperatures of

25° and 150°C produced predominately β-$Ni(OH)_2$-rich films. Decreasing the pH of the electrolyte at 150°C resulted in an increase in the Cr_2O_3 and $Cr(OH)_3$ content of the oxide films formed on the alloy surfaces. Reactions on metallic Ni and NiCr surfaces under highly oxidizing potentials (1.5 V vs. Ag/AgCl) in basic solutions resulted in an increase in the NiO content of these films compared to similar exposures carried out at milder oxidation conditions. This was attributed to accelerated dehydration of the β-$Ni(OH)_2$ phase. In addition, an increase in the $Cr(OH)_3$ contribution on the alloy surface oxidized at a more oxidative potential suggested a more rapid dissolution of Cr under these conditions. The composition of the corrosion product formed after an exposure to a highly oxidizing potential was found to be unchanged following a subsequent reaction of equivalent length a much lower oxidizing potential.

Keywords: Ni oxidation, Cr oxidation, NiCr alloy oxidation, XPS, ToF SIMS

CO-AUTHORSHIP

This thesis is comprised of manuscripts prepared by Brad Payne that had previously been published in accredited journals as well as material that at the time of thesis completion, were either submitted to or intended to be submitted for peer review and publication. Brad Payne's Ph.D. research supervisor Prof. N. Stewart McIntyre is a co-author on all of the papers presented in this work. Prof. McIntyre's tireless work in helping to prepare each manuscript is gratefully acknowledged. Mr. Mark C. Biesinger is also a co-author on the papers presented in Chapters 2-5. Dr. Andrew Grosvenor and Mr. Brad Kobe also contributed to the work presented in Chapter 2. Finally, Dr. Peter Keech is a co-author of the manuscript presented in Chapter 6.

Brad Payne was responsible for carrying out all gas phase surface reactions and subsequent XPS spectral analyses presented in Chapters 2-4. All dosing experiments and subsequent surface analyses were carried out using the Kratos Axis Ultra spectrometer located at SSW. Mr. Mark Biesinger and Dr. Andrew Grosvenor were responsible for training Brad Payne in the operation of the instrument as well as in the use of the data analysis programs. The XPS imaging experiment and subsequent data analysis presented in Chapter 2 were carried out with the help of Mr. Mark Biesinger and Mr. Brad Kobe. Dr. James T. Francis and Dr. Heng-Yong Nie collected and helped Brad Payne analyze the ToF SIMS data presented in Chapter 2. Dr. Luan Xi and Dr. James T. Francis were responsible for acquiring the ToF SIMS data shown in Chapter 3. This SIMS data was analyzed with the help of Mr. Mike Edwards. Dr. Peter Keech's expertise in electrochemistry helped us to interpret the data obtained for Chapter 6.

All electrochemical experiments presented in Chapters 5 and 6 were carried out using the laboratory and equipment of Prof. David Shoesmith, a Faculty member in the Department of Chemistry at the University of Western Ontario. The use of his laboratory space is also warmly acknowledged. Dr. Jamie Noël and Dr. Pellumb Jakupi were responsible for instructing Brad Payne in the use of the electrochemical equipment. All XPS surface analyses for the electrochemically oxidized surfaces presented in Chapters 5 and 6 were completed by Brad Payne using the Kratos Axis Spectrometer located at SSW. The ToF SIMS experiments shown in Chapter 6 were carried out by Dr. Heng-Yong Nie. Mr. Mike Edwards aided Brad Payne in the analysis of this SIMS data.

ACKNOWLEDGEMENTS

I would first like to express my deepest thanks to my research supervisor Prof. N. Stewart McIntyre for taking me on as a graduate student. Working for Prof. McIntyre has allowed me to grow as both a researcher and as a person. I am grateful for his tireless dedication to our project as well as his encouragement and help along the way.

I would also like to thank the other members of our research group past and present, Dr. Marina Suominen Fuller, Dr. Andrew Grosvenor, Mr. Mike Edwards and Ms. Jing Chao, for all of their support during my time at Western. I couldn't have asked for a better group of colleagues to work with. You were always there for me when I needed to bounce ideas off of someone. In addition, Mike I will miss the afternoons we spent discussing chemistry at the GC.

I would not have been able to complete my Ph.D. research if it were not for the wonderful people who work at Surface Science Western. Thank you for all your help with sample preparation and instrumentation. In particular, I have to thank Mr. Mark Biesinger for all his guidance with XPS. Mark you were my go to guy for almost all of my experimental problems. Thank you for your patience and assistance on an almost daily basis, as well as for the odd round of golf.

Professor David Shoesmith is also thanked for allowing us to use his laboratory and equipment for all of our aqueous oxidation experiments. Additionally, Dr. Jamie Noël is acknowledged for instructing me on how to set up electrochemical experiments using an autoclave. I would not have been able to complete my research project without their time, effort and help.

I would also like to acknowledge all the friends I have made in the Department of Chemistry over the years. Thank you Pam Yakabuskie, Michael Murphy, Pellumb Jakupi, Monica Kumala, Peter Keech, Brent Sherar, Peter Ko, Chhatra Khadka, and Darryl Dixon. Here is to all of the good and not so good (DB) times we have had together.

The financial support of the Natural Science and Engineering Research Council of Canada is also warmly acknowledged.

I would finally like to thank my father Warren, mother Carolyn, and sister Jen for all of their love and support throughout my life. Thank you for helping me to get to where I am today.

Table of Contents

CERTIFICATE OF EXAMINATION ii

ABSTRACT iii

CO-AUTHORSHIP v

ACKNOWLEDGEMENTS vii

TABLE OF CONTENTS ix

LIST OF TABLES xiii

LIST OF FIGURES xv

LIST OF APPENDICES xxvii

LIST OF ABBREVIATIONS AND SYMBOLS xxviii

CHAPTER 1 INTRODUCTION 1

1.1 The Study of Thin Films 1

1.2 Project Overview 2

1.3 Oxidation Mechanisms 3

1.4 X-ray Photoelectron Spectroscopy 9

1.5 Time of Flight Secondary Ion Mass Spectrometry 23

1.6 Thesis Outline 24

1.7 References 26

CHAPTER 2 STRUCTURE AND GROWTH OF OXIDES ON POLYCRYSTALLINE NICKEL SURFACES 28

2.1 Introduction 28

2.2 Experimental 29

2.3 Results and Discussion 34

2.3.1 Reactions at 300°C and 130 Pa 34

2.3.2 Reactions at 25°C and 130 Pa 46

2.4 Conclusions 52

2.5 References 54

CHAPTER 3 THE STUDY OF NICKEL METAL OXIDATION BY WATER VAPOUR 57

3.1 Introduction 57

3.2 Experimental 59

3.3 Results and Discussion 69

3.4 Conclusions 84

3.5 References 85

CHAPTER 4 X-RAY PHOTOELECTRON SPECTROSCOPY STUDIES OF REACTIONS ON CHROMIUM METAL AND CHROMIUM OXIDE SURFACES 88

4.1 Introduction 88

4.2 Experimental 89

4.3 Results and Discussion 95

4.3.1 Spectral refinements for Cr_2O_3 95

4.3.2 Spectral refinements for $Cr(OH)_3$ 102

4.3.3 Reactions of metallic Cr with O_2 and H_2O 104

4.3.4 Aqueous reaction of metallic NiCr 108

4.4 Conclusions 108

4.5 References 110

CHAPTER 5 USE OF OXYGEN/NICKEL RATIOS IN THE XPS CHARACTERIZATION OF OXIDE PHASES ON NICKEL METAL AND NICKEL ALLOY SURFACES 112

5.1 Introduction 112

5.2 Experimental 113

5.3 Results and Discussion 116

5.3.1 Polycrystalline NiO, β-$Ni(OH)_2$, γ-NiOOH, and $NiCr_2O_4$ samples 116

5.3.2 Aqueous reaction of metallic Ni and NiCr 124

5.4 Conclusions 126

5.5 References 128

CHAPTER 6 X-RAY PHOTOELECTRON STUDY OF THE OXIDES FORMED ON NICKEL METAL AND NICKEL-CHROMIUM 20% ALLOY SURFACES UNDER REDUCING AND OXIDIZING POTENTIALS IN BASIC, NEUTRAL AND ACIDIC SOLUTIONS 130

6.1 Introduction 130

6.2 Experimental 131

6.3 Results and Discussion 138

6.3.1 Surface analysis using XPS 138

6.3.2 Surface reaction products under strongly reducing conditions in a basic environment at 25°C 140

6.3.3 Surface reaction products under mildly oxidizing conditions in basic environments at 25°C 141

6.3.4 Surface reaction products under mildly oxidizing conditions in basic environments at 150°C 143

6.3.5 Possible conductivity issues in the basic solutions 146

6.3.6 Surface reaction products under mildly oxidizing conditions in neutral environments at 150°C 146

6.3.7 Surface reaction products under mildly oxidizing conditions in acidic environments at 150°C 148

6.3.8 Surface reaction products under highly oxidizing conditions in basic environments at 150°C 150

6.3.9 Surface reaction products under highly oxidizing conditions followed by exposure to more mildly oxidizing potential in a basic environment at 150°C .. 152

6.4 Conclusions 152

6.5 References 153

CHAPTER 7 SUMMARY AND CONCLUSIONS 156

7.1 General Summary 156

7.2 Impact of work 162

7.3 Future work 170

7.4 References 173

CURRICULUM VITAE……..……...…187

LIST OF TABLES

Table 2.1: Determination of Oxide Thickness (nm) at 300°C and 130 Pa using QUASES™ 43

Table 2.2: Determination of Oxide Thickness (nm) at 25°C and 130 Pa using QUASES™ 51

Table 3.1: Near-surface compositions of Ni and O species for surfaces exposed to H_2O vapour at 300°C. 73

Table 3.2: Calculated film thickness and surface coverage using QUASES™ and Strohmeier equation. 76

Table 4.1: XPS surface composition in at.% of Cr metal and oxide samples..... 92

Table 4.2: Summary of the organic C 1s peak areas and calculated contributions to the corresponding O 1s spectra. 94

Table 4.3: Cr $2p_{3/2}$ peak fits for the polycrystalline Cr_2O_3, $Cr(OH)_3$ and Cr metal samples. 98

Table 4.4: O 1s peak fits for the Cr_2O_3, $Cr(OH)_3$, oxidized Cr and oxidized NiCr metal samples. 100

Table 4.5: O/Cr ratios calculated from the normalized surface concentrations..... 101

Table 5.1: Summary of the O 1s peak fitting results for the O^{2-}, O def, OH^- and interstitial H_2O species. 122

Table 5.2: Calculated O/M ratios using the normalized O, Ni, and Cr atomic concentrations in at.%. 123

Table 6.1: High-resolution Ni $2p_{3/2}$ peak fitting results and normalized atomic concentrations (in at.%) for the Ni metal samples. 135

Table 6.2: High-resolution Ni $2p_{3/2}$ and Cr $2p_{3/2}$ peak fitting results and normalized atomic concentrations (in at.%) for the NiCr alloy samples. 136

LIST OF FIGURES

Figure 1.1: The mechanism for the oxidation of a metal (M) surface exposed to O_2 gas. The initial place exchange reaction resulting in the first layers of oxide is shown in (a). The continuous growth of a film following logarithmic or parabolic kinetics beyond the place exchange process is shown in (b). The vacancies (□) present within the film provide pathways for ion migration.... 6

Figure 1.2: Simplified diagram of the PDM model showing the major cationic, anionic and vacancy species involved in the growth of an MO type oxide during reaction with a H_2O molecule. 8

Figure 1.3: An electron energy diagram for a Ni^{2+} cation showing the absorption of a photon and resultant expulsion of a 2p level photoelectron. 10

Figure 1.4: (a) Simplified schematic following a photoelectron (e^-) through a Kratos Axis Ultra spectrometer. (b) The expanded view of the energy analyzer setup in spectrum mode employing the CHA. Under these conditions the photoelectrons enter the energy analyzer at point A and travel between two negatively charged plates. The grey lines represent possible pathways these electrons may travel through the energy analyzer. Only the photoelectrons with the selected pass energies will exit the analyzer at point B and enter the detector. (c) The expanded view of the energy analyzer setup in imaging mode employing the SMA. The presence of the mesh hemispherical electrode and additional slit allows for specific photoelectron BEs to be selected allowing for high-resolution images to be collected. 12

Figure 1.5: (a) The survey spectrum collected for a polycrystalline NiO powder sample containing a small C impurity. The elemental concentrations in at.% for the Ni, O and C species have been calculated using Equation 1.6 and are also presented. (b) The high-resolution Ni 2p spectrum taken for the same NiO sample. The electronic structural features arising from j-j coupling (Ni $2p_{3/2}$, Ni $2p_{1/2}$), multiplet splitting and shake up interactions are clearly visible.... 15

Figure 1.6**:** The high resolution Ni 2p spectrum for an atomically clean Ni metal surface. The asymmetric nature of the Ni $2p_{3/2}$ and Ni $2p_{1/2}$ mainlines is clearly visible. Additional structures due to plasmon losses are also observed at higher BE on both the Ni $2p_{3/2}$ and $2p_{1/2}$ lines..... 20

Figure 1.7: Diagram showing the differences in the extrinsic background for the Cu 2p peak as a function of the atomic distribution within the near surface region. The grey areas represent the portion of the sample containing the Cu atoms. (b) The five different QUASES™ depth profiles are also shown. The grey areas represent the material that is being modeled [29]. 22

Figure 2.1: High-resolution Ni $2p_{3/2}$ spectra of (a) a polished, sputtered, and annealed Ni metal surface and (b) a sample of a polycrystalline NiO powder. 32

Figure 2.2: High-resolution Ni $2p_{3/2}$ photoelectron spectra following O_2 exposure times of 1, 4, 20, and 60 minutes at 300°C and 130 Pa. The identification of the spectral components lying above Ni metal is clarified in Figure 2.3. 35

Figure 2.3: High-resolution Ni $2p_{3/2}$ spectra following subtraction of the Ni metal component showing the contributions from Ni^{2+} and Ni^{3+}. The spectra are shown for O_2 exposure times of 1, 4, 20, and 60 minutes at 300°C and 130 Pa.

As exposure time increases, the resulting oxide more closely resembles NiO. 37

Figure 2.4: High-resolution Ni $2p_{3/2}$ spectra after subtraction of both the Ni metal and NiO components showing the residual spectra of Ni^{3+} for O_2 exposure times of 1 and 4 minutes at 300°C and 130 Pa. The subtracted spectra are similar to that of NiOOH, which is shown in reference [26]. The spike at 853.9 eV in both spectra is due to an incomplete subtraction process..... 38

Figure 2.5: O 1s high-resolution spectra following 1, 4, 20, and 60 minute exposures to O_2. These four spectra correlate with the four Ni spectra shown in Figure 2.2(a-d). There appears to be three distinct oxygen species present (O^{2-}, O (ads), and O_2 (ads)). As exposure time is increased the contribution from the adsorbed species decreases substantially. These spectra were not corrected for charging. 40

Figure 2.6: QUASES™ 'Analyze' modeled peaks from a Ni surface exposed to ultra pure O_2 at 300°C and 130 Pa for 60 minutes: (a) Ni 2s using Zr L X-ray source; (b) O 1s using Al Kα X-ray source..... 41

Figure 2.7: Change in overall oxide thickness on Ni metal for O_2 doses (Langmuirs (L)) at 300°C and 130 Pa as determined by QUASES™ 'Analyze'. Results are best fitted to a parabolic relationship. The determined R^2 value for a parabolic fit was 0.94, while R^2 values of 0.87, and 0.56 were observed for the direct and inverse logarithmic plots respectively. 43

Figure 2.8: The Ni 2s QUASES™ 'Generate' result of a Ni metal surface exposed to dry O_2 for 60 minutes at 300°C and 130 Pa analyzed using Zr L radiation. A very

good overlap is found between the modeled and the experimental spectra along the extrinsic loss portion. 45

Figure 2.9: High-resolution Ni $2p_{3/2}$ Ni metal subtracted spectra showing the contributions from Ni^{2+} and Ni^{3+} following O_2 exposure times of 10, 25, 50, and 100 minutes at 25°C and 130 Pa. The subtracted spectra show very little change in oxide composition as exposure time is increased. 48

Figure 2.10: O 1s high-resolution spectra following 10, 25, 50, and 100 minute exposures to O_2. These were *not* charge corrected. These four spectra correlate with the four subtracted Ni metal spectra shown in Figure 2.9(a-d). Three distinct oxygen species are present: (O^{2-}, O (ads), and O_2 (ads)). As exposure time is increased the contribution from the lattice oxide species increases but there is still a strong adsorbate signal. The spectrum in (a) is noisy because of the very small quantity of oxide formed at this stage in the process. 49

Figure 2.11: Change in overall oxide thickness on Ni metal at 25°C and 130 Pa as determined by QUASES™ 'Analyze'. The results are best fit using a direct logarithmic relationship. The determined R^2 value for a direct logarithmic fit was 0.83, while R^2 values of 0.78, and 0.65 were observed for the parabolic and inverse logarithmic plots respectively. 51

Figure 2.12: XPS map of NiO thickness for a Ni metal surface exposed to O_2 for 10 minutes at 25°C and 130 Pa (a). Oxide thickness is greatest in the neighbourhood of grain a in (b). This grain is known to be more susceptible to oxidation on the basis of the O^- secondary ion image in (c)..... 52

Figure 3.1: High-resolution spectrum of the C 1s region of a Ni metal surface exposed to H_2O vapour showing the BE shifts of the C (adv), –COH, –CO, and –COO– species (a). The corresponding peak positions in the O 1s region for the –COH, –CO, and –COO– species are shown in (b), with an expanded view of this region shown in (c). 63

Figure 3.2: High-resolution Ni $2p_{3/2}$ spectra of (a) a clean Ni metal surface, (b) a polycrystalline NiO powder, and (c) a polycrystalline $Ni(OH)_2$ powder. High-resolution O 1s spectra of (d) NiO and (e) $Ni(OH)_2$. Part of the metal Ni $2p_{1/2}$ line can be observed in (a). 65

Figure 3.3: High-resolution Ni $2p_{3/2}$ spectra of (a) γ-NiOOH and (b) β-NiOOH powders. High-resolution O 1s spectra of (c) γ-NiOOH and (d) β-NiOOH. 66

Figure 3.4: High-resolution Ni $2p_{3/2}$ spectra collected after (a) 1.2 x 10^9 L, (b) 3.6 x 10^9 L, (c) 8.4 x 10^9 L, and (d) 3.0 x 10^{10} L of exposure to H_2O at 300°C. A small contribution from the metal Ni $2p_{1/2}$ peak is visible on all spectra. 71

Figure 3.5: Ni $2p_{3/2}$ spectra with the Ni metal component subtracted following exposures of (a) 3.6 x 10^9 L, (b) 8.4 x 10^9 L, and (c) 3.0 x 10^{10} L of H_2O vapour. A doublet structure of the main line is visible, suggesting the formation of NiO. The resulting spectra following removal of the NiO contributions for doses of (d) 3.6 x 10^9 L, (e) 8.4 x 10^9 L, and (f) 3.0 x 10^{10} L of H_2O vapour are also shown. A small signal from NiS is also visible at the low BE end of the spectrum. The remaining Ni signal resembles that of NiOOH, a Ni^{3+} containing material. 72

Figure 3.6: High-resolution O 1s spectra for exposures of (a) 1.2 x 10^9 L, (b) 3.6 x 10^9 L, (c) 8.4 x 10^9 L, and (d) 3.0 x 10^{10} L. Two O species bound to Ni are proposed: O^{2-}, O (def), along with −COH, −CO, and −COO− adsorbates. The spectrum in (a) is noisy due to the small amount of O present. 75

Figure 3.7: QUASES™ 'Generate' fit for a Ni metal surface exposed to H_2O vapour for a dose of 3.0 x 10^{10} L. The experimental spectrum was fit using reference spectra acquired from a clean Ni metal surface and polycrystalline NiO powder. The surface was modeled using the 'island active' profile for the Ni metal component and the 'buried layer' profile for the NiO powder. The peaks located near 1033 eV and 965 eV are assigned to Ni 2s and Na 1s photoelectrons respectively. 77

Figure 3.8: Depth profiles through the near surface areas of Ni metal samples exposed to H_2O vapour for (a) 3.6 x 10^9 L, (b) 8.4 x 10^9 L, and (c) 3.0 x 10^{10} L. There is one distinct oxide phase identified: NiO and the 'Generate' analysis in all cases indicated island oxide growth. 78

Figure 3.9: ToF-SIMS depth profile of a polycrystalline Ni metal surface exposed to approximately 1.2 x 10^9 L of D_2O vapour in the temperature range of 300-400°C. The negative secondary ions monitored were D^-, $^{16}O^-$, NiO^-, $^{58}Ni^-$, and $^{12}C^-$. 79

Figure 3.10: Comparison of oxide growth curves for Ni metal reacted with O_2 [35] and H_2O. The oxide thicknesses in each case are plotted *versus* dose$^{1/2}$. 80

Figure 3.11: High-resolution (a) Ni $2p_{3/2}$ and (b) O 1s spectra collected following a H_2O vapour exposure of 3.0 x 10^9 L at 25°C. There is no evidence to suggest any

Ni^{2+} or Ni^{3+} has formed. The O 1s scan does show the presence of four O species: OH (ads), –COH, –CO, and –COO–. The start of the Ni $2p_{1/2}$ line is visible at high BE. 81

Figure 3.12: Comparison of the rates of oxidation of polycrystalline Ni metal surfaces exposed to H_2O vapour at 300°C with the oxidation of polycrystalline Fe surfaces dosed with H_2O at 150°C [39]. The rate of Ni oxidation is found to be much slower when compared to that of Fe. 83

Figure 4.1: A representative high-resolution C 1s spectrum collected from a sample of polycrystalline Cr_2O_3 powder. 93

Figure 4.2: The high-resolution (a) Cr $2p_{3/2}$ and (b) O 1s spectra for a polycrystalline Cr_2O_3 powder. 96

Figure 4.3: The high-resolution (a) Cr $2p_{3/2}$ and (b) O 1s spectra of a vacuum fractured Cr_2O_3 aggregate following annealing at 550°C for 3 h. 97

Figure 4.4: The high-resolution Cr $2p_{3/2}$ spectrum of a polycrystalline Cr_2O_3 powder fit with two sets of overlapping multiplet splitting peaks representing Cr^{3+} atoms in the (0001) plane (black lines) and all other crystallographic orientations (grey lines). 101

Figure 4.5: The high-resolution (a) O 1s and (b) Cr $2p_{3/2}$ spectrum for $Cr(OH)_3 \cdot xH_2O$. The Cr $2p_{3/2}$ spectrum was fit with contributions from both Cr_2O_3 (black lines) and $Cr(OH)_3$ (grey lines). The high-resolution spectrum for pure $Cr(OH)_3$ was reconstructed using the combined intensities of the obtained 5 multiplet splitting peaks and is shown in (c). The original Cr $2p_{3/2}$ spectrum was presented previously by Biesinger et al. [11]. 103

Figure 4.6: The high-resolution Cr $2p_{3/2}$ spectra collected from metal surfaces following doses of (a) 2.4 x 10^8 L of O_2 gas and (b) 3.0 x 10^8 L of H_2O vapour at 300°C and 130 Pa. The O 1s spectra for the doses of (c) 2.4 x 10^8 L of O_2 gas and (d) 3.0 x 10^8 L of H_2O vapour are also shown. The metal component was removed from each Cr $2p_{3/2}$ spectrum and the resultant subtracted spectra for doses of (e) 2.4 x 10^8 L of O_2 gas and (f) 3.0 x 10^8 L of H_2O vapour are also presented. The subtracted spectra show the possible presence of a hypo-stoichiometric Cr_2O_3 oxide. 105

Figure 4.7: The high-resolution (a) Cr $2p_{3/2}$ spectrum from a NiCr alloy surface containing a mixture of Cr_2O_3 (black lines) and $Cr(OH)_3$ (grey lines). The corresponding (b) Ni $2p_{3/2}$ and (c) O 1s spectra are also shown. 109

Figure 5.1: Fitted high-resolution (a) Ni $2p_{3/2}$ and (b) O 1s spectra from a polycrystalline NiO powder loaded into the spectrometer through an Ar filled glove box. The Ni $2p_{3/2}$ spectrum was fit using the empirical peak fit for NiO tabulated in reference [4]. The O 1s spectrum has been fit with contributions from O^{2-} and O def species. The remaining spectral intensity was assigned to organic contamination. 117

Figure 5.2: Fitted high-resolution Ni $2p_{3/2}$ and O 1s spectra collected from three β-$Ni(OH)_2$ samples. The spectra illustrate the Ni $2p_{3/2}$ and O 1s line shapes for (a) and (b) stoichiometric β-$Ni(OH)_2$, (c) and (d) stoichiometric β-$Ni(OH)_2$ containing interstitial H_2O (H_2O (int)) within the brucite lattice, and (e) and (f) OH^- deficient β-$Ni(OH)_2$. The Ni $2p_{3/2}$ spectra were fit using the empirical peak fit for β-$Ni(OH)_2$ tabulated in reference [4]. 119

Figure 5.3: Fitted high-resolution (a) Ni $2p_{3/2}$ and (b) O 1s spectra for γ-NiOOH powder. The Ni $2p_{3/2}$ spectrum was modeled using a peak fit originally presented in reference [18]. The O 1s spectrum shows contributions from O^{2-} and OH^- species along with additional intensity assigned to organic contamination at higher BE. The expected 1:1 O^{2-}:OH^- peak area ratio is not observed here and suggests that the γ-NiOOH sample has started to decompose..... 120

Figure 5.4: Fitted high-resolution (a) Ni $2p_{3/2}$, (b) Cr $2p_{3/2}$ and (c) O 1s spectra for a powder sample of $NiCr_2O_4$. The high-resolution Ni $2p_{3/2}$ and Cr $2p_{3/2}$ spectra are shown with the fits presented in references [1 and 19]. The O 1s spectrum shows the presence of lattice O^{2-} species along with small amounts of organic contamination. An additional peak was also required to completely fit the envelope and was assigned to H_2O (int). 121

Figure 5.5: Fitted high-resolution (a) Ni $2p_{3/2}$ and (b) O 1s spectra collected from a polycrystalline Ni metal disk subjected to aqueous oxidation. The Ni $2p_{3/2}$ spectrum showed contributions from metallic Ni, NiO and β-$Ni(OH)_2$. Fitting of the O 1s spectrum showed corresponding contributions from NiO, β-$Ni(OH)_2$, H_2O (int), and organic contamination. 125

Figure 5.6: Fitted high-resolution (a) Ni $2p_{3/2}$, (b) Cr $2p_{3/2}$, and (c) O 1s spectra collected from a NiCr disk subjected to aqueous oxidation. The Ni $2p_{3/2}$ spectrum showed contributions from metallic Ni, NiO and β-$Ni(OH)_2$. The Cr $2p_{3/2}$ spectrum was best fit with contributions from metallic Cr, Cr_2O_3, $Cr(OH)_3$, and a Cr^{6+}-containing oxide. Fitting of the O 1s spectrum showed corresponding contributions from NiO, Cr_2O_3, a Cr^{6+}-containing oxide, β-

$Ni(OH)_2$, and $Cr(OH)_3$. Two additional components representing H_2O (int) species associated with both β-$Ni(OH)_2$ and $Cr(OH)_3$ were also observed. The remainder of the O 1s intensity was determined to result from organic contamination. 127

Figure 6.1: The high-resolution (a) Ni $2p_{3/2}$ and (b) Cr $2p_{3/2}$ spectra collected from a polished and sputter cleaned polycrystalline NiCr surface. Parts of the metal Ni $2p_{1/2}$ and Cr $2p_{1/2}$ lines are observed at higher BEs. 135

Figure 6.2: The high-resolution (a) Ni $2p_{3/2}$ and (b) O 1s spectra collected following 1 h of surface cleaning of sample Ni-1 at 25°C at a reducing $E_{app} = -1.5$ V in a basic solution vs. a Ag/AgCl reference electrode ($pH_{25°C} = 10.1$). 140

Figure 6.3: The high-resolution (a) Ni $2p_{3/2}$ and (b) O 1s spectra collected for a Ni metal surface following aqueous oxidation at 25°C in a basic solution ($pH_{25°C} = 10.1$) for 48 h at a slightly oxidizing potential $E_{app} = 0.0$ V vs. a Ag/AgCl reference electrode. The high-resolution (c) Ni $2p_{3/2}$, (d) Cr $2p_{3/2}$ and (e) O 1s spectra for a NiCr surface oxidized for 48 h under the same temperature, solution and potential conditions. 142

Figure 6.4: The high-resolution (a) Ni $2p_{3/2}$ and (b) O 1s spectra collected for a Ni metal surface following aqueous oxidation at 150°C in a basic solution ($pH_{150°C} = 7.8$) for 3 h at a slightly oxidizing $E_{app} = 0.0$ V vs. a Ag/AgCl reference electrode. The high-resolution (c) Ni $2p_{3/2}$, (d) Cr $2p_{3/2}$ and (e) O 1s spectra for a NiCr surface oxidized for 3 h under the same temperature, solution pH and potential conditions. 144

Figure 6.5: The ToF SIMS images mapping the Ni and Cr distribution across a 200 μm x 200 μm area and corresponding depth profiles collected from the NiCr surfaces oxidized for 24 h at 150°C at a mildly oxidizing E_{app} = 0.0 V vs. a Ag/AgCl reference electrode. (a) top view, and (b) depth profile in basic solution, $pH_{150°C}$ = 7.8; (c) top view, and (d) depth profile in neutral solution, $pH_{150°C}$ = 5.8; and (e) top view, and (f) depth profile in acidic solution, $pH_{150°C}$ = 4.1. The yellow areas represent the regions of highest Ni or Cr concentrations, while the black areas indicate the positions where no signal was detected. The solution/oxide (X_1) and oxide/alloy (X_2) interfaces are also marked on the depth profiles..... 145

Figure 6.6: The high-resolution (a) Ni $2p_{3/2}$, (b) Cr $2p_{3/2}$ and (c) O 1s spectra collected for a NiCr alloy sample following 3 h of aqueous oxidation at 150°C under a slightly oxidizing E_{app} = 0.0 V vs. a Ag/AgCl reference electrode in a neutral solution ($pH_{150°C}$ = 5.8). 147

Figure 6.7: The high-resolution (a) Ni $2p_{3/2}$, (b) Cr $2p_{3/2}$ and (c) O 1s spectra collected for NiCr alloy samples following 3 h of aqueous oxidation at 150°C under a slightly oxidizing E_{app} = 0.0 V vs. a Ag/AgCl reference electrode in acidic solution ($pH_{150°C}$ = 4.1). The high-resolution (d) Ni $2p_{3/2}$, (e) Cr $2p_{3/2}$ and (f) O 1s spectra for a NiCr surface oxidized for 24 h under the same temperature, solution pH and potential conditions..... 149

Figure 6.8: The high-resolution (a) Ni $2p_{3/2}$ and (b) O 1s spectra collected for a Ni metal surface following aqueous oxidation for 3 h at 150°C in basic solution ($pH_{150°C}$ = 7.8) at a highly oxidizing potential of 1.5 V vs. a Ag/AgCl

reference electrode. The high-resolution (c) Ni $2p_{3/2}$, (d) Cr $2p_{3/2}$ and (e) O 1s spectra for a NiCr surface oxidized for 48 h under the same temperature, solution pH and potential conditions. 151

LIST OF APPENDICES

Appendix A The Ni and O surface concentrations in at.% for Ni metal surfaces exposed to doses of O_2 gas.....175

Appendix B Copyright release from Wiley Inter Science for the publication in Surface and Interface Analysis 39 (2007) 582.....176

Appendix C Copyright release from Elsevier for the publication in Journal of Electron Spectroscopy and Related Phenomena 175 (2009) 55.....179

Appendix D Copyright release from Elsevier for the publication in Journal of Electron Spectroscopy and Related Phenomena 184 (2011) 29.....183

LIST OF ABBREVIATIONS AND SYMBOLS

a	half the ion jump distance
Ag	silver
AgCl	silver chloride
AL	attenuation length
Al	aluminum
γ-Al_2O_3	gamma aluminum oxide
Ar	argon
Ar^+	argon ion
ARXPS	angle resolved X-ray photoelectron spectroscopy
at.%	atomic percent
Au	gold
Bi^+	bismuth ion
Bi^{3+}	trivalent bismuth ion
BE	binding energy
ΔBE	change in binding energy
–C–C–,–C–H/C (adv)	hydrocarbon/adventitious carbon
–C=O	carbonyl group
–COC–	ether functional group
–COH	alcohol functional group
–COOH	carboxylic acid functional group
–COO–/O=CO–	ester functional group
C	constant in the inverse logarithmic rate equation
C	carbon
C’	constant in the direct logarithmic rate equation
C”	constant in the parabolic rate equation
CEM	channel electron multiplier
CHA	concentric hemispherical analyzer
Ca	calcium
Cl	chlorine
Co	cobalt
Cr	chromium
Cr^{2+}	divalent chromium cation
Cr^{3+}	trivalent chromium cation
Cr^{6+}	hexavalent chromium cation
Cr_2O_3	chromium (III) oxide
CrO_3	chromium (VI) oxide
$Cr(OH)_3$	chromium hydroxide
Cs^+	cesium ion
Cu	copper
d	analysis depth/overlayer thickness/oxide thickness
D	deuterium
e^-	electron

E_{app}	applied potential
EDX	energy dispersive X-ray analysis
E_{Fermi}	Fermi level
E_P	pass energy
ESCA	electron spectroscopy for chemical analysis
eV	electron volt
Fe	iron
$Fe(OH)_2$	iron hydroxide
FeOOH	iron oxyhdroxide
FWHM, ΔE	full width half maxium
γ	increase in the activation energy with increasing film thickness
GL	Gaussian-Lorentzian
GS	Gupta and Sen
H	hydrogen
H_2	hydrogen gas
H (ads)	adsorbed hydrogen
H_2O	water
H_2O (ads)	adsorbed water
H_2O (int)	interstitial water
$h\nu$	photon energy
$I_{0,d}$	photoelectron intensity at the surface, at depth d
$I_{A,n}$	photoelectron peak area for element A, element n
$I_{m,o}$	photoelectron peak area for the clean metal/the metal oxide
IMFP, λ	inelastic mean free path
j	total angular momentum quantum number
k	Boltzmann's constant
KE	kinetic energy
keV	kiloelectron volt
kV	kilovolt
l	angular momentum quantum number
$\lambda_{m,o}$	inelastic mean free path of the clean metal/the metal oxide
LEED	low energy electron difraction
L	Langmuir
Li	lithium
M	metal
M^{2+}	divalent metal cation
MCM	mixed conduction model
µm	micrometre
Mg	magnesium
Mn	manganese
MO	metal oxide
MΩ	mega ohm
n	principal quantum number
N	nitrogen
$N_{m,o}$	volume density of the clean metal/the metal oxide

Na	sodium
nA	nano Ampere
Ni	nickel
Ni^{2+}	divalent nickel cation
Ni^{3+}	trivalent nickel cation/electron hole
NiCr	nickel-chromium
NiCr (20%)	nickel-chromium containing 20% chromium
NiCrFe	nickel-chromium-iron
$NiCr_2O_4$	nickel chromite
NIST	National Institute of Standards and Technology
nm	nanometre
NiO	nickel (II) oxide
Ni_2O_3	nickel (III) oxide
β-$Ni(OH)_2$	beta nickel hydroxide
$Ni(OH)_2$	nickel hydroxide
NiOOH	nickel oxyhydroxide
β-NiOOH	beta nickel oxyhydroxide
γ-NiOOH	gamma nickel oxyhydroxide
NRA	nuclear reaction analysis
O	oxygen
O^-	negative oxygen ion fragment
O^{2-}	oxygen anion/lattice oxide
O (ads)	adsorbed atomic oxygen
O_2	oxygen gas
O_2 (ads)	adsorbed oxygen gas
O (def)	defective oxygen
OH^-	hydroxide anion
OH (ads)	adsorbed hydroxyl group
Pa	Pascal
PDM	point defect model
$\phi_{spectrometer}$	work function of the spectrometer
pA	pico Ampere
Pt	platinum
PWR	pressurized water reactor
q	ionic charge
q	valence charge
QUASES™	Quantitative Analysis of Surfaces by Electron Spectroscopy
r	radius
R	universal gas constant
REELS	reflection electron energy loss spectroscopy
RSF, $S_{A,n}$	relative sensitivity factor, relative sensitivity factor for element A, element n
RGA	residual gas analyzer
s	electron spin angular momentum quantum number
S	sulfur
SEM	scanning electron microscopy

SG	steam generator
Si	silicon
SMA	spherical mirror analyzer
SIMS	secondary ion mass spectrometry
θ	electron take off angle
t	exposure time
T	temperature
Ti	titanium
ToF	time of flight
ToF SIMS	time of flight secondary ion mass spectrometry
V	potential
x	oxide thickness
XPS	X-ray photoelectron spectroscopy
XRD	X-ray diffraction
V_M^{2-}	metal vacancy having a divalent negative charge
V_O^{2+}	oxygen vacancy having a divalent positive charge
W	tungsten
$X_{A,n}$	elemental atomic concentration of element A, element n
z	atomic number
Zr	zirconium

Chapter 1 Introduction

1.1 The Study of Thin Films

An understanding of the structure and composition of the oxides formed on metals and their alloys is important as these films provide a barrier of protection between the material and the environment. Of particular interest is an understanding of the reaction products formed during the initial stages of reaction, as the nature of the oxides formed at this juncture will greatly affect long term surface passivation and/or metal degradation. To accurately monitor these films the surface analytical techniques employed must be sensitive to low elemental concentrations, differences in elemental chemical states and/or bonding environments, and have an information depth of 10 nm or less.

X-ray Photoelectron Spectroscopy (XPS) or Electron Spectroscopy for Chemical Analysis (ESCA) is a technique that meets all of these criteria. Present day instruments are able to detect all elements in the periodic table except for H and He and have detection limits of 0.1 atomic % (at.%). Certain spectrometers (i.e. Kratos Axis Ultra) have tuneable spatial resolutions that allow for the analysis of areas as large as 700 μm x 300 μm to spots as small as 10 – 20 μm in diameter to be probed. XPS can also provide information on the oxidation state and local bonding environment of atoms within a surface. Due to the high elemental sensitivity and tuneable spatial resolution of XPS, changes in oxide chemistry can be monitored over relatively large (few hundred μm) or more localized (tens of μm) areas. The ability of XPS to differentiate between atoms of the same oxidation state having different bonding arrangements allows for the quantitative analysis of surfaces containing mixed oxide phases. This is of particular importance when studying the corrosion products formed in aqueous environments where,

depending on the reaction conditions and the material being studied, many different metal oxides, hydroxides and oxyhydroxides may be present. The inability of XPS to detect H does not completely limit this technique when it comes to studying metal hydroxides and oxyhydroxides, as the local electronic densities around a metal cation and oxygen anion (O^{2-}) change depending on whether a H atom is present or not. That being said, investigating the role of atomic H in an oxidation process requires the use of a complementary surface analytical technique. Finally, depending on the material being analyzed XPS has a maximum analysis depth of approximately 10 nm and as a result, the thickness and/or structure of any oxide overlayers thinner than this detection depth can be modeled using complementary analytical algorithms [1-2].

1.2 Project Overview

In this thesis XPS was used as the primary investigative tool to study the oxides formed on polycrystalline samples of Ni metal, Cr metal and NiCr (20%) (NiCr) alloy surfaces exposed to O_2 gas, H_2O vapour or aqueous solutions under controlled electrochemical potentials and pHs. In order to better understand the reaction products formed on these surfaces the XPS spectra of a number of well characterized Ni- and Cr-containing oxide and hydroxide powders were also examined. The role of H in the oxidation processes on Ni and the NiCr alloys studied was monitored using another analytical technique Secondary Ion Mass Spectrometry (SIMS).

This work is intended to provide a knowledge base to which the study of the oxides grown on more complex NiCr-containing alloys can be compared in the future. Currently, NiCr-containing alloys are used in a number of highly reactive environments including, but not limited to, turbines, jet engines and the steam generator (SG) tubing of

pressurized water reactors (PWR) [3]. Of particular interest to our research group are the ternary NiCrFe alloys 600 and 690, which are used in the latter application.

1.3 Oxidation Mechanisms

The initial oxidation of a bare metal surface is generally understood to begin with the adsorption of O_2 gas, which subsequently dissociates into adsorbed atomic oxygen (O (ads)) [4-5]. The O (ads) atoms then covalently bond to adjacent metal atoms, weakening the attachment of the latter to the metal crystal. This is followed by the place exchange of a metal and an O^{2-} ion at the metal/gas interface resulting in the formation of the first one or two monolayers of oxide (see Figure 1.1(a)). The formation of thin passive films beyond the place exchange process can be described using either inverse logarithmic, direct logarithmic or parabolic rate laws [4-10]. Typically, the logarithmic mechanisms best describe film formation at low temperature, while the parabolic law better models oxide growth at higher temperatures. The transition temperature from logarithmic growth to parabolic growth is ambiguous and dependent on the metal being oxidized.

The theory of inverse logarithmic kinetics was first suggested by Mott [6] and Mott and Cabrera [7]. They proposed that, at low temperatures oxidation was driven by the tunnelling of electrons from the metal to O (ads) species at the surface. This tunnelling of electrons produces an electric field, in which ions are mobile, resulting in the thickening of the oxide with time (see Figure 1.1(b)). The potential across the oxide is assumed to be constant and as a result the strength of the field diminishes with time. Oxidation is terminated when the electric field is no longer strong enough to support ion migration. The integrated form of the inverse logarithmic rate equation is shown below [8]:

$$\frac{1}{x} = -\left[\frac{kT}{qaV}\right] \ln t + C \qquad 1.1$$

where x is the oxide thickness, k represents Boltzmann's constant, T is the reaction temperature, q is the ionic charge, a is equal to half of the ion jump distance, V is the potential across the oxide, t is the exposure time, and C is a constant.

The inverse logarithmic theory was unable to accurately model the low temperature oxidation of all metal surfaces. As a result, the direct logarithmic kinetic model was later proposed by Eley and Wilkinson [4]. As with the inverse logarithmic mechanism, oxidation is driven by ion migration in an electric field created by tunnelling electrons. In this model the electric field, not the potential, across the oxide film is assumed to be constant and oxide growth continues until the potential can no longer support ion migration. The direct logarithmic rate equation is presented below in its integrated form [4]:

$$x = \left[\frac{RT}{\gamma}\right] \ln t + C' \qquad 1.2$$

where x represents the film thickness, R is the universal gas constant, T is the reaction temperature, γ is the observed increase in activation energy as the oxide film thickens, t is the exposure time and C' is a constant.

At elevated temperatures the oxidation of metal surfaces tends to follow parabolic kinetics as described by Wagner [7,11-13]. The Wagner model assumes that the oxide formed is compact and adherent, the reaction rate is controlled by either cation or anion diffusion through the film, thermodynamic equilibria are established at both the metal/oxide and oxide/gas interfaces, thermodynamic equilibrium also exists throughout the film, and the oxide formed only deviates slightly from stoichiometry. For oxides in

which cations are the mobile species diffusion is driven along the metal chemical potential gradient across the film. Conversely, for oxides in which anion diffusion dominates, the driving force of the reaction is proportional to the O_2 chemical potential gradient. In both cases, as the film thickens, the rate of oxidation decreases until the reaction terminates. The full integrated parabolic kinetic rate equation is shown below [7,11-13]:

$$x = C''t^{1/2} \qquad 1.3$$

where x represents the film thickness, C" is the parabolic rate constant and t is the exposure time. The parabolic rate constant is dependent on the volume of the oxide present per metal atom, the diffusion coefficient and the concentration of mobile species.

Metal oxides can generally be grouped into three different classes; p-type, n-type and amphoteric semi-conductors [13]. During the growth of a p-type oxide a small number of cation vacancies and electron holes are created within the oxide lattice (cation deficient). In p-type oxides the mobile species are cations, which migrate/diffuse through lattice defect sites such as vacancies and/or grain boundaries to the oxide/gas interface where they react with O_2. In the case of NiO, defect formation involves the creation of a Ni^{2+} vacancy at the oxide/gas interface and, in order to balance charge, two neighbouring Ni^{2+} atoms each lose an electron forming two Ni^{3+} (electron holes). Conversely, n-type oxides can be grouped into two classes. In the first class oxidation proceeds via the migration of free electrons and excess metal ions through interstitial lattice positions in the oxide, while in the second class film growth proceeds via the formation of anion vacancies (anion deficient) and anion migration. In the former case the oxide grows at

a) Place exchange model

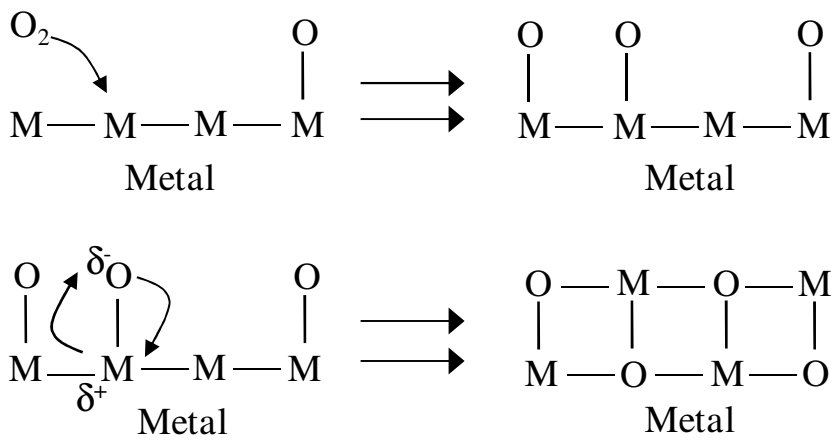

b) Oxide growth in the presence of an electric field

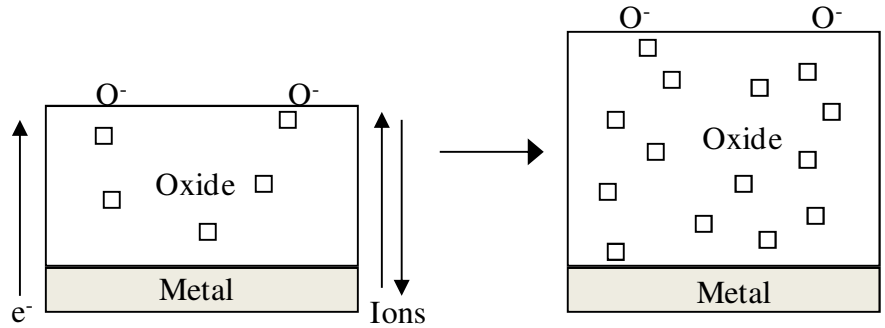

Figure 1.1: The mechanism for the oxidation of a metal (M) surface exposed to O_2 gas. The initial place exchange reaction resulting in the first layers of oxide is shown in (a). The continuous growth of a film following logarithmic or parabolic kinetics beyond the place exchange process is shown in (b). The vacancies (□) present within the film provide pathways for ion migration.

the oxide/gas interface while in the latter case oxidation occurs at the metal/oxide boundary. Some oxides such as Cr_2O_3 are known as amphoteric and will exhibit either p-type or n-type characteristics depending on the reaction conditions. For example at low O_2 pressures Cr_2O_3 behaves like a cation excess n-type semiconductor, while at higher O_2 activities it exhibits p-type properties.

Oxide film growth on metal surfaces exposed to aqueous solutions is best described using the Point Defect Model (PDM) proposed by Macdonald et al. [14-15]. A simplified version of the PDM is presented in Figure 1.2 for a MO type oxide. This model is similar to the direct logarithmic mechanism proposed by Eley and Wilkinson [4], in which the electric field across the film is assumed to be constant. In simplified terms, film growth proceeds via the dissolution of metal cations ($M^{2+} \rightarrow M^{2+}_{(aq)}$) at the oxide/solution interface. This introduces cationic vacancies (V_M^{2-}) to the film similar to the p-type oxide growth discussed earlier. These vacancies will migrate in the electric field towards the oxide/metal interface where they are filled with metal cations (M^{2+}) produced at the metal surface. The oxidation of metal atoms at the metal surface introduces oxygen vacancies (V_O^{2+}) to the oxide which will diffuse towards the oxide/solution interface. At the film/electrolyte boundary adsorbed H_2O and/or dissolved O_2 gas are reduced creating O^{2-} anions, destroying the anionic vacancies. In the PDM model the film behaves like an electronically doped semi-conductor due to the presence of the cationic and anionic vacancies. More recently, the PDM has been expanded by Bojinov et al. to include film properties such as capacitance, resistance, thickness and conductivity in the theoretical calculations [16-17]. The model of Bojinov et al. is termed the Mixed Conduction Model (MCM).

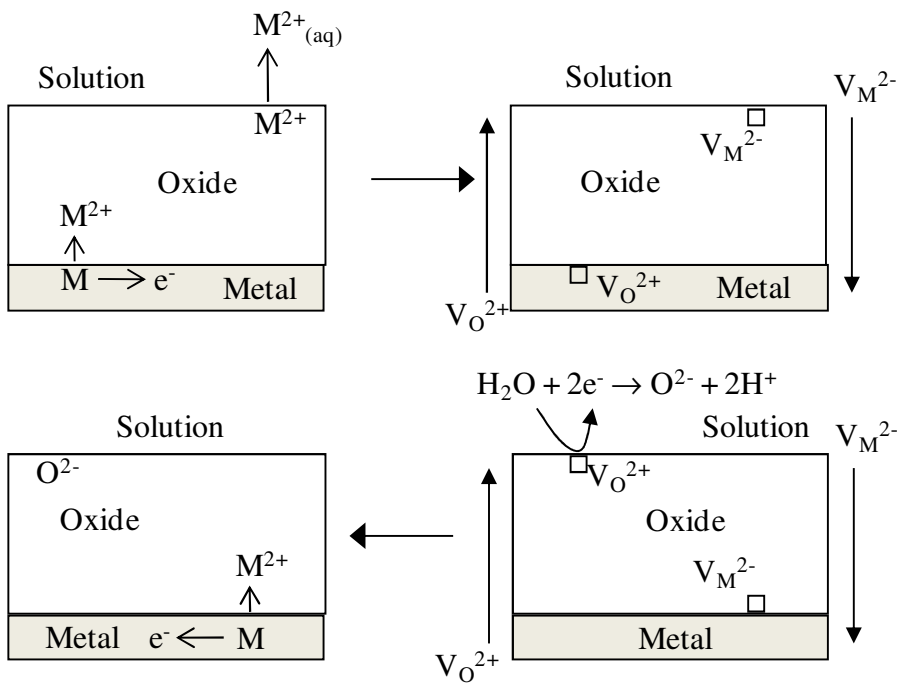

Figure 1.2: Simplified diagram of the PDM model showing the major cationic, anionic and vacancy species involved in the growth of an MO type oxide during reaction with a H_2O molecule.

1.4 X-ray Photoelectron Spectroscopy

XPS uses soft X-rays to excite core and valence electrons within the atoms of a surface. If the X-ray energy is large enough photoelectrons are expelled from the material and their kinetic energies (KE) are measured by the instrument. This excitation process is known as the photoelectric effect and is illustrated in Figure 1.3. Differences in chemical elements within the near surface region are identified on the basis of their binding energy (BE), which is measured relative to the Fermi level (E_{Fermi}) of the individual atoms. The KE and BE of the photoelectron are related via the following equation:

$$KE = h\nu - BE - \phi_{spectrometer} \qquad 1.4$$

where $h\nu$ represents the energy of the absorbed photon and $\phi_{spectrometer}$ is the work function of the spectrometer.

In general, X-rays having energies in the 1-2 keV range will penetrate several hundred nm into a surface ionizing atoms to that depth. In order for the resultant photoelectrons to be detected they first must escape from the surface without interacting with overlaying atoms; which may lead to loss of KE (inelastic scattering). The probability that a photoelectron will reach the surface without losing any of its KE can be approximated using the Beer-Lambert Law:

$$I_d = I_0 e^{-d/\lambda} \qquad 1.5$$

where I_d is the photoelectron intensity originating from atoms at depth d, I_0 is the signal emanating from the surface atoms, and λ is the electron inelastic mean free path (IMFP). The IMFP represents the average distance a photoelectron can travel before undergoing inelastic scattering and is dependent on both the material properties (i.e. density) and

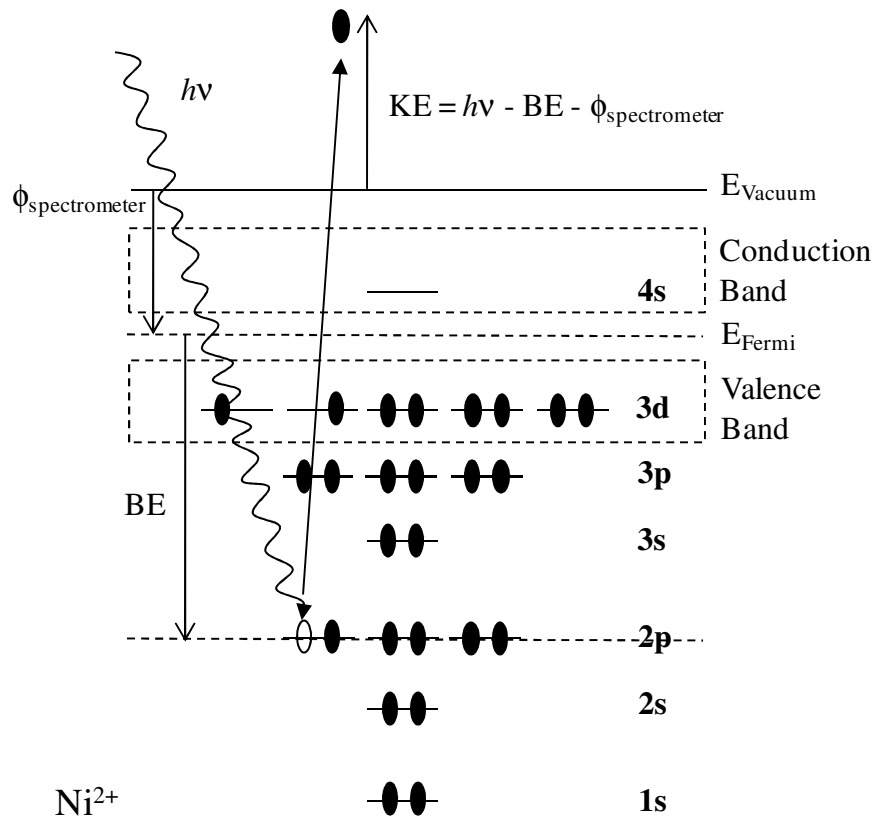

Figure 1.3: An electron energy diagram for a Ni^{2+} cation showing the absorption of a photon and resultant expulsion of a 2p level photoelectron.

electron KE. If a Gaussian probability distribution is assumed, then 95% of the photoelectrons detected would have been produced within a depth of 3λ. Typical IMFPs for the metal 2p core photoelectrons for transition metals and their oxides are calculated to be on the order of 1.1 – 1.8 nm (using Al Kα) [18-19] resulting in an information depth between 3.3 – 5.4 nm for these systems.

All XPS analysis completed as part of this work was performed at Surface Science Western, located at the University of Western Ontario, using a Kratos Axis Ultra Spectrometer. Figure 1.4(a) shows a simplified layout of the main components of the XPS instrument. The Kratos Axis Ultra spectrometer is equipped with a monochromatic Al Kα X-ray source having a characteristic excitation energy of 1486.6 eV and a line width between 0.3 – 0.4 eV. This instrument also contains a dual X-ray source capable of producing achromatic Mg Kα and Zr Lα photons with respective energies/line widths of 1253.6/0.7 eV and 2042.4/1.7 eV. The base pressures in the analytical chamber are typically near 3 x 10^{-7} Pa prior to introduction of the sample.

Photoelectrons ejected from a sample surface are focused towards the entrance slit of a combined concentric hemispherical (CHA) and spherical mirror (SMA) energy analyzer. Prior to entering the analyzer the energies of the photoelectrons are retarded to a fixed pass energy (E_P). To monitor the photoelectron counts as a function of BE (spectrum mode) the CHA is used. Once inside the CHA the photoelectrons travel between two curved plates (hemispheres) having focusing potentials $-V_1$ and $-V_2$ (see Figure 1.4(b)). The instrument transmission function is defined as the fraction of the total number of photoelectrons collected at the sample surface that pass through the CHA into the detector. The transmission function is dependent on the CHA slit width, CHA radius

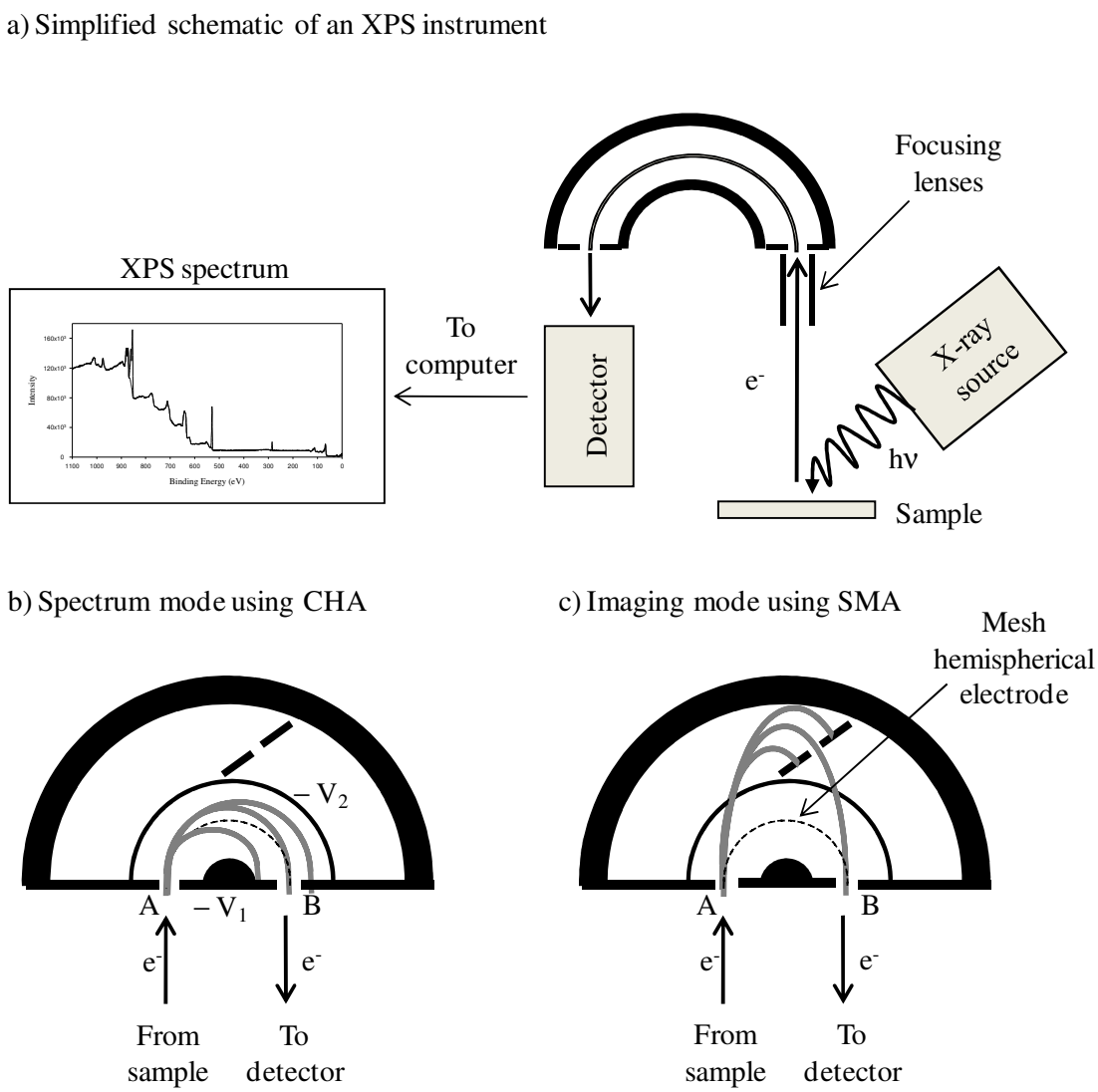

Figure 1.4: (a) Simplified schematic following a photoelectron (e^-) through a Kratos Axis Ultra spectrometer. (b) The expanded view of the energy analyzer setup in spectrum mode employing the CHA. Under these conditions the photoelectrons enter the energy analyzer at point A and travel between two negatively charged plates. The grey lines represent possible pathways these electrons may travel through the energy analyzer. Only the photoelectrons with the selected pass energies will exit the analyzer at point B and enter the detector. (c) The expanded view of the energy analyzer setup in imaging mode employing the SMA. The presence of the mesh hemispherical electrode and additional slit allows for specific photoelectron BEs to be selected allowing for high-resolution images to be collected.

and the initial KE of the photoelectrons. The absolute resolution (ΔE) of the instrument is defined by the full width at half maximum (FWHM) of the resultant photoelectron peaks. The absolute resolution of the instrument increases with decreasing pass energy. Any increase in spectral resolution results in a loss of photoelectron signal due to a higher dispersion of the electrons around the exit slit.

To collect chemical state images on the surface of the sample the SMA is employed. Similar to the CHA portion of the analyzer the SMA has two hemispherical electrodes. The main differences between the two analyzers is that an inner mesh electrode and an additional energy selecting slit are employed in the SMA design (see Figure 1.4(c)). These two advancements allow chemical state images to be collected over a range of photoelectron BEs. The image datasets can then be combined using analytical software [1] and converted into spectral datasets producing XPS spectra at each image pixel [20-21].

Once the electrons exit the CHA they enter a channel plate detector which consists of several semiconducting glass tubes connected in series known as channel electron multipliers (CEMs). Electrons entering the CEMs collide with the walls of the tubes resulting in a cascade effect as secondary electrons are produced. The cascade effect results in an increase in the electron signal by a factor of $> 10^4$.

By convention XPS spectra are plotted as a function of photoelectron intensity vs. BE. Survey spectra, sometimes termed wide or broad scans, are collected using a high pass energy (> 120 eV), a high energy step (0.7 eV) and a large BE window (> 1000 eV). These spectra have low resolution however, the large BE range allows for the photoelectron peaks for all elements present to be analyzed. Figure 1.5 shows the survey

spectrum acquired for a sample of polycrystalline NiO powder containing a small C impurity. Several electronic structures are observed and attributed to photoelectrons excited from the Ni (2s, 2p, 3s, 3p), O (1s) and C (1s) core energy levels, photoelectrons ejected from the Ni (3d) and O (2s) valence orbitals, as well as electrons originating from Ni LMM and O KLL Auger processes. In all cases only the electrons that had escaped from the surface without undergoing any inelastic scattering interactions contributed to the intensity of these peaks. At higher BEs (> 600 eV) an increase in the spectral background is observed and arises from the detection of photoelectrons having undergone one or more energy loss events while escaping the surface (see Equation 1.4).

From the XPS survey spectrum the elemental concentration for a surface containing two or more elements (except for H and He) can be determined using the following formula:

$$X_A = \frac{\frac{I_A}{S_A}}{\sum_n \frac{I_n}{S_n}} \qquad 1.6$$

where X_A, I_A and S_A represent the atomic concentration (in at%), the peak area and the relative sensitivity factor (RSF) for element A, in a surface having n elements. Any contributions from the energy loss background to the photoelectron peak intensities are removed using a subtraction algorithm. In Figure 1.5(a) all spectral background intensity was removed using a Shirley baseline. The RSF values correct for differences in peak intensities resulting from the probability a specific photoelectron transition will occur (cross-section), element IMFP, instrument transmission function and detector efficiency. A library of RSF values has been compiled for the Kratos Axis Ultra spectrometer and are based on the empirically derived cross-sections of Wagner [1,22-23]. Using Equation

a) Survey spectrum for polycrystalline NiO powder

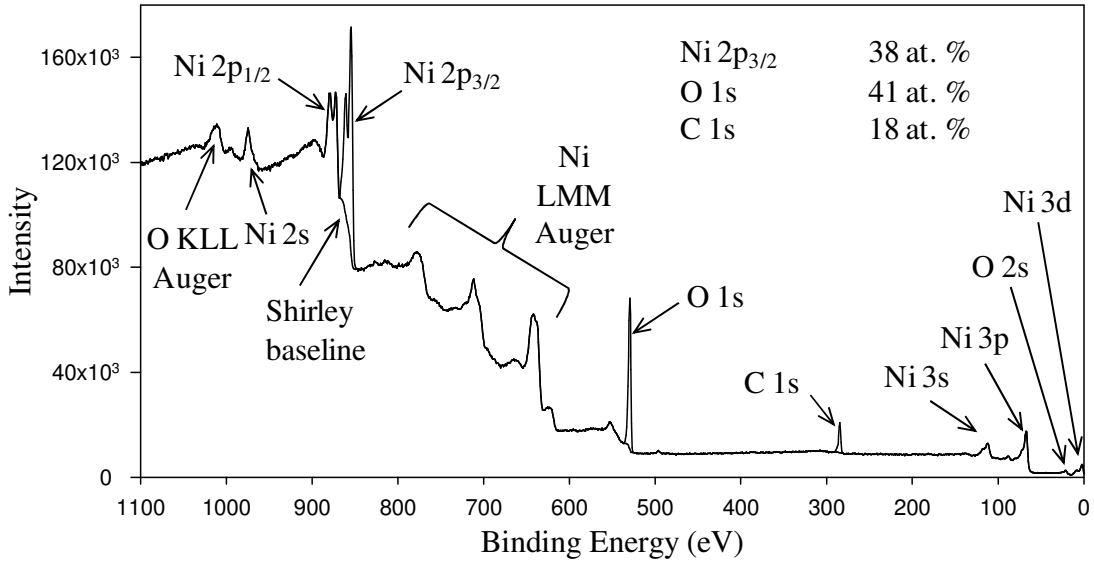

b) High-resolution Ni $2p_{3/2}$ spectrum for polycrystalline NiO powder

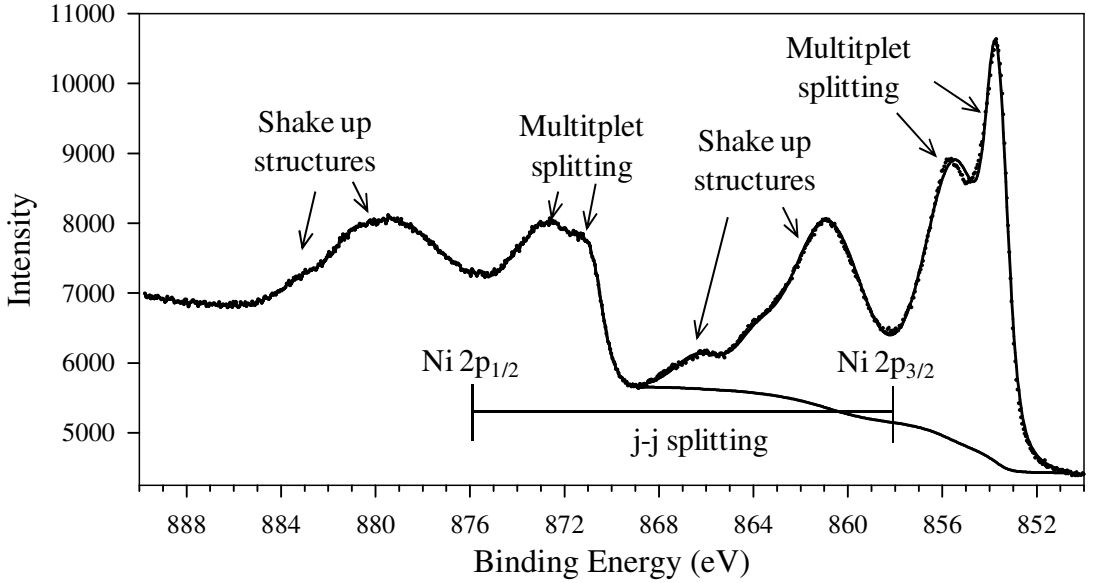

Figure 1.5: (a) The survey spectrum collected for a polycrystalline NiO powder sample containing a small C impurity. The elemental concentrations in at.% for the Ni, O and C species have been calculated using Equation 1.6 and are also presented. (b) The high-resolution Ni 2p spectrum taken for the same NiO sample. The electronic structural features arising from j-j coupling (Ni $2p_{3/2}$, Ni $2p_{1/2}$), multiplet splitting and shake up interactions are clearly visible.

1.6 and the Ni $2p_{3/2}$, O 1s and C 1s peak areas the relative concentrations of these three surface species were calculated (see Figure 1.5(a)).

The oxidation state and local bonding environments of atoms within a surface are monitored using high-resolution spectra. These scans are typically collected at a low pass energy (10 – 20 eV), a low energy step (0.1 – 0.05 eV) and BE windows ranging from 20 – 40 eV. An example Ni 2p high-resolution spectrum for a polycrystalline NiO powder is presented in Figure 1.5(b).

At the atomic level, absorption of a photon results in the expulsion of a photoelectron producing an atom in an excited state. The observed BE of this photoelectron is defined as the difference in energy between the photoionized atom (final state) and the unexcited atom (initial state). The chemical shift refers to the small changes in photoelectron BE of an atom based on its local bonding environment and/or chemical state. These BE differences can be explained qualitatively using the charged sphere model. In this model the individual atoms of a surface are considered to be hard spheres having a valence charge q at a fixed radius of r. Inside the sphere the charge distribution is considered to be uniform and as a result any change in the valence charge density will shift the BE of all core electrons by:

$$\Delta BE = q/r \qquad 1.7$$

As an example, consider the oxidation of metallic Cr to Cr^{3+}. The loss of 3 valence electrons would result in the remaining electrons being held more tightly by the nucleus of the atom and thereby an increase in BE would be observed.

In the case of an insulating material the continued exposure to a monochromated X-ray source will result in a build-up of positive charge on the surface over time. As a

result the photoelectron peaks become broadened and no chemical state information can be obtained. This "charging" effect is minimized by flooding the sample surface with low energy electrons.

The cross-section (peak shape and intensity) for each core energy level photoelectron peak is defined by the principal quantum number *n*, the angular momentum quantum number *l*, and the electron spin angular momentum quantum number *s*. Following photoionization from an orbital where $l = 0$ (i.e. 1s shell) a singlet photoelectron peak is observed as only one final state is possible. For orbitals where $l > 0$ (i.e. 2p shells) the orbital angular momentum and spin angular momentum of the remaining electron can couple either in parallel (lower energy) or anti-parallel (higher energy), resulting in two possible final states. This gives rise to a doublet structure defined by the following relationship:

$$j = (l \pm s) \qquad 1.8$$

where *j* is the total angular momentum quantum number. This phenomenon is referred to as spin-orbit or *j-j* coupling (see Figure 1.5(b)). In the case of the 2p spectral line *j* values of 3/2 ($2p_{3/2}$) and 1/2 ($2p_{1/2}$) are obtained. The separation between the doublet peaks increases with atomic number *z* and is scaled by a factor of $1/r^3$, with r representing the radius of the orbital from which the photoelectron has been ionized. The relative electron populations of the respective doublet peaks are defined by $2j + 1$ resulting in a $2p_{3/2}$:$2p_{1/2}$ ratio of 2:1.

The 2p spectra for transition metal cationic species having unpaired d electrons are further complicated by additional fine structures resulting from multiplet splitting (see Figure 1.5(b)). These structures arise from the parallel or anti-parallel coupling of the

spin angular momentum of an unpaired core electron with the spin angular momentum of unpaired 3d valence electrons. Exchange interactions between electrons with parallel spins are lower in energy than the interactions between electrons with anti-parallel spins, producing a doublet structure. Additional contributions from atomic relaxation and ligand interactions also contribute to the multiplet structures observed. Other high BE spectral features common to many transition metals are shake up and/or shake off peaks (see Figure 1.5(b)). Shake up peaks arise from simultaneous loss of a photoelectron and excitation of a valence electron to a higher unoccupied bound state. Shake off are similar in origin only instead of the valence electron being excited to an unoccupied energy level it is lost to the continuum, resulting in a doubly ionized final state. The observed BE of the latter peaks are much higher than those for the former. In the mid 1970s Gupta and Sen (GS) used a Hartree-Fock free ion method to model the 2p core line final states for many of the transition metals [24-25]. Their models produced a good approximation of the observed line shapes for most transition metals.

The core line shape of the photoelectron peaks collected for pure metal surfaces tend to have an asymmetric character that tail off to higher BE. The degree of asymmetry of the core line peak for any metal is related to its density of states at the Fermi level. In metals the valence and conduction bands overlap and as a result electrons are easily promoted above the Fermi level to any number of unoccupied energy levels. Moving valence electron density away from the nucleus effectively strengthens the “hold” the nucleus has on the core electrons, resulting in the ejection of photoelectrons having slightly less KE than the ground state atom. Some metal spectra also exhibit plasmon loss features, which arise from photoelectrons that have excited oscillations in valence

electrons while passing through the surface. These collective oscillations require specific amounts of energy leading to set KE losses and the appearance of characteristic peaks at higher BE. An example Ni 2p spectrum collected for a sputter cleaned Ni metal surface showing the asymmetry of the main line peak and plasmon loss structures is presented in Figure 1.6.

XPS can also be employed to model the thickness of oxide films provided that the thickness of the oxide is less than the maximum photoelectron escape depth. For the Kratos Axis Ultra Spectrometer the maximum analytical depth is obtained when the detector is positioned normal (at 90°) to the sample surface. The surface sensitivity of the instrument can be increased by changing the angle at which the photoelectrons enter the detector. The depth from which photoelectrons are detected is described by:

$$d = 3\lambda\sin\theta \qquad 1.9$$

where θ represents the angle the photoelectrons are detected relative to the sample surface. This type of scan is known as a shallow angle measurement or angle resolved XPS (ARXPS) and can be used to determine if a particular chemical species is confined to the very near surface.

The thickness of an oxide overlayer can also be calculated using the intensities of the metal and oxide phases derived from fitted high-resolution XPS spectra. The overlayer equation shown here was first derived by Carlson [26] and later rearranged in terms of oxide thickness d by Strohmeier [27]:

$$d = \lambda_o \sin\theta \ln\left[\frac{N_m\lambda_m}{N_o\lambda_o}\frac{I_o}{I_m} + 1\right] \qquad 1.10$$

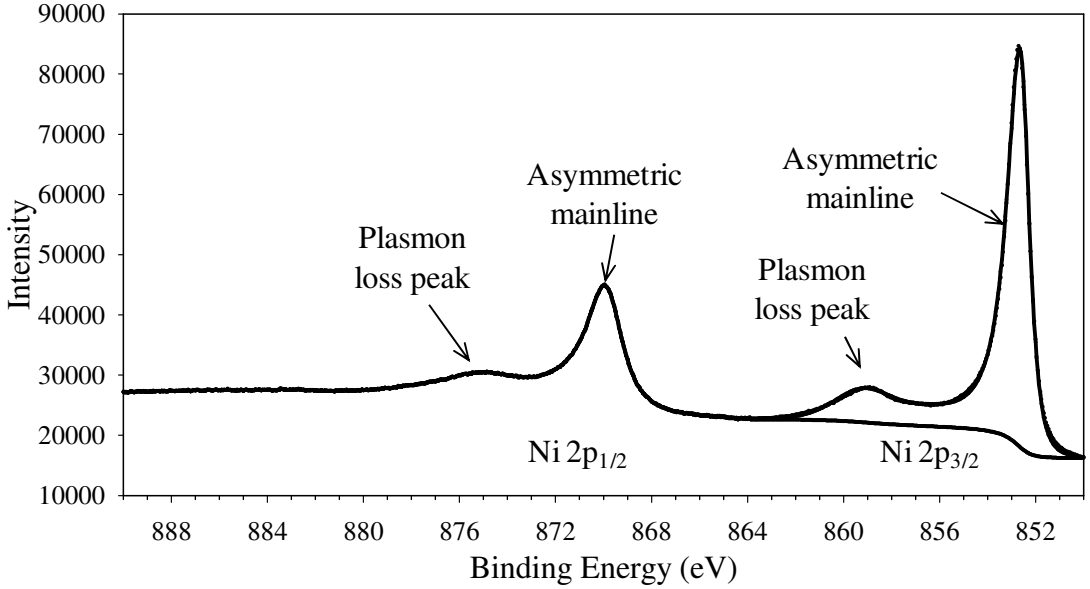

Figure 1.6**:** The high resolution Ni 2p spectrum for an atomically clean Ni metal surface. The asymmetric nature of the Ni $2p_{3/2}$ and Ni $2p_{1/2}$ mainlines is clearly visible. Additional structures due to plasmon losses are also observed at higher BE on both the Ni $2p_{3/2}$ and $2p_{1/2}$ lines.

where m and o represent the metal and oxide phases respectively, λ is the IMFP, N stands for the volume density of metal atoms in either the metal or the oxide phase, I is the peak area for either the metal or the oxide, and θ is the take off angle of the electrons.

A third method for measuring oxide thickness was developed by Tougaard and is commercially available in a software package called QUASES™ [2,28]. The basis for the Tougaard algorithms is the concept of inelastic scattering. When a photoelectron travels through a surface it may undergo one or more energy loss events. The probability that an electron will experience one or more energy loss interactions increases sharply with depth. From Equation 1.4 a loss in KE due to scattering will result in an increase in the observed BE and leads to the formation of the extrinsic background located on the higher BE side of a photoelectron peak. The Tougaard algorithms model the photoelectron energy loss (extrinsic) backgrounds using material dependent IMFPs and energy loss cross-sections. The IMFP was previously described as the average distance a photoelectron can travel before undergoing an inelastic collision, while the energy loss cross-section represents the average amount of energy a photoelectron will lose per scattering event (20 – 30 eV). Based on the typical IMFP lengths QUASES™ has maximum operational depth between 5 to 10 nm, depending on the surface being analyzed. The change in the spectral background with the distribution of atoms in a surface is shown in Figure 1.7(a).

The QUASES™ software package is divided into two analytical programs ‘Analyze’ and ‘Generate’. The ‘Analyze’ program calculates overlayer thicknesses by modeling the extrinsic background associated with any photoelectron peak by determining the depth from which photoelectrons originated. The ‘Generate’ program

a) Changes in spectral background based on elemental distribution

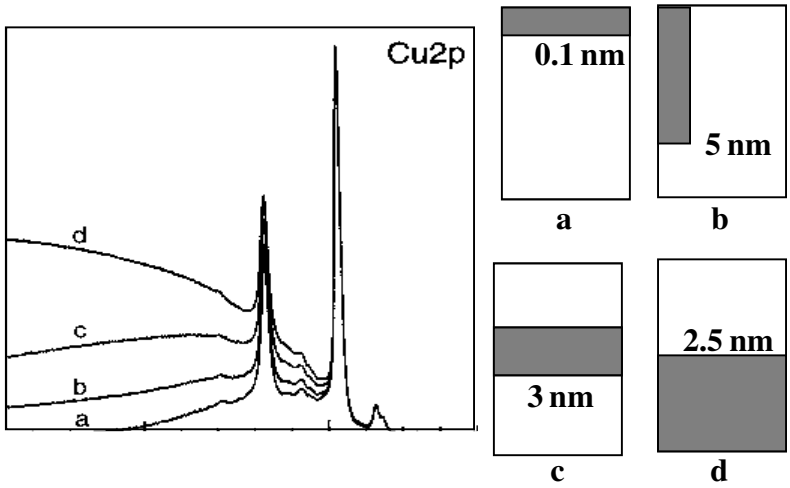

b) The five QUASES™ depth profiles

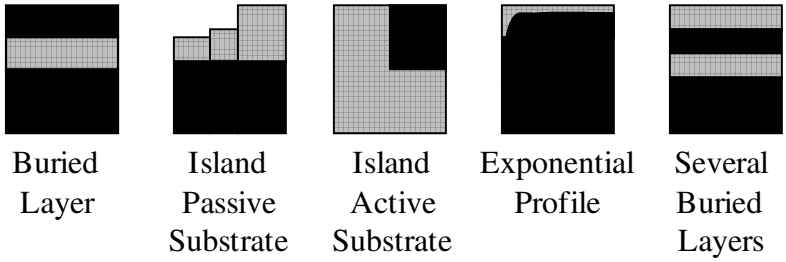

Figure 1.7: Diagram showing the differences in the extrinsic background for the Cu 2p peak as a function of the atomic distribution within the near surface region. The grey areas represent the portion of the sample containing the Cu atoms. (b) The five different QUASES™ depth profiles are also shown. The grey areas represent the material that is being modeled [29].

determines the surface structure of the oxide by modeling the distribution of atoms in the experimental spectrum using a combination of reference spectra whose extrinsic backgrounds have been modified for the depth from which they are situated in the surface. The advantage to the 'Generate' programs is that it allows for the near surface morphology to be modeled using five different profiles (see Figure 1.7(b)).

1.5 Time of Flight Secondary Ion Mass Spectrometry

Time of Flight Secondary Ion Mass Spectrometry (ToF SIMS) is another primary surface analytical technique that is extremely sensitive to the outermost surface layers (monolayer resolution). The detection limit of ToF SIMS is much lower than that of XPS and is on the order of ppm and ppb. Typical analysis areas using ToF SIMS range in size from 500 μm x 500 μm to 50 μm x 50 μm. Unlike XPS, SIMS is able to detect all elements in the periodic table and thus the location of H within an oxide film can be examined. Any analysis of H is typically completed using deuterium (D) to minimize the contributions from atmospheric H to the measurement. In contrast to XPS, chemical state information is not easily obtained from SIMS data however detailed images of surface structures can be collected. This is of particular importance when investigating the effects grain boundaries or highly defective areas have on surface oxidation. The destructive nature of SIMS allows for in-depth profiles of the surface to be collected, and when used in conjunction with XPS, a detailed distribution of the oxide/hydroxide phases within a surface can be obtained.

In SIMS based techniques a sample's surface is bombarded with primary ions, which can knock out non-volatile secondary ions, molecular ion fragments and neutral atoms. In static SIMS a pulsed primary ion beam is used yielding monolayer resolution.

The ion beam employed will depend on the properties of the material being studied as well as the nature of analysis being performed. In ToF SIMS the ions ejected from the surface enter a Time of Flight (ToF) mass analyzer where they are accelerated by a constant electric field. The velocity at which the ions travel through the analyzer is dependent on their mass to charge ratio; with the smallest ions reaching the detector first. A channeltron detector is typically used to amplify the ion signal, which is similar to the electron multiplier used in XPS. All SIMS experiments were carried out with a ToF SIMS IV GbmH Secondary Ion Mass Spectrometer, with a bismuth cluster analysis ion source and cesium ion sputtering source.

1.6 Thesis Outline

In this thesis detailed analysis of the oxidation of polycrystalline Ni, Cr and NiCr surfaces are presented. In addition, the XPS O 1s:Metal 2p atomic ratios for a number of well characterized Ni- and Cr-containing oxides and hydroxides were investigated.

In Chapters 2 and 3 detailed XPS studies of the oxidation of polycrystalline Ni metal surfaces by ultra pure O_2 gas (Chapter 2) and H_2O vapour (Chapter 3) are presented. The oxide chemistry (i.e. Ni^{2+} and Ni^{3+} content) of the resultant films was monitored using high-resolution Ni $2p_{3/2}$ spectra. Changes in oxide thickness and film surface structures with both temperature (25° and 300°C) and increasing O_2/H_2O dose were modeled using QUASES™ 'Analyze' and 'Generate'. The QUASES™ results were also used to determine the kinetics of the respective Ni-O_2/H_2O reactions. ToF SIMS was also employed to monitor localized oxide growth (Chapter 2) and H distribution within these oxide films (Chapter 3).

The high-resolution Cr $2p_{3/2}$ spectra for Cr_2O_3 collected from polycrystalline powder and vacuum fractured and annealed aggregate samples were compared in Chapter 4. In addition, a possible line shape for the Cr $2p_{3/2}$ spectrum of $Cr(OH)_3$ was empirically derived and is also presented. The oxidation of polycrystalline Cr metal surfaces exposed to either ultra pure O_2 gas or H_2O vapour was studied as well. Finally, corrosion products formed on a NiCr alloy exposed to an acidic aqueous solution were also monitored and discussed.

The high-resolution O 1s XPS spectra of a number of well characterized NiO, β-$Ni(OH)_2$, NiOOH and $NiCr_2O_4$ powder samples were examined in Chapter 5. Particular emphasis was placed on separating the O 1s intensities of species bound to Ni in the oxide/hydroxide crystals from surface adsorbed and/or interstitial species. The O/Ni ratios for the different powder samples were calculated and found to mirror the expected stoichiometry for those compounds.

In Chapter 6 a detailed study of the corrosion products formed on Ni metal and NiCr alloy surfaces was completed. The changes in film composition with temperature, exposure time, pH and electrochemical potential were modeled by rigorously fitting the high-resolution Ni $2p_{3/2}$, Cr $2p_{3/2}$ and O 1s XPS spectra. The thicknesses of the oxides formed on the pure Ni metal surfaces were calculated using the Strohmeier formula. ToF SIMS was used to monitor the changes in the distributions of the Ni- and Cr- containing oxidation products on the NiCr surfaces.

Chapter 7 provides a summary of the results obtained in this work.

1.7 References

[1] N. Fairley, CasaXPS Version 2.215, 1999-2009.

[2] S. Tougaard, QUASES™, Version 4.4, Software for Quantitative XPS/AES of Surface Nano-Structures by Analysis of the Peak Shape Background, 2000.

[3] L. Liu, Y. Li, F. Wang, Electrochim. Acta 52 (2007) 2392.

[4] D. Eley, P.R. Wilkinson, Proc. R. Soc. London A 254 (1960) 327.

[5] F.P. Fehlner, N.F. Mott, Oxidation of Metals and Alloys: Papers Presented at a Seminar of the American Society for Metals, October 17 and 18, 1970, American Society for Metals, Metals Park, 1971, p. 37.

[6] N.F. Mott, Trans. Faraday Soc. 43 (1947) 429.

[7] N. Cabrera, N.F. Mott, Report Progr. Phys. 12 (1948) 163.

[8] F.P. Fehlner, M.J. Graham, In Corrosion Mechanisms in Theory and Practice, P. Marcus, J. Oudar (eds.) Marcel Dekker Inc.: New York, 1995; 123.

[9] F.P. Fehlener, N.F. Mott, Oxidation of Metals 2 (1970) 59.

[10] H.H. Uhlig, R.W. Winston, In Corrosion and Corrosion Control An Introduction to Corrosion Science and Engineering, John Wiley and Sons: Toronto, 1985; p. 187.

[11] C. Wagner, Z. Physik. Chem. B 21 (1933) 25.

[12] W.W. Smeltzer, Oxidation of Metals and Alloys: Papers Presented at a Seminar of the American Society for Metals, October 17 and 18, 1970, American Society for Metals, Metals Park, 1971, p. 115.

[13] M Danielewski, in S.D. Cramer and B.S. Covino Jr. (Eds.), ASM Handbook Volum 13A Corrosion: Fundamentals, Testing, and Protection, ASM International, Metals Park Ohio, 2003, p. 97.

[14] D.D. Macdonald, S. R. Biaggio, H. Song, J. Electrochem. Soc. 139 (1992) 3434.

[15] D.D. Macdonald, J. Electrochem. Soc. 71 (1999) 951.

[16] M. Bojinov, T. Laitinen, K. Mäkelä, T. Saario, G. Sundholm, Electrocheimica Acta, 45 (200) 2029.

[17] M. Bojinov, A. Galtayries, P. Kinnunen, A. Machet, P. Marcus, Electrochemica Acta, 52 (2007) 7475.

[18] S. Tanuma, C.J. Powel, D.R. Penn, Surf. Interface Anal. 11 (1998) 577.

[19] NIST Electron Inelastic Mean Free Path Database (Version 1.1)©, U.S. Secretary of Commerce, 2000.

[20] K. Artyushkova, J.E. Fulghum, Surf. Interface Anal. 36 (2004) 1304.

[21] E.F. Smith, D. Briggs, N. Fairley, Surf. Interface Anal. 38 (2006) 69.

[22] C.D Wagner, L.E. Davis, M.V. Zeller, J.A. Taylor, R.M. Raymond, L.H. Gale, Surf. Interface Anal. 3 (1981) 211.

[23] C.D. Wagner, J. Electron Spectrosc. Relat. Phenom. 32 (1983) 99.

[24] R.P. Gupta, S.K. Sen, Phys Rev. B 10 (1974) 71.

[25] R.P. Gupta, S.K. Sen, Phy. Rev. B 12 (1975) 15.

[26] T.A. Carlson, Surf. Interface Anal. 4 (1982) 125.

[27] B.R. Strohmeier, Surf. Interface Anal. 15 (1990) 51.

[28] S. Tougaard, Surf. Interface Anal. 26 (1998) 249.

[29] S. Tougaard, User's Guide, QUASES™, Version 4.4, Software for Quantitative XPS/AES of Surface Nano-structures by Analysis of the Peak Shape Background, 2000.

Chapter 2 Structure and growth of oxides on polycrystalline nickel surfaces

2.1 Introduction

The oxidation of Ni metal surfaces at ambient temperatures leads to the formation of thin passive films that tend to be described best using logarithmic kinetics [1]. Following passivation there is little subsequent change in oxide thickness with time [2]. The mechanism is believed to follow that which was first suggested by Mott and Cabrera[a] [3]. Reactant O_2 molecules adsorb onto the surface of the metal and decompose into atomic oxygen (O (ads)) [4]. The O (ads) then bonds covalently with the Ni metal atoms at the surface, weakening their attachment to the lattice [4]. Owing to the difference in electronegativity between Ni and O, a dipole forms which allows the two atoms to exchange places [4]. Such a place exchange mechanism is responsible for the formation of the first one or two monolayers of oxide only [4]. Further oxidation is driven by the formation of an electric field created by the tunnelling of electrons from the Ni atoms in the metal, through the thin oxide layer, to the O (ads) sitting on the surface [1]. The presence of this electric field induces the movement of ions through the oxide leading to the formation of a thicker film [1]. After the film reaches a certain thickness, the electric field is no longer strong enough to promote ion diffusion and oxidation stops [1].

At higher temperatures, the exposure of Ni metal to O_2 results in the formation of thicker films than those found at lower temperatures. The oxidation kinetics is best described using a parabolic relationship [1]. Parabolic kinetics was first suggested by Wagner in the 1930s when he observed that cations could move through defects in an

[a] For clarification the oxidation of Ni metal surfaces exposed to gas phase O_2 has been shown to be modeled best using the direct logarithmic kinetic rate law proposed by Eley and Wilkinson [1]. Their theory was based on the inverse logarithmic mechanism first suggested by Mott and Cabrera [3].

oxide film [2]. The increased thermal energy due to the elevated temperatures allows for more cations to be mobile, leading to further reaction with O_2 [4].

This paper compares the structure and growth rate of the oxide films deposited on polycrystalline and single crystal (100) Ni surfaces when exposed to doses of O_2 in the range of many thousands of Langmuirs (L, 1L = 1.33 x 10^{-4} Pa·s); this is a regime much higher than that used in the many studies of the initial attachment of O to a clean Ni surface [5-11]. This particular research is intended to form a base with which the oxidation of more complex Ni alloys will be compared.

2.2 Experimental

Ni metal (Alpha 99.995 % pure) samples were cut from a polycrystalline metal rod and polished to a mirror finish using 0.05 μm γ-Al_2O_3 paste. Typical grain size observed after oxidation varied, with the larger grains being between 150 and 175 μm across. In addition, a (100) single crystal obtained from MacTecK GmbH (99.95 % pure) was used without further polishing. A 4 mm diameter area of the surface was sputter cleaned for 15 min using a 4 kV argon ion (Ar^+) beam and a 15 mA emission current. This was followed by annealing at 600°C for 30 min to minimize the point defects formed as a result of ion bombardment. Fresh areas were used for each experiment because it was found that, even after annealing, some residual damage was sometimes left by the sputter treatment. The single crystal surface was particularly prone to transformation to a polycrystalline form after extended ion bombardment and annealing. Following cleaning and annealing, polycrystalline and single crystal surfaces were exposed to high purity O_2 (99.99% pure) at a pressure of about 130 Pa at a temperature of 25° or 300°C for periods ranging from 1 to 100 min. The pressure gauge located in the

reaction chamber was calibrated using a Baratron® Absolute Capacitance Manometer. The gauge was found to report an absolute pressure within 6 Pa of the manometer.

Most structural and kinetic measurements were carried out by XPS. Of particular interest were the structures of the initial Ni and O species as revealed by the Ni 2p and O 1s spectra. In addition, a measure of the thickness of each oxide formed was made using QUASES™-based methods described in earlier publications [12-16]. All XPS analysis was carried out using a Kratos AXIS Ultra XPS generally using both monochromatic Al Kα (1486.7 eV) and achromatic Zr L (2042.4 eV (Lα)) X-ray sources. Use of the latter source for QUASES™ measurements was necessitated by the presence of a background from Ni and O Auger lines when the Al source was used. The XPS analyses were all carried out using the following parameters: a 90° electron take off angle, the hybrid focus lens, the charge neutralizer set to 1.6 A, 2.4 eV, and an analysis area of 700 x 300 μm. Broad scan survey spectra were collected using a pass energy of 160 eV and a 0.7 eV energy step, while high-resolution scans of the Ni 2p, O 1s, and C 1s regions were taken at a pass energy of 20 eV and an energy step of 0.05 eV. Also, Ni 2p high-resolution 27-μm scans were obtained using a pass energy of 40 eV and an energy step of 0.1 eV in an attempt to see the difference in oxide growth from grain to grain.

It was determined, using the C 1s line, that some of the thicker oxide films formed exhibited evidence of differential charging by as much as 0.3 eV. The binding energies in these spectra were corrected such that the adventitious carbon peak had a binding energy (BE) of 285.0 eV[b].

[b] In all other chapters a BE calibration of 284.8 eV was applied using the C 1s main line peak.

Spectra of both metallic Ni and NiO figure prominently in all of the experimental data; spectral representatives are required both for peak subtractions and for the QUASES™ fitting described below. Representative spectra were obtained using sputtered polycrystalline metallic Ni (Alpha 99.995% pure) and polycrystalline NiO powder (Alpha 99.998% pure). The Ni 2p spectra used in peak subtractions are shown in Figure 2.1.

Spectral analysis was carried out using Casa XPS Version 2.2.107 [17]. This was used both for subtraction of Ni 2p spectra and the analysis of XPS images. For spectral subtraction, the Ni metal contribution along with its extrinsic loss region were removed by normalizing the intensity of a clean Ni 2p scan to the metal portion in each of the oxidized spectra. This was followed by the removal of the NiO contribution and its satellite structure to reveal if any other Ni species were present. This second subtraction involved normalizing the intensity of the main NiO line at 854.0 eV to the peak having the same BE on the Ni metal subtracted spectra.

Computer-corrected XPS images were acquired in an attempt to see variation in the oxidation of various grains. Images were collected over a range covering the Ni $2p_{3/2}$ envelope of 870 eV–848 eV at an interval of 0.2 eV, using medium magnification (400 x 400 μm), an 80 eV pass energy, imaging aperture 2, charge neutralizer set to 1.6 A, 2.8 eV, and a dwell time of 240 s. X-ray focusing was assisted by drilling two holes into the surface of the Ni metal to produce regions of zero photoelectron counts. Our procedure is similar to that used by Barkshire et al. [18-19], Prutton et al. [20], Artyushkova and Fulghum [21-22], Walton and Fairley [23-24], and Smith, Briggs, and Fairley [25]. The image data set was then processed using the CasaXPS software. This

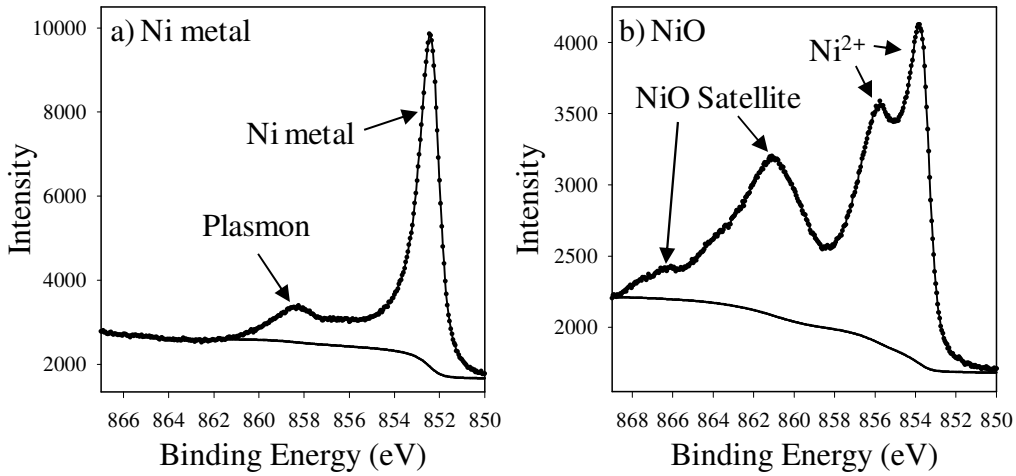

Figure 2.1: High-resolution Ni $2p_{3/2}$ spectra of (a) a polished, sputtered, and annealed Ni metal surface and (b) a sample of a polycrystalline NiO powder.

technique converts the image data set into a spectral data set and then uses a multivariate routine to maximize the signal to noise ratio. From these spectra, the metallic Ni (852.6 eV) [26-27], Ni plasmon (858.6 eV) [26], and Ni^{2+} (854.6 eV) [26-28] contributions were determined using asymmetric (metal) [12,29] and Gaussian-Lorentzian peaks [17]. Following compositional analysis the Ni metal and Ni^{2+} VAMAS files were converted to be read using MATLAB version 6.5 [21,22,30]. In MATLAB a matrix was constructed using the Strohmeier formula to calculate the oxide thickness at each of the image pixels (every 0.2 eV) by using the percent contribution of each of the Ni metal and Ni^{2+} components.

Measurements on the overall surface oxides were carried out using QUASES™ 'Analyze' and 'Generate' [16]. Total surface film thicknesses were determined using the 'Analyze' program and the O 1s extrinsic loss structure of XPS survey scans collected with an Al Kα X-ray source. From XPS survey scans, it was also found that all Ni metal surfaces were covered with small amounts of carbon contaminates. The resultant carbon

overlayer thicknesses were also measured with 'Analyze' this time using the background associated with the Ni 2p region obtained from Zr L survey scans. The photoelectron inelastic mean free paths (IMFPs) used to analyze all spectra were determined using the TPP-2M formula [31]. In previous work on metallic Fe, Grosvenor et al. used an electron attenuation length (AL) for Fe 2p photoelectrons that was roughly 20% shorter than the IMFP calculated using the TPP-2M calculator [14,15]. A similar correction for Ni has been assumed and ALs of 1.35 and 1.43 nm were determined for the O 1s and Ni 2p photoelectrons respectively[c]. The major difference between this study and the previously mentioned work [12-15] is the use of a Ni specific energy loss cross-section to determine film thicknesses. Most analysis of the transition metals, such as Fe, and their oxides, is done using the universal cross-section developed by Tougaard [32]. For the oxidized Ni metal samples, it was found that the universal cross-section did not properly model the spectral background due to the presence of the strong Ni plasmon peaks. To develop the new cross-section REELS data were collected from a sample of NiO powder (Alpha 99.998 % pure) using a PHI P660 AES/SAM spectrometer and a 0.5 keV electron beam. The new Ni cross-section was then kindly calculated by Tougaard using the QUASES-XS-REELS software [33].

Following the depth analysis of the individual samples, their surface composition was determined using QUASES™ 'Generate'. By modeling the Ni 2p energy loss region using different contributions from Ni metal and NiO reference spectra the atomic distribution in the near surface of all the oxidized samples was determined. Respective

---

[c] During the preparation of a subsequent manuscript (see Chapter 3) it was determined that the IMFP values calculated for both metallic Ni and NiO were overestimated by approximately 20%. The IMFPs for these species were recalculated and the new values were applied to estimate the thickness of the oxide films formed on Ni metal surfaces exposed to H_2O vapour. In addition, the thicknesses of the films studied in this work were re-evaluated using the shorter IMFP values and the results are summarized in Appendix A.

ALs of 1.41 and 1.43 nm[c] were calculated for the metal and NiO components using the TPP-2M calculator.

To verify the oxide thicknesses determined by QUASES™ 'Analyze', the results were compared to values calculated using the Strohmeier equation. The Strohmeier method uses the intensities of the metal and oxide phases derived from fitted high-resolution XPS spectra [34]. This technique is limited to films of 10 nm or less, the operational depth of XPS. The Strohmeier equation is expressed below [34]:

$$d = \lambda_o \sin\theta \ln\left[\frac{N_m \lambda_m}{N_o \lambda_o}\frac{I_o}{I_m} + 1\right] \qquad 2.1$$

The thickness of the film is represented by d, λ_o is the AL, m and o denote the metal and oxide components respectively, N stands for the volume density of metal atoms in either the metal or the oxide phase, I is the peak area for either the metal or the oxide, and θ is the take off angle of the electrons.

An ION-TOF ToF-SIMS IV Secondary Ion Mass Spectrometer, equipped with a bismuth cluster ion source was also used to obtain secondary electron and O^- secondary ion images showing the grain boundaries on a Ni metal surface.

2.3 Results and Discussion

2.3.1 Reactions at 300°C and 130 Pa

Ni metal samples were exposed to high purity O_2 for several periods of 1, 4, 20, and 60 min. The resulting high-resolution spectra of the Ni $2p_{3/2}$ regions are shown in Figure 2.2(a-d). The first two spectra are dominated by the presence of metallic Ni from the substrate; increased oxidation clearly diminishes the importance of the metallic contribution. In order to derive more detail from the oxidic components, the pure

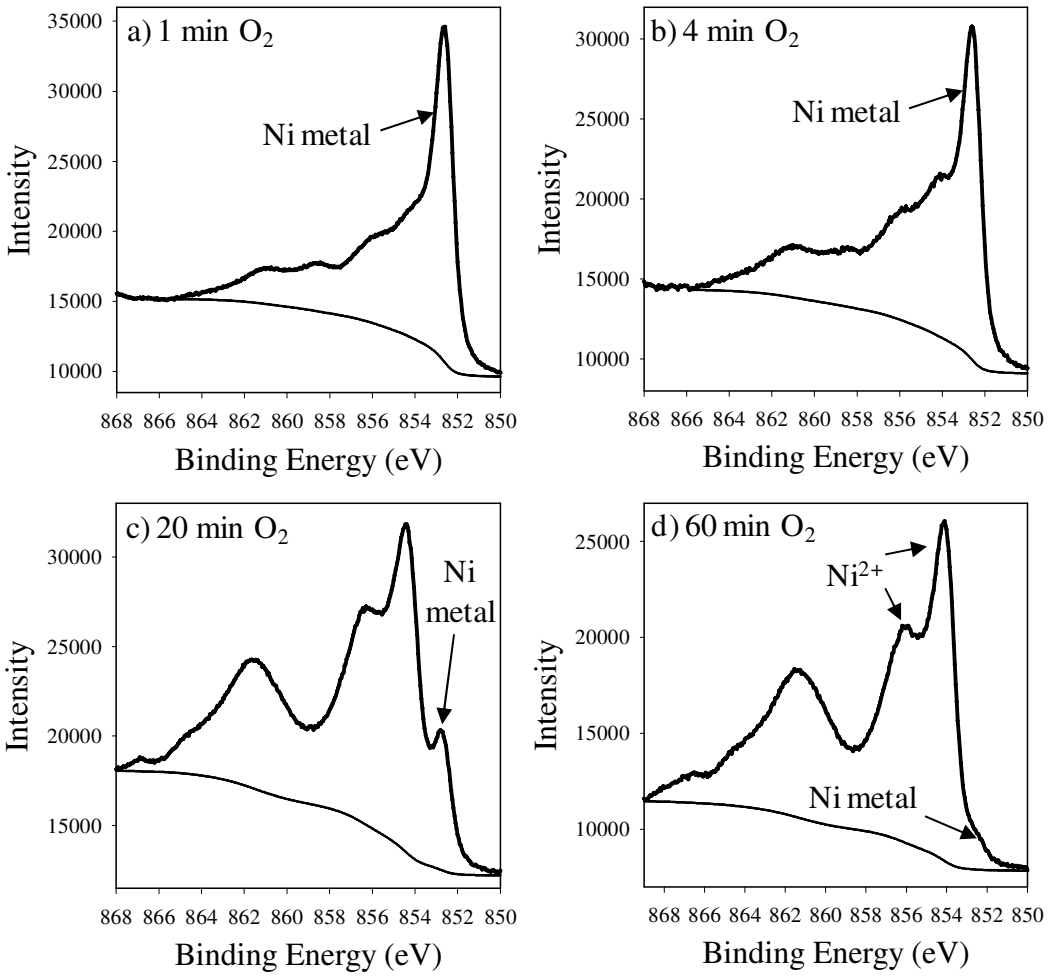

Figure 2.2: High-resolution Ni $2p_{3/2}$ photoelectron spectra following O_2 exposure times of 1, 4, 20, and 60 minutes at 300°C and 130 Pa. The identification of the spectral components lying above Ni metal is clarified in Figure 2.3.

metallic Ni components (see Figure 2.1(a)) were removed in such a manner that all intrinsic and extrinsic loss components from the metal were included in the process. The subtracted spectra are shown in Figure 2.3(a-d).

After a 60 min exposure, the subtracted spectrum (see Figure 2.3(d)) had a position and shape that exactly matched the very characteristic spectrum of NiO (see Figure 2.1(b)) whose origin was recently discussed [26]. The Ni $2p_{3/2}$ spectrum has a principal line at 854.0 eV, and a prominent shoulder at 855.7 eV. Inspection of the subtracted Ni $2p_{3/2}$ spectra (see Figure 2.3(a-b)) for surface oxides formed at earlier stages also shows the dual peak structure of NiO, but in addition, the presence of a second component superimposed on the above mentioned shoulder is apparent. This second component becomes less important with increased oxidation. We attribute this second component to the presence of Ni^{3+} species within the NiO matrix. A shallow angle measurement (15°) was carried out on one of the 4 min exposures. When the Ni metal component was subtracted from this spectrum (not shown), the Ni^{3+} spectral component was found to increase when compared to the 90° take off angle. This suggests that the distribution of the Ni^{3+} within the oxide film is skewed to the surface, as one might have predicted, on the basis of electron hole (Ni^{3+}) creation [35]. Therefore, in the early stages of oxide growth, the reduction of O_2 to O^{2-} occurs through the removal of electrons from Ni^{2+} atoms in the outermost layers of NiO, producing Ni^{3+}. The 'positive' charge located at the oxide surface pulls electrons from the Ni metal, creating Ni^{2+} cations. These cations will migrate towards the surface where they will react with O_2, while at the same time the Ni holes will move inwards towards the metal in the electric field created by the tunnelling electrons. After longer exposures to O_2 (see Figure

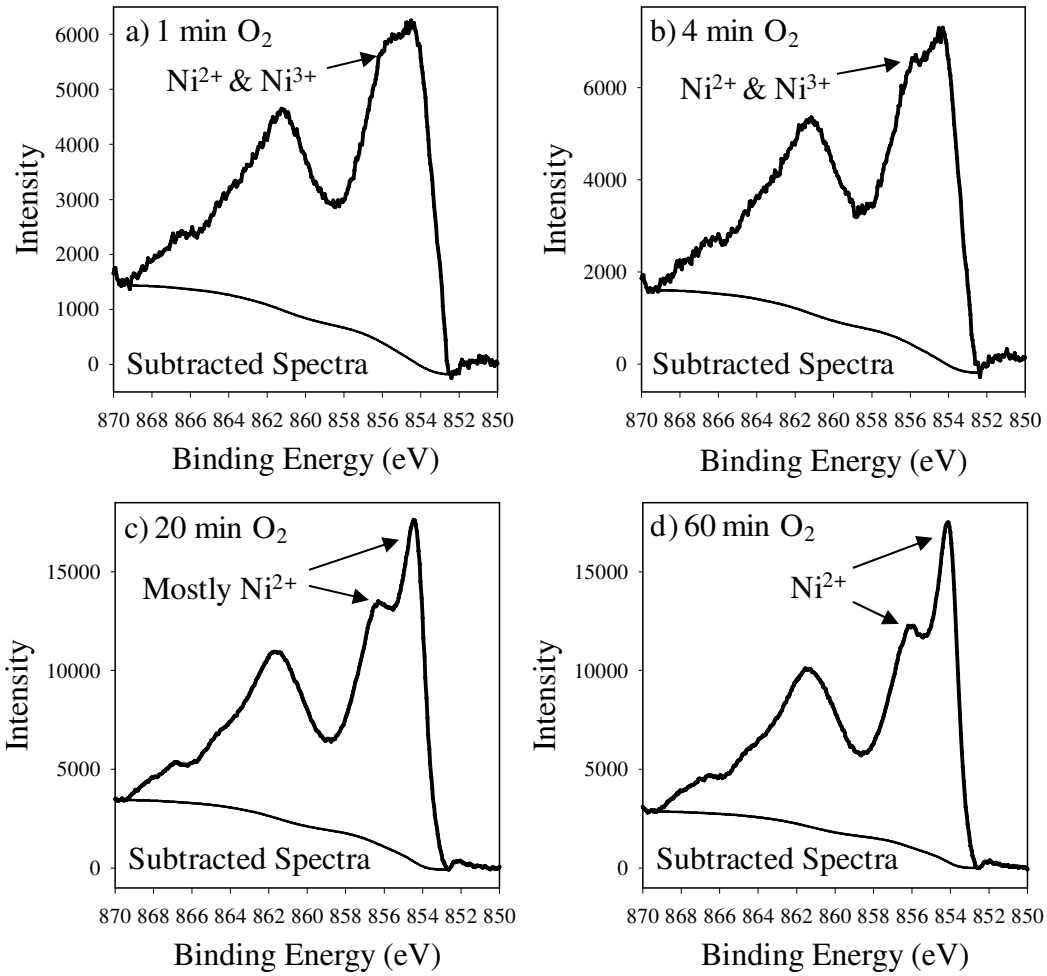

Figure 2.3: High-resolution Ni $2p_{3/2}$ spectra following subtraction of the Ni metal component showing the contributions from Ni^{2+} and Ni^{3+}. The spectra are shown for O_2 exposure times of 1, 4, 20, and 60 minutes at 300°C and 130 Pa. As exposure time increases, the resulting oxide more closely resembles NiO.

2.3(c-d)), the subtracted spectra more resembled pure NiO, with little contribution from Ni^{3+}. From this result, it appears that there is a change in the transport mechanism sometime around 20 min of exposure. At this point, transport occurs via O vacancies and Ni cation migration from the metal/oxide interface.

The spectra in Figure 2.3 were again subtracted, this time to remove the NiO component along with its satellite structure. The results for the shortest exposures are shown in Figure 2.4(a-b). These spectra should reflect only the Ni^{3+} component. The shape of the principal Ni $2p_{3/2}$ line is similar to the experimental spectra observed for Ni^{3+} in NiOOH that is discussed in ref. 26. The sharp peak located at approximately 853.9 eV in both spectra is the result of an incomplete subtraction process.

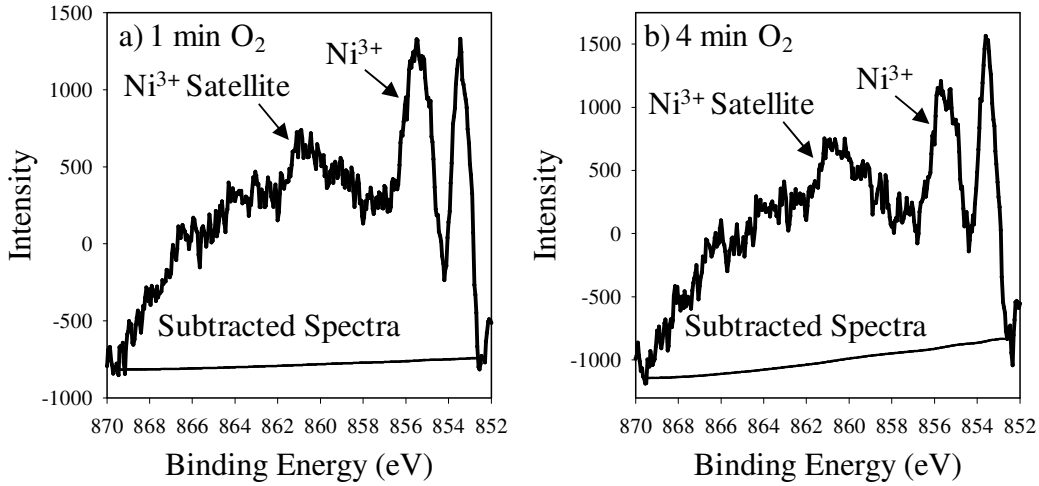

Figure 2.4: High-resolution Ni $2p_{3/2}$ spectra after subtraction of both the Ni metal and NiO components showing the residual spectra of Ni^{3+} for O_2 exposure times of 1 and 4 minutes at 300°C and 130 Pa. The subtracted spectra are similar to that of NiOOH, which is shown in reference [26]. The spike at 853.9 eV in both spectra is due to an incomplete subtraction process.

High-resolution spectra of the O 1s region were also collected and analyzed to identify the O species present (see Figure 2.5(a-d)). The O 1s signal following a 1 min

exposure (see Figure 2.5(a)) revealed the presence of a doublet that was distorted at the higher BE end, thus suggesting the presence of three distinct O species. The peak centred at 529.6 eV was assigned to O^{2-} species bound to Ni^{2+} in bulk NiO [36,37]. The next higher BE photoelectron peak (531.4 eV) has the chemical shift of an O (ads) species[d] [38]. A small peak located at 533.1 eV is attributed to the presence of adsorbed O_2 (O_2 (ads))[d] at the oxide surface. These latter species were shown to be highly concentrated at the outer surface by angular dependent XPS (not shown). The peak at 533.1 eV was not labelled as an absorbed water species because ultra pure O_2 (< 3 ppm H_2O) was used. In addition, prior to all gas exposures, the reaction chamber was scanned for the top 50 contaminates using a Residual Gas Analyzer (RGA), a quadrapole mass spectrometer. The RGA results showed that the water levels in the chamber were typically around 1.30×10^{-5} Pa, seven orders of magnitude less than the dosing pressure. With further oxidation (see Figure 2.5(b-d)), there is an observably large decrease in the relative concentrations of the two adsorbate species compared to the bulk oxide.

Oxide growth kinetics measurements primarily used the two QUASES™ software routines to analyze XPS survey spectra. Overlayer thicknesses from deposited adventitious carbon were first determined by analysis of the Ni 2s region using the 'Analyze' program and Zr L excitation. The film thicknesses were then modeled using 'Analyze' and the O 1s region of the Al Kα survey spectrum. Figure 2.6(a-b) show the Ni 2s and O 1s regions fitted by QUASES™ 'Analyze' for a sample exposed to O_2 gas for 60 min at 300°C and 130 Pa. Both spectra in Figure 2.6 show a good overlap of the

[d] Following publication of this work the O (ads) and O_2 (ads) species were reassigned as defective oxygen (O (def)) and adsorbed carbonaceous species. These redesignations were based on observed O/Ni and O/C peak area ratios derived from more thorough analyses of the Ni $2p_{3/2}$, O 1s and C 1s high-resolution spectra (see Chapters 3 and 5).

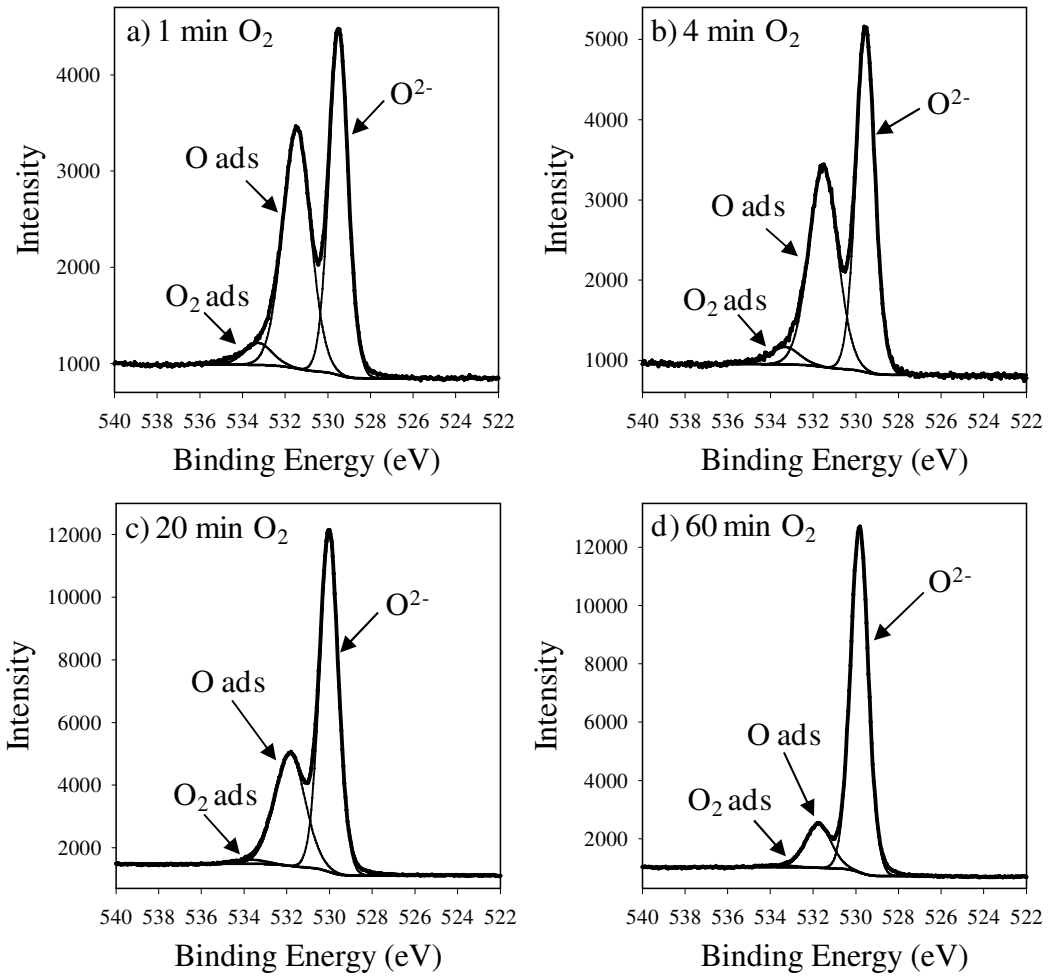

Figure 2.5: O 1s high-resolution spectra following 1, 4, 20, and 60 minute exposures to O_2. These four spectra correlate with the four Ni spectra shown in Figure 2.2(a-d). There appears to be three distinct oxygen species present (O^{2-}, O (ads), and O_2 (ads)). As exposure time is increased the contribution from the adsorbed species decreases substantially. These spectra were not corrected for charging.

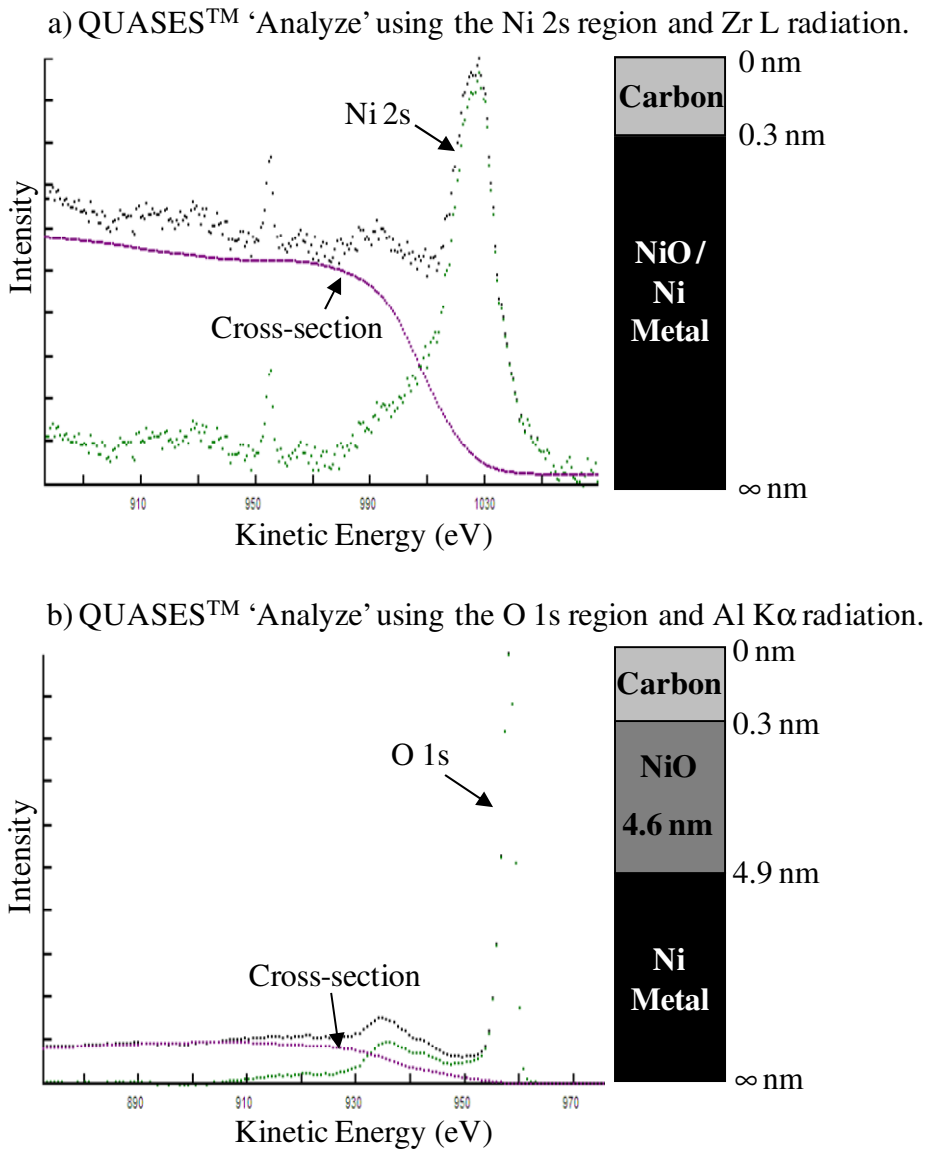

Figure 2.6: QUASES™ 'Analyze' modeled peaks from a Ni surface exposed to ultra pure O_2 at 300°C and 130 Pa for 60 minutes: (a) Ni 2s using Zr L X-ray source; (b) O 1s using Al Kα X-ray source.

energy loss cross-section with the extrinsic loss portion of the scans. From 'Analyze', a carbon overlayer of 0.3 nm and an overall film thickness of 4.6 nm were determined. In order to verify the 'Analyze' results, film thicknesses were also estimated using the Strohmeier equation. The values obtained with this method were found to be within 0 to 0.3 nm of the 'Analyze' data. A complete summary of all overlayer and oxide thickness data is presented in Table 2.1. Contrary to what was observed with the XPS survey scans, the 'Analyze' fits showed that two samples did not contain a contaminant overlayer. The reason for this discrepancy may be due to the use of the higher energy Zr X-ray source, which produced much noisier spectra than Al Kα radiation. For QUASES™ background subtractions, the line of best fit is set by eye, thus the increased spectral noise leads to a higher error in the overlayer calculations. Plotting the 'Analyze' depth results versus exposure time in Langmuirs, using the parabolic, direct, and indirect logarithmic kinetic models, determined the reaction kinetics. The resulting R^2 values from the three models were 0.94, 0.87, and 0.56, respectively. The parabolic relationship was found to be the best fit for the data; this plot is presented in Figure 2.7.

The structure of each of the surface oxides was then modeled using QUASES™ 'Generate'. The 'Generate' result for the sample oxidized for 60 min and 300°C is displayed in Figure 2.8. Again, there is very good overlap between the experimental and the reference spectra within the modeling energy range. The experimental spectrum was best fitted for the 'island active substrate' model for Ni metal, and the 'buried layer' model for the NiO reference spectra. When the 'island active substrate' is selected, only the photoelectrons having been emitted from substrate atoms and passed through the island overlayers are analyzed [16]. The combination of the 'island active substrate' and

Table 2.1: Determination of Oxide Thickness (nm) at 300°C and 130 Pa using QUASES™

Exposure Time (min)	Overlayer Thickness (nm)	QUASES™ Oxide Thickness (nm)	Fraction of Surface Coverage	Strohmeier Oxide Thickness (nm)
1	0.5	1.2	0.8	1.0
1	0.5	0.6	0.6	0.6
1	0.2	1.4	0.7	1.2
1	0.2	1.5	0.9	1.3
4	0.4	1.5	0.7	1.3
4	0.2	1.0	0.7	0.8
4	0.4	1.3	0.8	1.2
4	0.3	1.8	0.6	1.7
20	0.4	3.1	0.4	3.1
20	0.5	3.0	0.5	—
60	0.0	4.7	0.8	4.6
60	0.3	4.2	0.8	3.9
60	0.0	4.6	0.7	4.5

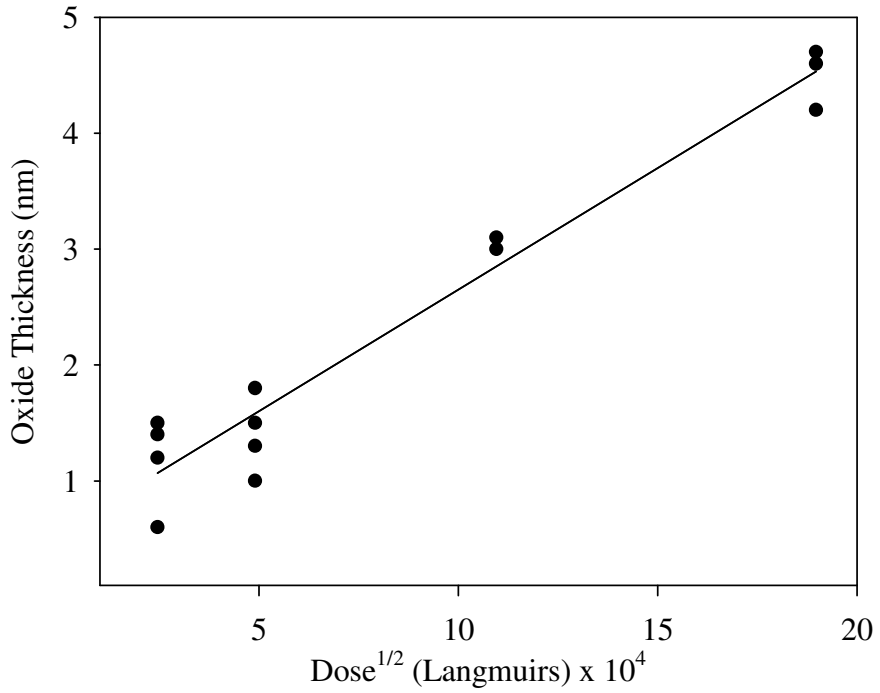

Figure 2.7: Change in overall oxide thickness on Ni metal for O_2 doses (Langmuirs (L)) at 300°C and 130 Pa as determined by QUASES™ 'Analyze'. Results are best fitted to a parabolic relationship. The determined R^2 value for a parabolic fit was 0.94, while R^2 values of 0.87, and 0.56 were observed for the direct and inverse logarithmic plots respectively.

'buried layer' models suggests that, following the initial adsorption of O_2, oxidation begins at localized areas, or by forming islands of oxide on the surface. These islands are separated by adsorbate covered Ni metal ('island active substrate') and grow thicker with increasing exposure time. NiO is a p-type oxide, meaning that the mobile species are the Ni^{2+} cations, which can migrate through vacancies or along grain boundaries to the surface where they can react with the incoming O_2 [2]. The output of the 'Generate' program also gives a fraction of surface coverage indicating how much of the analyzed area (700 x 400 μm) is topped by the oxide/overlayer. The surface coverage values can range between 0 and 1, with the former representing no oxidation at all, and the latter, the complete coverage of the spot analyzed. For the example shown in Figure 2.8, 'Generate' determined a surface coverage of 0.8, meaning that the oxidized area could be covered by either one large island or many smaller ones separated by spaces that are too small for XPS to detect under these conditions. Surface coverage values for the 'Generate' fits ranged from 0.4 to 0.9; these values are recorded in Table 2.1. As the surface becomes more saturated with O, the islands will begin to coalesce, leading to the eventual passivation of the surface. Finally, this oxide film is covered with a thin layer of adventitious carbon, leading to the 'buried layer' appearance.

Oxide growth rate on a single crystal (100) surface was compared to that of polycrystalline Ni. The (100) Ni metal sample was exposed to O_2 at the same temperature and pressure conditions specified above for 60 min. Two separate exposures produced oxide thicknesses of 0.9 and 1.2 nm. The average thickness of 1.0 nm is about four times less than the average thickness (4.5 nm) found for oxide grown on polycrystalline Ni exposed under the same condition. The oxidation of Ni metal single

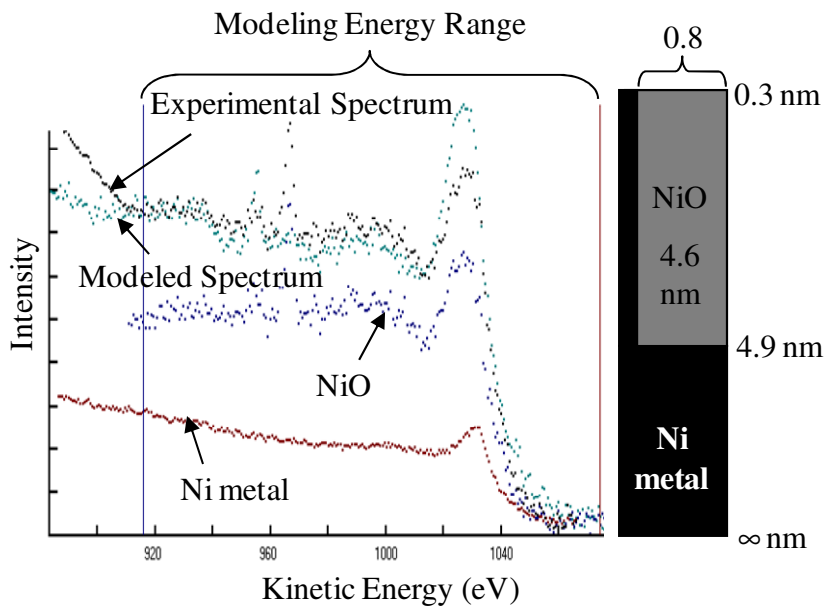

Figure 2.8: The Ni 2s QUASES™ 'Generate' result of a Ni metal surface exposed to dry O_2 for 60 minutes at 300°C and 130 Pa analyzed using Zr L radiation. A very good overlap is found between the modeled and the experimental spectra along the extrinsic loss portion.

crystals has previously been studied following exposures to O_2 following doses of up to a few hundreds of Langmuirs [5,39]. The faster growth on the polycrystalline surfaces must occur primarily via grain boundaries.

XPS was used to study the influence of the grain orientation of specific metal grains on the growth rate of their surface oxides; these measurements were made using the 27-µm aperture. The small size of the aperture compared to the typical grain size of 150 to 175 µm would suggest that most microanalyses would fall within one grain face. For a sample oxidized for 20 min, having an average oxide thickness from Table 2.1 of 3.0 nm, four separate 27-µm area measurements were made at random points on the sample surface. The oxide thicknesses measured using the Strohmeier equation were 3.0, 3.1, 3.0, and 3.1 nm. Thus, it appears that there is no evidence of differential oxide

growth as a result of grain orientation. This could suggest that oxide growth is driven by a mechanism other than that at the grain face. While this result indicates an even oxide growth, the QUASES™ results suggest otherwise. This contradiction could arise from an island growth that is nanometric in size.

Any excessive cleaning and annealing of polycrystalline Ni caused the sample to undergo oxidation at a significantly reduced rate. This result is similar to what Haugsrud observed, as he found that annealing the surface lowered the oxidation rate by a factor of three [40]. Two Ni metal samples were exposed to multiple sputter and anneal cycles without repolishing, then oxidized for 60 min at 300°C and 130 Pa. The surfaces were examined using XPS, and oxide thicknesses of 3.1 and 2.7 nm were determined using QUASES™. These films are 32 and 40% thinner than the average oxide thickness of 4.5 nm found on newly polished Ni surfaces oxidized under the same conditions. Sample areas that had been subjected to more than one cleaning and annealing cycle were found to have grains that had transformed into a highly twinned structure. Polycrystalline specimens are thus susceptible to more damage mechanisms during surface preparation than are single crystal specimens.

2.3.2 Reactions at 25°C and 130 Pa

Similar studies to those above were conducted at 25°C with exposures to O_2 for periods of 10, 25, 50, and 100 min. The high-resolution Ni $2p_{3/2}$ spectra for all exposures were dominated by a strong Ni metal line; as a consequence, the metallic contributions were removed just as in the case of the samples oxidized at 300°C. The resulting Ni $2p_{3/2}$ subtracted spectra are shown in Figure 2.9(a-d). Based on the interpretation of the Ni 2p spectra in Figure 2.3, it appears that even after a 100 min exposure there is still a

considerable contribution from Ni^{3+}. This contrasts with what was observed at 300°C; in this case Ni^{3+} remains an important contributor to transport throughout the process.

The O1s spectra for the four exposure times at 25°C are shown in Figure 2.10(a-d). As with the 300°C exposures, three discrete O species were found: O^{2-}, O (ads)[d], and O_2 (ads)[d]. Compared to the 300°C exposures, a higher proportion of the O present is in the adsorbed state, the result of a slower conversion to oxide and the formation of much thinner films. Little change in the relative adsorbate proportions is found in the longer exposures, presumably because the oxide is nearing its limiting thickness. As with the 300°C samples, the O (ads) peak areas were compared, but this time only a small decrease was observed with oxide thickness; this is likely due to the passivation of the surface with a thin oxide film.

Measurement of the oxide growth rate at this temperature again employed the use of QUASES™ 'Analyze' and followed the same procedure as for the 300°C exposures. The 'Analyze' oxide thicknesses were all within 0.3 nm of the values obtained using the Strohmeier equation. The results of both analytical methods along with sample overlayer thicknesses are summarized in Table 2.2. Comparison of the oxide thicknesses found at 25° and 300°C shows a reaction rate four to five times slower at the lower temperature. The 'Analyze' results were again plotted against O_2 exposure in Langmuirs and fit with the three kinetic models. The direct logarithmic relationship gave the best fit, having an R^2 value of 0.83 (see Figure 2.11), while the parabolic and indirect logarithmic plots gave R^2 values of 0.78 and 0.65, respectively. As expected, the growth of oxide on polycrystalline Ni metal at 25°C obeys the Mott-Cabrera model[a] for low temperature oxidation [3].

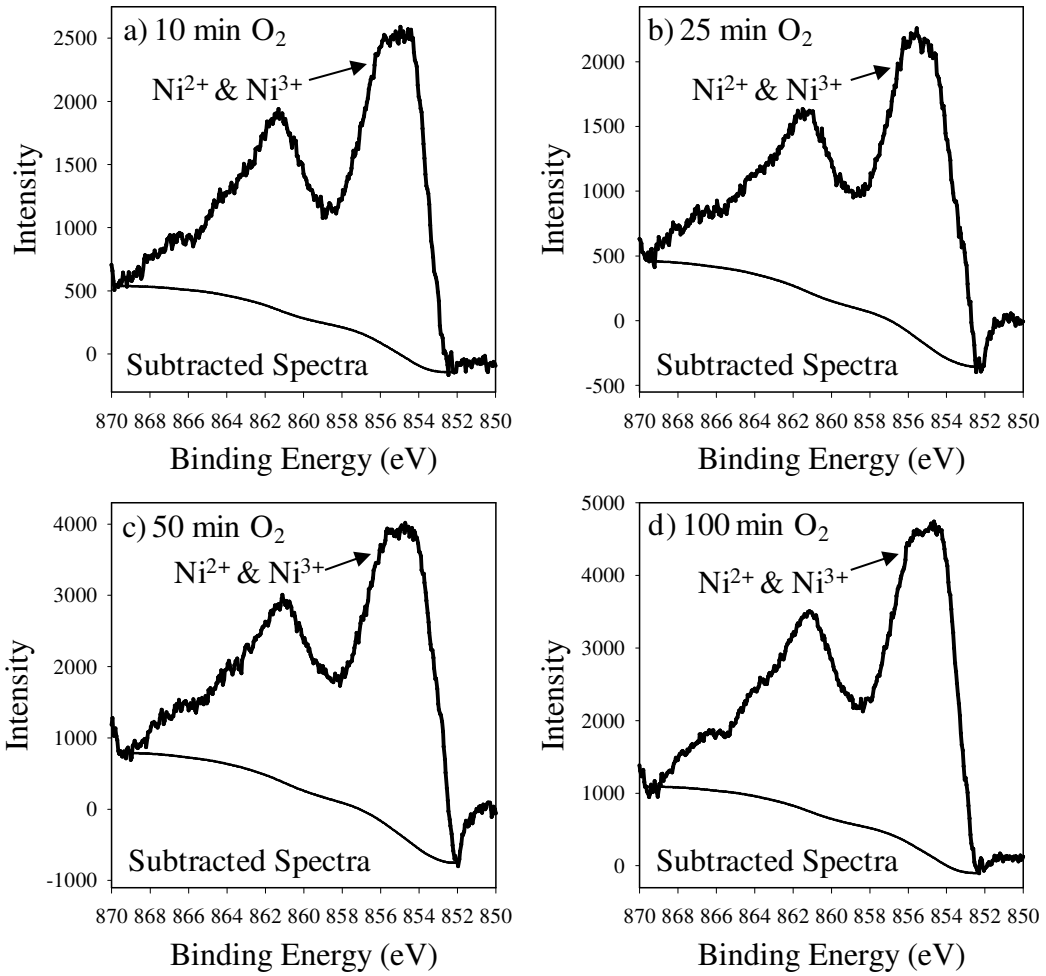

Figure 2.9: High-resolution Ni $2p_{3/2}$ Ni metal subtracted spectra showing the contributions from Ni^{2+} and Ni^{3+} following O_2 exposure times of 10, 25, 50, and 100 minutes at 25°C and 130 Pa. The subtracted spectra show very little change in oxide composition as exposure time is increased.

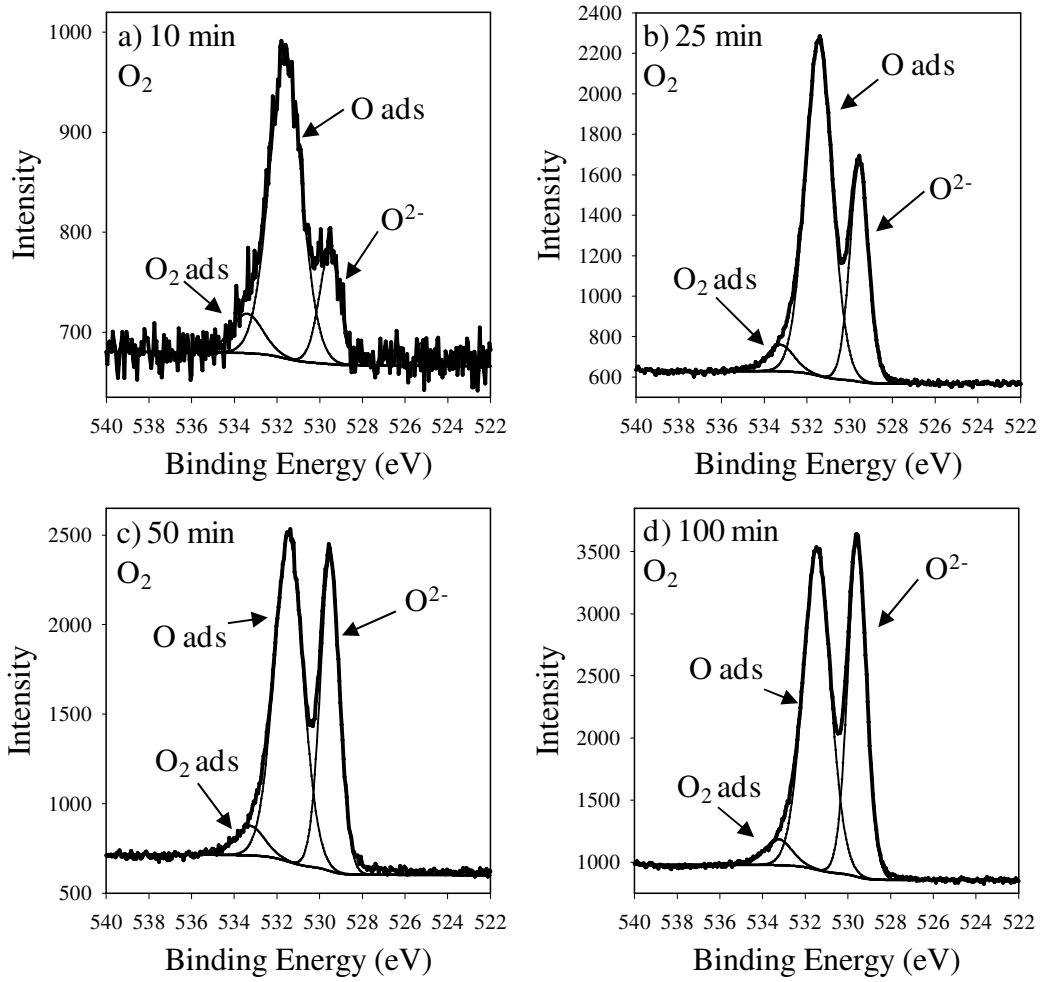

Figure 2.10: O 1s high-resolution spectra following 10, 25, 50, and 100 minute exposures to O_2. These were *not* charge corrected. These four spectra correlate with the four subtracted Ni metal spectra shown in Figure 2.9(a-d). Three distinct oxygen species are present: (O^{2-}, O (ads), and O_2 (ads)). As exposure time is increased the contribution from the lattice oxide species increases but there is still a strong adsorbate signal. The spectrum in (a) is noisy because of the very small quantity of oxide formed at this stage in the process.

Surface oxide structures for the films grown at 25°C were modeled using QUASES™ 'Generate'. As with the 300°C exposures, the experimental spectra were best fit with the 'island active substrate' and 'buried layer' depth concentration profiles for the Ni metal and NiO standards, respectively. The 'Generate' results indicate that oxidation is occurring at localized areas on the surface. Surface coverage fractions for the analyzed areas ranged from 0.4 to 1; and are presented in Table 2.2. Film thickening at this temperature is the result of ion movement due to the presence of an electric field created by tunnelling electrons [1]. As time progresses, the oxide film thickens until the electric field is no longer strong enough to support ion diffusion [1]. As with the 300°C results, the 'buried layer' appearance of the oxide is due to an overlayer of adventitious C.

Evidence for localized growth was also sought using XPS imaging, employing a specimen that had been exposed to O_2 for 10 min at 25°C and 130 Pa. The images showing the NiO and Ni metal distribution near the surface were processed and replotted as a distribution of Log I_{NiO}/I_{Ni}. This is effectively a map of the thickness of NiO on the surface, as determined by the Strohmeier equation. The resulting 'Strohmeier map' is shown in Figure 2.12(a); the greatest thickness corresponds to the darkest red coloration and the thinnest to the darkest blue. The color scale shows what we believe to be random variation in the oxide thickness across most of the image. However, thicker oxides were found in the upper right corner. Secondary electron and secondary ion images generated with a bismuth cluster ion showed that this area contained a large grain that is more susceptible to O uptake (see Figure 2.12(b-c)). This imaging result suggests that there could be some dependence on grain surface orientation during oxidation at this temperature.

Table 2.2: Determination of Oxide Thickness (nm) at 25°C and 130 Pa using QUASES™

Exposure Time (min)	Overlayer Thickness (nm)	QUASES™ Oxide Thickness (nm)	Fraction of Surface Coverage	Strohmeier Oxide Thickness (nm)
10	0.4	0.2	0.7	0.08
10	0.5	0.1	1.0	0.03
10	0.4	0.2	1.0	0.2
25	0.1	0.4	0.6	0.2
25	0.5	0.8	0.8	0.7
50	0.2	0.7	0.4	0.5
50	0.3	0.9	0.5	0.7
50	0.5	1.1	0.8	1.0
100	0.4	1.3	0.6	1.0
100	0.4	0.9	0.7	—

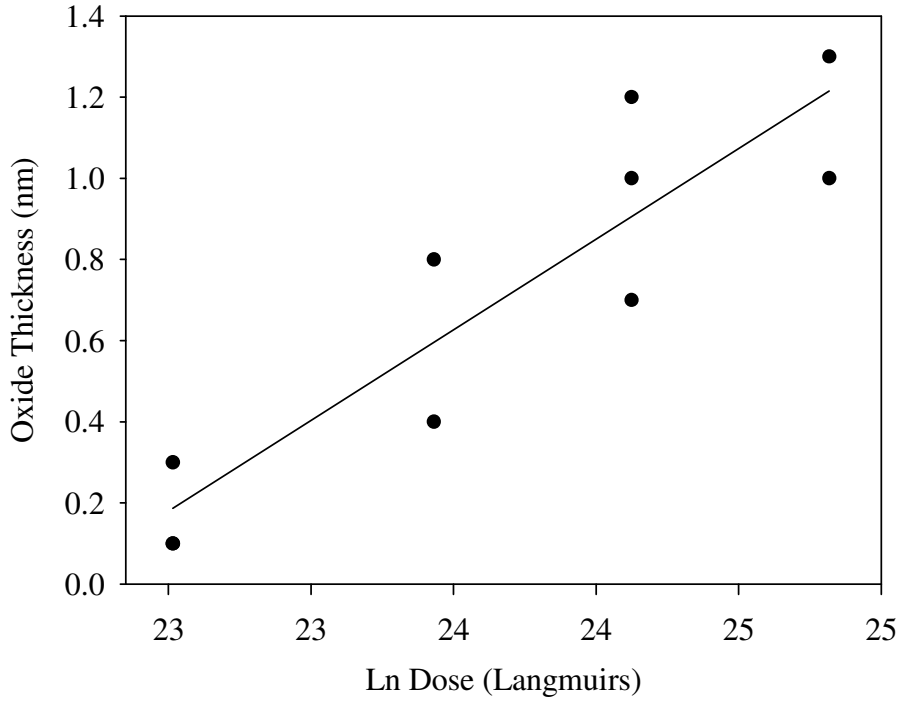

Figure 2.11: Change in overall oxide thickness on Ni metal at 25°C and 130 Pa as determined by QUASES™ 'Analyze'. The results are best fit using a direct logarithmic relationship. The determined R^2 value for a direct logarithmic fit was 0.83, while R^2 values of 0.78, and 0.65 were observed for the parabolic and inverse logarithmic plots respectively.

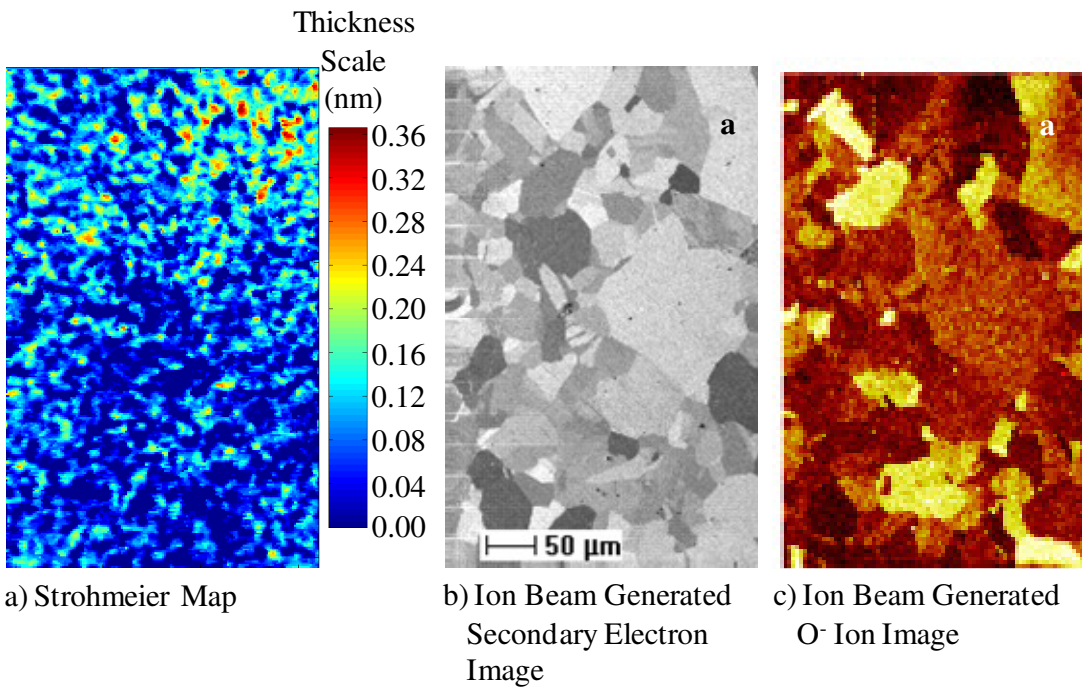

a) Strohmeier Map

b) Ion Beam Generated Secondary Electron Image

c) Ion Beam Generated O^- Ion Image

Figure 2.12: XPS map of NiO thickness for a Ni metal surface exposed to O_2 for 10 minutes at 25°C and 130 Pa (a). Oxide thickness is greatest in the neighbourhood of grain a in (b). This grain is known to be more susceptible to oxidation on the basis of the O^- secondary ion image in (c).

2.4 Conclusions

In this paper we were able to show via spectral subtraction that both Ni^{2+} and Ni^{3+} species are present on Ni oxidized surfaces. Oxidation of Ni surfaces at 25°C seemed to proceed mainly via Ni hole formation at the NiO surface. Similar findings were observed for the initial stages of oxidation at 300°C, however, the mechanism appeared to change around 20 min of exposure. After 20 min, there was a noticeable reduction in Ni^{3+} present, suggesting that O vacancies possibly play a role in ion migration.

Analysis of O 1s spectra for the two temperature regimes showed the presence of three O species: O^{2-}, O (ads), and O_2 (ads). At 300°C, the contribution from the O_2 (ads) disappeared with exposure time, whereas at 25°C, it remained relatively constant and in significantly higher relative concentrations.

QUASES™ analytical algorithms were used not only to determine the oxide thickness, but also its surface distribution. Oxidation at both 25° and 300°C was found to occur through 'island growth'. QUASES™ is a powerful means of interfacial analysis because it not only determines film thickness, but also maps the oxide-metal interface. Other methods, such as the Strohmeier formula, are accurate for depth analysis, but assume a uniform coverage of oxide, which may not always be accurate. Oxidation kinetics for the 25° and 300°C experiments determined using QUASES™ measurements were found to be direct logarithmic and parabolic respectively.

Comparison of the oxide kinetics on an active single crystal Ni surface with a polycrystalline Ni surface revealed a decidedly higher oxide growth rate on the polycrystalline surface. This indicates that ion transport on the latter surface is likely to occur mostly at grain boundaries, rather than at the grain face. Our small spot and imaging studies do not, however, show localized growth at the grain boundaries; rather, the oxide thicknesses on samples exposed to 300° and 25°C appear to be mostly even. This suggests that, following diffusion to the surface, ion transport occurs readily across most grain faces, and that the surface orientation plays a relatively small part in accommodating the transported ions to a place exchange reaction. Evidence of some grain dependent growth was, however, observed on a sample surface reacted at 25°C.

The absence of localized growth, as determined by micro XPS, should not be confused with the evidence of localized growth, as determined by QUASES™. The latter phenomenon could be very short range (on a nanometric scale) responding to early formation of islands [4] following nucleation of an oxide structure.

Samples that had been prepared by multiple annealing steps were found to be transformed to a highly twinned grain structure and a much-reduced rate of surface oxidation. This could result in the number of high angle boundaries available for ion transport.

2.5 References

[1] F.P. Fehlner, M.J. Graham, in: P. Marcus, J. Oudar, (Eds.), Corrosion Mechanisms in Theory and Practice, Marcel Dekker Inc., New York, 1995, (Chapter 4).

[2] H.H. Uhlig, R.W. Revie, in: Corrosion and Corrosion Control: An Introduction to Corrosion Science and Engineering, John Wiley & Sons Inc, New York, 1985, (Chapter 10).

[3] N. Cabrera, N.F. Mott. Rep. Prog. Phys. 12 (1948-1949) 163.

[4] F.P. Fehlner, N.F. Mott, in: Oxidation of Metals and Alloys; papers presented at a seminar of the American Society for Metals, October 17 and 18, 1970, American Society for Metals: Metals Park, 1971, (Chapter 3).

[5] P.R. Norton, R.L. Tapping, J.W. Goodale, Surf. Sci. 65 (1977) 13.

[6] P.R. Norton, R.L. Tapping, Faraday Discuss. 60 (1976) 71.

[7] T. Fleisch, N. Winograd, W.N. Delgass, Surf. Sci. 78 (1978) 141.

[8] P.R. Norton, P.E. Binder, T.E. Jackman, Surf. Sci. 175 (1986) 313.

[9] S.J. Bushby, T.D. Pope, B.W. Callen, K. Griffiths, P.R. Norton, Surf. Sci. 256 (1991) 301.

[10] I.V. Mitchell, G.R. Massoumi, W.N. Lennard, S.Y. Tong, P.F.A Alkemade, K. Griffiths, S.J. Bushby, P.R. Norton, Nucl. Instrum. Meth. B B45 (1990) 107.

[11] C.M. Kim, H.S. Jeong, E.H. Kim, Surf. Sci. 459 (2000) L457.

[12] A.P. Grovsenor, B.A. Kobe, N.S. McIntyre, Surf. Sci. 565 (2004) 151.

[13] A.P. Grovsenor, B.A. Kobe, N.S. McIntyre, S. Tougaard, W.N, Lennard, Surf. Interface Anal. 36 (2004) 632.

[14] A.P. Grovsenor, B.A. Kobe, N.S. McIntyre, Surf. Sci. 572 (2004) 217.

[15] A.P. Grovsenor, B.A. Kobe, N.S. McIntyre, Surf. Interface Anal. 36 (2004) 1637.

[16] S. Tougaard, QUASES™, Version 4.4, Software for Quantitative XPS/AES of Surface Nano-Structures by Analysis of the Peak Shape Background, 2000.

[17] Fairley N. CasaXPS Version 2.2.107, 1999-2005.

[18] I.R. Barkshire, P.G. Kenny, I.W. Fletcher, M. Prutton, Ultramicroscopy 63 (1996) 193.

[19] I.R. Barkshire, M. Prutton, J.C. Breenwood, P.G. Kenny, Appl. Surf. Sci. 55 (1992) 245.

[20] M. Prutton, D.K. Wilkinson, P.G. Kenny, D.L. Mountain, Appl. Surf. Sci. 144-145 (1999) 1.

[21] K. Artyushkova, J.E. Fulghum, Surf. Interface Anal. 36 (2004) 1304.

[22] K. Artyushkova, J.E. Fulghum, Surf. Interface Anal. 33 (2002) 185.

[23] J. Walton, N. Fairley, Surf. Interface Anal. 36 (2004) 89.

[24] J. Walton, N. Fairley, J. Electron Spectrosc. Relat. Phenom. 148 (2005) 29.

[25] E.F. Smith, D. Briggs, N. Fairley, Surf. Interface Anal. 38 (2006) 69.

[26] A.P. Grovsenor, M.C. Biesinger, R.St.C. Smart, N.S. McIntyre, Surf. Sci. 600 (2006) 1771.

[27] A.F. Carley, S.D. Jackson, J.N. O'Shea, M.W. Roberts, Surf. Sci. 440 (1999) L868.

[28] S. Oswald, W Brükner, Surf. Interface Anal. 36 (2004) 17.

[29] S. Doniach, M. Sunjic, J. Phys. C 3 (1970) 285.

[30] MATLAB Version 6.5 Release 13, 2002 From The MathWorks, Inc.

[31] S. Tanuma, C.J. Powell, D.R. Penn, Surf. Interface Anal. 11 (1988) 577.

[32] S. Tougaard, Surf. Interface Anal. 11 (1988) 453.

[33] S. Tougaard, QUASES-XS-REELSTM, Version 1.2, Software for Quantitative Analysis of Surface Electron Spectra Cross Sections determined by Reflection Electron Energy Loss Spectroscopy, 2004.

[34] B.R. Strohmeier, Surf. Interface Anal. 15 (1990) 51.

[35] K. Hauffe, in Oxidation of Metals, Plenum Press, 1965, (Chapter 4).

[36] N.S. McIntyre, T.C. Chan, Oxid. Met. 33 (1990) 457.

[37] N.S. McIntyre, M.G. Cook, Anal. Chem. 47 (1975) 2208.

[38] M.W. Roberts, R.St.C. Smart, J. Chem. Society. Faraday Trans. I 80 (1984) 2957.

[39] D.F. Mitchell, M.J. Graham, Intern. Corrosion Conf. Ser. NACE-6 (1981) p.18.

[40] H. Haugsrud, Corros. Sci. 45 (2003) 211.

Chapter 3 The study of nickel metal oxidation by water vapour

3.1 Introduction

The reaction of Ni metal surfaces with H_2O vapour has been found to be much slower than with gaseous O_2 [1]. This difference is important in view of the corrosion-resistant nature of Ni and its alloys. Previous studies of the Ni-H_2O reaction have used single crystals and low doses and dose rates of H_2O [1-6].

The initial reaction of single crystal Ni (100) surfaces and H_2O vapour was studied using XPS by Benndorf et al., particularly at low temperatures [2-3]. At temperatures below -120°C adsorbed H_2O molecules (H_2O (ads)) were the sole source of an O 1s signal with a binding energy (BE) that increased with increasing dose (533.1–534.4 eV) [3]. This shift was attributed to a decrease in the O-surface interaction due to the formation of multiple layers of H-bonded clusters of H_2O molecules. At higher temperatures, formation of an O 1s oxidic peak was observed, along with peaks in the BE range of 532.6-532.8 eV. The possibility of adsorbed OH (OH (ads)) was eliminated using isotope exchange measurements. It was concluded that the reaction occurred by H_2O (ads) dissociating into adsorbed O (O (ads)) and H_2 gas.

The reaction of H_2O vapour with clean as well as O pre-covered single crystal Ni (210) metal surfaces was also studied by Carley et al. using XPS at low temperatures [6]. After adsorption of H_2O at temperatures below -100°C, heating of the surface resulted in an O 1s peak at 531.5 eV, which is attributed to the formation of OH (ads) species. The group of Norton et al. also exposed clean and pre-covered single crystal Ni (100) and (111) metal surfaces to H_2O vapour as well as O_2 gas and air containing H_2O at temperatures near 20°C [1]. The reactivity of clean single crystal metal surfaces was

determined to be almost 10^3 times less reactive towards H_2O vapour than O_2 gas. Reactions of clean or pre-oxidized Ni with H_2O vapour at ambient conditions produced a new peak at 531.3 eV [1]. The presence of any $Ni(OH)_2$ species was eliminated using nuclear reaction analysis (NRA). Rather, the authors proposed a Ni_2O_3-like species with some involvement by H.

A study from this laboratory of the equivalent Fe-H_2O vapour reaction [7-8] has identified OH groups as one product of the reaction and has suggested that their subsequent decomposition produces H atoms that could assist in blocking migration of cations to the surface [7-9].

From the studies described above it can be seen that the surface products of this very important Ni reaction are still ambiguous. Much of this is due to differing interpretations of XPS O 1s spectra of the products. Such spectra are potentially the single most useful means for identifying different products, but unfortunately there have been large uncertainties both with the species represented as well as with their line positions.

This paper reports another study of the Ni-H_2O vapour reaction. In addition to a study of the kinetics of oxide growth over an exposure regime much wider than the previous studies, the present work undertakes a detailed analysis of possible interpretations of the O 1s spectra associated with each reaction.

Most of the surface characterization done in this work was carried out using XPS and algorithms developed by Tougaard [10]. These algorithms have been incorporated into a software package called QUASES™, which is separated into two analytical routines ‘Analyze’ and ‘Generate’ [11]. The ‘Analyze’ program can be used to determine

the thicknesses of surface overlayers, such as oxide films, by modeling the depth from which the detected photoelectrons originated. The 'Generate' program maps the atomic distribution throughout the surface using a combination of reference spectra whose extrinsic backgrounds have been modified as a result of the depth from which they are located [11-12]. Similar oxidation studies using Ni and O_2, as well as Fe and O_2, and Fe and H_2O have been completed using this same program [7-8,12-16].

In this paper the oxidation of Ni metal surfaces was studied following doses of up to 3.0 x 10^{10} Langmuir (L) of H_2O vapour at pressures around 130 Pa and temperatures of 25°C and 300°C. The pressure of the vapour reactant used here is many orders of magnitude higher than those used in most surface reaction studies. Pressure differences have been shown to change the reaction mechanism in other surface oxidation studies [13,17]. In fact, the pressures used here are within a few orders of magnitude to those used in liquids.

3.2 Experimental

Polycrystalline Ni metal samples were cut into 3.4 mm thick discs from a polycrystalline rod (Alfa Aesar, 99.995% pure) and one face was polished to a mirror finish using 0.05 μm γ-Al_2O_3 paste. The size of the grains found on each surface typically ranged from 70-175 μm in diameter. From a qualitative analysis of texture using SEM to compare channeling contrast, the distribution of contrasting grain shades appeared to be relatively even. From a previous study it was suggested that grain boundaries play a dominant role in the outward transport of Ni cations and that the character of the boundaries is likely to play a more important role here than the orientation(s) of the grain faces themselves [14]. After polishing, the samples were

sonicated in methanol and then placed into an isolated chamber in a Kratos AXIS Ultra XPS having base pressures ranging between 4 x 10^{-6}–7 x 10^{-7} Pa for surface cleaning. All Ni metal samples were Ar^+ sputtered for 15 minutes using a 4 kV beam with an emission current of 15 mA. Following sputter cleaning, the samples were annealed at 600°C for 30 minutes. The roughness of the surfaces following ion bombardment and annealing was not measured however, examination of these surfaces showed brightened regions where the sputtering had occurred. During the annealing process the chamber pressure increased to around 3 x 10^{-5} Pa. To verify that an atomically clean surface had been obtained (no detectable impurities) the samples were transferred under vacuum to an analytical chamber having pressures close to 7 x 10^{-7} Pa where XPS survey scans were collected. The survey scans showed that surface contamination from either O or C was no more than 0.3 atom %.

All oxidation experiments were carried out in a reaction chamber attached to the XPS instrument having a base pressure of 7 x 10^{-6} Pa. Prior to any vapour exposures, a Residual Gas Analyzer (RGA), a quadrapole mass spectrometer, was used to monitor the amount of contaminant gases present. The Ni metal surfaces were then exposed to doses of H_2O vapour that had been heated to remove as much O_2 and CO as possible. Any remaining contaminant gas was removed through multiple freeze-pump-thaw cycles. After several cycles, the amount of O_2 present in the H_2O container was undetectable by RGA analysis. The H_2O vapour exposures were carried out at 25°C and 300°C for doses of 1.2 x 10^9, 3.0 x 10^9, 3.6 x 10^9, 8.4 x 10^9, and 3.0 x 10^{10} L[a]. The pressures in the reaction chamber were measured using a combination Pirani and Penning gauge.

---

[a] Ni metal surfaces were exposed to H_2O vapour at a constant pressure of ~ 130 Pa for 20 (1.2 x 10^9 L) , 50 (3.0 x 10^9 L), 60 (3.6 x 10^9 L), 140 (8.4 x 10^9 L), and 500 (3.0 x 10^{10} L) min.

All Ni metal surfaces were analyzed using both monochromatic Al Kα and achromatic Zr Lα X-ray sources. The XPS survey scans were collected using the following parameters: hybrid focussing lens, pass energy = 160 eV, an energy step size = 0.7 eV, charge neutralizer = 1.6 A and 2.4 eV, and the slot beam size (700 x 300 μm). The Al Kα spectra were taken over a binding energy (BE) range = 1100–0 eV, a scan time = 180 s, and the number of sweeps = 10. The Zr Lα excited scans were acquired over a BE range = 1800–0 eV, a scan time = 360 s, and the number of sweeps = 20. High-resolution XPS analysis of the Ni 2p, O 1s, and C 1s envelopes used Al Kα excitation only at pass energy = 20 eV over energy windows ranging between 20-40 eV, depending on the element being analyzed. An analysis region of 700 x 300 μm would encompass an area involving 8-10 separate crystals based on the grain sizes stated above.

CasaXPS Version 2.3.14 was used for the analysis of all the XPS spectra [18]. The surface at.% of each element present was determined using XPS survey spectra. The total amount of Ni on each surface was calculated using the area of the Ni $2p_{3/2}$ peak only [18]. To monitor the oxide composition, high-resolution XPS was employed on the Ni 2p, O 1s, and C 1s regions. Relative elemental concentrations were determined using Scofield cross-sections[b] corrected for the kinetic energy of the particular photoelectrons. This was particularly useful for estimating surface coverage of the metal.

It was determined that each Ni surface contained small amounts of adventitious carbon (C (adv)) on the surface; this was used for spectral calibration as the C (adv) peak was set to a BE of 284.8 ± 0.1 eV. Each C 1s spectrum also showed the presence of three

[b] All elemental concentrations were calculated using relative sensitivity factors (RSFs) specifically derived for use with a Kratos Axis Ultra Spectrometer and not those calculated by Scofield. The origin of these RSF values is discussed in Chapter 5.

additional C species centred at 286.3 ± 0.2 eV, 287.7 ± 0.1 eV and 288.6 ± 0.1 eV (see Figure 3.1(a)). These peaks are assigned to alcohol (–COH), carbonyl (–CO), and ester (–COO–) functional groups respectively [19]. The identification of these adsorbate species becomes important when analyzing the O 1s spectra (see Figure 3.1(b)), as they will also add to the observed photoelectron signal here, and thus complicate the analysis of this spectrum. Four small peaks associated with O-containing adsorbates are visible at higher BE in most O 1s spectra; all their intensities are tied to those in the corresponding C 1s spectrum. Figure 3.1(c) shows an expanded view of this region illustrating more clearly the BE positions of the –COH (532.7 ± 0.2 eV), –CO (532.1 ± 0.1 eV) and –COO– (532.1 ± 0.3 eV, 533.6 ± 0.1 eV) adsorbate species [19].

The CasaXPS software was also used for spectral subtractions; in these the contribution from the Ni metal substrate was removed to reveal the underlying structures resulting from oxidation. Each subtraction entailed a normalizing of the intensity of a clean Ni metal reference component having a BE of 852.6 eV (see Figure 3.2(a)) with the intensity of the same peak found on the oxidized scans. A second subtraction was then undertaken to remove the NiO contribution this time by normalizing the intensity of the main NiO line at 854.0 ± 0.2 eV. Care had to be taken to separate the correction of the charging components (oxides) from those of the metallic substrate. An identical method for spectral analysis was reported in previous publications [14,20]. Figure 3.2(b-c) also contains the high-resolution spectra of powdered polycrystalline NiO and $Ni(OH)_2$. Both powders contain Ni^{2+} species, however the shapes of the two main lines are distinctly different [21]. Spectra of possible Ni^{3+} structures, such as γ-NiOOH and β-NiOOH are presented in Figure 3.3(a-b).

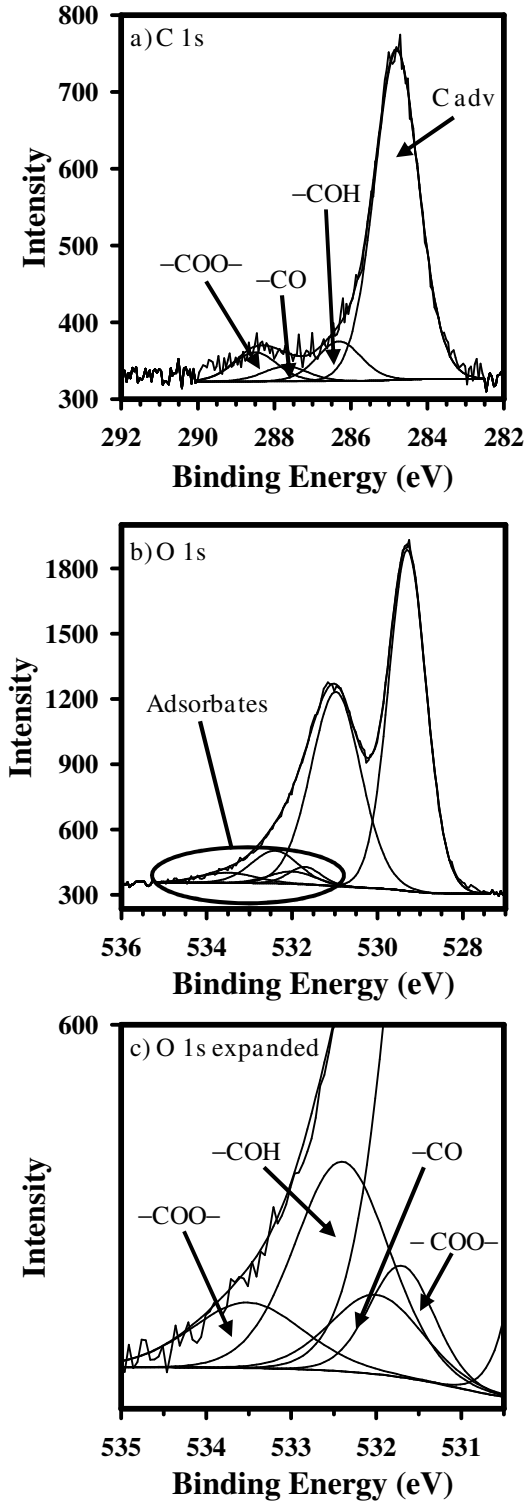

Figure 3.1: High-resolution spectrum of the C 1s region of a Ni metal surface exposed to H_2O vapour showing the BE shifts of the C (adv), –COH, –CO, and –COO– species (a). The corresponding peak positions in the O 1s region for the –COH, –CO, and –COO– species are shown in (b), with an expanded view of this region shown in (c).

Comparison of the Ni spectra in Figures 3.2 and 3.3 shows an overlap between the Ni $2p_{1/2}$ peak of the clean metal scan with the satellite structure in the Ni $2p_{3/2}$ portion of the NiO, $Ni(OH)_2$, and both NiOOH standard spectra. This overlap must be taken into account to accurately analyze surfaces containing Ni metal along with one or more oxidized Ni species. All Ni 2p envelopes collected as a part of this study were subject to analysis using the Ni metal, NiO, $Ni(OH)_2$ and NiOOH peak fitting parameters presented recently by Biesinger et al., where the BE of each peak was allowed to drift by ± 0.1 eV [20]. The fits developed by Biesinger et al. employ an off-set in the Shirley background to more accurately model the Ni 2p spectra of surfaces containing both metallic and oxidized species.

The corresponding O 1s spectra for the NiO and $Ni(OH)_2$ powders are shown in Figure 3.2(d-e). The NiO powder appears to contain two major O species at 529.3 eV and 531.0 eV. The BE of the first peak is assigned to O bonded within a regular oxide crystal (O^{2-}) and the second is assigned to oxygen atoms in positions adjacent to Ni vacancies (O (def)) within the oxide structure. Similar assignments of this peak have been made previously by several other authors [1,20,22-25]. In the case of the $Ni(OH)_2$ powder only one major O species at 531.1 eV is evident and is assigned to a hydroxide bound to Ni (OH^-). Fitting of the γ-NiOOH O 1s spectrum (see Figure 3.3(c)) showed both O^{2-} and OH^- signals at 529.5 eV and 531.1 eV respectively. The same two O^{2-} and OH^- components appear in the β-NiOOH spectrum (see Figure 3.3(d)) with BE shifts of 529.3 eV and 530.8 eV respectively. All the O 1s envelopes were also fit with the four small peaks associated with the C and O adsorbates mentioned previously. A more detailed analysis of these spectra is given in Chapter 5.

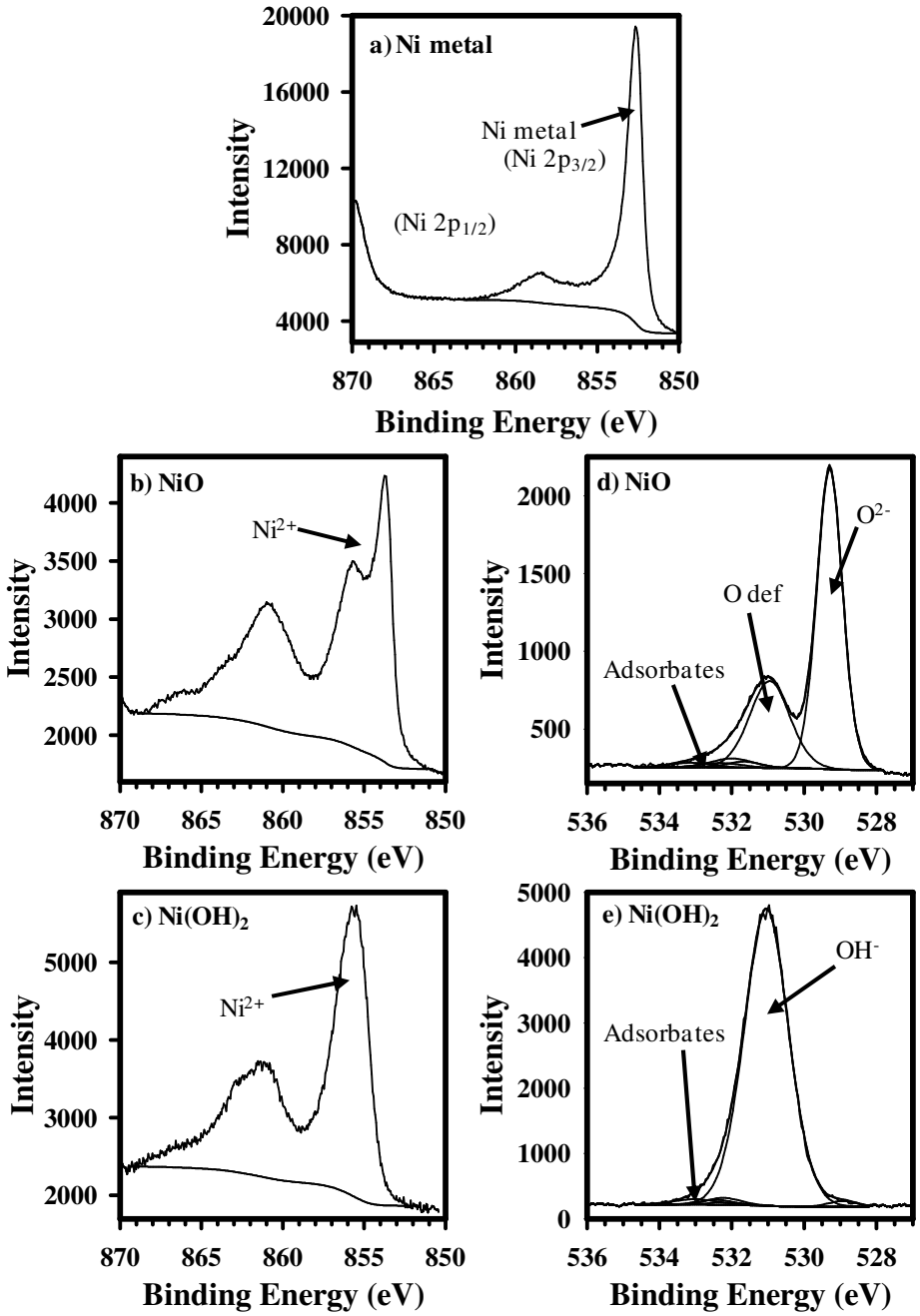

Figure 3.2: High-resolution Ni $2p_{3/2}$ spectra of (a) a clean Ni metal surface, (b) a polycrystalline NiO powder, and (c) a polycrystalline $Ni(OH)_2$ powder. High-resolution O 1s spectra of (d) NiO and (e) $Ni(OH)_2$. Part of the metal Ni $2p_{1/2}$ line can be observed in (a).

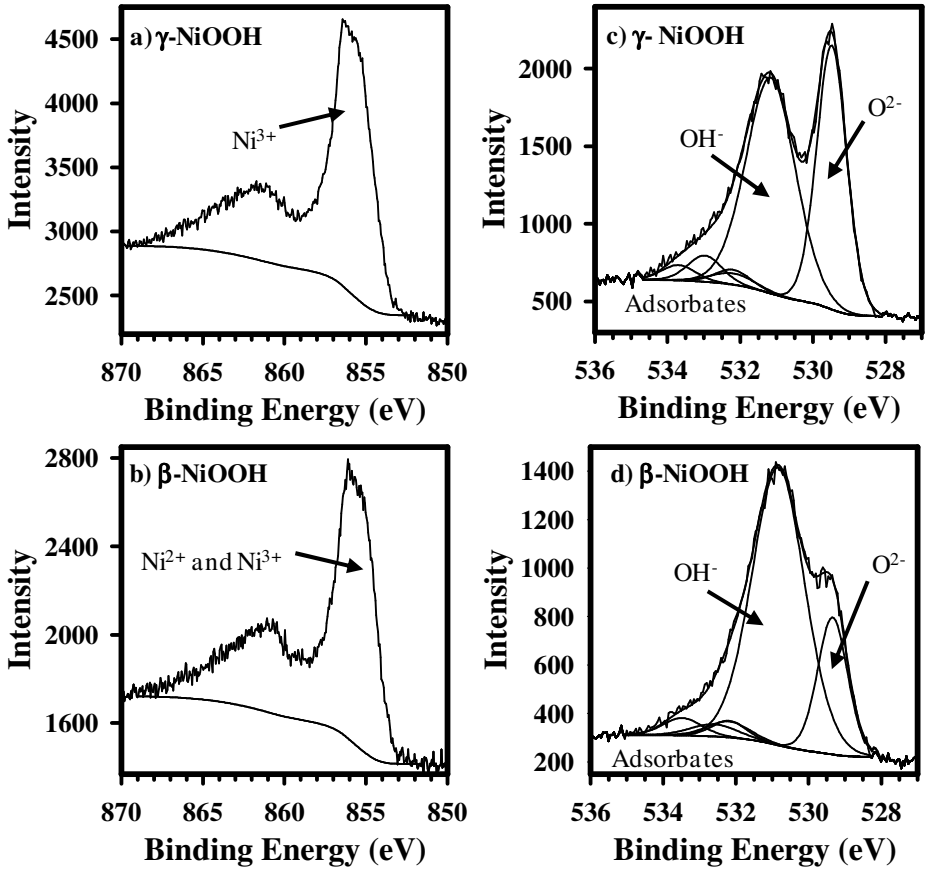

Figure 3.3: High-resolution Ni $2p_{3/2}$ spectra of (a) γ-NiOOH and (b) β-NiOOH powders. High-resolution O 1s spectra of (c) γ-NiOOH and (d) β-NiOOH.

Further analysis of the oxidized surfaces was carried out using algorithms that were developed by Tougaard [10]. The basis of the Tougaard approach is that photoelectrons moving through a surface can undergo multiple scattering events prior to escaping to the vacuum phase. These energy loss interactions lead to the formation of the background found on the low kinetic energy (KE) side of the peaks in XPS spectra [10]. The shape of the background is defined by the distribution of atoms within the near surface region. Modeling of these structures can be undertaken using one of the five depth concentration profiles that are included with the QUASES™ software package; 'buried layer, 'island active substrate', 'islands passive substrate', 'exponential profile', or 'several buried layers' [12]. For the purposes of this work both the 'buried layer' and 'island active substrate' profiles were employed during surface analysis. The 'buried layer' profile models the energy lost by the photoelectrons emitted from atoms contained within a homogenous layer as they pass through an overlying material having a different composition. The 'island active substrate' models the extrinsic losses of photoelectrons emitted from substrate atoms as they pass through overlying islands. These islands do not have to be uniform in size and/or shape [12]. The probability that an electron emitted from an atom located at a certain depth will reach the surface is dependent on both a material-specific inelastic mean free path (IMFP) and the energy loss cross-section. The latter term simply represents both the likelihood the photoelectron would undergo a scattering event as well as the average energy lost per collision [10]. The IMFP values for the different Ni-containing species were calculated using the NIST Electron Inelastic Mean Free Path Database (Version 1.1) [26] software, which uses the TPP-2M equation [27]. Previous IMFP calculations completed by this group were then subsequently

shortened by 20% to give the actual photoelectron attenuation length (AL) [14]. It was later determined that the IMFPs estimated as part of Ni-O_2 work were calculated incorrectly. The current IMFPs calculated as part of this work compare well to the ALs presented in reference [14] and are now used for analysis of all oxide films. The same database was used by Biesinger et al. to determine their IMFP values [20].

Sample oxide thicknesses were calculated with the 'Analyze' program using an IMFP of 1.4 nm and the O 1s region of XPS survey spectra excited with Al Kα X-rays. The oxide surface structures were modeled using 'Generate', and the Ni 2s peak collected from Zr Lα excited scans. Each sample was fit using reference spectra acquired from a clean polycrystalline Ni metal surface and a sample of powdered polycrystalline NiO. Photoelectron IMFPs of 1.4 nm and 1.5 nm were calculated for the metal and NiO standards respectively. All QUASES™ 'Generate' analysis used a Ni-specific energy loss cross-section that was calculated by Tougaard [14].

The QUASES™ 'Analyze' results were verified using the Strohmeier method [28]. The Strohmeier overlayer equation is given below,

$$d = \lambda_o \sin\theta \ln\left[\frac{N_m \lambda_m}{N_o \lambda_o}\frac{I_o}{I_m} + 1\right] \qquad 3.1$$

where d represents the thickness of the overlayer, λ_o is the photoelectron IMFP, m and o denote the metal and oxide components respectively derived from fitted high-resolution XPS spectra, N stands for the volume density of metal atoms in either the metal or the oxide phase, I is the peak area for either the metal or the oxide, and θ is the take off angle of the electrons.

For a study using ToF-SIMS, a sample of polycrystalline Ni metal was cut from the same rod above and polished with 0.05 μm γ-Al_2O_3 paste. Following polishing, the sample was sonicated in methanol then introduced into an ION-TOF (GmbH) ToF-SIMS IV single-reflection mass spectrometer. The surface was sputtered using a 3 kV Ar^+ beam and with 140 nA target current for 8100 s.

After sputtering, the surface was heated into the range of 300-400°C, and then exposed to H_2O vapour containing high purity deuterium (D) for 20 minutes (~ 1.2 x 10^9 L) at an average pressure of 130 Pa. During the dose, the pressure dropped to as low as 10 Pa, and spiked to as high as 530 Pa for no more than a few seconds. D_2O was used instead of H_2O because of the high probability of H contamination from within the vacuum system. A shallow depth profile into the surface was collected using the dual beam mode, monitoring negative secondary ions. The analysis beam was a 25 kV pulsed Bi^+ with a 0.5 pA target current, rastered over a 200 x 200 μm area. The sputter beam was a 3 kV Cs^+ rastered over 500 x 500 μm with a target current of 10 nA. The Bi^+ analysis region was centred within the Cs^+ sputter crater to avoid edge effects. The ToF SIMS results were analyzed using the IONSPEC program [29].

3.3 Results and Discussion

Figure 3.4 contains Ni $2p_{3/2}$ high-resolution spectra collected from metal surfaces exposed to H_2O vapour at 300°C for doses of 1.2 x 10^9, 3.6 x 10^9, 8.4 x 10^9, and 3.0 x 10^{10} L. A small contribution from the metal Ni $2p_{1/2}$ peak is visible on all spectra at high BE. With continuing exposure time, an increase in the Ni 2p line shape and background was observed as a result of surface oxidation. The intensity of the Ni metal

peak found in the Ni 2p spectra in Figure 3.4 makes it difficult to observe, in its entirety, the line shape of the oxidized species. The metal contribution was therefore removed, and the subtracted spectra for the 3.6 x 10^9, 8.4 x 10^9, and 3.0 x 10^{10} L exposures are shown in Figure 3.5(a-c). Subtraction of the metal component from the surface exposed to 1.2 x 10^9 L produced a very noisy spectrum (not shown), indicating that very little oxidation has occurred. From the subtracted spectra, the characteristic shape and BE positions of NiO suggests it to be the major non-metal phase present for these doses. However, the intensities under the doublet shape of the NiO main line suggest the presence of an additional component near 856 eV. To further investigate the Ni species present following H_2O vapour exposures the NiO component was removed and the resulting spectra are shown in Figure 3.5(d-f). In all the subtracted spectra two additional components near 856 eV and 853 eV were found. The peak near 856 eV is thought to be the result of a Ni^{3+} species at the very near surface brought on by the presence of Ni vacancies. A similar result had been observed following the exposure of Ni metal surfaces to O_2 gas at 25°C and during the initial stages of reaction at 300°C [14]. The sharp peak near 853 eV is thought to be the result of S contamination. All of the oxidized surfaces were found to contain between 1 to 5% S. Although no high-resolution analysis of the S 2p region was undertaken the BE associated with these S species from XPS survey spectra was found to range between 162.1 eV to 162.9 eV indicative of a NiS [30].

From the subtraction results shown above it is evident that any analysis of the Ni 2p envelopes is complicated by the presence of Ni metal, Ni^{2+} (from NiO), Ni^{3+} (from defective NiO) and NiS on each surface. Fitting of the Ni 2p spectra entailed using contributions from Ni metal, NiO and NiOOH components [20]. The NiOOH component

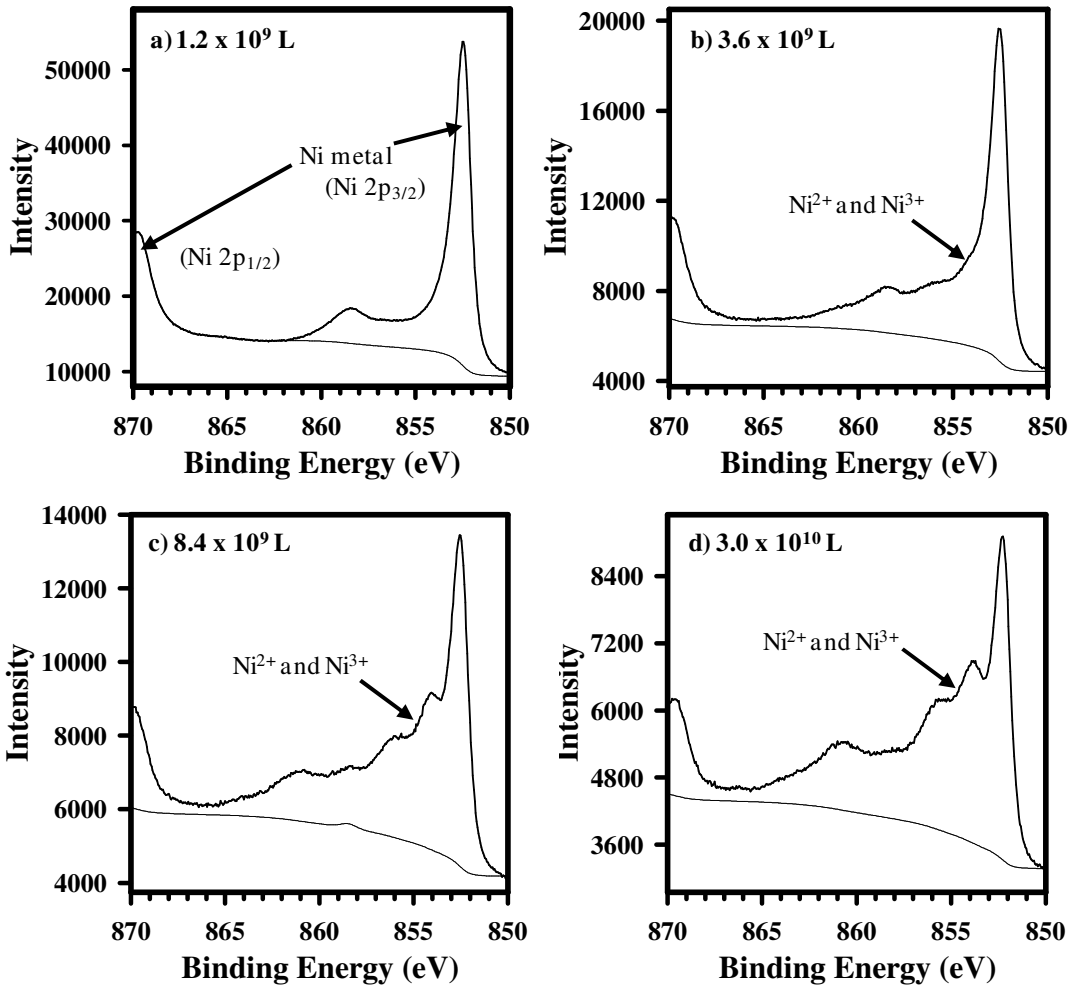

Figure 3.4: High-resolution Ni $2p_{3/2}$ spectra collected after (a) 1.2 x 10^9 L, (b) 3.6 x 10^9 L, (c) 8.4 x 10^9 L, and (d) 3.0 x 10^{10} L of exposure to H_2O at 300°C. A small contribution from the metal Ni $2p_{1/2}$ peak is visible on all spectra.

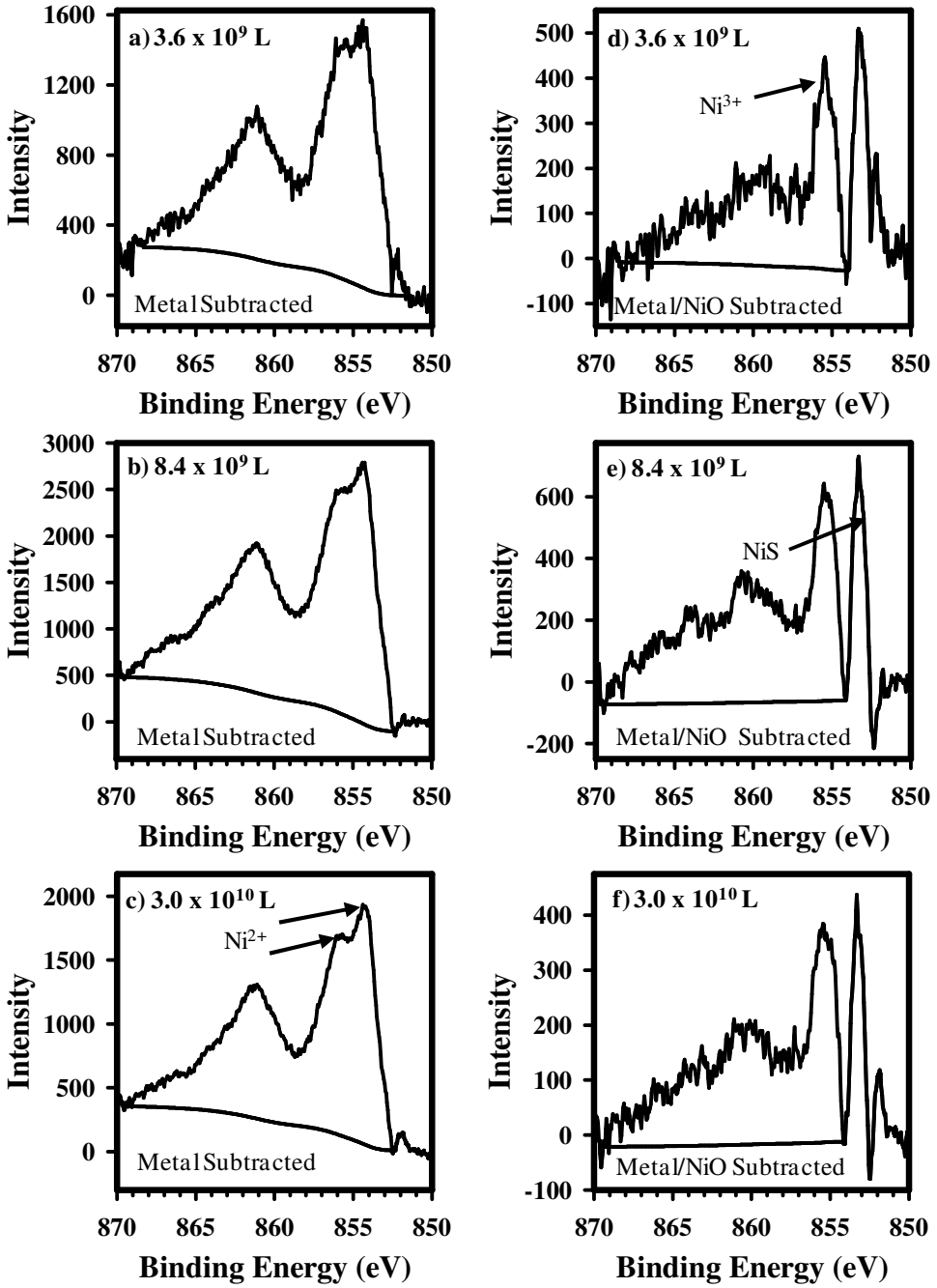

Figure 3.5: Ni $2p_{3/2}$ spectra with the Ni metal component subtracted following exposures of (a) 3.6 x 10^9 L, (b) 8.4 x 10^9 L, and (c) 3.0 x 10^{10} L of H_2O vapour. A doublet structure of the main line is visible, suggesting the formation of NiO. The resulting spectra following removal of the NiO contributions for doses of (d) 3.6 x 10^9 L, (e) 8.4 x 10^9 L, and (f) 3.0 x 10^{10} L of H_2O vapour are also shown. A small signal from NiS is also visible at the low BE end of the spectrum. The remaining Ni signal resembles that of NiOOH, a Ni^{3+} containing material.

was chosen to represent the defective NiO because it contains Ni^{3+} species and has a similar line shape to the subtracted spectra shown in Figure 3.5(d-f). The surface percentages calculated for the Ni metal, Ni^{2+} and Ni^{3+} species obtained from these peak fittings are presented in Table 3.1. It appears that following doses of 3.6 x 10^9, 8.4 x 10^9, and 3.0 x 10^{10} L each surface contains between 3 to 5 % Ni^{3+} (see Figure 3.4(b-d)). For the case of the lowest dose, a Ni^{3+} component of around 1% with a large uncertainty was determined.

Table 3.1: Near-surface compositions of Ni and O species for surfaces exposed to H_2O vapour at 300°C.

Dose (L)	Ni metal (%)	Ni^{2+} (%)	Ni^{3+} (%)	Ni^{2+} + Ni^{3+} (%)	O^{2-} (%)	O (def) (%)	O^{2-} + O (def) (%)	O/Ni
1.2 x 10^{9a}	71	-	1	1	-	1	1	1
3.6 x 10^9	46	12	4	16	8	10	18	1.1
3.6 x 10^9	41	14	5	19	9	11	20	1.1
8.4 x 10^9	26	20	3	23	16	8	24	1.0
8.4 x 10^9	26	18	5	23	13	14	27	1.2
3.0 x 10^{10}	26	20	5	25	15	14	29	1.2
3.0 x 10^{10}	20	21	4	25	16	12	28	1.1

[a] Large uncertainty in the measurement due to the small amount of oxide present.

Analysis of the O 1s envelopes collected from surfaces subjected to H_2O exposures of 3.6 x 10^9 L or greater showed two major peaks at 529.4 ± 0.1 eV and 531.2 ± 0.1 eV (see Figure 3.6(b-d)). The first peak is assigned to O^{2-} and the second peak is believed to be the result of an O (def) species. When the combined intensities of both the O^{2-} and O (def) species are compared to the surface Ni^{2+} and Ni^{3+} percentages obtained from the Ni 2p analysis, O/Ni ratios of close to 1 are observed (see Table 3.1). This result suggests that the films formed here are similar in structure to that of the reference NiO (see Chapter 5). The peak attributed to O (def) cannot represent a bound OH^-

species since reference OH^- compounds studied had O/Ni ratios between 1.6 and 2.0 (see Chapter 5). For the O 1s spectrum collected following a dose of 1.2 x 10^9 L the peak at 531.3 eV was assigned to O (def). The O/Ni ratio calculated for this surface was found to be 1 (see Table 3.1). In this case the presence of an adsorbed O species cannot be completely ruled out due to both the large uncertainty in the Ni 2p fit above and the QUASES™ analysis described below. There is no evidence for the presence of H_2O (ads) on any of these surfaces at this temperature. This suggests that any H_2O reactant dissociates quickly on the surface and is not observed as an intermediate.

The oxide thicknesses on all samples exposed to H_2O vapour at 300°C were calculated using QUASES™ 'Analyze'; the results are tabulated in Table 3.2. No 'Analyze' data was reported for the surface exposed to a dose of 1.2 x 10^9 L, as the background could not be modeled. This indicates that either, very little oxide was formed, or that an adsorbed O species is present here. The overlayer thickness for this sample was calculated using the Strohmeier equation. From Table 3.2, exposures of 3.6 x 10^9 L of H_2O vapour at 300°C lead to a determined average oxide thickness of 0.6 nm. In a previous publication by our group, the same dose of O_2 molecules at 300°C produced films averaging 4.5 nm thick [14]. It is evident that the oxides grown following exposures to H_2O vapour are much thinner compared to similar doses of O_2. Further examination of the 'Analyze' results shows that there was very little change in the oxide thicknesses at doses of greater than 8.4 x 10^9 L. It appears that the oxidation rate has reduced significantly between these two exposures, and the surface is becoming passivated.

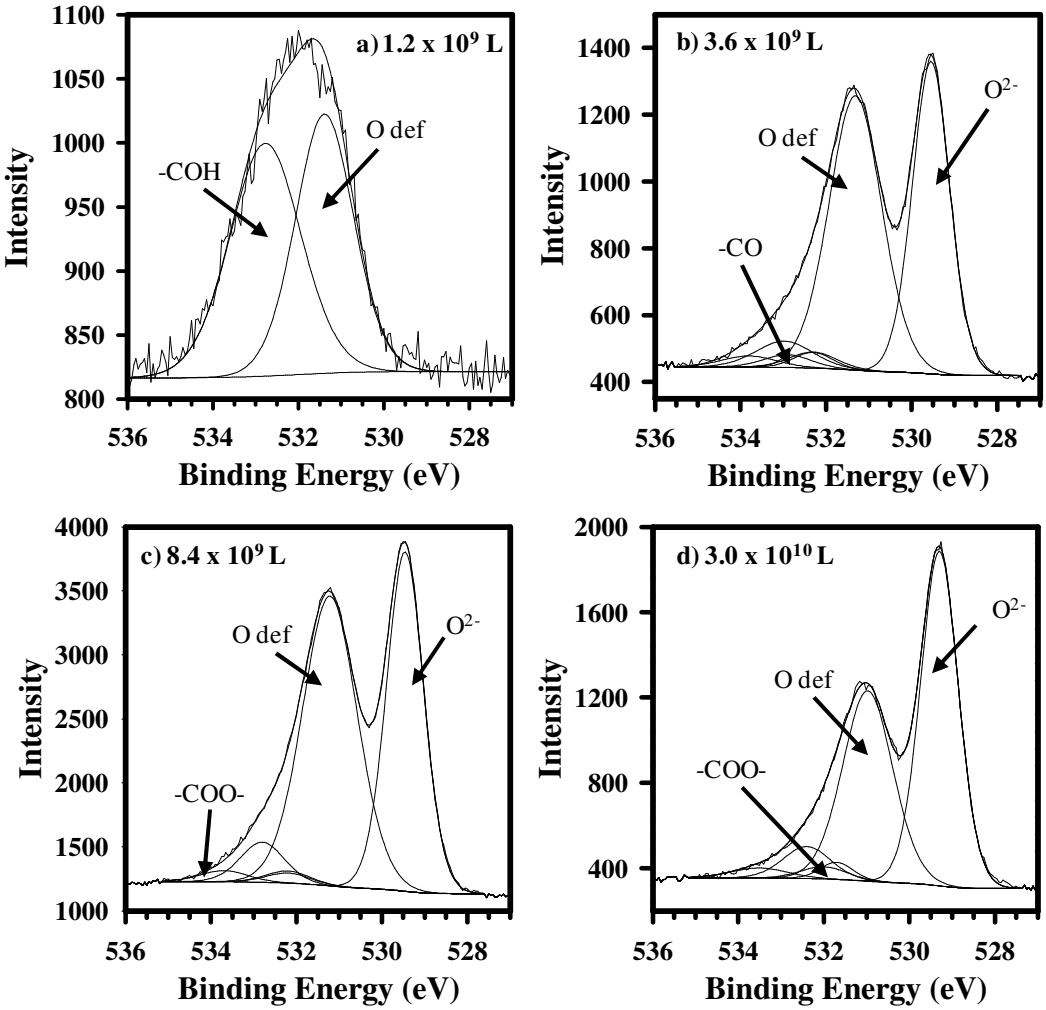

Figure 3.6: High-resolution O 1s spectra for exposures of (a) 1.2 x 10^9 L, (b) 3.6 x 10^9 L, (c) 8.4 x 10^9 L, and (d) 3.0 x 10^{10} L. Two O species bound to Ni are proposed: O^{2-}, O (def), along with –COH, –CO, and –COO– adsorbates. The spectrum in (a) is noisy due to the small amount of O present.

Table 3.2: Calculated film thickness and surface coverage using QUASES™ and Strohmeier equation.

Dose of H_2O vapour (L)	'Analyze' oxide thickness (nm)	'Generate' oxide thickness (nm)	'Generate' oxide surface coverage (%)	Strohmeier oxide thickness (nm)
1.2×10^{9} [a]	-	-	-	0.2
3.6×10^{9}	0.6	0.6	20	0.5
3.6×10^{9}	0.7	0.6	40	0.6
8.4×10^{9}	1.2	1.2	75	1.1
8.4×10^{9}	1.3	1.3	65	1.2
3.0×10^{10}	1.4	1.4	75	1.2
3.0×10^{10}	1.3	1.3	80	1.4

[a] Surface overlayer calculated with the Strohmeier equation.

All Ni surfaces oxidized at 300°C were also subject to analysis using QUASES™ 'Generate' and modeled overlayers of NiO. Figure 3.7 shows a representative fit for a Ni surface exposed to H_2O for a dose of 3.0×10^{10} L. The best fit was obtained using the 'island active substrate' depth profile for the Ni metal reference spectrum and the 'buried layer' depth profile for the NiO reference spectrum. Here there is a very good overlap between the reference and experimental spectra within the modeling KE range 940 eV – 1060 eV. The peak centred near 1033 eV is assigned to Ni 2s photoelectrons in the Ni metal and NiO reference spectra, as well as in the experimental spectrum. A peak found near 965 eV on both the NiO reference and experimental spectra is the result of a Na impurity. All of the oxidized surfaces were modeled using these same parameters, and representative depth profiles of the cross-sections of the surface regions following exposures of 3.6×10^{9}, 8.4×10^{9}, and 3.0×10^{10} L are shown in Figure 3.8. The 'Generate' analysis suggests that oxidation proceeds through island growth across the surface with the formation of localized NiO clusters. The advantage to using the 'Generate' program is that it allows for a more detailed modeling of the near surface.

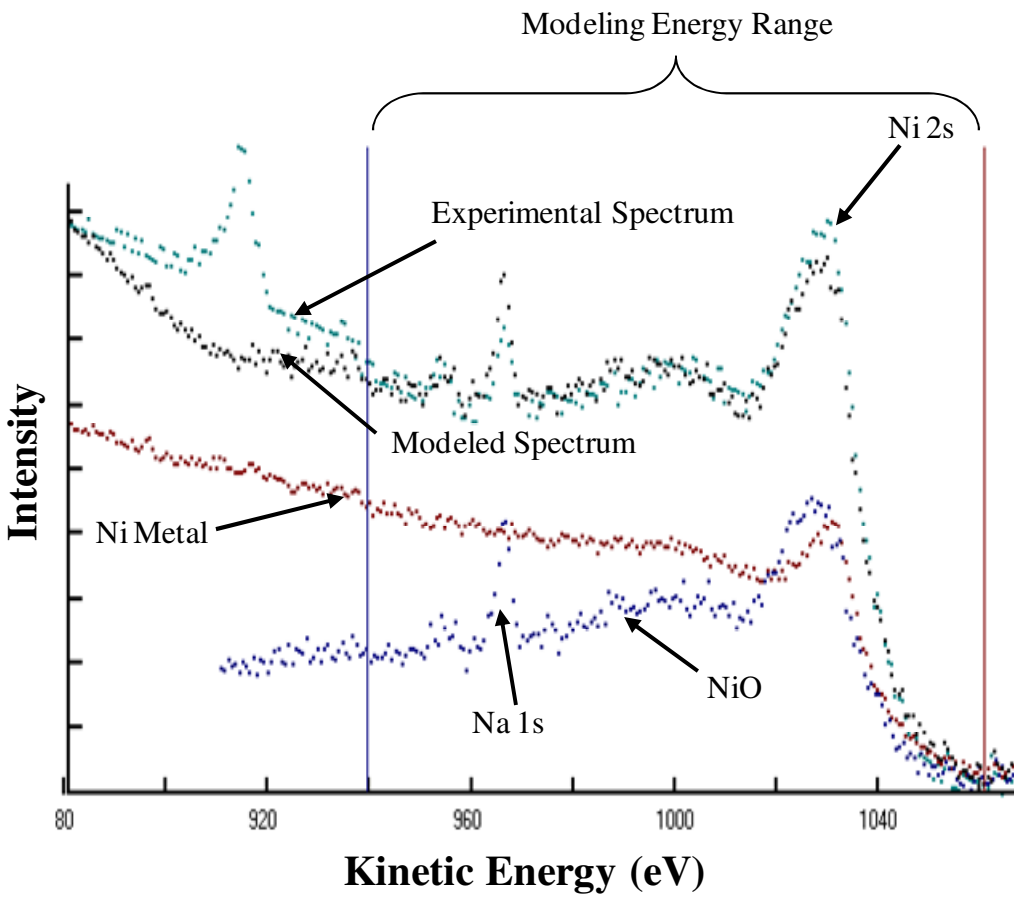

Figure 3.7: QUASES™ 'Generate' fit for a Ni metal surface exposed to H_2O vapour for a dose of 3.0 x 10^{10} L. The experimental spectrum was fit using reference spectra acquired from a clean Ni metal surface and polycrystalline NiO powder. The surface was modeled using the 'island active' profile for the Ni metal component and the 'buried layer' profile for the NiO powder. The peaks located near 1033 eV and 965 eV are assigned to Ni 2s and Na 1s photoelectrons respectively.

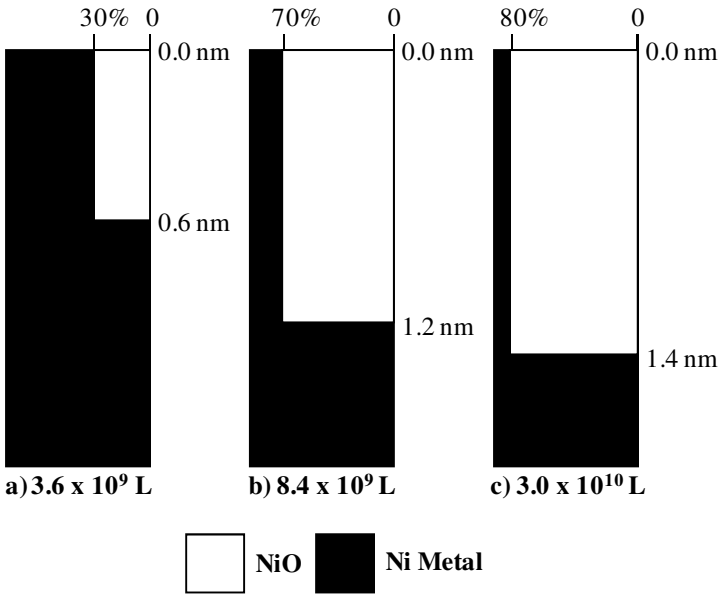

Figure 3.8: Depth profiles through the near surface areas of Ni metal samples exposed to H_2O vapour for (a) 3.6 x 10^9 L, (b) 8.4 x 10^9 L, and (c) 3.0 x 10^{10} L. There is one distinct oxide phase identified: NiO and the 'Generate' analysis in all cases indicated island oxide growth.

While both 'Analyze' and 'Generate' can be used to accurately model non-uniform overlayers the latter program also yields compositional information. 'Generate' uses reference spectra collected from samples with known composition to map the in-depth concentration profile of atoms in a surface [10-12]. The results show that with increasing vapour exposure the oxide islands cover more of the analyzed area. Following doses of 8.4 x 10^9 and 3.0 x 10^{10} L average surface coverages of 70 and 80 % were determined. Comparison of both the QUASES™ 'Analyze' and 'Generate' results to the Strohmeier calculated values show very close agreement of film thickness. All QUASES™ 'Generate' data is shown in Table 3.2.

The shallow SIMS depth profile collected from a surface exposed to D_2O for approximately 1.2 x 10^9 L is shown in Figure 3.9. The point labelled (A) represents the oxide/bulk metal interface that was reached after about 100 s of sputtering as the signals

from each secondary ion fragments has become constant. The D fragment is clearly associated with a species at or near the outer surface, and the signal diminishes sharply with depth into the surface. In the case of the Ni-D_2O reaction, it appears that the D is confined to the outer atomic layers.

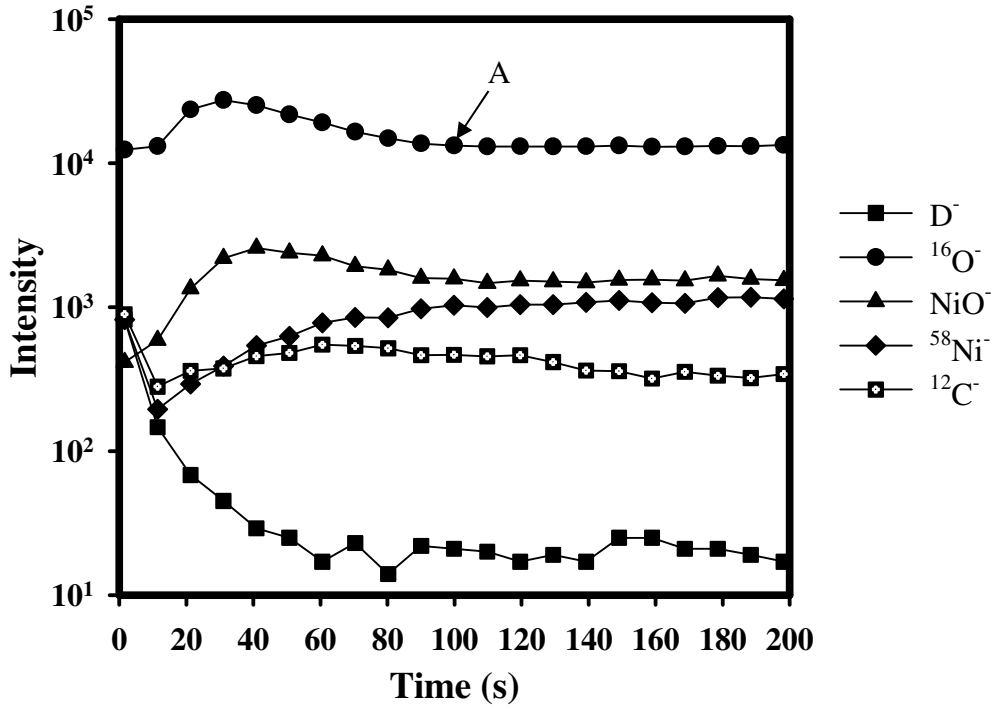

Figure 3.9: ToF-SIMS depth profile of a polycrystalline Ni metal surface exposed to approximately 1.2 x 10^9 L of D_2O vapour in the temperature range of 300-400°C. The negative secondary ions monitored were D^-, $^{16}O^-$, NiO^-, $^{58}Ni^-$, and $^{12}C^-$.

The oxide thicknesses measured by QUASES™ were plotted against dose using the three kinetic models [31-34] parabolic (R^2 = 0.99), direct logarithmic (R^2 = 0.98), and inverse logarithmic (R^2 = 0.80). The logarithmic model seems more sensible in view of the evidence for Ni^{3+} hole formation. The thickness measured for the highest H_2O dose does not fit the same mechanistic regime; from this dose it appears that the surface has become effectively unreactive toward H_2O. It is interesting to compare the oxide growth

curves for Ni exposed to O_2 at 300°C [14] and H_2O at 300°C (see Figure 3.10). For the O_2 exposures the reaction was found to follow a parabolic relationship with dose and the rate of growth for the O_2 reaction is four times that for the initial stages for the H_2O vapour reaction. Second, there is no evidence for termination of reactivity for the O_2 reaction (at least within this dose range), while this is clearly evident for the H_2O reaction after the formation of a thin oxide film. Finally, the H_2O reaction only begins to cause detectable oxide growth after a very large dose.

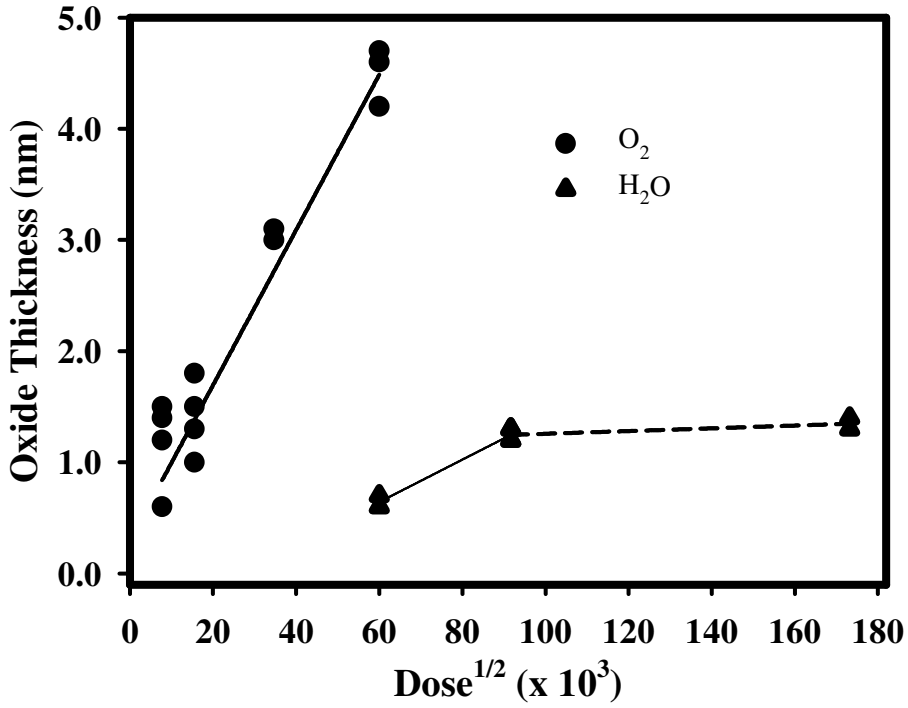

Figure 3.10: Comparison of oxide growth curves for Ni metal reacted with O_2 [35] and H_2O. The oxide thicknesses in each case are plotted *versus* dose$^{1/2}$.

The H_2O vapour Ni reaction was also studied briefly at 25°C. The Ni $2p_{3/2}$ and O 1s spectra collected following a dose of 3.0 x 10^9 L are shown in Figure 3.11. As with the 300°C exposures a small portion of the metal Ni $2p_{1/2}$ line is also present within the BE window shown here. Fitting of the Ni 2p envelope indicates that very little oxidized

Ni is present. The corresponding O 1s spectrum has a peak at 531.1 eV, but in this case there is no equivalent amount of oxidized Ni. We therefore assign this to an oxidic species adsorbed on the metal, prior to its place exchange and incorporation as an oxide. The existence of an O (ads) is unlikely: our previous study of Ni oxidation with O_2 showed that this species is highly reactive, with oxide nucleation occurring after relatively small doses [14]. Thus, the oxidic species is likely to be an OH (ads). Its presence suggests that its rate of conversion to an oxide is much slower at this temperature compared to 300°C as no detectable oxide has formed following this dose.

A comparison of the H_2O water reaction processes on clean Fe [7] and Ni surface under high flux is shown in Figure 3.12. Although the temperature used for the Fe reaction (150°C) differed from that used for Ni, the effects of temperature on the oxide thickness *versus* dose are not important on the scale shown. The most important conclusion is that the time taken to begin nucleation and growth of oxide on Ni is much

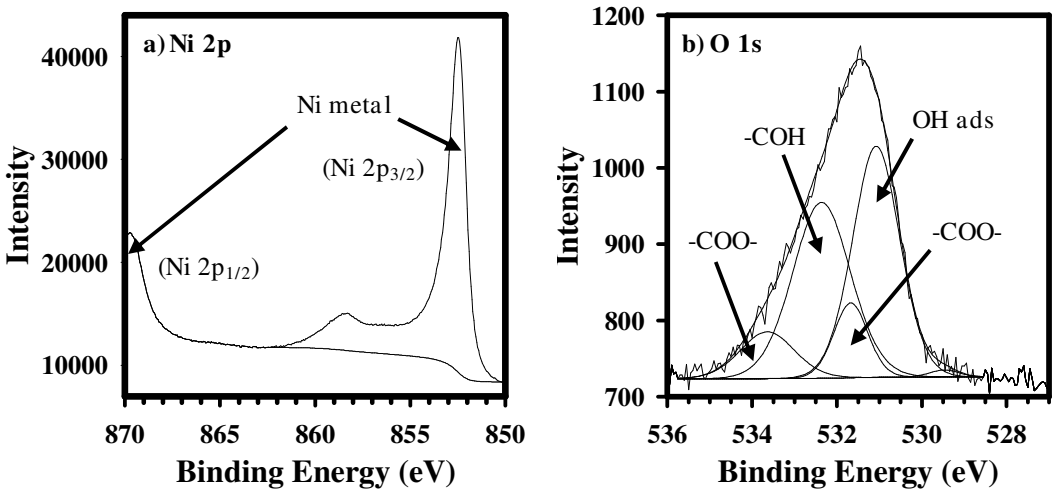

Figure 3.11: High-resolution (a) Ni $2p_{3/2}$ and (b) O 1s spectra collected following a H_2O vapour exposure of 3.0 x 10^9 L at 25°C. There is no evidence to suggest any Ni^{2+} or Ni^{3+} has formed. The O 1s scan does show the presence of four O species: OH (ads), –COH, –CO, and –COO–. The start of the Ni $2p_{1/2}$ line is visible at high BE.

longer than for Fe. In the cases of both Fe and Ni oxidized under high flux conditions, the recombination and desorption reactions compete successfully with place exchange for most reactant species on the surface. The lack of spectral evidence for the presence of any H_2O (ads) species on these surfaces suggests quick dissociation of this reactant upon interaction with Ni metal at both 25°C and 300°C. On the basis of these observations we propose that the H_2O quickly dissociates into OH (ads) and H (ads) species. However, the initial formation of a thin oxide film was found to occur much slower as compared to the similar exposures of O_2 to Ni where the reactive intermediate was shown to be O (ads) [14] (see Figure 3.10). The rate-determining step for this Ni-H_2O reaction is thought to be the slow place exchange of an OH (ads) with Ni metal and subsequent loss of H. Some of this H may become trapped in the oxide vacancies (Ni holes) and retard the migration of such vacancies, thus slowing the oxide growth even further. Analysis of the depth profile collected with the ToF SIMS did show the presence of some H at the surface. A similar explanation was also used to explain the reduction in oxidation rate of Fe surfaces following exposure to H_2O vapour [7-9].

Examples showing the stability of OH (ads) species on transition metal surfaces are available in the literature [6,36-38]. Andersson et al. have studied the dissociation of H_2O (ads) on single crystal (110) Cu surfaces following low doses of H_2O vapour (< 3.0 x 10^7 L) [36-37]. They showed using XPS that within the temperature range of 150°C and 250°C the only O species present was that of an OH (ads), while between 0°C and 150°C both H_2O (ads) and OH (ads) were present. A similar result was also reported by Schiros et al. on single crystal (111) Pt surfaces exposed to low doses of H_2O vapour at temperatures below 0°C [38].

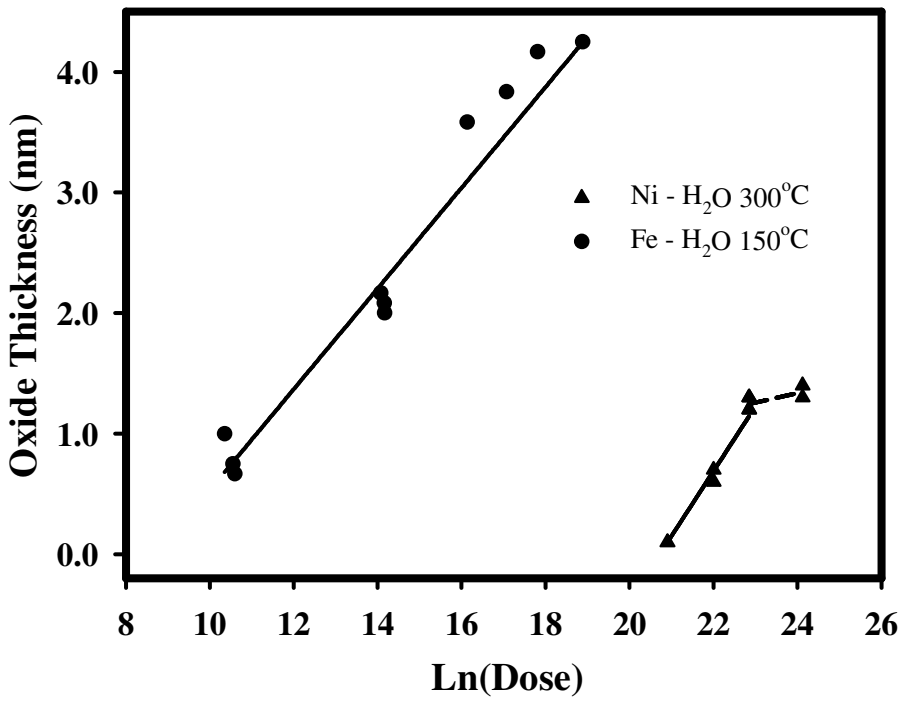

Figure 3.12: Comparison of the rates of oxidation of polycrystalline Ni metal surfaces exposed to H_2O vapour at 300°C with the oxidation of polycrystalline Fe surfaces dosed with H_2O at 150°C [39]. The rate of Ni oxidation is found to be much slower when compared to that of Fe.

In the case of the Ni-H_2O reactions carried out at 300°C described above there was no spectral evidence to support the presence of any OH (ads) species on the metal surfaces (see Figure 3.6). These surfaces were subjected to much larger doses ($\geq 1.2\ 10^9$ L) than the Cu and Pt single crystals [36-38]. It is therefore possible that any OH (ads) species that may have been present has reacted to form an oxide. The O 1s spectrum (see Figure 3.11(b)) collected from a Ni surface exposed to H_2O vapour at 25°C did show the presence of OH (ads) at this temperature. However, unlike with the cases of Cu and Pt a peak resulting from H_2O (ads) was not detected. Heras et al. have shown that H_2O (ads) readily undergoes desorption from Ni metal and Ni oxidized surfaces even at low temperatures [4-5].

The termination of this reaction was found to occur following the formation of very thin films. We propose that the decomposition of OH (ads) cannot be sustained in the absence of a metallic surface. Therefore after the metal phase becomes effectively unavailable to an OH (ads) reactant, the reaction is terminated and the surface is passivated. This could correspond to the 1-1.4 nm thick film of NiO observed here. This conclusion is supported by the work of Heras et al. in which they showed that H_2O (ads) would decompose on Ni metal, but not on oxidized or passivated surfaces [4-5]. This result could have implications for Ni surfaces in high temperature steam conditions. Under reducing conditions, where no O is present, the surface layer would be expected to be composed of a very thin film of oxide that does not grow with extended exposure. The rate of reaction of Fe and H_2O is much faster when compared to that of Ni metal. In the case of the Fe reaction $Fe(OH)_2$ and FeOOH species were found to be stabilized on the surface [7-8]. Although it is believed that small amounts of OH (ads) were found on Ni, the analogous $Ni(OH)_2$ and NiOOH species were not present. Such species may act to increase the rate of reaction with H_2O on Fe, by increasing the number of possible reaction pathways.

3.4 Conclusions

The initiation and subsequent rate of oxidation of polycrystalline Ni by H_2O vapour is slower than with O_2 gas and is limited to a few surface atomic layers under the conditions studied. What oxidation occurs is the result of a reaction of OH (ads) with metallic Ni to form NiO and H, some of which is incorporated in the film. The reaction terminates after all metallic sites are covered. The rate at which H_2O is converted to oxide is many orders of magnitude slower on Ni than it is on Fe under similar conditions.

3.5 References

[1] P.R. Norton, R.L. Tapping, J.W. Goodale, Surf. Sci., 65 (1977) 13.

[2] C. Benndorf, C. Nöble, M. Rüsenberg, F. Thieme, Appl. Surf. Sci., 11/12 (1982) 803.

[3] C. Benndorf, C. Nöble, F. Thieme, Surf. Sci., 121 (1982) 249.

[4] J.M. Heras, E.V. Albano, Appl. Surf. Sci., 17 (1983) 207.

[5] J.M. Heras, E.V. Albano, Appl. Surf. Sci., 17 (1983) 220.

[6] A.F. Carley, S. Rassias, M.W. Roberts, Surf. Sci., 135 (1983) 35.

[7] A.P. Grosvenor, B.A. Kobe, N.S. McIntyre, Surf. Sci., 572 (2004) 217.

[8] A.P. Grosvenor, J.T. Francis, B.A. Kobe, N.S. McIntyre, Surf. Interface Anal., 37 (2005) 495.

[9] B.L. Maschhoff, N.R. Armstrong, Langmuir, 7 (1991) 693.

[10] S. Tougaard, Surf. Interface Anal., 26 (1998) 249.

[11] S. Tougaard, QUASES™, Version 4.4, Software for Quantitative XPS/AES of Surface Nano-Structures by Analysis of the Peak Shape Background, 2000.

[12] S. Tougaard, User's Guide, QUASES™, Version 4.4, Software for Quantitative XPS/AES of Surface Nano-Structures by Analysis of the Peak Shape Background, 2000.

[13] A.P. Grosvenor, B.A. Kobe, N.S. McIntyre, Surf. Sci., 565 (2004) 151.

[14] B.P. Payne, A.P. Grosvenor, M.C. Biesinger, B.A. Kobe, N.S. McIntyre, Surf. Interface Anal., 39 (2007) 582.

[15] A.P. Grosvenor, B.A. Kobe, N.S. McIntyre, S. Tougaard, W.N. Lennard, Surf. Interface Anal., 36 (2004) 632.

[16] A.P. Grosvenor, B.A. Kobe, N.S. McIntyre, Surf. Interface Anal., 36 (2004) 1637.

[17] T. Do, N.S. McIntyre, in Proceedings of the 2nd International Symposium on Aluminum Surface and Technology (ASST 2000), May 21-25, 2000, Manchester, England, UK, 37.

[18] N. Fairley, CasaXPS Version 2.2.107, 1999-2005.

[19] G. Beamson, D. Briggs, in High-resolution XPS of Organic Polymers The Scienta ESCA300 Database, John Wiley and Sons, Toronto, 1992, Appendices 1-3.

[20] M.C. Biesinger, B.P. Payne, L.W.M. Lau, A. Gerson, R.St.C. Smart, Surf. Interface Anal., 41 (2009) 324.

[21] A.P. Grosvenor, M.C. Biesinger, R.St.C. Smart, N.S McIntyre, Surf. Sci., 600 (2006) 1771.

[22] M.W. Roberts, R.St.C. Smart, J Chem Soc., Faraday Trans., 80 (1984) 2957.

[23] A.F. Carley, P.R. Chalker, M.W. Roberts, Proc. R. Soc. Lond. A., 399 (1985) 167.

[24] M.W. Roberts, Surf Sci., 299/300 (1994) 769.

[25] A.F. Carley, S.R. Grubb, M.W. Roberts, J. Chem. Soc. Chem. Commun., (1984) 459.

[26] NIST Electron Inelastic Mean Free Path Database (Version 1.1) © 2000, U.S. Secretary of Commerce.

[27] S. Tanuma, C.J. Powell, D.R. Penn, Surf. Interface Anal., 11 (1998) 577.

[28] B.R. Strohmeier, Surf. Interface Anal., 15 (1990) 51.

[29] Ion-ToF(GmbH). IONSPEC, v. 3.14.9. Ion-ToF: Münster, Germany, 1995-2000.

[30] H.W. Nesbitt, D. Legrand, G.M. Bancroft, Phys. Chem. Minerals, 27 (2000) 357.

[31] F.P. Fehlner, N.F. Mott, in Oxidation of Metals and Alloys; papers presented at a seminar of the American Society for Metals, October 17 and 18, 1970, American Society for Metals: Metals Park OH, 1971; 37.

[32] F.P. Fehlner, M.J. Graham, in P. Marcus and J. Oudar (Eds.), Corrosion Mechanisms in Theory and Practice, Marcel Decker Inc., New York, 1995, Chapter 4.

[33] N. Cabrera, N.F. Mott, Rep. Prog. Phys., 12 (1948-1949) 163.

[34] F.P Fehlner, N.F. Mott, Oxidation of Metals., 2 (1970) 59.

[35] Reprinted from Surface and Interface Analysis, Vol. 39, B.P. Payne, A.P. Grosvenor, M.C. Biesinger, B.A. Kobe, N.S. McIntyre, Structure and growth of oxides on polycrystalline nickel surfaces, page 588, Copyright 2007, with permission from Wiley InterScience.

[36] K. Andersson, G. Ketteler, H. Bluhm, S. Yamamoto, H. Ogasawara, L.G.M. Pettersson, M.Salmeron, A. Nilsson, J. Phys. Chem. C, 111 (2007) 14493.

[37] K. Andersson, G. Ketteler, H. Bluhm, S. Yamamoto, H. Ogasawara, L.G.M. Pettersson, M.Salmeron, A. Nilsson, J. Am. Chem. Soc., 130 (2008) 2793.

[38] T. Schiros, L.-Å. Näsland, K. Andersson, J. Gyllenpalm, G.S. Karlberg, H. Ogasawara, L.G.M. Pettersson, A. Nilsson, J. Phys. Chem. C, 111 (2007) 15003.

[39] Reprinted from Surface Science, Vol. 572, A.P. Grosvenor, B.A. Kobe, N.S. McIntyre, Studies of the oxidation of iron by water vapour using X-ray photoelectron spectroscopy and QUASES™, page 225, Copyright 2004, with permission from Elsevier.

Chapter 4 X-ray photoelectron spectroscopy studies of reactions on chromium metal and chromium oxide surfaces

4.1 Introduction

An understanding of the reactions that occur on Cr surfaces is important as the element is added to many materials to increase their corrosion resistance. At temperatures below 400°C thin Cr_2O_3 film growth on metallic Cr has been shown to follow a Cabrera-Mott model [1-6], where oxidation is driven by an electric field created by electrons tunnelling through the oxide film from the Cr metal substrate. Cations and/or anions are mobile in this electric field and move through defect sites and grain boundaries, resulting in the formation of thin oxide films [1-5]. It has been shown that Cr_2O_3 is primarily a p-type oxide where cations are most mobile, however some anion migration has also been identified [1-6].

This paper presents an XPS study of Cr metal surfaces following reactions with O_2 gas, H_2O vapour, and in an aqueous solution. This work was done to provide a more complete base for the subsequent study of surfaces of a Ni-Cr (20%) alloy subjected to aqueous corrosion at controlled electrochemical potentials and temperatures. XPS is useful for such studies as it provides both compositional and chemical state information over an information depth of ~ 5 nm – a thickness encompassing both the metal substrate and the surface oxides. The XPS spectra of Cr oxides are rich in additional structure from multiplet splitting; previous papers have provided significant details on these spectral structures [7-11], but additional information regarding both Cr_2O_3 and $Cr(OH)_3$ spectral features and elemental intensity ratios have been obtained in this work. Using this information, surfaces of polycrystalline Cr metal following gas phase reactions with

O_2 or H_2O at 300°C could be shown to contain a sub-stoichiometric Cr_2O_3 ($Cr_{2+\delta}O_{3-\delta}$) component. By contrast, during aqueous oxidation of a NiCr alloy, only Cr_2O_3 and $Cr(OH)_3$ contributions were detected.

4.2 Experimental

All XPS analysis was carried out using a Kratos Axis Ultra spectrometer employing a monochromatic Al Kα (15 mA, 14 kV) X-ray source. The work function and the dispersion of the instrument were calibrated to give metallic Au $4f_{7/2}$ and Cu $2p_{3/2}$ signals of 83.95 eV and 932.63 eV respectively. All XPS analysis employed the hybrid-focusing lens, a scan time of 180 s, and an analysis area of 700 x 300 μm. Differential surface charging on insulating samples was minimized using the Kratos charge neutralizer system with a filament current between 1.7-1.8 A and a charge balance of 2.8 V. Survey spectra were collected at a pass energy of 160 eV with a 0.7 eV energy step over a binding energy (BE) range of 1100-0 eV. Analyses of the Cr 2p, O 1s and C 1s envelopes were carried out at a pass energy of 20 eV, an energy step size of 0.05 eV, over energy ranges of 595-565 eV (30-70 sweeps), 540-520 eV (5-15 sweeps), and 295-275 eV (10-20 sweeps) respectively. Pressures near 5 x 10^{-7} Pa were observed in the analytical chamber during surface analysis.

A polycrystalline Cr_2O_3 powder was obtained from Sigma Aldrich having 99.9 % purity. Polycrystalline Cr_2O_3 aggregates (~ 2-3 mm in size) and polycrystalline Cr metal pieces (1-25 mm in size) were obtained from Alfa Aesar having purity levels of 99.6 % and 99.9 % respectively. A NiCr rod was obtained from ACI Alloys Incorporated. Samples of a Cr_2O_3 powder were pressed into a double-sided, non-conducting

polyethylene polymer prior to XPS analysis to minimize the chance of differential surface charging. The Cr_2O_3 aggregates were fractured under vacuum in a chamber having a base pressure of 1 x 10^{-6} Pa and then heated in the same chamber for 3 h (plus 30 min ramp time) at 550°C. Samples of Cr metal were prepared for gas phase oxidation by polishing to a mirror finish using 0.05 μm γ-Al_2O_3 paste followed by sonication in methanol for 20 min. Following sonication, the specimens were introduced to the XPS system (1 x 10^{-6} Pa) for surface cleaning. Surfaces were sputtered for 15 min using a 4 kV Ar^+ ion beam having an emission current of 15 mA followed by annealing at 600°C for 30 min. The respective amounts of O and C present following ion etching were found to be less than 5 at.% by XPS. This amount of contamination could not be removed with additional sputtering/annealing cycles.

In situ oxidation of Cr metal samples was carried out in an adjacent chamber having a base pressure of 7 x 10^{-5} Pa. Metallic surfaces were exposed to high purity O_2 (99.99 %) gas for doses of 6.0 x 10^7 and 2.4 x 10^8 Langmuir (L) at 300°C and 130 Pa. Additional samples were exposed to H_2O vapour for doses of 3.0 x 10^8 L at 300°C and 130 Pa. Similar experiments studying the reactivity of Fe and Ni with both O_2 gas and H_2O vapour have been completed in this chamber [12-15].

A metal disk (~ 3 mm thick) was cut from the polycrystalline NiCr rod and prepared by polishing to a mirror finish using 0.05 μm γ-Al_2O_3 paste followed by sonication in methanol for 20 min. The sample was oxidized electrochemically at 150°C in an autoclave for 72 h in 0.001 M $(NH_4)_2SO_4$ adjusted to a pH of 5 with H_2SO_4. The potential was held constant at 0 V versus a 0.1 M saturated Ag/AgCl reference electrode.

All XPS spectra were analyzed using CasaXPS Version 2.3.14 [16]. The background for all spectra was subtracted using a Shirley baseline [16]. The at.% of each element present was determined from XPS survey spectra (see Table 4.1). The total amount of Cr present on each surface was calculated using the area of the Cr $2p_{3/2}$ peak only. In each case the relative sensitivity factor (RSF) [16] for the Cr 2p envelope (2.427) was adjusted to a value of 1.618 as the $2p_{3/2}$ region contains 2/3 of the total area of the Cr 2p peak. The same correction factor was previously employed by this group to study the oxidation of polycrystalline Ni metal surfaces with H_2O vapour [15]. This area correction was applied because a definitive end to the M $2p_{3/2}$ (M = Cr or Ni) region was not evident from sample to sample, while a very distinct separation between the $2p_{3/2}$ and $2p_{1/2}$ peaks was observed on all survey spectra. The RSF values for the O 1s and C 1s spectra were 0.780 and 0.278 respectively. Fitting of the high-resolution spectra was completed using components having mixed Gaussian-Lorentzian character. The Cr $2p_{3/2}$ envelopes were best fit using Gaussian (40%)-Lorentzian (60%) line shapes, which are denoted as GL(60) in CasaXPS. The O 1s and C 1s regions were best fit with components having GL(50) and GL(30) profiles respectively. To compare the different Cr, O, and C species present the total atomic concentrations (see Table 4.1) were corrected using the peak area ratios obtained from the fitting of the respective high-resolution spectra (see Tables 4.2-4.4).

All specimens studied as a part of this work were found to contain significant amounts of adventitious C (see Table 4.1). A representative C 1s spectrum collected from the Cr_2O_3-2 powder sample is shown in Figure 4.1. All C 1s spectra were dominated by a strong hydrocarbon (C–C,C–H) signal, which was used for spectral

Table 4.1: XPS surface composition in at.% of Cr metal and oxide samples.

Sample/Treatment	Composition (at.%)			
	Cr	O	C	Other
Cr_2O_3-1 (powder pressed into a polyethylene tape)	23.3	47.9	28.8	
Cr_2O_3-2 (powder pressed into a polyethylene tape)	22.4	48.2	28.6	Na 0.8
Cr_2O_3-3 (fractured aggregate, heated 550°C, 3 h)	22.4	45.0	22.5	Ca 0.6, Cl 0.5, Mg 1.1, Na 5.3, Si 2.7
Cr_2O_3-4 (fractured aggregate, heated 550°C, 3 h)	22.9	46.8	19.8	Ca 1.4, Cl 0.6, Mg 0.7, Na 4.8, Si 3.0
$Cr(OH)_3 \cdot xH_2O$ (powder pressed into a polyethylene tape)	6.4	29.4	63.7	Ca 0.5
Cr metal (polished, Ar^+ sputtered, 15 min, annealed, 600°C, 30 min)	92.1	3.7	1.9	Ar 2.3
Cr metal-1 + O_2, 300°C, 1 Torr, 6.0 x 10^7 L	34.6	43.0	20.7	Ar 1.3, N 0.3
Cr metal-2 + O_2, 300°C, 1 Torr, 2.4 x 10^8 L	32.6	46.3	20.0	Ar 1.1
Cr metal-3 + H_2O, 300°C, 1 Torr, 3.0 x 10^7 L	42.9	29.1	26.5	Ar 1.5
Cr metal-4 + H_2O, 300°C, 1 Torr, 3.0 x 10^7 L	46.5	29.9	22.2	Ar 1.5
NiCr metal + pH 5, $(NH_4)_2SO_4$, 150°C, 72 h	4.4	45.4	33.2	Cl 1.5, Ni 12.3, N 0.7, S 2.6

calibration of insulating samples and corrected to a BE of 284.8 ± 0.1 eV. Additional spectral intensity assigned to alcohol/ether (–COH, –COC–, O=C(O–C*)), carbonyl (–C=O), and ester (O=CO–) functionalities were also observed at respective BEs of 286.2 ± 0.1 eV, 287.7 ± 0.1 eV, and 288.6 ± 0.2 eV [17]. A small peak was found at 289.6 ± 0.2 eV on all of the oxidized metallic Cr samples and attributed to a carbonate ($-CO_3^{2-}$) species. A previous publication by this group had assigned the peak at 286.2 ± 0.1 eV solely to a –COH group [15]. For the above peak assignments to be valid a minimum area ratio of 1:1 was required between the components centered at 286.2 ± 0.1

eV and 288.6 ± 0.2 eV. In cases where the intensity of the lower BE peak was found to be greater than the peak at 288.6 ± 0.2 eV the additional spectral intensity was assumed to be split equally between C atoms bound as −COH and −COC−. The organic contribution to the O 1s spectra was estimated by first calculating the surface normalized C intensities. From these intensities the corresponding normalized O concentrations were obtained using the expected O/C ratios for the individual functional groups (i.e. 1:1 for −C=O). The normalized O concentrations were then converted to the respective O 1s peak areas. This procedure is summarized in Table 4.2.

The CasaXPS program was also used for spectral subtractions. To simplify the analysis of the oxidized metal surfaces, the metal contribution was removed. A similar technique was previously employed by this group to study the oxidation of Ni metal [14-15,18].

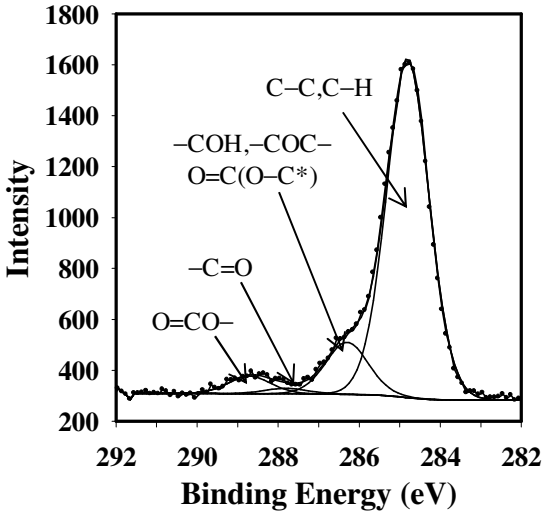

Figure 4.1: A representative high-resolution C 1s spectrum collected from a sample of polycrystalline Cr_2O_3 powder.

Table 4.2: Summary of the organic C 1s peak areas and calculated contributions to the corresponding O 1s spectra.

	Contributions from C to the C 1s spectra										Calculated contributions from O to the O 1s spectra								
		–COH/–COC–/ O=C(O–C*)			–C=O		O=CO–		$–CO_3^{2-}$			O=CO–		–C=O		–COH/ –COC–		$–CO_3^{2-}$	
Sample	Total C 1s (at.%)	C 1s (%)	[a]at. %	[b]at.%	C 1s (%)	at.%	C 1s (%)	at. %	C 1s (%)	at. %	Total O 1s (at. %)	at. %	O 1s (%)	at. %	O 1s (%)	at. %	O 1s (%)	at. %	O 1s (%)
Cr_2O_3-1	28.8	19.2	0.9	4.6	0.8	0.2	3.1	0.9			47.9	1.8	3.8	0.2	0.4	3.1	6.5		
Cr_2O_3-2	28.6	12.6	1.2	2.4	1.4	0.4	4.2	1.2			48.2	2.4	5.0	0.4	0.8	1.6	3.3		
Cr_2O_3-3	22.5	3.2	0.5	0.2	1.8	0.4	2.1	0.5			45.0	1.0	2.2	0.4	0.9	0.1	0.2		
Cr_2O_3-4	19.8	2.5	0.2	0.3	1.3	0.3	1.2	0.2			46.8	0.4	0.9	0.3	0.6	0.2	0.4		
$Cr(OH)_3$	63.7	7.9	3.5	1.5	0.2	0.1	5.5	3.5			29.4	7.0	23.8	0.1	0.3	1.0	3.4		
Cr metal-1	20.7	5.1	1.1		8.1	1.7	5.1	1.1	2.5	0.5	43.0	2.2	5.1	1.7	4.0			1.5	3.5
Cr metal-2	20.0	6.3	1.3		9.1	1.8	6.3	1.3	3.7	0.7	46.3	2.6	5.6	1.8	3.9			2.1	4.5
Cr metal-3	26.5	5.1	1.4		2.5	0.7	5.1	1.4	0.8	0.2	29.1	2.8	9.6	0.7	2.4			0.6	2.1
Cr metal-4	22.2	6.0	1.3		4.1	0.9	6.0	1.3	1.5	0.3	29.9	2.6	8.7	0.9	3.0			0.9	3.0
NiCr metal	33.2	6.1	0.3	1.7	0.8	0.3	0.9	0.3			45.4	0.6	1.3	0.3	0.7	1.1	2.4		

[*] C atom giving rise to the C 1s signal.

[a] Normalized surface C concentration for the O=C(O–C*) group.

[b] Combined normalized surface concentration for the assumed 1:1 mixture of –COH/–COC– species.

[c] The normalized surface O could be calculated using either the O=C(O–C*) or O=CO– values from the C 1s analyses.

[d] The normalized surface O concentration for the assumed 1:1 mixture of –COH/–COC– species was estimated using an O/C ratio of 2:3.

4.3 Results and Discussion

4.3.1 Spectral refinements for Cr_2O_3

Two samples of a polycrystalline Cr_2O_3 powder were analyzed with XPS and a representative high-resolution Cr $2p_{3/2}$ spectrum is shown in Figure 4.2(a). The spectra collected from both samples were fit with 5 peaks representing the multiplet splitting of the Cr^{3+} cations following photoionization (see Table 4.3). The fits produced using this approach agree well with the $2p_{3/2}$ line shape calculated for a Cr^{3+} free ion by Gupta and Sen [7-8,11]. Two polycrystalline Cr_2O_3 aggregates were fractured and heated (550°C) *in vacuo* and the freshly fractured surfaces were analyzed by XPS. The Cr $2p_{3/2}$ fitting results were found to be very similar to those for the polycrystalline Cr_2O_3 powder (see Table 4.3). Heating of the aggregates resulted in a narrowing of the 5 multiplet splitting components relative to what was observed for the polycrystalline Cr_2O_3 powder samples (see Table 4.3). As well, a small component near 574 eV [11] was also required to fit the envelope. A fitted representative Cr $2p_{3/2}$ spectrum is shown in Figure 4.3(a). The observed difference in peak widths is attributed to the formation of an oxide surface that is primarily oriented in the (0001) direction following heating at 550°C. Previous LEED studies have shown that annealing of polycrystalline Cr_2O_3 surfaces near this temperature leads to a crystal reorganization to form the low surface energy (0001) plane [19-20].

The O 1s spectra collected for all polycrystalline Cr_2O_3 samples were fit with an O^{2-} component at 530.2 ± 0.2 eV, along with additional broad peaks at BEs ranging from 531.2-533.2 eV (see Table 4.4). Example spectra are presented in Figures 4.2(b) and 4.3(b). As was shown in a previous publication, some of the intensity of the high BE peaks can be attributed to the presence of organic species associated with adventitious C [15]. The contribution of these organic species to the O 1s spectra have been estimated

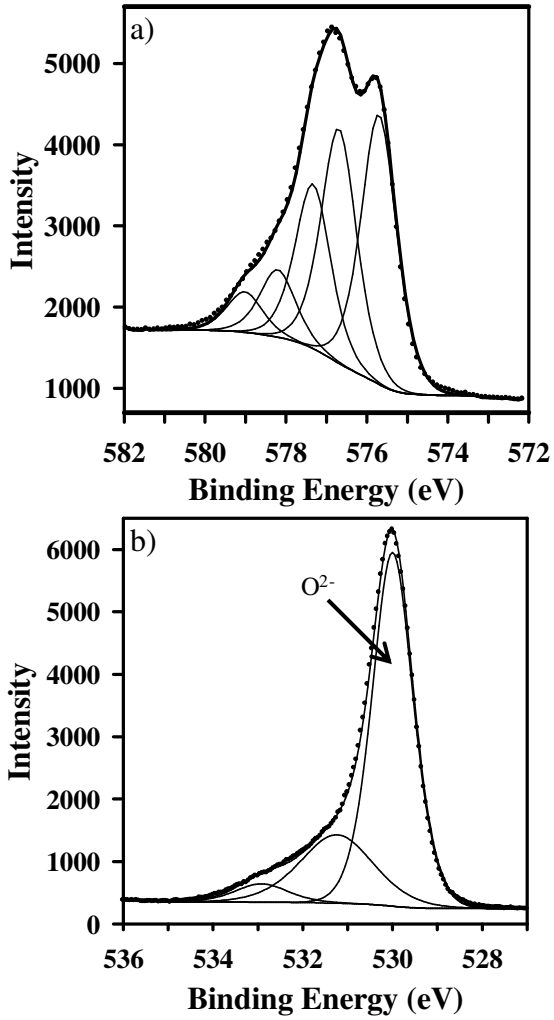

Figure 4.2: The high-resolution (a) Cr $2p_{3/2}$ and (b) O 1s spectra for a polycrystalline Cr_2O_3 powder.

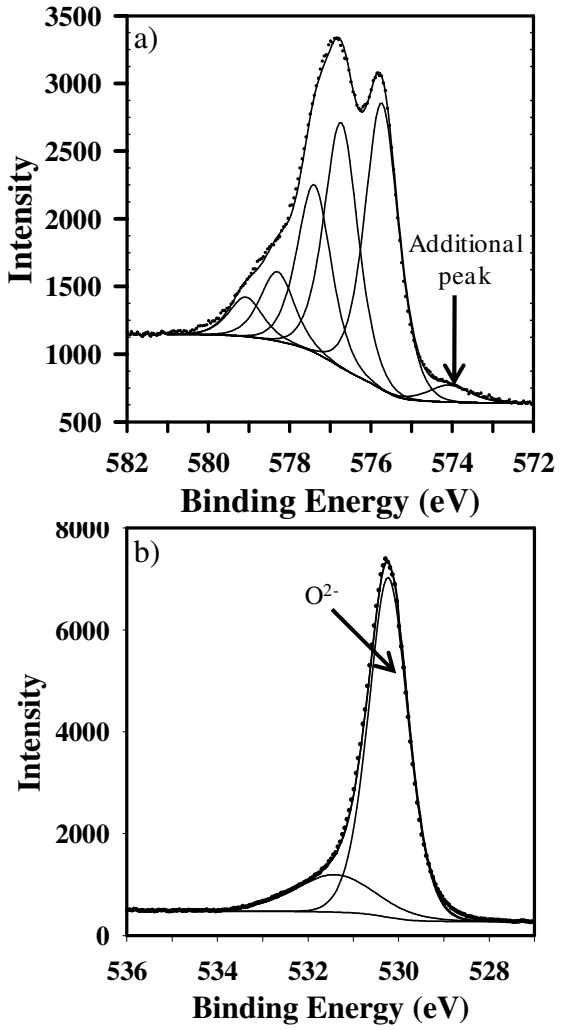

Figure 4.3: The high-resolution (a) Cr $2p_{3/2}$ and (b) O 1s spectra of a vacuum fractured Cr_2O_3 aggregate following annealing at 550°C for 3 h.

Table 4.3: Cr $2p_{3/2}$ peak fits for the polycrystalline Cr_2O_3, $Cr(OH)_3$ and Cr metal samples.

Sample	FWHM (eV)	Peak 1 (eV)	Area (%)	Peak 2 (eV)	Area (%)	Peak 3 (eV)	Area (%)	Peak 4 (eV)	Area (%)	Peak 5 (eV)	Area (%)
Cr_2O_3-1	1.05	575.4	34.2	576.4	29.4	577.1	22.1	578.0	9.1	578.8	5.2
Cr_2O_3-2	1.03	575.7	34.7	576.7	30.2	577.3	21.2	578.2	8.7	579.0	5.2
Cr_2O_3-3[a]	0.96	575.6	34.1	576.6	30.3	577.3	19.8	578.2	8.5	579.0	5.1
Cr_2O_3-4[a]	0.99	575.8	34.9	576.8	30.2	577.5	19.7	578.4	8.6	579.2	4.7
$Cr(OH)_3$ oxide component[b]	1.03	575.7	4.7	576.7	4.1	577.4	2.9	578.2	1.2	579.0	0.8
hydroxide component	1.32	576.3	28.1	577.1	23.3	577.8	21.9	578.5	9.3	579.5	3.8
Cr metal[c]		574.1	75.2	574.8	20.3	576.8	4.5				

[a] Additional peaks at 574.0 ± 0.1 eV were also required to completely fit the Cr $2p_{3/2}$ spectra for the fractured and heated aggregates.

[b] The oxide contribution was estimated using the fit obtained for the Cr_2O_3-2 powder sample.

[c] The Cr metal Cr $2p_{3/2}$ spectrum was fit with 3 peaks which do not represent Cr species in different chemical environments. The envelope was fit with an asymmetric component having the line shape LA(1.3,2.3,10) and a FWHM of 0.77 eV, while peaks 2 and 3 had a line shape of GL(30) and FWHM values of 2.16 eV.

and the results are presented in Table 4.4. Additional contributions from adsorbed O and/or OH surface species cannot be ruled out. Small amounts of Ca, Mg, Na, and Si (see Table 4.1) were also detected on the aggregate samples during compositional analysis and some of the intensity in the O 1s peaks may arise from the presence of the oxides and/or hydroxides of these species. The O/Cr ratios for the polycrystalline powder samples were calculated using the normalized surface intensities of the O^{2-} and Cr^{3+} components and were determined to be 1.5 (see Table 4.5). This result indicates that the presence of significant amounts of surface $Cr(OH)_3$ is unlikely as the calculated O/Cr ratios are identical to the expected value of 1.5 for pure Cr_2O_3. A similar method was used to determine the O/Ni ratios in a previous publication [15]. A slight increase in the O/Cr ratio was observed on the heated polycrystalline aggregate samples (see Table 4.5) relative to pure Cr_2O_3. This result may be attributed to the presence of Ca, Mg, and Na oxide impurities, which have O^{2-} BE shifts similar to that of Cr_2O_3 [21-23]. As with the Cr_2O_3 powder samples, this result suggests that little $Cr(OH)_3$ is present on the aggregate surfaces.

The Cr $2p_{3/2}$ spectra collected from the polycrystalline powder samples were re-fit using two overlapping sets of the 5 multiplet splitting peaks obtained from the analysis of sample Cr_2O_3-3 (see Table 4.3). A representative Cr $2p_{3/2}$ spectrum is shown in Figure 4.4, in which the centroids of the 5 peaks for the two Cr_2O_3 components are offset by 0.3 eV. Analysis of the Cr $2p_{3/2}$ spectrum of the second polycrystalline powder sample yielded a separation of 0.4 eV between the centroids of the two overlapping components. This small observed shift is attributed to the differences in BE between the Cr^{3+} atoms orientated in the (0001) plane (black lines) and those in the other major crystallographic

Table 4.4: O 1s peak fits for the Cr_2O_3, $Cr(OH)_3$, oxidized Cr and oxidized NiCr metal samples.

Sample	Peak 1 (eV)	Area (%)	FWHM (eV)	Peak 2 (eV)	Area (%)	FWHM (eV)	Peak 3 (eV)	Area (%)	FWHM (eV)	Organics (%)
Cr_2O_3-1	530.0	70.7	1.07	531.2	24.5	1.92	532.9	4.8	1.39	10.7
Cr_2O_3-2	530.3	69.7	1.04	531.6	27.6	2.01	533.2	2.7	1.40	9.1
Cr_2O_3-3	530.2	81.7	1.03	531.4	18.3	2.09				3.3
Cr_2O_3-4	530.4	79.2	1.03	531.6	20.8	2.24				1.9
$Cr(OH)_3$	529.7	4.5	1.02	531.6	87.5	1.81	533.5	8.0	1.25	27.5
OH^- only[a]					60.0					
Cr metal-1	530.2	72.4	1.37	531.9	27.6	1.57				12.6
Cr metal-2	530.2	74.2	1.41	531.8	25.8	1.53				14.0
Cr metal-3	530.0	64.2	1.29	531.5	35.8	1.81				14.1
Cr metal-4	530.0	61.2	1.32	531.5	38.8	1.81				14.7
NiCr metal	529.6	1.5	1.35	531.7	97.0	1.65	533.6	1.4	1.45	4.4

[a] Peak area calculated by subtracting the total organic contribution from the OH^- component.

Table 4.5: O/Cr ratios calculated from the normalized surface concentrations.

Sample	Normalized surface concentration (at.%)			O/Cr
	O^{2-} or OH^-	Cr metal	Oxidized Cr	
Cr_2O_3-1	33.9		23.3	1.5
Cr_2O_3-2	33.6		22.4	1.5
Cr_2O_3-3	36.8		22.4	1.6
Cr_2O_3-4	37.1		22.9	1.6
$Cr(OH)_3 \cdot xH_2O$ oxide	1.3		0.9	1.5
[a]hydroxide	17.6		5.5	3.2
Cr metal-1	31.1	16.4	18.2	1.7
Cr metal-2	34.4	12.3	20.3	1.7
Cr metal-3	18.7	31.9	11.0	1.7
Cr metal-4	18.3	35.8	10.7	1.7

[a] The hydroxide surface concentration was calculated using the organic subtracted OH^- peak area from Table 4.4.

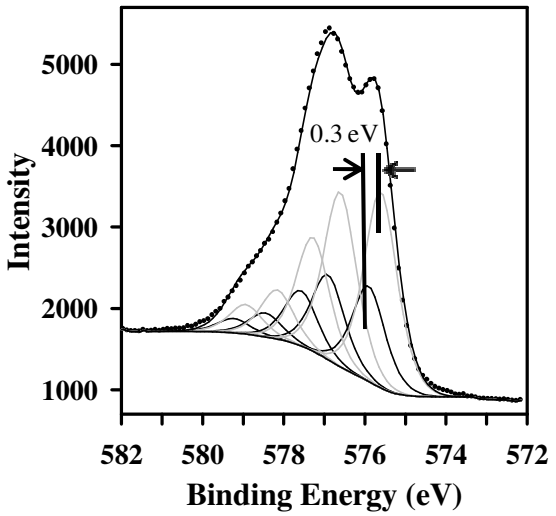

Figure 4.4: The high-resolution Cr $2p_{3/2}$ spectrum of a polycrystalline Cr_2O_3 powder fit with two sets of overlapping multiplet splitting peaks representing Cr^{3+} atoms in the (0001) plane (black lines) and all other crystallographic orientations (grey lines).

orientations (grey lines) [24]. The spectrum for a polycrystalline powder would be expected to be somewhat broadened by the presence of the oxide in orientations each with its own particular BE; and this could be one of several reasons for the broadening observed in the 2p spectra of many metal oxides. Although spectral broadening due to differential surface charging cannot be completely ruled out, any charging effects are thought to be small due to the use of a charge neutralizer during XPS analysis and the fact that the samples were pressed into a non-conducting polyethylene tape. Thus, this work has served to better define the Cr $2p_{3/2}$ and O 1s line shapes and positions for differing orientations of Cr_2O_3, as well as show that an O/Cr ratio for the appropriate peaks mirrors that for the known stoichiometry.

4.3.2 Spectral refinements for $Cr(OH)_3$

The XPS spectra collected from a hydrated $Cr(OH)_3 \cdot xH_2O$ powder presented in an earlier publication (see Figure 4 in reference 11) has been reanalyzed here. In the original analysis it was determined that a small Cr_2O_3 impurity was present [11]. Refitting of the O 1s spectrum (see Figure 4.5(a)) showed a small O^{2-} component at 529.7 eV, a large peak representing the overlapping signal from substitutional OH^- and adsorbed organic species at 531.6 eV, and a third peak attributed to H_2O of hydration at 533.5 eV[a] (see Table 4.4). From the O 1s analysis it was determined that 4.5 % of the total O present was in the O^{2-} state (see Table 4.4). Using the O/Cr ratio for Cr_2O_3 (1.5), the corresponding Cr^{3+} contribution to the Cr $2p_{3/2}$ spectrum was estimated to be 13.7 % and was modeled using the fits obtained from analysis of the polycrystalline powder

[a] The O 1s peak was initially attributed to H_2O of hydration based on the previous assignment of Biesinger et al. in reference [11]. Subsequent reanalysis of the O 1s spectrum following publication of this work indicated that all of the spectral intensity in this region was the result of C contamination (see Chapter 5).

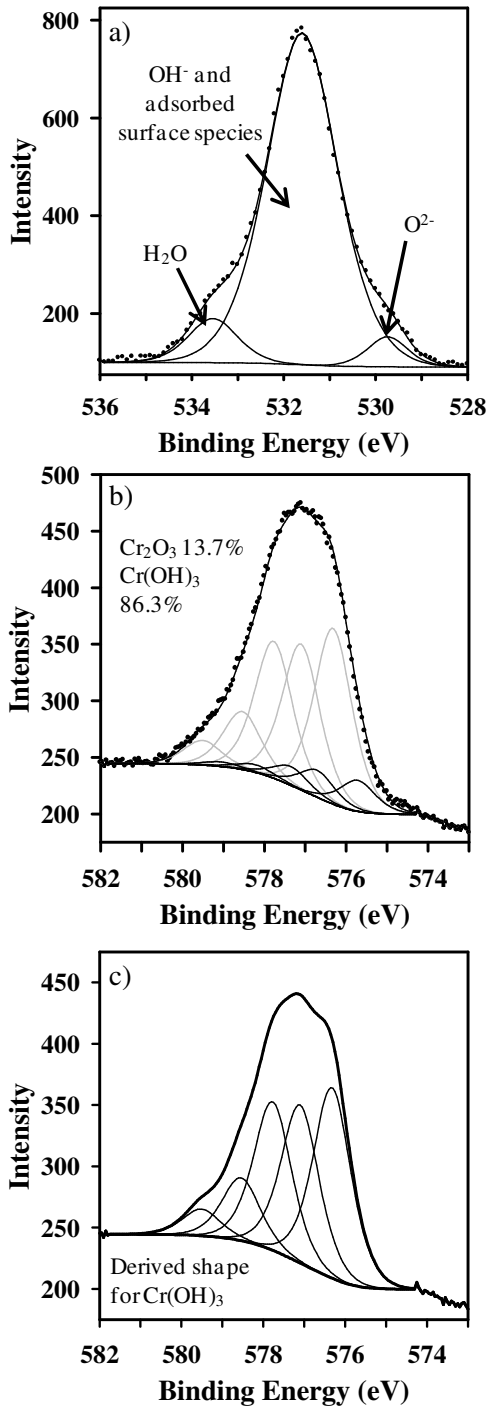

Figure 4.5: The high-resolution (a) O 1s and (b) Cr $2p_{3/2}$ spectrum for $Cr(OH)_3 \cdot xH_2O$. The Cr $2p_{3/2}$ spectrum was fit with contributions from both Cr_2O_3 (black lines) and $Cr(OH)_3$ (grey lines). The high-resolution spectrum for pure $Cr(OH)_3$ was reconstructed using the combined intensities of the obtained 5 multiplet splitting peaks and is shown in (c). The original Cr $2p_{3/2}$ spectrum was presented previously by Biesinger et al. [11].

sample Cr_2O_3-2 (see Table 4.3). After constraining the area of the Cr_2O_3 component to account for 13.7 % of the total Cr $2p_{3/2}$ spectrum, the remaining intensity representing pure $Cr(OH)_3$ was fit with 5 multiplet splitting peaks having identical FWHM values (see Table 4.3). Figure 4.5(b) shows the Cr $2p_{3/2}$ spectrum fit with both Cr_2O_3 (black lines) and $Cr(OH)_3$ (grey lines) components. The resultant pure spectrum for $Cr(OH)_3$ is presented in Figure 4.5(c). An O/Cr ratio of 3.2 was obtained when the surface normalized substitutional OH^- component from the O 1s spectrum was compared to the surface corrected $Cr(OH)_3$ contribution determined from the fitting of the Cr $2p_{3/2}$ spectrum. This result is close to the expected value of 3 for pure $Cr(OH)_3$ and suggests that the hydroxide and oxide components have been cleanly separated using this method. It is important to note that the total OH^- surface concentration was determined by subtracting the contribution from the adsorbed organic species from the total area of the peak located at 531.6 eV in the O 1s spectrum (see Table 4.4).

4.3.3 Reactions of metallic Cr with O_2 and H_2O

Clean polycrystalline Cr metal surfaces were exposed to ultra pure O_2 gas for doses of 6.0×10^7 and 2.4×10^8 L at 300°C and a pressure of 130 Pa. Two additional metal samples were exposed to a 3.0×10^8 L dose of H_2O vapour under the same temperature and pressure conditions. Representative Cr $2p_{3/2}$ spectra produced by reactions with O_2 gas for a dose of 2.4×10^8 L and H_2O vapour for a dose of 3.0×10^8 L are shown in Figure 4.6(a-b). A strong metal signal at 573.6 ± 0.1 eV was observed on all surfaces indicating the formation of thin oxide films. Fitting of the Cr $2p_{3/2}$ spectra shown in Figure 4.6(a-b) was undertaken to separate the metallic contributions from those of the oxide. The metal portion of each spectrum was fit using the metal

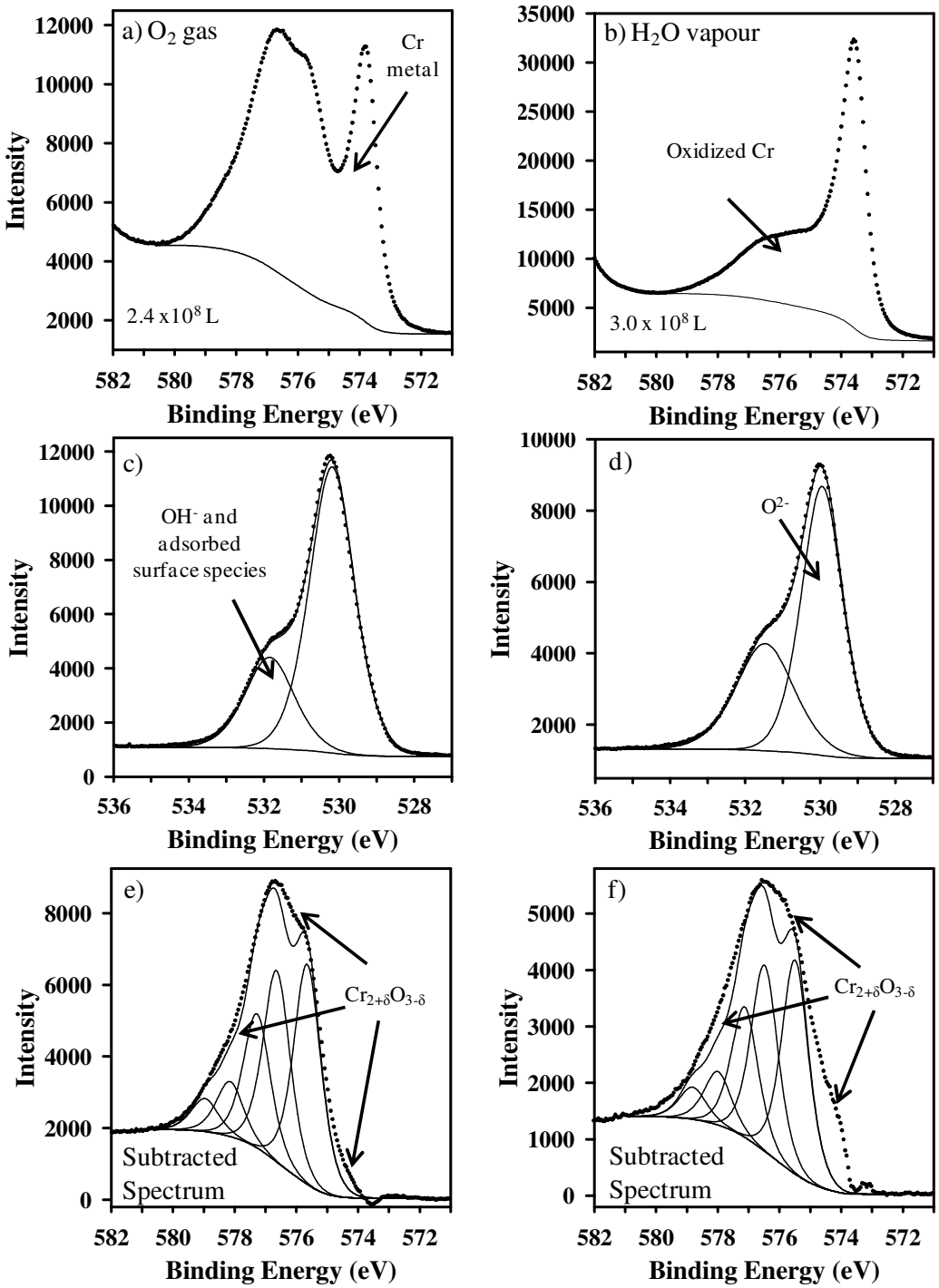

Figure 4.6: The high-resolution Cr $2p_{3/2}$ spectra collected from metal surfaces following doses of (a) 2.4 x 10^8 L of O_2 gas and (b) 3.0 x 10^8 L of H_2O vapour at 300°C and 130 Pa. The O 1s spectra for the doses of (c) 2.4 x 10^8 L of O_2 gas and (d) 3.0 x 10^8 L of H_2O vapour are also shown. The metal component was removed from each Cr $2p_{3/2}$ spectrum and the resultant subtracted spectra for doses of (e) 2.4 x 10^8 L of O_2 gas and (f) 3.0 x 10^8 L of H_2O vapour are also presented. The subtracted spectra show the possible presence of a hypo-stoichiometric Cr_2O_3 oxide.

components presented in Table 4.3. The remaining spectral intensity was then assigned to the oxidic component. The corresponding O 1s spectra (see Figure 4.6(c-d)) were fit with an O^{2-} component at 530.1 ± 0.1 eV and a peak attributed to adsorbed surface species at 531.7 ± 0.2 eV (see Table 4.2). The O/Cr ratios were calculated using the corrected O^{2-} and non-metallic Cr surface intensities and found to be 1.7 for all samples (see Table 4.5). This result suggests that these films are deficient in Cr^{3+} and is supported by the low temperature oxidation mechanism first presented by Cabrera and Mott for p-type transition metal oxides [1-5]. In the case of Cr metal, the oxidation reaction involves the formation of Cr^{3+} vacancies at the oxide/gas interface. Over time there is an inward migration of these vacancies towards the metal substrate in an electric field setup by electrons tunnelling through the oxide film. At the same time metallic Cr atoms are oxidized at the metal/oxide interface and travel through these vacancy sites as well as grain boundaries to the oxide/gas interface, where they react with either O_2 or H_2O promoting further film growth [1-5]

To better observe the structure of the oxidized Cr species, the metal peak was removed and the resultant subtracted spectra are shown in Figure 4.6(e-f). After spectral subtraction the oxide components were cleanly separated. These spectra were then fit with the line shape obtained previously for the polycrystalline Cr_2O_3 powder (Cr_2O_3-2 from Table 4.3). Most of the envelope was well fitted with the line shape for Cr_2O_3, however additional contributions to the reaction spectra were clearly detected at the low BE side of the Cr_2O_3 envelopes. We attribute this to a hypo-stoichiometric Cr_2O_3 ($Cr_{2+\delta}O_{3-\delta}$) component that is likely formed during the initial stages of the reaction. To our knowledge this species has not been observed previously using XPS; its presence is

somewhat comparable to the formation of Ni^{3+} during initial oxidation of Ni metal [14-15]. The exact nature of this Cr species is not identified here as there was no model structure available. However, in a previous study on the oxidation of Cr metal, it was suggested that film growth proceeded through the formation of Cr^{3+} and O^{2-} vacancies [6,25]. Both of these vacancies are said to carry a negative charge and to maintain charge balance, Cr^{2+} cations are created and are situated in the interstitial sites of the Cr_2O_3 film [6,25]. The subtracted Cr $2p_{3/2}$ spectra collected from the H_2O dosed surfaces showed the largest contributions from the hypo-stoichiometric component relative to the regular Cr_2O_3. This is probably the result of the thin nature of these films, as the sub-stoichiometric component would comprise a larger portion of the oxide. However, it is also possible that incorporation of other species such as H, a product of the dissociation of H_2O, into some of the Cr^{3+} vacancies may lead to increased formation of this hypo-stoichiometric film. The presence of H in cation vacancy sites has previously been suggested to retard film growth on both Ni and Fe metal surfaces following reaction with H_2O vapour [13,15,26]. Some contributions are also observed in the subtracted spectra around 580 eV that may be attributed to the formation of Cr cations in higher oxidation states. It is unlikely that the peak broadening observed in the subtracted spectra (Figure 4.6(e-f)) is due to differential charging, given the proximity of the metal substrate.

The high BE peak found near 531.7 ± 0.2 eV in the O 1s spectra has a similar chemical shift to that of OH^- (see Table 4.4) however, the presence of significant levels of $Cr(OH)_3$ on any of the oxidized surfaces is unlikely on the basis of the observed O/Cr ratios. From the analysis of the accompanying C 1s spectra it was determined that a significant amount of the intensity of the high BE O 1s peak results from the presence of

adsorbed organic species (see Tables 4.2 and 4.4). It is believed that the remaining intensity would result from the presence of adsorbed O and/or OH species, which are possible intermediates in the oxidation reaction [5].

4.3.4 Aqueous reaction of metallic NiCr

Figure 4.7(a) contains the Cr $2p_{3/2}$ high-resolution spectra collected from a Ni-Cr alloy electrochemically oxidized at 150°C for a 72 h period at a pH of 5. The spectrum was fit with contributions from the polycrystalline Cr_2O_3 (black lines, Cr_2O_3-2) and $Cr(OH)_3$ (grey lines) powders presented in Table 4.3, and a good fit of the envelope was observed. A small O^{2-} peak in the O 1s spectrum at 529.6 eV was observed and verified the presence of Cr_2O_3 (see Figure 4.7(c)). None of the O^{2-} signal could be attributed to NiO, as the analysis of the Ni $2p_{3/2}$ spectrum (see Figure 4.7(b)) showed all oxidized Ni species were present as $Ni(OH)_2$. The Ni 2p spectrum was fit using the components for $Ni(OH)_2$ presented in a previous publication [18]. There was no spectral evidence to suggest that a sub-stoichiometric Cr species formed under these oxidation conditions.

4.4 Conclusions

The Cr $2p_{3/2}$ spectra collected from samples of polycrystalline Cr_2O_3 powder were found to exhibit a multiplet structure very similar to that predicted by Gupta and Sen for the free Cr^{3+} ion. The narrowest Cr $2p_{3/2}$ spectra were obtained following annealing of fractured surfaces to 550°C. Heating of the samples is believed to result in conversion of polycrystalline surface structures to a single (0001) orientation having a slightly different BE than that for the polycrystalline surface. A small separation in BE was observed between the Cr^{3+} atoms oriented in the (0001) direction relative to those found in the

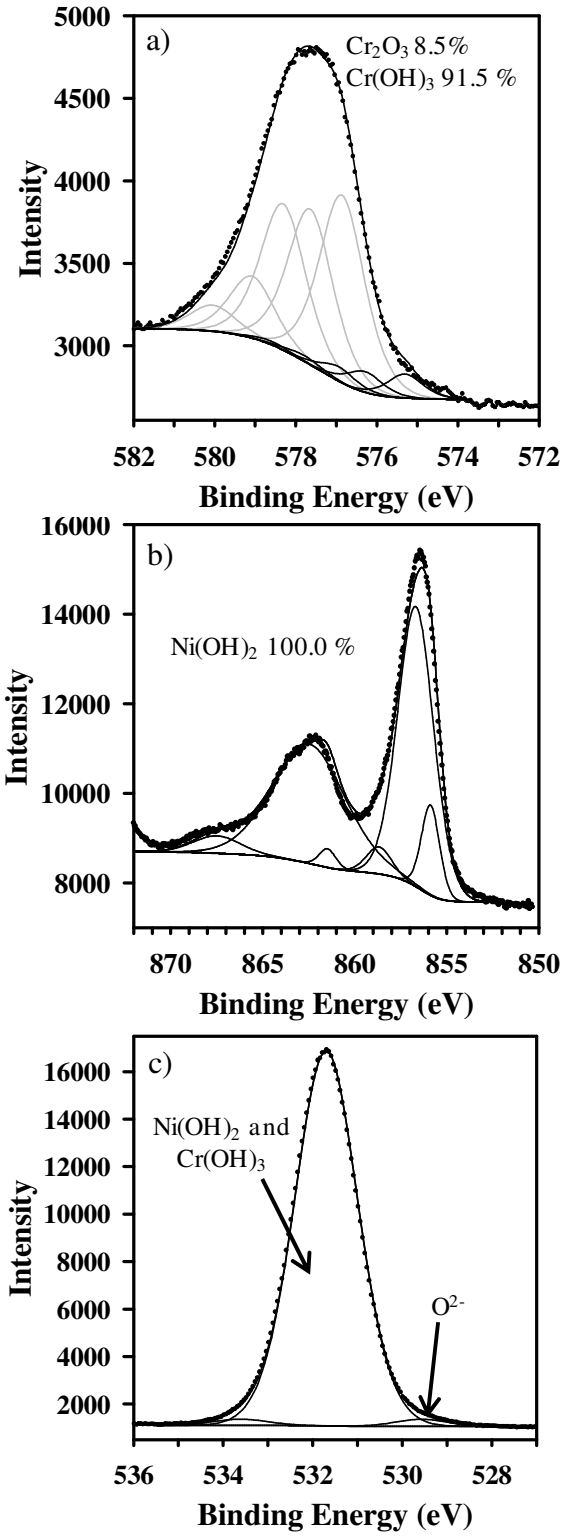

Figure 4.7: The high-resolution (a) Cr $2p_{3/2}$ spectrum from a NiCr alloy surface containing a mixture of Cr_2O_3 (black lines) and $Cr(OH)_3$ (grey lines). The corresponding (b) Ni $2p_{3/2}$ and (c) O 1s spectra are also shown.

other major crystallographic arrangements. Additionally, a possible line shape for the Cr $2p_{3/2}$ spectrum for $Cr(OH)_3$ was modeled using synthetic components from a sample containing contributions from both Cr_2O_3 and $Cr(OH)_3$.

Analysis of the Cr $2p_{3/2}$ spectra collected from metallic Cr surfaces exposed to both O_2 gas and H_2O vapour showed the formation of thin Cr^{3+} deficient Cr_2O_3 films with a contribution from a hypo-stoichiometric component ($Cr_{2+\delta}O_{3-\delta}$). The concentration of this Cr species was found to be greater on the surfaces exposed to H_2O vapour. No $Cr(OH)_3$ appears to form following exposure to H_2O vapour. A different result was observed following the aqueous oxidation of a Ni-Cr (20%) alloy, with contributions from both Cr_2O_3 and $Cr(OH)_3$ observed in the Cr $2p_{3/2}$ spectrum. There was no spectral evidence to suggest the formation of a hypo-stoichiometric Cr species.

4.5 References

[1] G.A. Hope, I.M. Ritchie, J. Chem. Soc., Faraday Trans. 1 77 (1981) 2621.

[2] F.P. Fehlner, N.J. Graham, in: P. Marcus, J. Oudar (Eds.), Corrosion Mechanisms in Theory and Practice, Marcel Decker Inc., New York, 1995 (Chapter 4).

[3] D.J. Young, M. Cohen, J. Electrochem. Soc.: Solid-State Science and Technology 124 (1977) 769.

[4] J.S. Arlow, D.F. Michell, M.J. Graham, J. Vac. Soc. Technol. A 5(4) (1987) 572.

[5] N. Cabrera, N.F. Mott, Rep. Prog. Phys. 12 (1948-1949) 163.

[6] K. Hauffe, in: Oxidation of Metals, Plenum Press, New York, 1965 (Chapter 4).

[7] R.P. Gupta, S.K. Sen, Phys. Rev. B 10 (1) (1974) 71.

[8] R.P. Gupta, S.K. Sen, Phys. Rev. B 12 (1) (1975) 15.

[9] A.R. Pratt, N.S. McIntyre, Surf. Interface Anal. 24 (1996) 529.

[10] N.S. McIntyre, A.R. Pratt, H. Piao, D. Maybury, S.J. Splinter, Appl. Surf. Sci. 144-145 (1999) 156.

[11] M.C. Biesinger, C. Brown, J.R. Mycroft, R.D. Davidson, N.S. McIntyre, Surf. Interface Anal. 36 (2004) 1550.

[12] A.P. Grosvenor, B.A. Kobe, N.S. McIntyre, Surf. Sci. 565 (2004) 151.

[13] A.P. Grosvenor, B.A. Kobe, N.S. McIntyre, Surf. Sci. 572 (2005) 217.

[14] B.P. Payne, A.P. Grosvenor, M.C. Biesinger, B.A. Kobe, N.S. McIntyre, Surf. Interface Anal. 39 (2007) 582.

[15] B.P. Payne, M.C. Biesinger, N.S. McIntyre, J. Electron. Spectrosc. 175 (2009) 55.

[16] N. Fairley, CasaXPS Version 2.2.107, 1999-2005.

[17] G. Beamson, D. Briggs, High-resolution XPS of Organic Polymers The Scienta ESCA300 Database, John Wiley and Sons, Toronto, 1992 (Appendices 1−3).

[18] M.C. Biesinger, B.P. Payne, L.W.M. Lau, A. Gerson, R.St.C. Smart, Surf. Interface Anal. 41 (2009) 324.

[19] V. Maurice, S.Cadot, P. Marcus, Surf. Sci. 458 (2000) 195.

[20] C.P. Huggins, R.M. Nix, Surf. Sci. 594 (2005) 163.

[21] H. Van Doveren, J.A.Th. Verhoeven, J. Electron Spectrosc. Relat. Phenom. 21 (1980) 265.

[22] V.I. Nefedov, M.N. Firsov, I.S. Shaplygin, J. Electron Spectrosc. Relat. Phenom. 26 (1982) 65.

[23] A. Barrie, F.J. Street, J. Electron Spectrosc. Relat. Phenom. 7 (1977) 1.

[24] S.P. McBride, A.J. Bell, ISAF 2002: Proceedings of the 13th IEEE International Symposium on Applications of Ferroelectrics (2002) 451.

[25] K. Hauffe, J. Block, Z. Physik. Chem. 198 (1951) 232.

[26] A.P. Grosvenor, J.T. Francis, B.A. Kobe, N.S. McIntyre, Surf. Interface Anal. 37 (2005) 495.

Chapter 5 Use of oxygen/nickel ratios in the XPS characterization of oxide phases on nickel metal and nickel alloy surfaces

5.1 Introduction

X-ray photoelectron spectroscopy has extensively been used to study the oxidation and corrosion products formed on surfaces of Ni metal and its alloys [1-17]; the technique has provided chemical information about the oxides produced that is generally not available elsewhere. The information depth available (~ 5nm) is sufficient to allow oxide structures and growth rates to be followed to a considerable length. While XPS chemical shifts have been useful in separating oxidic phases from the base alloy, clear identification of specific structures has been lacking because of complex Ni 2p line shapes and a large number of contributing sources to the O 1s line shape [13-17]. In the past, our laboratory has produced evidence for unique Ni $2p_{3/2}$ and O 1s spectra for polycrystalline NiO, β-$Ni(OH)_2$, and γ-NiOOH [1,4,18] and have used this information to follow oxide growth structures on Ni metal during reaction with O_2 gas [3] and H_2O vapour [2]. Over the course of this work, it was found that most of the O/Ni atomic ratios, corrected for cross-section, energy and contributions from contaminants, appeared to provide a reliable measure of the actual atomic ratios. Such measurements, if accurate, could certainly provide additional information on the nature of the surface structures. For this reason, we have made additional O/Ni measurements of new- and previously-acquired spectra of NiO [2], β-$Ni(OH)_2$ [2], γ-NiOOH [18], and $NiCr_2O_4$ [19] and have used these reference results to determine the ratios for oxide structures on Ni metal and NiCr alloy surfaces that had undergone electrochemical oxidation. The O/Ni

measurements on the unknown electrochemically treated surfaces correspond well with analyses of the standard O 1s and Ni $2p_{3/2}$ spectral line shapes.

5.2 Experimental

All XPS analyses were carried out with a Kratos Axis Ultra spectrometer using a monochromatic Al Kα (15 mA, 14 kV) X-ray source. The work function and the dispersion of the instrument were calibrated to give metallic Au $4f_{7/2}$ and Cu $2p_{3/2}$ signals of 83.95 eV and 932.63 eV respectively. Differential surface charging was minimized using the Kratos charge neutralizer system with a filament current set between 1.7-1.9 A, and a charge balance ranging from 2.4-3.1 V. All XPS spectra were collected using the hybrid-focusing lens, a scan time of 180 s, and an analysis area of 700 μm x 300 μm. The survey spectra were obtained at a pass energy of 160 eV, a 0.7 eV energy step, over a binding energy (BE) range of 1100-0 eV. Analyses of the Ni 2p, Cr 2p, O 1s, and C 1s envelopes were carried out at pass energies of 10/20 eV, an energy step size of 0.05 eV, at energy ranges of 895-848 eV (30-40 sweeps), 595-570 (30 sweeps), 540-520 eV (15-20 sweeps), and 295-275 eV (10-20 sweeps) respectively. The base pressure of the analytical chamber during sample analysis was near 5×10^{-7} Pa.

Powder samples of polycrystalline NiO (99.998% pure, Puratronic) and β-$Ni(OH)_2$ (61% Ni) were obtained from Alfa Aesar (Ward Hill, MA, USA). The NiO powder was received in a sealed container and two samples were introduced to the spectrometer through an Ar filled glove box. Two additional NiO samples were exposed to air prior to X-ray analysis. The purity of the NiO powder was confirmed using both X-ray Diffraction (XRD) and Energy Dispersive X-ray analysis (EDX), while the purity of

the β-$Ni(OH)_2$ powder was confirmed solely by EDX [4]. The γ-NiOOH sample was originally obtained from Inco Limited and its characterization has been previously reported [18]. The β-$Ni(OH)_2$ and γ-NiOOH powders were both loaded into the spectrometer from the air. The $NiCr_2O_4$ powder (90% pure) was obtained from Alfa Aesar and was exposed to the air prior to X-ray analysis [19]. All powder samples were either mounted onto a double-sided non-conductive polyethylene polymer or pressed into indium foil prior to X-ray exposure to further minimize spectral broadening due to charging. A polycrystalline Ni metal disk approximately 3.4 mm thick was cut from a metal rod (99.995% pure) purchased from Alfa Aesar. A similar sized disc of NiCr alloy manufactured by ACI Alloys Inc. (San Jose CA USA) was also studied. Both metallic samples were mechanically polished to a mirror finish using 0.05 μm γ-Al_2O_3 paste, sonicated in methanol for 20 min, and cathodically cleaned for 1 h at a constant potential of -1.5 V versus a 0.1 M Ag/AgCl reference electrode. Following surface reduction the metal disks were then subjected to aqueous corrosion for 3 h at a constant potential of 1.5 V versus the same reference electrode in a sealed autoclave at temperatures of 150°C for Ni metal and 25°C for the NiCr alloy. The electrolyte used was a 1 x10^{-4} M LiOH solution (pH= 10 at 25˚C) prepared in deionized H_2O.

CasaXPS Version 2.3.15 was used to analyze all XPS spectra collected as part of this work [20]. The background for all survey and high-resolution spectra was removed using a standard Shirley baseline [20]. The elemental concentration in atomic % (at.%) for all samples was determined from the analysis of XPS survey spectra using Wagner relative sensitivity factors (RSFs) specifically modified for analyzing data obtained from a Kratos Axis Ultra spectrometer [20-22]. The Ni atomic concentrations presented in

Table 5.1 were calculated using the area of Ni $2p_{3/2}$ region only. Previous publications by this group have used the same data analysis methods [2,3,23]. Analysis of the Ni $2p_{3/2}$ and Cr $2p_{3/2}$ spectra were completed using the fits previously published for polycrystalline NiO, β-$Ni(OH)_2$, γ-NiOOH, Cr_2O_3, $Cr(OH)_3 \cdot xH_2O$ and $NiCr_2O_4$ [1,4,18-19,23]. Gaussian-Lorentzian line shapes of 50% (GL(50)) were found to be best for fitting the O 1s spectra, while the C 1s envelopes were best fitted with a 30% Lorentzian (GL(30)) contribution in the mixture.

All samples studied as a part of this work were determined to contain small amounts of adventitious C. Analyses of the high-resolution C 1s spectra showed a strong hydrocarbon line (C–C, C–H), which was used for spectral calibration and corrected to a BE of 284.8 ± 0.1 eV. Additional contributions from alcohol/ether (–COH, –COC–, O=C(O–C*), carbonyl (–C=O), and ester (O=CO–) organic functional groups were also observed at average BEs of 286.1 ± 0.2 eV, 287.8 ± 0.2 eV, and 288.7 ± 0.2 eV respectively. The (*) denotes the atom giving rise to the signal. Contamination of the O 1s line shape from O-containing adventitious C was corrected as described in earlier publications and was modelled using five peaks representing O*=CO– (531.7 ± 0.2 eV), –C=O (532.0 ± 0.2 eV), –COC– (532.2 ± 0.2 eV), –COH (532.5 ± 0.2 eV), and O=CO*– (532.9 ± 0.2 eV) O species [2,23-24].

The relative atomic concentrations for the different Ni, Cr, O, and C species were determined using methods described in previous publications [2,23]. The error in the resultant O/M (M = Ni or Cr) ratios was estimated to be 10% (2 standard deviations). The CasaXPS software also allows for the normalized atomic ratios to be calculated directly from the high-resolution spectra using the “Standard Comps Report” button

found under the "Report Spectra" tab in the "Quantification Window" [20]. However, during the course of this work O/Ni ratios calculated using this method were found to deviate significantly from what was stoichiometrically expected. In a previous publication by this group the O/Cr ratios for a number of Cr oxides were calculated. When these ratios were modelled using the "Standard Comps Report" function the same O/Cr ratios were observed. It appears that this method works for systems containing Cr and O because the two peaks used for analysis (Cr $2p_{3/2}$ and O 1s) are only separated in kinetic energy (KE) by approximately 50 eV, while the difference between the Ni $2p_{3/2}$ and O 1s peaks is greater than 300 eV. As a result any calculation of atomic concentrations for Ni should be completed using the survey spectra (pass energy 160 eV) and not the high-resolution spectra.

5.3 Results and Discussion

5.3.1 Polycrystalline NiO, β-$Ni(OH)_2$, γ-NiOOH, and $NiCr_2O_4$ samples

Representative high-resolution Ni $2p_{3/2}$ and O 1s spectra for NiO, β-$Ni(OH)_2$, γ-NiOOH, and $NiCr_2O_4$ are shown in Figures 5.1-5.4. All Ni $2p_{3/2}$ and Cr $2p_{3/2}$ envelopes were modelled using the fits tabulated in references [1,4,18-19,23]. The M $2p_{3/2}$ spectra of these compounds have been well characterized previously and were included solely as a reference for the corresponding O 1s spectra. For each O 1s spectrum, it was necessary to determine if each spectral component was associated intimately with the oxide structure or was associated with an ancillary phase such as organic contamination, or interstitial H_2O molecules.

Representative high-resolution Ni $2p_{3/2}$ and O 1s spectra for polycrystalline NiO powder are shown in Figure 5.1. The O 1s spectra for all NiO samples contained the well

recognized lattice oxide peak (O^{2-}) with centroids that could be fitted to 529.3 eV or 529.4 eV depending on the sample (see Table 5.1). In addition, a higher BE peak was observed at either 531.1 eV or 530.9 eV; this has been previously attributed by ourselves [2] and others [5-8] to oxygen atoms adjacent to vacancies and thus deemed to be 'defective oxygen" (O def). Such an assignment is unique to NiO in all the oxides studied; it may result from a particularly disordered structure during nucleation. The summed intensities of these peaks were used in the compilation of the O/Ni ratios for NiO shown in Table 5.2. All additional intensity in the O 1s spectra for NiO could be attributed to organic components present; thus no additional contributions from interstitial H_2O was found in any of the NiO examples studied (see below). Table 5.2 shows that, for NiO, the O/Ni ratios obtained are close to 1.0, within experimental error.

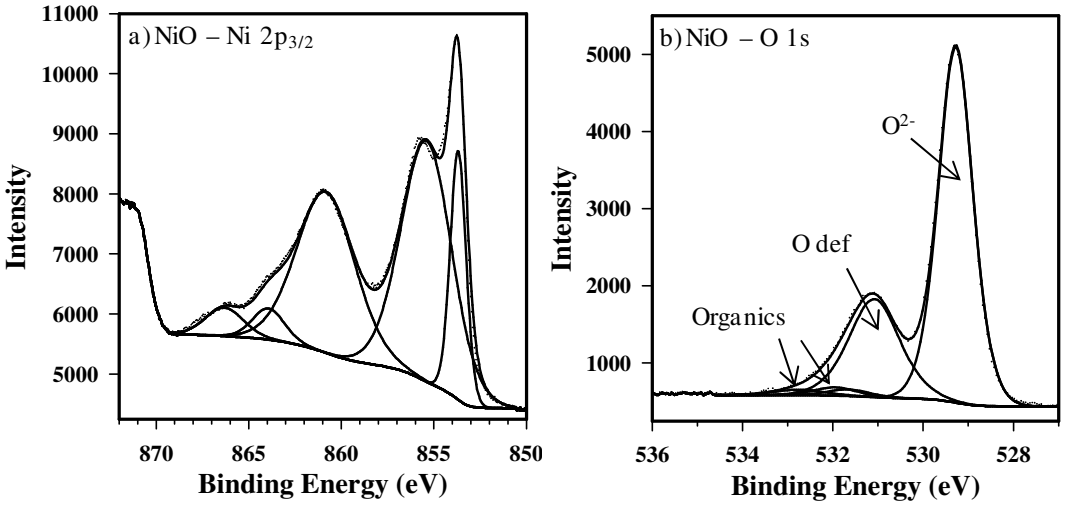

Figure 5.1: Fitted high-resolution (a) Ni $2p_{3/2}$ and (b) O 1s spectra from a polycrystalline NiO powder loaded into the spectrometer through an Ar filled glove box. The Ni $2p_{3/2}$ spectrum was fit using the empirical peak fit for NiO tabulated in reference [4]. The O 1s spectrum has been fit with contributions from O^{2-} and O def species. The remaining spectral intensity was assigned to organic contamination.

Figure 5.2(a-d) contains the Ni $2p_{3/2}$ and O 1s spectra collected from two samples of the β-$Ni(OH)_2$ powder. Fitting of the respective O 1s spectra showed a strong peak representing bound hydroxide groups (OH^-) centred at either 530.8 eV or 530.9 eV depending on the sample (see Table 5.1) along with contributions from organic contamination at higher BEs. The O/Ni ratios were calculated and values of 2.0 were observed (see Table 5.2). To completely fit the O 1s spectrum shown in Figure 5.2(d) an additional component at 531.5 eV was also required. The relative atomic contribution from this additional peak was not included in the atomic ratio calculations shown in Table 5.2 and this result indicated that this species was not chemically bound to any Ni^{2+} cations. We suggest that this species might result from interstitially positioned H_2O molecules within the layered brucite-like β-$Ni(OH)_2$ structure [25]. Three additional β-$Ni(OH)_2$ powder samples were analyzed and the O/Ni ratios were found to range from 1.5-1.6. These may represent a structure that is undergoing degradation through loss of OH^-. The BE of the OH^- groups in this structure was found to be statistically higher (531.1 ± 0.1 eV) than in the hydroxides with the measured 2:1 O/Ni ratio (see Table 5.1). Representative high-resolution Ni $2p_{3/2}$ and O 1s spectra for a OH^- deficient β-$Ni(OH)_2$ powder are shown in Figure 5.2(e-f).

The Ni $2p_{3/2}$ and O 1s spectra collected from the γ-NiOOH powder are presented in Figure 5.3. The O 1s spectrum was fitted with an O^{2-} component at 529.5 eV, an OH^- peak at 531.2 eV, along with contributions from adsorbed organic species (see Table 5.1). An O/Ni ratio of 1.9 was obtained when the combined intensities of the OH^- and O^{2-} components were compared to the total Ni^{3+} concentration (see Table 5.2). Although this

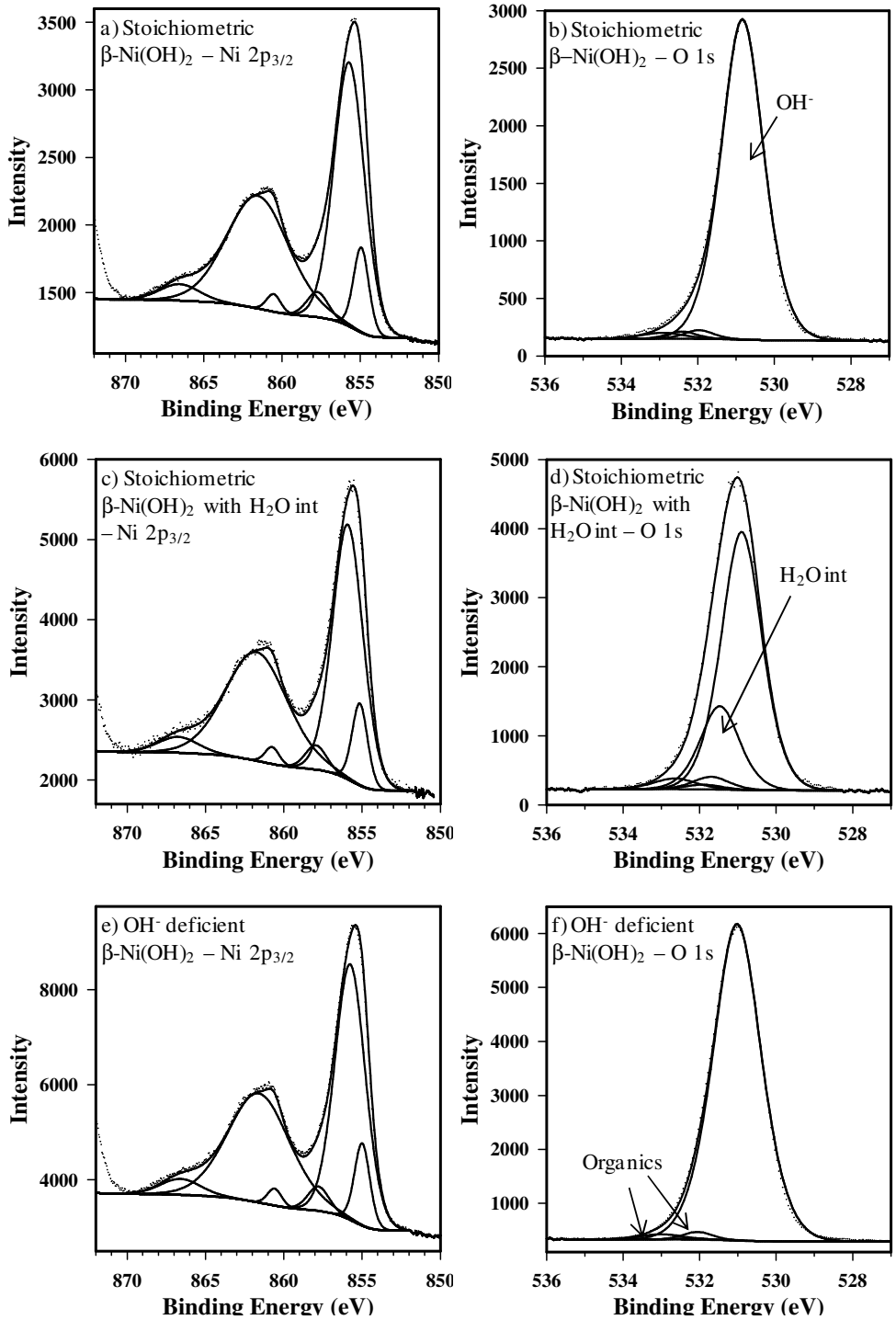

Figure 5.2: Fitted high-resolution Ni $2p_{3/2}$ and O 1s spectra collected from three β-$Ni(OH)_2$ samples. The spectra illustrate the Ni $2p_{3/2}$ and O 1s line shapes for (a) and (b) stoichiometric β-$Ni(OH)_2$, (c) and (d) stoichiometric β-$Ni(OH)_2$ containing interstitial H_2O (H_2O (int)) within the brucite lattice, and (e) and (f) OH^- deficient β-$Ni(OH)_2$. The Ni $2p_{3/2}$ spectra were fit using the empirical peak fit for β-$Ni(OH)_2$ tabulated in reference [4].

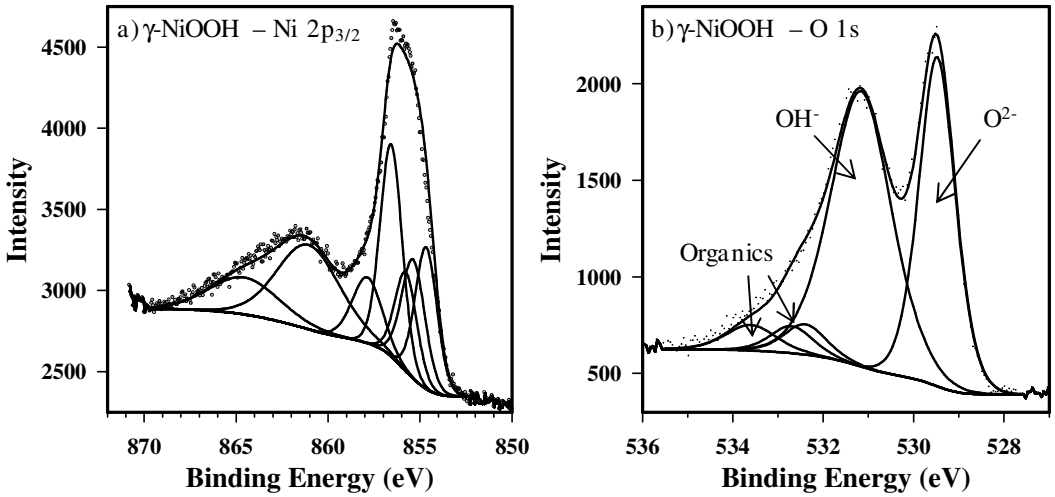

Figure 5.3: Fitted high-resolution (a) Ni $2p_{3/2}$ and (b) O 1s spectra for γ-NiOOH powder. The Ni $2p_{3/2}$ spectrum was modeled using a peak fit originally presented in reference [18]. The O 1s spectrum shows contributions from O^{2-} and OH^- species along with additional intensity assigned to organic contamination at higher BE. The expected 1:1 O^{2-}:OH^- peak area ratio is not observed here and suggests that the γ-NiOOH sample has started to decompose.

ratio is close to the expected value of 2, the 1:1 O^{2-}/OH^- ratio is not observed here. This suggests that the γ-NiOOH sample had started to decompose.

Figure 5.4 contains representative Ni $2p_{3/2}$, Cr $2p_{3/2}$ and O 1s spectra collected from a powder sample of $NiCr_2O_4$. The O 1s spectra for both $NiCr_2O_4$ powders showed a strong component at either 529.9 eV or 530.0 eV attributed to lattice O^{2-}, a smaller peak located at 531.2 eV, and small contributions from organic material at higher BEs (see Table 5.1). The normalized Ni/Cr, O/Ni, and O/Cr ratios were found to be close to 2.0, 4.0, and 2.0 respectively (see Table 5.2). Thus the peaks at 529.9 eV and 530.0 eV represent all lattice O^{2-} sites within the inverse spinel structure and the small peak at 531.2 eV may be associated to the presence of interstitial H_2O molecules.

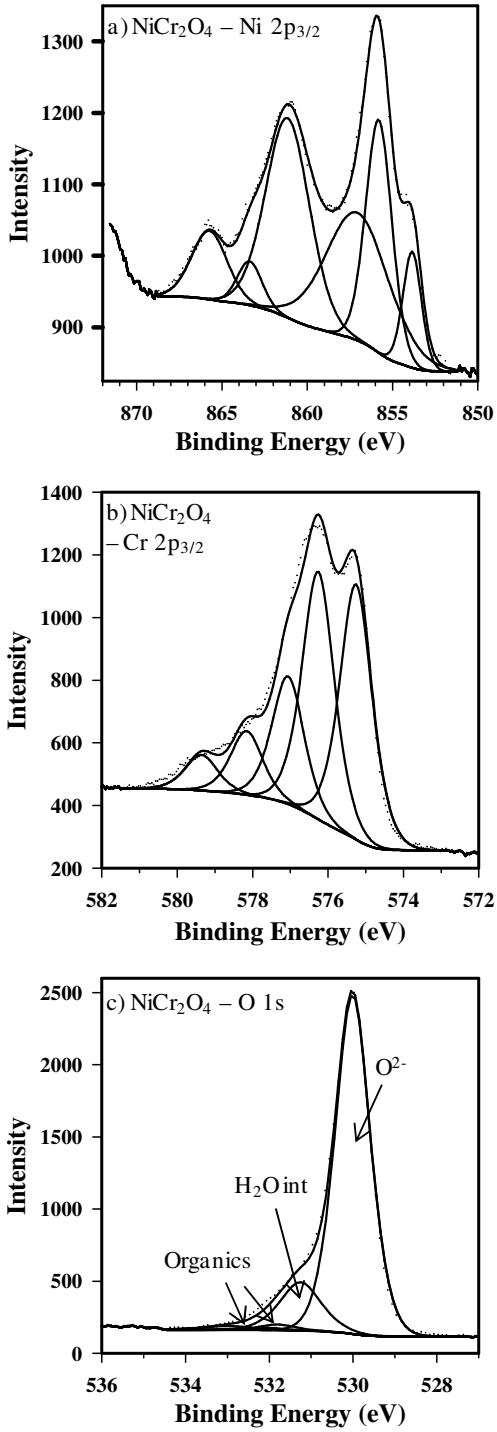

Figure 5.4: Fitted high-resolution (a) Ni $2p_{3/2}$, (b) Cr $2p_{3/2}$ and (c) O 1s spectra for a powder sample of $NiCr_2O_4$. The high-resolution Ni $2p_{3/2}$ and Cr $2p_{3/2}$ spectra are shown with the fits presented in references [1 and 19]. The O 1s spectrum shows the presence of lattice O^{2-} species along with small amounts of organic contamination. An additional peak was also required to completely fit the envelope and was assigned to H_2O (int).

Table 5.1: Summary of the O 1s peak fitting results for the O^{2-}, O def, OH^- and interstitial H_2O species.

	O^{2-}			O def			OH^-			Interstitial H_2O		
Sample	BE (eV)	FWHM (eV)	Area (eV)	BE (eV)	FWHM (eV)	Area (eV)	BE (eV)	FWHM (eV)	Area (eV)	BE (eV)	FWHM (eV)	Area (eV)
NiO-1	529.3	0.90	68	531.1	1.32	27						
NiO-2	529.3	0.91	71	531.1	1.24	23						
NiO-3	529.4	0.94	69	530.9	1.30	20						
NiO-4	529.4	0.94	71	530.9	1.20	18						
β-$Ni(OH)_2$-1							530.8	1.30	95			
β-$Ni(OH)_2$-2							530.9	1.25	71	531.5	1.20	22
β-$Ni(OH)_2$-3							531.0	1.47	97			
β-$Ni(OH)_2$-4							531.2	1.41	93			
β-$Ni(OH)_2$-5							531.2	1.39	93			
γ-NiOOH	529.5	0.95	37				531.2	1.59	52			
$NiCr_2O_4$-1	529.9	1.02	77							531.2	1.52	20
$NiCr_2O_4$-2	530.0	0.97	82							531.2	1.25	15
Ni metal	529.2	1.00	23				531.1	1.34	51	531.7	1.20	13
NiCr metal												
Ni oxides	529.3	1.10	4				531.2	1.60	24	531.8[a]	1.28	7
Cr oxides	529.5[b]	1.10	6				531.3	1.56	30	530.2[d]	1.28	9
	530.0[c]	1.10	3									

[a]The observed BE shift for the interstitial H_2O species associated with $Ni(OH)_2$.

[b]The observed BE shift for the O^{2-} species bound in Cr_2O_3

[c]The observed BE shift for the O^{2-} species bound in the Cr^{6+}-containing oxide.

[d]The observed BE shift for the interstitial H_2O species associated with $Cr(OH)_3$.

Table 5.2: Calculated O/M ratios using the normalized O, Ni, and Cr atomic concentrations in at.%.

	M $2p_{3/2}$		O 1s			
Sample	Ni or Cr species	at.%	O^{2-} at.%	O def at.%	OH^- at.%	O/M
NiO-1	Ni^{2+}	38	28	11		1.0[a]
NiO-2		37	29	9.7		1.1[a]
NiO-3		38	30	8.6		1.0[a]
NiO-4		37	30	7.6		1.0[a]
$Ni(OH)_2$-1	Ni^{2+}	20			40	2.0
$Ni(OH)_2$-2		29			57	2.0
$Ni(OH)_2$-3		36			56	1.6
$Ni(OH)_2$-4		34			50	1.5
$Ni(OH)_2$-5		33			51	1.5
γ-NiOOH	Ni^{3+}	20	16		22	1.9[b]
$NiCr_2O_4$-1						
Ni	Ni^{2+}	10	40			4.0
Cr	Cr^{3+}	21				1.9
$NiCr_2O_4$-2						
Ni	Ni^{2+}	11	44			4.0
Cr	Cr^{3+}	23				1.9
Ni metal						
Ni metal	Ni^0	1.3				
NiO	Ni^{2+}	8.8	9.0			1.0[c]
$Ni(OH)_2$		10			20	2.0
NiCr metal						
Ni metal	Ni^0	0.9				
NiO	Ni^{2+}	1.6	1.6			1.0[c]
$Ni(OH)_2$		5.0			10	2.0
Cr metal	Cr^0	0.5				
Cr_2O_3	Cr^{3+}	1.8	2.7			1.5
$Cr(OH)_3$		4.1			13	3.2
Cr^{6+}	Cr^{6+}	0.4	1.2			3.0

[a] The O/Ni ratio was calculated using the combined atomic concentrations of the O^{2-} and O def species.
[b] The O/Ni ratio was calculated using the combined atomic concentration of the O^{2-} and OH^- species.
[c] The O/Ni ratio was calculated using the atomic concentration of the O^{2-} peak only. Based on the observed ratio there appeared to be no evidence to suggest that an O def species had formed.

5.3.2 Aqueous reaction of metallic Ni and NiCr

The concept of using both peak shape and oxide ratio to identify and to estimate the relative proportions of mixed oxide systems, has been applied to some spectra produced during electrochemical oxidation of both polycrystalline Ni and NiCr alloy surfaces during simulation of solution conditions in PWR secondary coolant systems. Metallic Ni and NiCr alloy disks were subjected to 3 h aqueous exposures in a 1 x 10^{-4} M LiOH solution (pH = 10 at 25°C), at a constant potential of 1.5 V versus a 0.1 M Ag/AgCl reference electrode, and temperatures of 150°C (Ni metal) and 25°C (NiCr alloy) in a sealed autoclave. Following the aqueous reactions the metallic samples were removed from the autoclave and exposed to air prior to surface analysis. Modeling of the Ni $2p_{3/2}$ and Cr $2p_{3/2}$ spectra involved using different combinations of the fits presented in references [1,4,18-19,23] for metallic polycrystalline Ni, powdered polycrystalline NiO, β-$Ni(OH)_2$, γ-NiOOH, $NiCr_2O_4$, metallic Cr, powdered polycrystalline Cr_2O_3, $Cr(OH)_3 \cdot xH_2O$, and CrO_3. Using the M $2p_{3/2}$ fitting results coupled with the expected O/M atomic ratios the corresponding O 1s peak areas for the O^{2-} and OH^- species were constrained. Contributions from any organic contaminants were estimated from the analysis of the C 1s high-resolution spectra and these intensities were then applied to the O 1s fit. The remaining spectral intensity was then attributed to the presence of interstitial H_2O molecules. From the XPS survey scans collected from both the Ni metal and NiCr alloy surfaces following aqueous oxidation a number of small impurities were also observed. The O 1s contribution of any possible oxide and or hydroxides associated with these species were assumed to be negligible and not included in the fit.

Figure 5.5 shows the Ni $2p_{3/2}$ and O 1s spectra collected for the polycrystalline Ni metal surface. The Ni $2p_{3/2}$ spectrum was rigorously fitted using contributions from Ni metal (6%), NiO (44%), and β-$Ni(OH)_2$ (50%), while the analysis of the O 1s spectrum showed contributions from lattice O^{2-} at 529.2 eV, lattice OH^- at 531.1 eV and interstitial H_2O at 531.7 eV (see Table 5.1). The normalized O/Ni ratios calculated for the respective NiO and β-$Ni(OH)_2$ components were 1.0 and 2.0 (see Table 5.2). Thus, in this oxide/hydroxide composite there was no evidence for the O vacancy structure found for thin films of essentially single phase NiO [2,3]. While some higher oxidation states of Ni (i.e. in NiOOH) are predicted thermodynamically [26], no evidence for these was found: no Ni^{3+} line shape contributions are found and the O/Ni ratios are consistent with nearly equivalent concentrations of NiO and β-$Ni(OH)_2$.

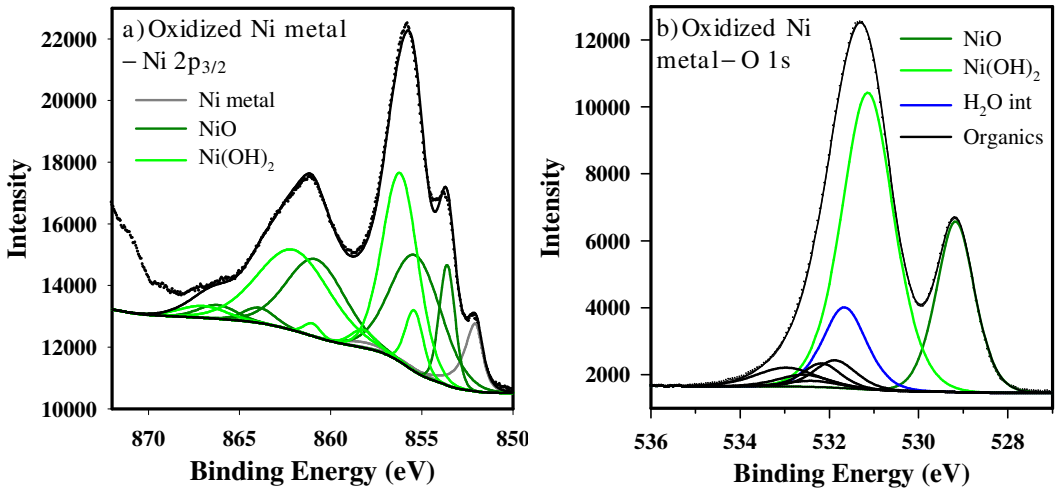

Figure 5.5: Fitted high-resolution (a) Ni $2p_{3/2}$ and (b) O 1s spectra collected from a polycrystalline Ni metal disk subjected to aqueous oxidation. The Ni $2p_{3/2}$ spectrum showed contributions from metallic Ni, NiO and β-$Ni(OH)_2$. Fitting of the O 1s spectrum showed corresponding contributions from NiO, β-$Ni(OH)_2$, H_2O (int), and organic contamination.

Figure 5.6(a-c) contains the high-resolution spectra collected from a NiCr surface following aqueous oxidation. The Ni $2p_{3/2}$ spectrum showed contributions from Ni metal (12%), NiO (21%) and β-$Ni(OH)_2$ (67%), while contributions from metallic Cr (8%) Cr_2O_3 (26%), $Cr(OH)_3$ (61%), and a fourth component attributed to a Cr^{6+} species (5%) were observed in the Cr $2p_{3/2}$ spectrum (see Table 5.1). Analysis of the O 1s spectrum showed signals at 529.3 eV (NiO), 529.5 eV (Cr_2O_3), 530.0 eV (Cr^{6+}-containing oxide), 531.2 eV (β-$Ni(OH)_2$), and 531.3 eV ($Cr(OH)_3$). The corresponding normalized O/M ratios for the NiO, Cr_2O_3, β-$Ni(OH)_2$, and $Cr(OH)_3$ components were calculated to be 1.0, 1.5, 2.0, and 3.0 respectively, while the O/Cr ratio for the Cr^{6+}-containing oxide was found to be 3.0 (see Table 5.2). There was no evidence to support the formation of either NiOOH and or $NiCr_2O_4$ films on this surface. Two additional peaks at 530.2 and 531.8 eV were also required to fit the envelope. The higher BE species was attributed to interstitial H_2O associated with β-$Ni(OH)_2$, while the lower BE species is believed to result from interstitial H_2O molecules associated with $Cr(OH)_3$; according to our reassessment of O 1s spectral data for $Cr(OH)_3 \cdot xH_2O$ originally shown in reference [23]. The normalized O/Cr atomic ratios for the Cr_2O_3 and $Cr(OH)_3$ components were calculated to be 1.5 and 3.0 respectively. The re-fitted O 1s spectrum for $Cr(OH)_3 \cdot xH_2O$ is shown in Figure 5.6(d).

5.4 Conclusions

The corrected O/Ni atom ratios were determined for powder samples of polycrystalline NiO, β-$Ni(OH)_2$, γ-NiOOH, and $NiCr_2O_4$ and were shown to correspond well to the expected atom ratios for these oxides. For some particular samples of β-

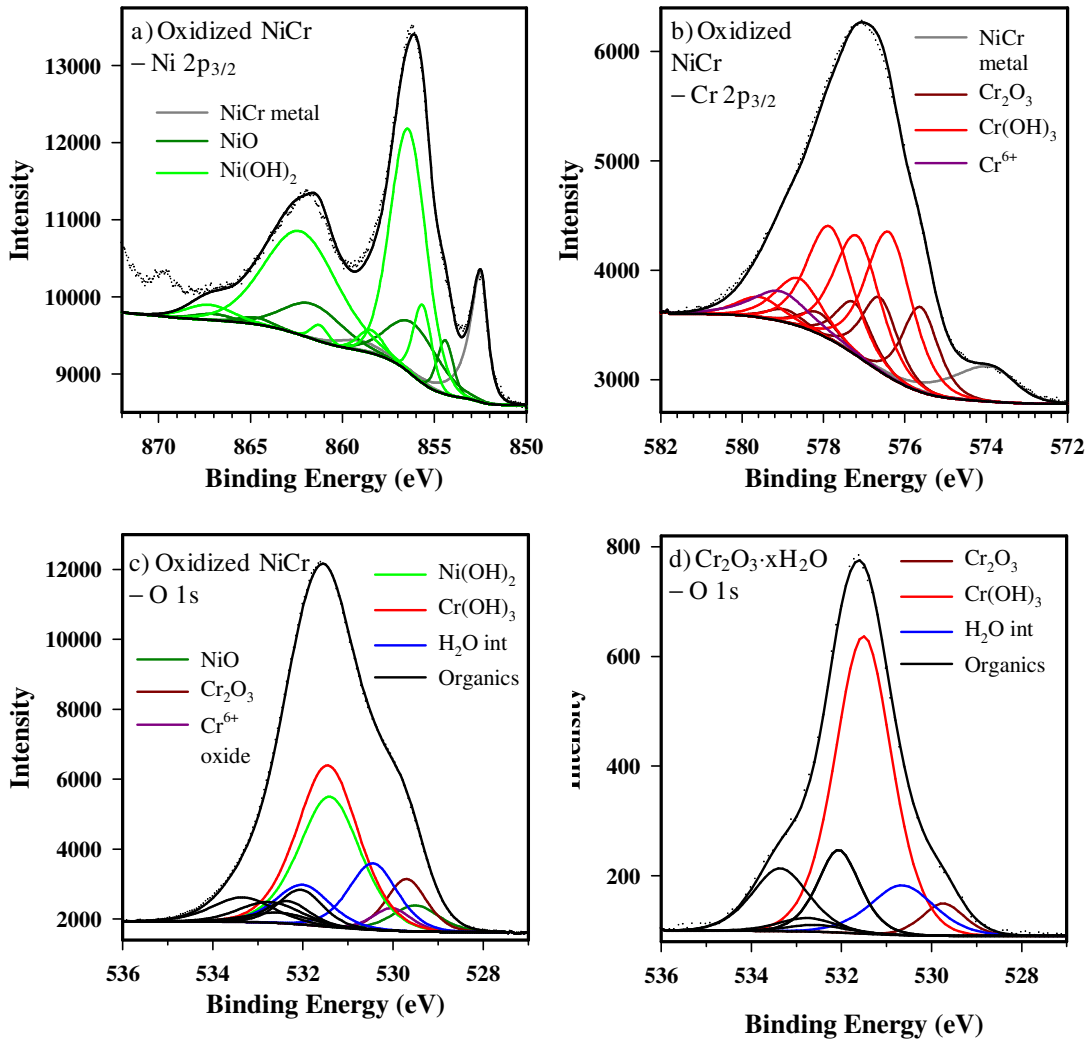

Figure 5.6: Fitted high-resolution (a) Ni $2p_{3/2}$, (b) Cr $2p_{3/2}$, and (c) O 1s spectra collected from a NiCr disk subjected to aqueous oxidation. The Ni $2p_{3/2}$ spectrum showed contributions from metallic Ni, NiO and β-$Ni(OH)_2$. The Cr $2p_{3/2}$ spectrum was best fit with contributions from metallic Cr, Cr_2O_3, $Cr(OH)_3$, and a Cr^{6+}-containing oxide. Fitting of the O 1s spectrum showed corresponding contributions from NiO, Cr_2O_3, a Cr^{6+}-containing oxide, β-$Ni(OH)_2$, and $Cr(OH)_3$. Two additional components representing H_2O (int) species associated with both β-$Ni(OH)_2$ and $Cr(OH)_3$ were also observed. The remainder of the O 1s intensity was determined to result from organic contamination.

$Ni(OH)_2$ and γ-NiOOH, the O/Ni ratios suggested that the sample was decomposing. The O/Ni and O/Cr ratios were then used to confirm the assignments of mixed oxide phases that formed on Ni metal and NiCr alloy surfaces during electrochemical oxidation.

5.5 References

[1] M.C. Biesinger, B.P. Payne, A.P. Grosvenor, L.W.M. Lau, A.R. Gerson, R.St.C. Smart, Appl. Sur. Sci. 257 (2011) 2717.

[2] B.P. Payne, M.C. Biesinger, N.S. McIntyre, J. Electron Spectrosc. Relat. Phenom. 175 (2009) 55.

[3] B.P. Payne, A.P. Grosvenor, M.C. Biesinger, B.A. Kobe, N.S. McIntyre, Surf. Interface Anal. 39 (2007) 582.

[4] M.C. Biesinger, B.P. Payne, L.W.M. Lau, A.R. Gerson, R.St.C. Smart, Surf. Interface Anal. 41 (2009) 324.

[5] M.W. Roberts, R.St.C. Smart, J. Chem. Soc., Faraday Trans. 80 (1984) 2957.

[6] M.W. Roberts, Sur. Sci. 299/300 (1994) 769.

[7] A.F. Carley, P.R. Chalker, M.W. Roberts, J. Chem. Soc., Chem. Commun. 80 (1984) 459.

[8] A.F. Carley, S. Rassias, M.W. Roberts, Sur. Sci. 135 (1983) 35.

[9] P.R. Norton, R.L. Tapping, J.W. Goodale, Surf. Sci. 65 (1977) 13.

[10] C. Benndorf, C. Nöble, F. Thieme, Surf. Sci. 121 (1982) 249.

[11] J.M. Heras, E.V. Albano, Appl. Surf. Sci. 17 (1983) 207.

[12] J.M. Heras, E.V. Albano, Appl. Surf. Sci. 17 (1983) 220.

[13] N.S. McIntyre, R.D. Davidson, T.L. Walzak, A.M. Brennenstuitl, F. Gonzalez, S. Corazza, Corros. Sci. 37 (1995) 1059.

[14] N.S. McIntyre, D.G. Zetaruk, D.Owen, J. Electrochem. Soc., Electrochem. Soc. 126 (1979) 750.

[15] N.S. McIntyre, T.E. Rummery, M.G. Cook, D.Owen, J. Electrochem. Soc. 123 (1976) 1164.

[16] A. Machet, A. Galtayries, S. Zanna, L. Klein, V. Maurice, P. Jolivet, M. Foucault, P. Combrade, P. Scott, P. Marcus, Electrochim. Acta 49 (2004) 3957.

[17] A. Machet, A. Galtayries, P. Marcus, P. Combrade, P. Jolivet, P. Scott, Surf. Interface Anal. 34 (2002) 197.

[18] A.P. Grosvenor, M.C. Biesinger, R.St.C. Smart, N.S. McIntyre, Surf. Sci. 600 (2006) 1771.

[19] M.C. Biesinger, C. Brown, J.R. Mycroft, R.D. Davidson, N.S. McIntyre, Surf. Interface Anal. 36 (2004) 1550.

[20] N. Fairley, CasaXPS Version 2.2.15, 1999-2009.

[21] C.D. Wagner, L.E. Davis, M.V. Zeller, J.A. Taylor, R.M. Raymond, L.H. Gale, Surf. Interface Anal. 3 (1981) 211.

[22] C.D. Wagner, J. Electron Spectrosc. Relat. Phenom. (32 (1983) 99.

[23] B.P. Payne, M.C. Biesinger, N.S. McIntyre, J. Electron Spectrosc. Relat. Phenom. 184 (2011) 2717.

[24] G. Beamson, D. Briggs, High-resolution XPS of Organic Polymers The Scienta ESCA300 Database, John Wiley and Sons, Toronto, 1992 (Appendices 1 – 3).

[25] C. Delmas, C. Faure, L.Gautier, L. Guerlou-Demourgues, A. Rougier, Phil. Trans. R. Soc. Lond. A 354 (1996) 1545.

[26] B. Beverskog, I. Puigdomenech, Corros. Sci. 39 (1997) 969.

Chapter 6 X-ray photoelectron study of the oxides formed on nickel metal and nickel-chromium 20% alloy surfaces under reducing and oxidizing potentials in basic, neutral and acidic solutions

6.1 Introduction

The corrosion resistant nature of Ni based alloys has led to the widespread use of these materials in high pressure and temperature environments such as those found in turbines, jet engines, and steam generator (SG) tubing in pressurized water reactors (PWR) [1]. Alloy 600[a] and Alloy 690[b] have been used in the latter application and their performance has been monitored by many techniques including those that measure the microstructural changes associated with alloy degradation. XPS has been a key investigative technique used to analyze the near surfaces of the alloys that have been exposed to real or simulated service conditions. XPS provides unique information on the thickness, composition and chemical state of the corrosion-formed deposits and films that result from degradative processes in the reactor coolant heat transport circuits [2-13]. This paper describes XPS studies of Ni metal and NiCr alloy samples that were exposed to SG conditions where the pH and/or oxidation potential of the simulated coolant were changed. Earlier publications by this group have shown that XPS can be used to analyze complicated line shapes observed for the mixed oxide/hydroxide films formed on Ni and Cr surfaces [14-19]. The relative changes with potential and pH on surface composition and chemistry contribute to a better understanding of surface condition of SG tubing during service, particularly in the context of mathematical models that predict the

[a]The approximate elemental composition of Alloy 600 in wt.%: Ni 72% minimum, Cr 14-17%, Fe 6-10%, balance C, Cu, Mn, S, Si and Ti.
[b]The elemental composition of Alloy 690 is: Ni 58% minimum, Cr 27-31%, Fe 7-11%, balance C, Cu, Mn, S, and Si.

chemical species based on thermodynamic data [20-22]. To complement XPS, the distribution of Ni and Cr species within the oxide films on selected NiCr samples were also monitored using ToF SIMS. This is the first time that the surface chemistry of these alloys has been explored as a function of both solution pH and oxidation potential.

6.2 Experimental

Polycrystalline Ni discs 3.4 mm thick were cut from a 12 mm diameter metal rod obtained from Alfa Aesar (99.995% pure). Samples of the same size were cut from a polycrystalline NiCr rod fabricated by ACI Alloys Inc. A small thread was drilled into one side of all metallic and alloy samples to allow the coupons to be suspended in various aqueous solutions via metal rods in a sealed autoclave. The specific experimental setup for all aqueous exposures is described below. Following drilling of the threads the second face of the Ni metal and NiCr alloy samples were polished to a mirror finish using 0.05 μm γ-Al_2O_3 paste. The freshly polished surfaces were then sonicated in methanol for 20 min.

The Ni metal and NiCr discs were exposed to aqueous oxidation in a sealed autoclave in aqueous solutions, all set to desired pH values at room temperature ($pH_{25°C}$). Solutions included 1 x 10^{-4} M LiOH (reagent grade ≥ 98%, Sigma Aldrich) adjusted to $pH_{25°C}$ = 10.1 (basic); 0.1 M $(NH_4)_2SO_4$ (purity ≥ 99%, BDH Inc.) adjusted with LiOH to $pH_{25°C}$ = 7 (neutral), and 0.1 M $(NH_4)_2SO_4$ corrected to a $pH_{25°C}$ = 4 (acidic) using H_2SO_4. Each electrolyte was prepared using deionized H_2O (resistivity 18 MΩ) and isolated from the walls of the autoclave by a Teflon™ liner. The pH of each solution was measured (at 25°C) using an Orion model 720 pH meter. During solution preparation, to

achieve desired neutral and acidic conditions, small amounts of 0.1 M LiOH or 0.1 M H_2SO_4 were added slowly to the appropriate electrolytes until the desired pH was reached. Ultra-pure Ar gas was bubbled through all solutions for 20 min prior to sealing the autoclave to minimize the amount of dissolved O_2 gas present. All samples were suspended in the respective electrolyte solutions using an Alloy-22[c] rod (Haynes). A piece of Alloy-22 was also used as a counter electrode, as this predominantly NiCr inert material has been demonstrated to be effective in the pressure vessel apparatus [23-24]. After the electrolytes were deaerated the autoclave was sealed and an overpressure of approximately 276 kPa of Ar gas was applied.

All Ni metal and NiCr alloy samples were oxidized in a sealed autoclave to keep the dissolved O_2 concentration to a minimum. For the experiments carried out at 150°C, a ramp time of 6 h was required to reach a stable temperature. The experimental setup was such that the pH of each solution could not be measured once the pressure vessel had been sealed. The temperature corrected pH ($pH_{150°C}$) values for all solutions were estimated using the following relationships:

$$pH_{150°C,\ basic\ (>7)} = pH_{25°C} + pK_{w150°C} - pK_{w25°C} \qquad 6.1$$

$$pH_{150°C,\ neutral\ (\sim 7)} = 1/2pK_{w150°C} \qquad 6.2$$

$$pH_{150°C,\ acidic\ (<7)} \approx pH_{25°C} \qquad 6.3$$

where K_w and K_{wt} are the ion products of pure H_2O at 25° and 150°C [25]. The $pK_{w25°C}$ and $pK_{w150°C}$ values used for pure H_2O at temperatures of 25° and 150°C were 14 and 11.7 respectively [26].

[c] The elemental composition of Alloy 22 in wt.%: Ni 56% maximum, Cr 22%, Mo 13%, Fe 3%, W 3%, Co 2.5%, balance C, Mn, S, and Si.

Prior to surface oxidation all metallic Ni and NiCr samples were cathodically cleaned for 1 h at a constant applied potential of -1.5 V versus a 0.1 M Ag/AgCl (in KCl solution) reference electrode. The design of the pressure vessel had the Ni/NiCr samples positioned approximately 31 mm from the reference electrode. Other authors have conducted experiments at similar temperatures using the same pressure vessel design [23-24]. Oxidation reactions were carried out at temperatures of 25° and 150°C for periods of 3, 24 or 48 h at controlled electrochemical applied potentials of 0.0 V (mildly oxidizing), 1.5 V or 1.6 V (highly oxidizing) versus the same Ag/AgCl reference electrode in one of the three electrolyte solutions. Surfaces oxidized at 25°C were immediately removed from the autoclave and transported in air to the XPS for surface analysis. The samples oxidized at 150°C were allowed to cool between 3–6 h prior to removal and transport to the XPS. To apply electrical potentials, a Solartron 1287 potentiostat was used, using Corrware software [27].

All surfaces studied as a part of this work were analyzed using a Kratos Axis Ultra spectrometer employing monochromatic Al Kα (15 mA, 14 kV) X-rays. The spectrometer work function and instrument dispersion were calibrated using the metallic Au $4f_{7/2}$ (83.95 eV) and Cu $2p_{3/2}$ (932.63 eV) signals. The base pressure of the analytical chamber during sample analysis was below 5×10^{-7} Pa. All XPS spectra were collected using the hybrid-focusing lens, a scan time of 180 s, and an analysis area of 700 μm x 300 μm. The survey spectra were obtained at a pass energy of 160 eV, a 0.7 eV energy step, over a binding energy (BE) range of 1100 eV – 0 eV. Analyses of the Ni 2p, Cr 2p, O 1s, and C 1s envelopes were carried out at pass energies of 20 eV, an energy step size

of 0.05 eV, at energy ranges of 895 eV – 848 eV (30–40 sweeps), 595–570 (30 sweeps), 540 eV – 520 eV (15–20 sweeps), and 295 eV – 275 eV (10–20 sweeps) respectively.

All XPS spectra were analyzed using CasaXPS Version 2.3.15 [28]. The backgrounds from both the survey and high-resolution scans were removed using a Shirley baseline [20]. All elemental concentrations were calculated using the relative sensitivity factors (RSFs) specific to the Kratos Axis Ultra spectrometer [28]. The elemental concentrations in at.% for the Ni and Cr species were calculated using the Ni $2p_{3/2}$ and Cr $2p_{3/2}$ regions from XPS survey spectra (see Tables 6.1 and 6.2). Other publications by this group have used this same method for determining the atomic concentrations for these elements [15,18-19].

Rigorous fitting of the high-resolution Ni $2p_{3/2}$ and Cr $2p_{3/2}$ spectra was undertaken to determine the composition of the oxidized surfaces. The metal (M) $2p_{3/2}$ line shapes for polycrystalline Ni metal and well characterized powder samples of NiO, β-$Ni(OH)_2$, γ-NiOOH, Cr_2O_3, $Cr(OH)_3 \cdot xH_2O$, CrO_3, and $NiCr_2O_4$ have been previously studied by this group [14-19]. Various combinations of these line shapes were used to model the Ni $2p_{3/2}$ and Cr $2p_{3/2}$ spectra collected from each oxidized surface; the combination that best reproduced the shapes of the respective envelopes was determined and applied to all the fits presented in this study. The line shapes for the metallic Ni and Cr species in the NiCr alloy were determined by fitting the M $2p_{3/2}$ spectra collected from a sputter cleaned (15 min, 4 kV Ar^+ beam) and annealed (30 min, 600°C) sample. The Ni and Cr atomic concentrations for the ion-etched and annealed sample, along with the associated fitting parameters, are presented in Table 6.2. The resulting high-resolution spectra are presented in Figure 6.1.

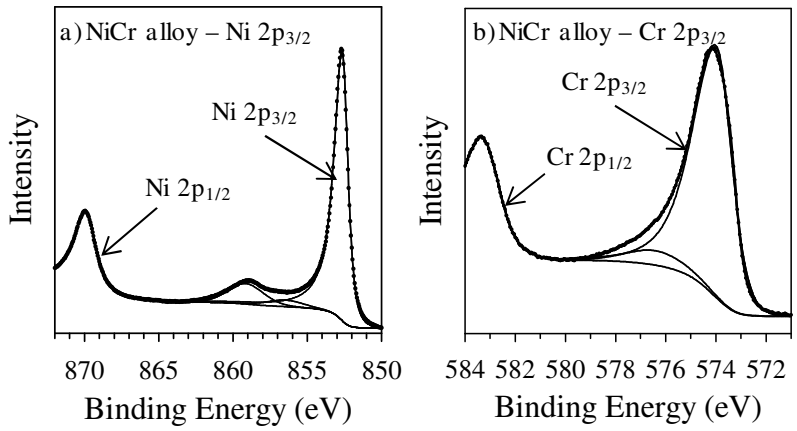

Figure 6.1: The high-resolution (a) Ni $2p_{3/2}$ and (b) Cr $2p_{3/2}$ spectra collected from a polished and sputter cleaned polycrystalline NiCr surface. Parts of the metal Ni $2p_{1/2}$ and Cr $2p_{1/2}$ lines are observed at higher BEs.

Table 6.1: High-resolution Ni $2p_{3/2}$ peak fitting results and normalized atomic concentrations (in at.%) for the Ni metal samples.

Sample	Total Ni (at.%)	Ni metal (%)	Ni metal (at.%)	NiO (%)	NiO (at.%)	$Ni(OH)_2$ (%)	$Ni(OH)_2$ (at.%)
Ni-1 (1 h, -1.5 V, 25°C, $pH_{25°C}$ = 10.1)[a]	14	36	5.0	25	3.5	39	5.5
Ni-2 (48 h, 0.0 V, 25°C, $pH_{25°C}$ = 10.1)	15	5	0.9	21	3.2	74	11
Ni-3 (3 h, 0.0 V, 150°C, $pH_{150°C}$ = 7.8)[b]	16			11	1.8	89	14
Ni-4 (3 h, 1.5 V, 150°C, $pH_{150°C}$ = 7.8)[b]	20	6	1.2	44	8.8	50	10

[a] A small Cr impurity of 1.6 at.% was detected on the surface following the surface reduction. Fitting of the Cr $2p_{3/2}$ envelope showed that all Cr species were bound in $Cr(OH)_3$.
[b] The $pH_{150°C}$ was calculated using Equation 6.1.

Table 6.2: High-resolution Ni $2p_{3/2}$ and Cr $2p_{3/2}$ peak fitting results and normalized atomic concentrations (in at.%) for the NiCr alloy samples.

Sample	Total Ni (at.%)	Ni metal (%)	Ni metal (at.%)	NiO (%)	NiO (at.%)	$Ni(OH)_2$ (%)	$Ni(OH)_2$ (at.%)
NiCr-1 (clean metal)[a]	67	100	67				
NiCr-2 (48 h, 0.0 V, 25°C, $pH_{25°C}$ = 10.1)	18	5	0.9	4	0.7	91	16
NiCr-3 (3 h, 0.0 V, 150°C, $pH_{150°C}$ = 7.8)[b]	4.0			4	0.2	96	3.8
NiCr-4 (24 h, 0.0 V, 150°C, $pH_{150°C}$ = 7.8)[b]	10			5	0.5	95	9.5
NiCr-5 (48 h, 0.0 V, 150°C, $pH_{150°C}$ = 7.8)[b]	8.2			4	0.3	96	7.9
NiCr-6 (3 h, 0.0 V, 150°C, $pH_{150°C}$ = 5.8)[c]	9.5			3	0.3	97	9.2
NiCr-7 (24 h, 0.0 V, 150°C, $pH_{150°C}$ = 5.8)[c]	12			5	0.6	95	11
NiCr-8 (3 h, 0.0 V, 150°C, $pH_{150°C}$ = 4.1)[d]	3.2	79	2.5	12	0.4	9	0.3
NiCr-9 (24 h, 0.0 V, 150°C, $pH_{150°C}$ = 4.1)[d]	2.3	63	1.4	12	0.3	25	0.6
NiCr-10 (48 h, 1.5 V, 150°C, $pH_{150°C}$ = 7.8)[b]	8.0	2	0.2	28	2.2	70	5.6
NiCr-11 (3 h, 1.5 V, 3 h 0.0 V 150°C, $pH_{150°C}$ = 7.8)[b]	14			23	3.2	77	11

Sample	Total Cr (at.%)	Cr metal (%)	Cr metal (at.%)	Cr_2O_3 (%)	Cr_2O_3 (at.%)	$Cr(OH)_3$ (%)	$Cr(OH)_3$ (at.%)	Cr^{6+} (%)	Cr^{6+} (at.%)
NiCr-1[e]	15	100	15						
NiCr-2	1.7	18	0.3	44	0.7	38	0.6		
NiCr-3	0.7			25	0.2	75	0.5		
NiCr-4									
NiCr-5	1.3			28	0.4	72	0.9		
NiCr-6	3.0			21	0.6	70	2.1	9	0.3
NiCr-7	3.3			25	0.8	69	2.3	6	0.2
NiCr-8	1.2	44	0.5	21	0.3	35	0.4		
NiCr-9	5.1	18	0.9	17	0.9	65	3.3		
NiCr-10	6.4			8	0.5	92	5.9		
NiCr-11	11			27	3.0	70	7.7		

[a] The Ni $2p_{3/2}$ peak fitting parameters: Peak 1 – 84%, LA(1.1,2.2,10), FWHM = 0.91 eV, at 852.6 eV: Peak 2 – 4%, GL(30), FWHM = 2.80 eV, at 856.5 eV: Peak 3 – 12%, GL(30), FWHM = 2.80 eV, at 859.2

[b] The $pH_{150°C}$ was calculated using Equation 6.1.

[c] The $pH_{150°C}$ was calculated using Equation 6.2.

[d] The $pH_{150°C}$ was calculated using Equation 6.3.

[e] The Cr $2p_{3/2}$ peak fitting parameters: Peak 1 – 93%, LA(2.1,5.2,10), FWHM = 1.48 at 574.0 eV, Peak 2 – 7%, GL(30), FWHM = 2.78 eV, at 576.4 eV

The atomic concentrations for the different Ni and Cr species (i.e. β-$Ni(OH)_2$ and Cr_2O_3) were calculated using the peak fitting results for the Ni $2p_{3/2}$ and Cr $2p_{3/2}$ spectra and the total Ni and Cr atomic concentrations detected in the survey scan (see Tables 6.1 and 6.2). The corresponding contributions to the O 1s spectra were derived by combining these calculated values with the expected O/Ni and O/Cr ratios for the different Ni and Cr oxide and hydroxide species (i.e. 2:1 O:Ni for β-$Ni(OH)_2$). All O 1s envelopes were modelled using peaks having 50% Gaussian – 50% Lorentzian line shapes denoted as GL(50) in CasaXPS.

All surfaces contained varying amounts of adventitious C. The C 1s envelopes were analyzed using components having GL(30) character (spectra not shown). Fitting of the C 1s spectra showed the presence of a strong hydrocarbon line (C−C, C−H) which was charge corrected to a BE of 284.8 ± 0.1 eV and used to calibrate all high-resolution spectra. The presence of additional organic components were observed at BEs of 286.2 ± 0.1 eV, 287.8 ± 0.2 eV and 288.7 ± 0.2 eV and attributed to alcohol/ether (−COH, −COC−, O=C(O−C^*), carbonyl (−C=O), and ester (O=CO−) functional groups, respectively [29]. The (*) indicates the atom giving rise to the photoelectron signal. The resultant O 1s contributions were modelled using peaks at 531.7 ± 0.3 eV, 532.0 ± 0.3 eV, 532.3 ± 0.2 eV, 532.5 ± 0.2 eV, and 532.8 ± 0.3 eV representing the O^*=CO−, −C=O, −COC−, −COH, and O=CO^*− species respectively. The same peak fitting methods have been applied in previous publications [15,18,19].

The thickness of the oxide films grown on the Ni metal surfaces were calculated using the mixed oxide/hydroxide formula presented by Biesinger et al. [16]. This model assumes the formation of a uniformly mixed oxide/hydroxide layer and was derived from

the overlayer models developed by Carlson [30] and Strohmeier [31]. The overlayer modeling could only be applied to the Ni surfaces where metallic signals were detected in the Ni $2p_{3/2}$ envelopes. The inelastic mean free paths (IMFPs) for metallic Ni, NiO and β-$Ni(OH)_2$ were calculated to be 1.1, 1.3 and 1.6 nm respectively using the NIST Electron Inelastic Mean Free Path Database (Version 1.1) [32].

Three alloy samples were subjected to surface analysis using an ION-TOF (GmbH) ToF SIMS IV single-reflections mass spectrometer. Shallow depth profiles into the oxide surfaces were collected using the dual beam mode, monitoring the negative secondary ions. The analysis beam was a 25 kV pulsed Bi^{3+} ion with a 0.5 pA target current rastered over a 200 μm x 200 μm area. A 3 kV Cs^+ sputter beam having a target current of 10 nA was rastered over a 500 μm x 500 μm area. The Bi^{3+} analysis regions were centred within the Cs^+ sputter crater to avoid edge effects. Two separate areas of each sample were analyzed and the profiles were terminated once the oxide/metal interfaces were reached. The ToF SIMS results were analyzed using the IONSPEC program [33].

6.3 Results and Discussion

6.3.1 Surface analysis using XPS

The composition of the films grown on oxidized Ni metal and NiCr alloy surfaces were modelled through fitting of the respective Ni $2p_{3/2}$, Cr $2p_{3/2}$ (where present) and O 1s high-resolution spectra. All Ni $2p_{3/2}$ spectra collected as part of this work were fit with contributions from β-$Ni(OH)_2$ and NiO. In addition, contributions from metallic Ni were also observed on some of the surfaces studied. The relative amount of each component in the Ni $2p_{3/2}$ spectra varied with the reaction conditions and exposure times. Summaries

of the Ni $2p_{3/2}$ peak fitting results for both the polycrystalline Ni metal and NiCr alloy samples are presented in Tables 6.1 and 6.2 respectively. The corresponding O 1s peak intensities for β-$Ni(OH)_2$ (531.1 ± 0.1 eV) and NiO (529.1 ± 0.2 eV) were constrained using the Ni $2p_{3/2}$ fitting results (see Tables 6.1 and 6.2) and the expected O/Ni atomic ratios of 2 and 1 for the respective oxides [15,19]. For the NiCr surfaces, fitting of the Cr $2p_{3/2}$ spectra showed the formation of mixed Cr_2O_3 and $Cr(OH)_3$ films. Low levels of Cr^{6+} were also observed on all alloy surfaces oxidized at neutral pH. In addition, metallic Cr contributions were observed on some alloy surfaces, and were found to coincide with the presence of metallic Ni. The complete Cr $2p_{3/2}$ fitting results are summarized in Table 6.2. The corresponding intensities for Cr_2O_3 (529.6 ± 0.2 eV), $Cr(OH)_3$ (531.4 ± 0.1 eV) and, where present, Cr^{6+} oxide (530.0 ± 0.2 eV) were also applied to the O 1s peak fits using O/Cr ratios of 1.5, 3 and 3 [18,19]. This applied ratio of 3 for the Cr^{6+} species produced the best O 1s fits and implied that a CrO_3-like oxide was present on these surfaces. However, Cr^{6+}-containing species have been shown to decompose readily during X-ray analysis [34]. Therefore, the actual O/Cr ratios could be greater than the experimentally detected values and some $HCrO_4^-$ or CrO_4^{2-} containing species, which are predicted to be thermodynamically stable under the applied experimental conditions [20,22], may be present on these surfaces. In some cases the atomic concentrations for the different oxidized Ni and Cr species approached the detection limit of XPS (see Tables 6.1 and 6.2). Higher error is associated with the O 1s peak assignments for these components. The remainder of the O 1s envelopes were then fit for contributions from organic contamination as well as for interstitial H_2O molecules associated with both β-$Ni(OH)_2$ (531.7 ± 0.1 eV) and $Cr(OH)_3$ (530.3 ± 0.1 eV) [15,18,19].

6.3.2 Surface reaction products under strongly reducing conditions in a basic environment at 25°C

Figure 6.2 shows the high-resolution Ni $2p_{3/2}$ and O 1s spectra collected from a polycrystalline Ni metal sample (Ni-1) exposed to a strongly reducing applied potential (E_{app}) of –1.5 V vs. an Ag/AgCl electrode at 25°C in a basic solution ($pH_{25°C}$ = 10.1) for 1 h. Exposure to these conditions produced a thin oxide film composed of both β-$Ni(OH)_2$ and NiO (see Table 6.1 and Figure 6.2). The thickness of this oxide, assuming an even coverage, was determined to be 2.2 nm using the formula of Biesinger et al. [16]. The presence of β-$Ni(OH)_2$ in this study suggests that the growth of this oxide component is the result of back precipitation from solution: β-$Ni(OH)_2$ is not found to be formed by a solid state reaction of Ni with H_2O vapour at these temperatures [15]. A small $Cr(OH)_3$ impurity (Cr $2p_{3/2}$ spectrum not shown) was also detected on this surface. For

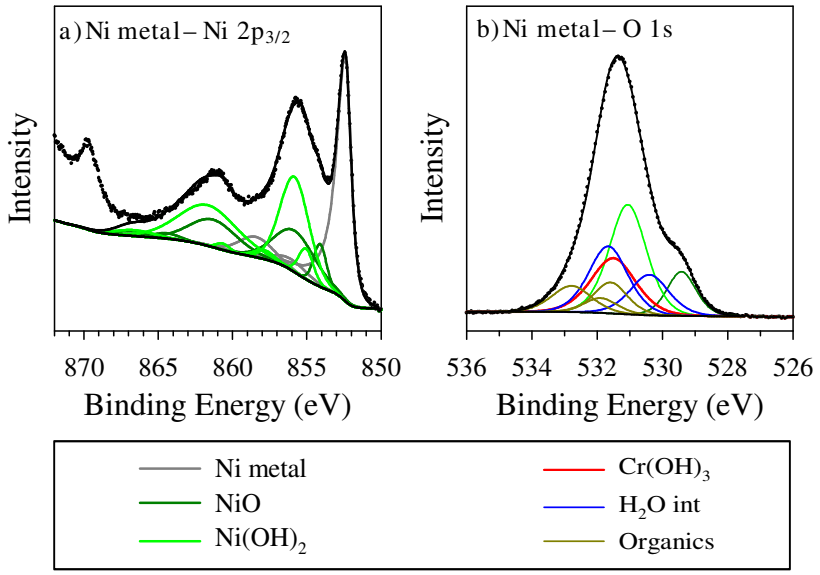

Figure 6.2: The high-resolution (a) Ni $2p_{3/2}$ and (b) O 1s spectra collected following 1 h of surface cleaning of sample Ni-1 at 25°C at a reducing E_{app} = – 1.5 V in a basic solution vs. a Ag/AgCl reference electrode ($pH_{25°C}$ = 10.1).

completeness the intensity for $Cr(OH)_3$ along with a corresponding contribution from interstitial H_2O were included in the O 1s fit. Under these highly reducing conditions, no oxide should have formed on the Ni surface according to the Pourbaix diagram for Ni [21]. However, this thin oxide may be indicative of incomplete reduction of the surface during the reducing conditions, or its rapid reformation during the period where the potential was switched off and the electrode was removed from the solution. Regardless of its origin, this result suggests that we are unable to completely remove oxides in preparation for XPS analysis, using strictly electrochemical methods.

6.3.3 Surface reaction products under mildly oxidizing conditions in basic environments at 25°C

Metallic Ni (Ni-2) and NiCr alloy (NiCr-2) surfaces were exposed to mildly oxidizing conditions of E_{app}= 0.0V vs. an Ag/AgCl electrode at 25°C in basic solution ($pH_{25°C}$ = 10.1) for 48 h. From a comparative surface analysis of these materials in Figure 6.3 and Tables 6.1 and 6.2, the oxides were of similar thickness and were greater than under the reducing condition (2.2 nm). The thickness of the oxide formed on sample Ni-2 was determined to be 5.5 nm using the mixed oxide/hydroxide formula [16]. The presence of the Cr in the alloy seems to have little influence on the oxide produced. Most of the corrosion product was of the β-$Ni(OH)_2$ form, particularly in the case of the NiCr alloy. The Ni species comprised most of the corrosion product: a reflection of the fact that Ni metal in the alloy is predicted in the Pourbaix diagram to be more soluble than Cr under these conditions [21-22], and more prone to formation via dissolution/precipitation.

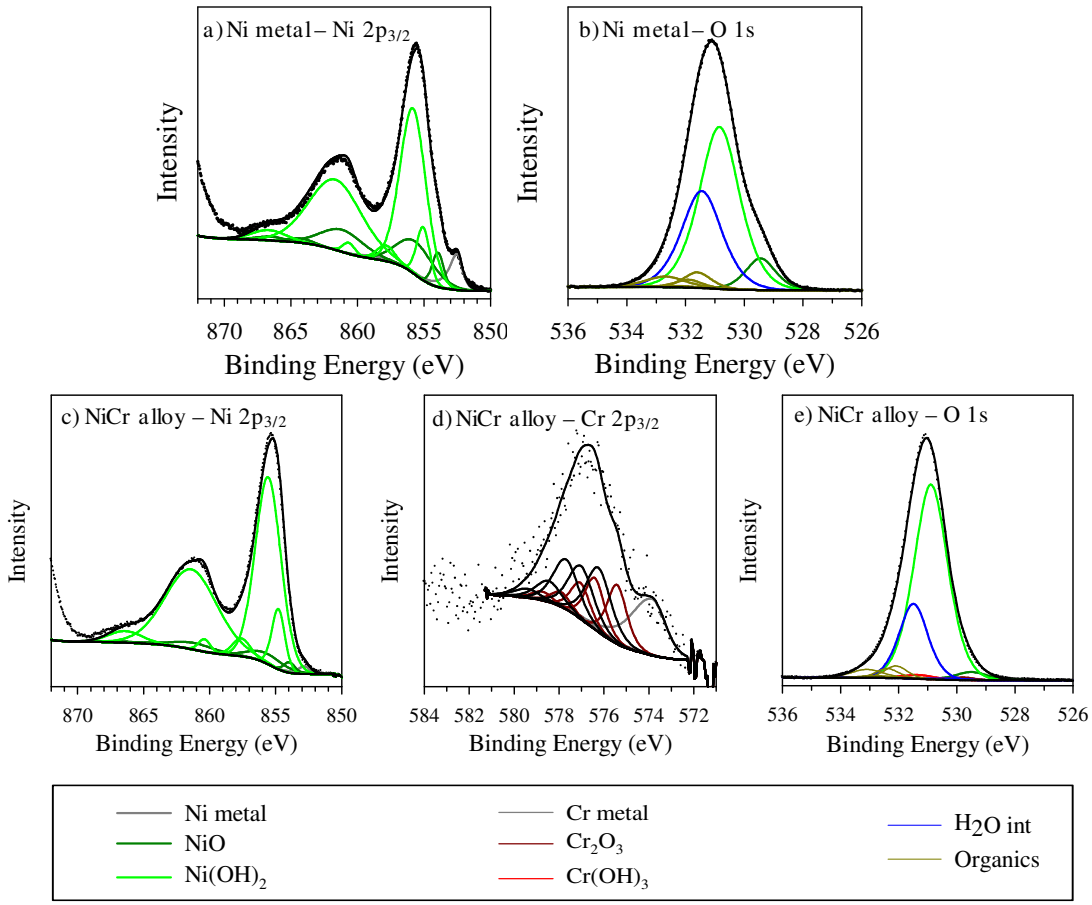

Figure 6.3: The high-resolution (a) Ni $2p_{3/2}$ and (b) O 1s spectra collected for a Ni metal surface following aqueous oxidation at 25°C in a basic solution ($pH_{25°C}$ = 10.1) for 48 h at a slightly oxidizing potential E_{app} = 0.0 V vs. a Ag/AgCl reference electrode. The high-resolution (c) Ni $2p_{3/2}$, (d) Cr $2p_{3/2}$ and (e) O 1s spectra for a NiCr surface oxidized for 48 h under the same temperature, solution and potential conditions.

6.3.4 Surface reaction products under mildly oxidizing conditions in basic environments at 150°C

In this test, an autoclave temperature of 150°C was used with a simulated coolant whose $pH_{150°C}$ was calculated to be 7.8, much lower than its room temperature value of 10.1. Figure 6.4 shows the representative high-resolution spectra for Ni metal (Ni-3) and NiCr samples (NiCr-3) exposed for 3 h periods at constant E_{app} of 0.0 V vs. the Ag/AgCl electrode. The oxide thicknesses in these cases exceeded the information depth available in the XPS experiment (~ 6 nm). The corrosion product composition was primarily β-$Ni(OH)_2$, even on the NiCr surface. Other NiCr alloy samples (NiCr-4 and NiCr-5) were exposed for periods of 24 h and 48h respectively (spectra not shown); the near-surface compositions were virtually identical to the shorter exposure (see Tables 6.1 and 6.2). The distribution of oxidized Ni and Cr was monitored using ToF SIMS on the alloy surface oxidized for 24 h in basic solution. A 200 μm x 200 μm area showing the detected intensities of the NiO_2^- and CrO_2^- negative ion fragments along with the corresponding depth profile are presented in Figure 6.5(a-b). The bright yellow colouration represents areas where the most intense signals were detected, while the black regions indicate locations were no signal was observed. These results show a mostly uniform distribution of Ni and Cr across the 200 μm x 200 μm analysis area (see Figure 6.5(a)) with an enrichment of oxidized Ni species at the very near surface (see Figure 6.5(b)). Thus, consistently at basic pH and 150˚C Ni dissolution and precipitation is the dominant corrosion process.

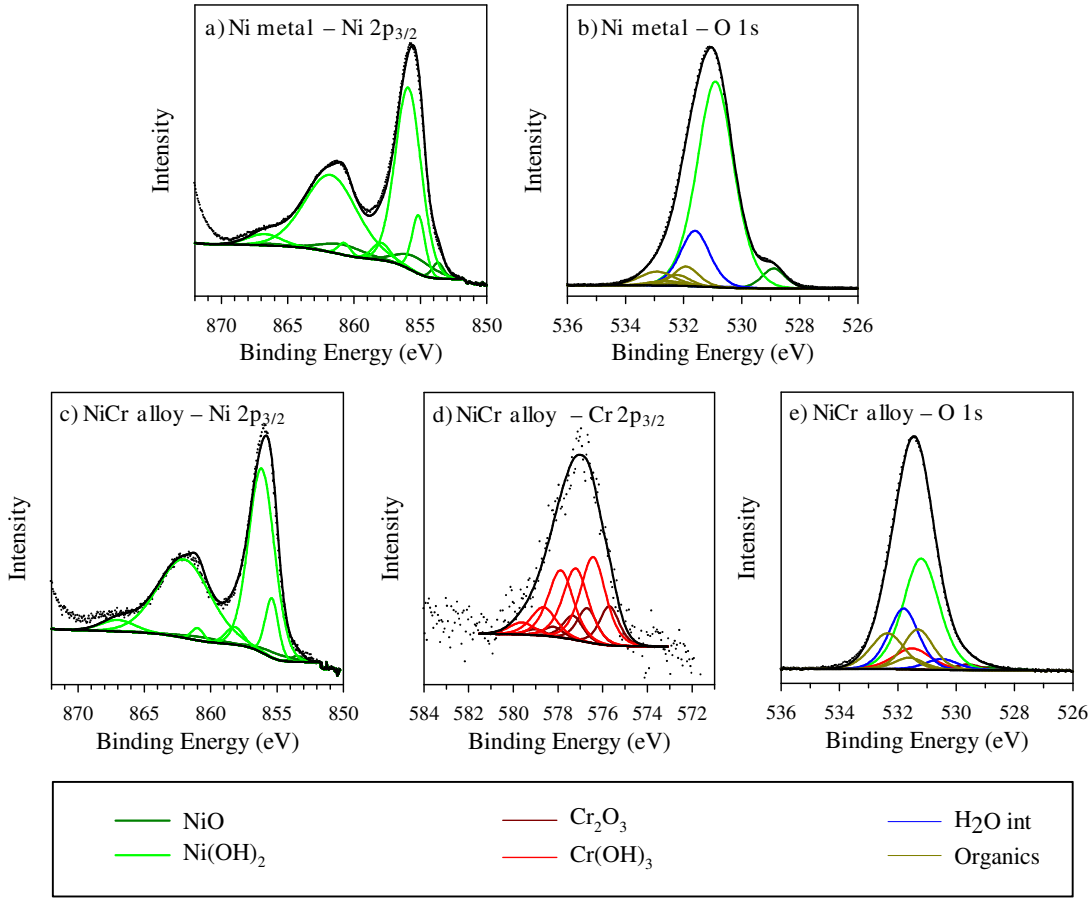

Figure 6.4: The high-resolution (a) Ni $2p_{3/2}$ and (b) O 1s spectra collected for a Ni metal surface following aqueous oxidation at 150°C in a basic solution ($pH_{150°C}$ = 7.8) for 3 h at a slightly oxidizing E_{app} = 0.0 V vs. a Ag/AgCl reference electrode. The high-resolution (c) Ni $2p_{3/2}$, (d) Cr $2p_{3/2}$ and (e) O 1s spectra for a NiCr surface oxidized for 3 h under the same temperature, solution pH and potential conditions.

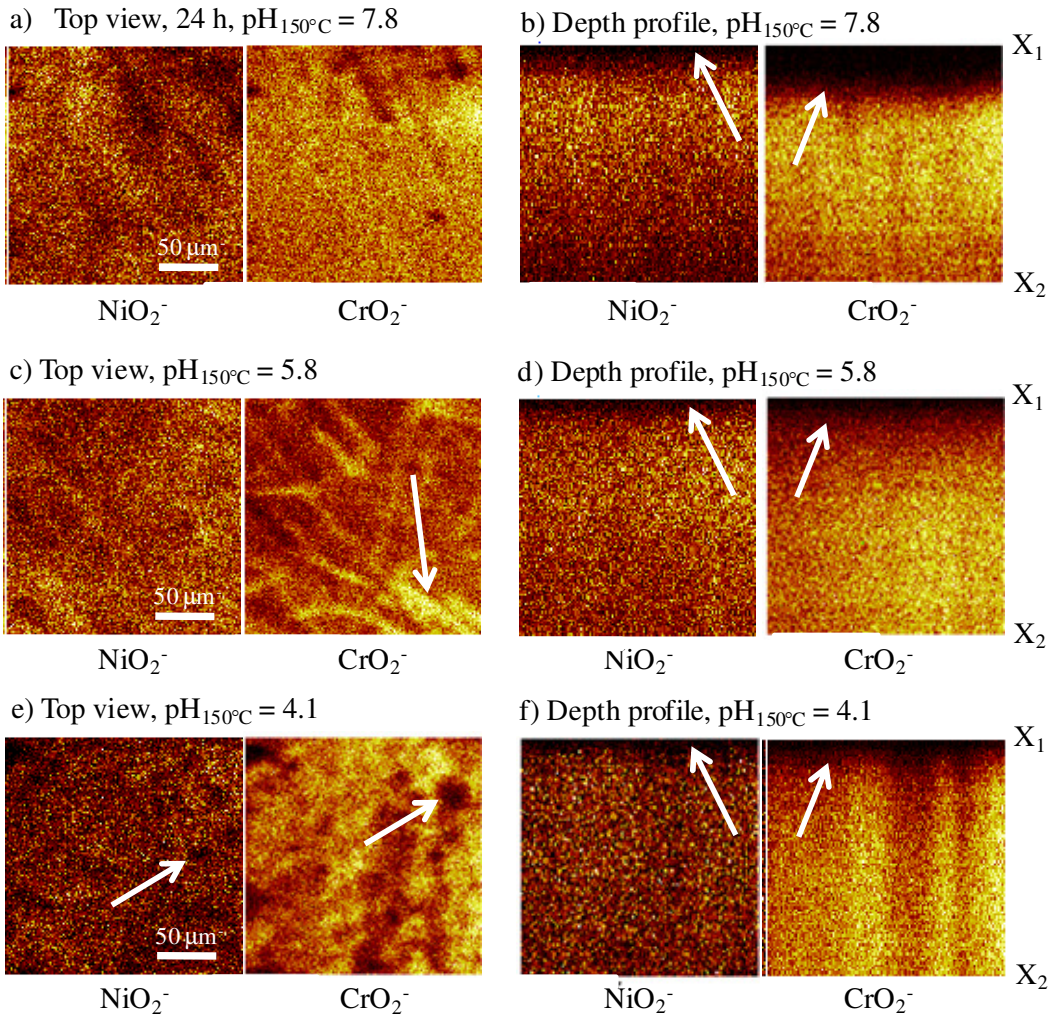

Figure 6.5: The ToF SIMS images mapping the Ni and Cr distribution across a 200 µm x 200 µm area and corresponding depth profiles collected from the NiCr surfaces oxidized for 24 h at 150°C at a mildly oxidizing E_{app} = 0.0 V vs. a Ag/AgCl reference electrode. (a) top view, and (b) depth profile in basic solution, $pH_{150°C}$ = 7.8; (c) top view, and (d) depth profile in neutral solution, $pH_{150°C}$ = 5.8; and (e) top view, and (f) depth profile in acidic solution, $pH_{150°C}$ = 4.1. The yellow areas represent the regions of highest Ni or Cr concentrations, while the black areas indicate the positions where no signal was detected. The solution/oxide (X_1) and oxide/alloy (X_2) interfaces are also marked on the depth profiles.

6.3.5 Possible conductivity issues in the basic solutions

The basic aqueous solutions used in this work were chosen to emulate, as closely as possible, those existing under possible SG chemistry conditions (i.e. alkaline with pH = 10) [12-13]. Accordingly, they were prepared with somewhat low ionic strengths (1 x 10^{-4} M), as this feature allowed us to maximize the probability that oxides would not contain impurities (i.e. supporting electrolyte, buffers, etc), and would most closely resemble those formed during SG operation [12-13]. However, the trade-off with this selection is that it leads to a possible increase to ohmic potential losses between working and reference electrodes, owing to higher solution resistance. As a result, for the basic conditions, we were unable to preselect an exact potential to apply at the electrode surface. This requirement introduces a measure of variability in directly comparing the oxide films grown in the different solutions, since the actual potential at the solution metal interface will differ from the applied potential, but more importantly, among different temperatures, potentials and solutions used in the experiments.

6.3.6 Surface reaction products under mildly oxidizing conditions in neutral environments at 150°C

Using the above temperature and oxidizing conditions, the $pH_{150°C}$ in the simulated coolant was changed to 5.8 (neutral) at temperature (150°C) for exposure times of 3 h (NiCr-6) and 24 h (NiCr-7). Under these solution conditions higher ionic strengths (e.g. > 0.1 M) were used and as a result potential losses due to poor ionic conductivity are believed to be negligible. The near surface corrosion products formed on these samples had significantly higher concentrations of Cr than at $pH_{150°C}$ = 7.8, mostly as $Cr(OH)_3$ (see Tables 6.1and 6.2). As was observed in basic solution the primary Ni containing

corrosion product was β-$Ni(OH)_2$. The high-resolution spectra collected following the 3 h reaction are shown in Figure 6.6. The presence of a Cr^{6+}-containing species under these conditions confirms that the dissolution processes involved both metallic Ni and Cr as predicted thermodynamically via the Pourbaix diagram [20-22]. Furthermore, both dissolved species formed back precipitates as corrosion products on these surfaces. Analysis of the alloy sample oxidized for 24 h using ToF SIMS showed regions enriched with Cr over the rastered area (see Figure 6.5(c)), while there was no clear separation between the Ni and Cr components with depth (see Figure 6.5(d)). The enrichment in Cr may have resulted from a decrease in the local pH (acidic) in these areas creating an environment in which Ni^{2+} species were stable in solution [20-22]. These areas could also represent regions of higher reactivity such as grain boundaries or defect sites, at which Cr oxidation may be more active.

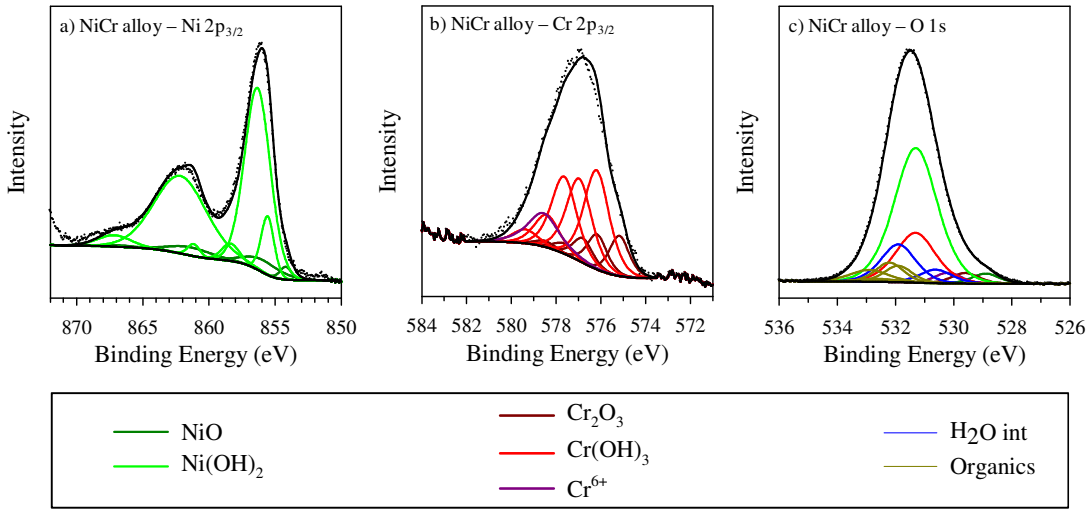

Figure 6.6: The high-resolution (a) Ni $2p_{3/2}$, (b) Cr $2p_{3/2}$ and (c) O 1s spectra collected for a NiCr alloy sample following 3 h of aqueous oxidation at 150°C under a slightly oxidizing E_{app} = 0.0 V vs. a Ag/AgCl reference electrode in a neutral solution ($pH_{150°C}$ = 5.8).

6.3.7 Surface reaction products under mildly oxidizing conditions in acidic environments at 150°C

Representative high-resolution spectra showing the change in surface condition following a 3 h and a 24 h exposure at E_{app} = 0.0V and 150°C in acidic solutions ($pH_{150°C}$ = 4.1) are shown in Figure 6.7. After a 3 h period (NiCr-8) the oxide film was largely dissolved and the thin oxide remnant was composed of almost equal amounts of oxidized Ni and Cr (see Table 6.2). The metal substrate compositions reflected a dissolution process that still favoured Ni, however oxide formation was much slower than the analogous reactions in either basic or neutral solutions at 150°C. Following the 24 h exposure (NiCr-9) a decrease in the metal intensities was observed in both M $2p_{3/2}$ spectra and suggested a slowing of the dissolution processes of both Ni and Cr. The corrosion product produced on this surface was largely $Cr(OH)_3$ with only a small contribution from β-$Ni(OH)_2$.

Analysis of the SIMS data collected from this surface showed areas with little to no oxidized Ni or Cr (see Figure 6.5(e)). Additionally, a clear separation of the oxidized Ni and Cr species was not observed in the corresponding depth profiles (see Figure 6.5(f)). Therefore, over the longer reaction period, the increased stability of Ni^{2+} species in solution resulted in the limited back deposition of β-$Ni(OH)_2$ and led to the formation of a $Cr(OH)_3$-rich thin oxide film [20-22]. The observation of patchiness of the film may also imply that the current was localizing within some regions of the electrode, where the Cr^{3+} species was not located, and that continuing dissolution occurred in other, bare regions.

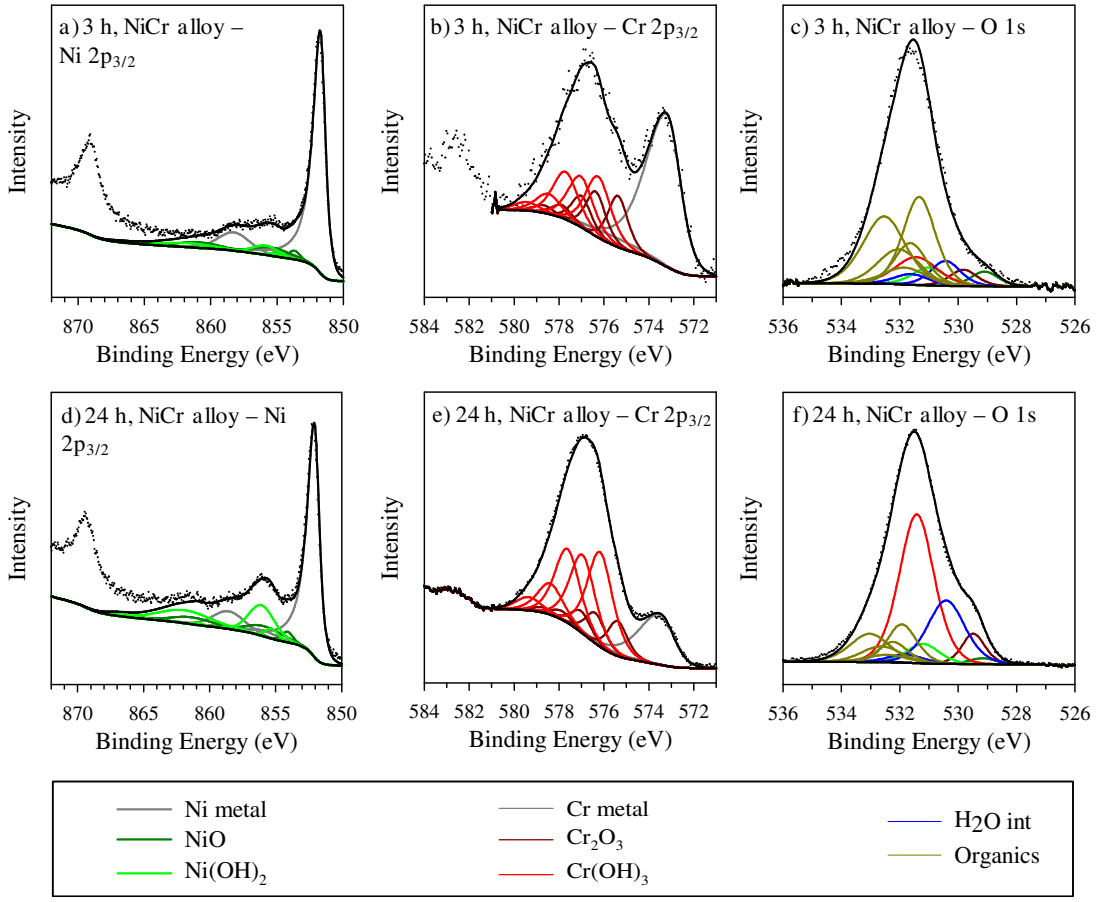

Figure 6.7: The high-resolution (a) Ni $2p_{3/2}$, (b) Cr $2p_{3/2}$ and (c) O 1s spectra collected for NiCr alloy samples following 3 h of aqueous oxidation at 150°C under a slightly oxidizing E_{app} = 0.0 V vs. a Ag/AgCl reference electrode in acidic solution ($pH_{150°C}$ = 4.1). The high-resolution (d) Ni $2p_{3/2}$, (e) Cr $2p_{3/2}$ and (f) O 1s spectra for a NiCr surface oxidized for 24 h under the same temperature, solution pH and potential conditions.

6.3.8 Surface reaction products under highly oxidizing conditions in basic environments at 150°C

A very high oxidation potential of 1.6 V vs. an Ag/AgCl electrode was applied to a metallic Ni (Ni-4) and a NiCr alloy specimen (NiCr-10) in basic solutions ($pH_{150°C}$ = 7.8). Figure 6.8 shows the high-resolution spectra collected after a 3 h exposure for the Ni metal sample and a 48 h reaction for the NiCr sample. Several differences can be seen between these results and those run under mildly oxidizing conditions (see Tables 6.1 and 6.2 and Figure 6.3). The oxide films grown under high oxidizing potentials were thinner, compared to their counterparts grown at milder conditions at this temperature (a thickness of 4.8 nm was calculated for the Ni-4 sample [16]). As well, the oxide grown at high potential on the alloy contained much higher concentrations of Cr, most of which was $Cr(OH)_3$. Thus, there is more rapid and complete dissolution of the metallic Cr phase compared to the mildly oxidizing conditions. Finally, the ratio of NiO/β-$Ni(OH)_2$ in each corrosion product was substantially higher than in the samples produced under milder oxidizing conditions. The higher potentials may be accelerating the dehydration of the film; in any case, it is a parameter that might be useful to diagnose the past chemical history of a corrosion product film.

The dissolution of both Ni and Cr phases are predicted in the Pourbaix diagrams for these materials at highly oxidizing potentials of 1.5 or 1.6 V at 150°C [20-22]. However, because of uncertainty in the actual oxidation potential achieved in our experiments a comparison of applied and predicted results is not very useful in this case. Further, the Ni Pourbaix diagrams predicted the formation of both Ni^{3+} and Ni^{4+} species

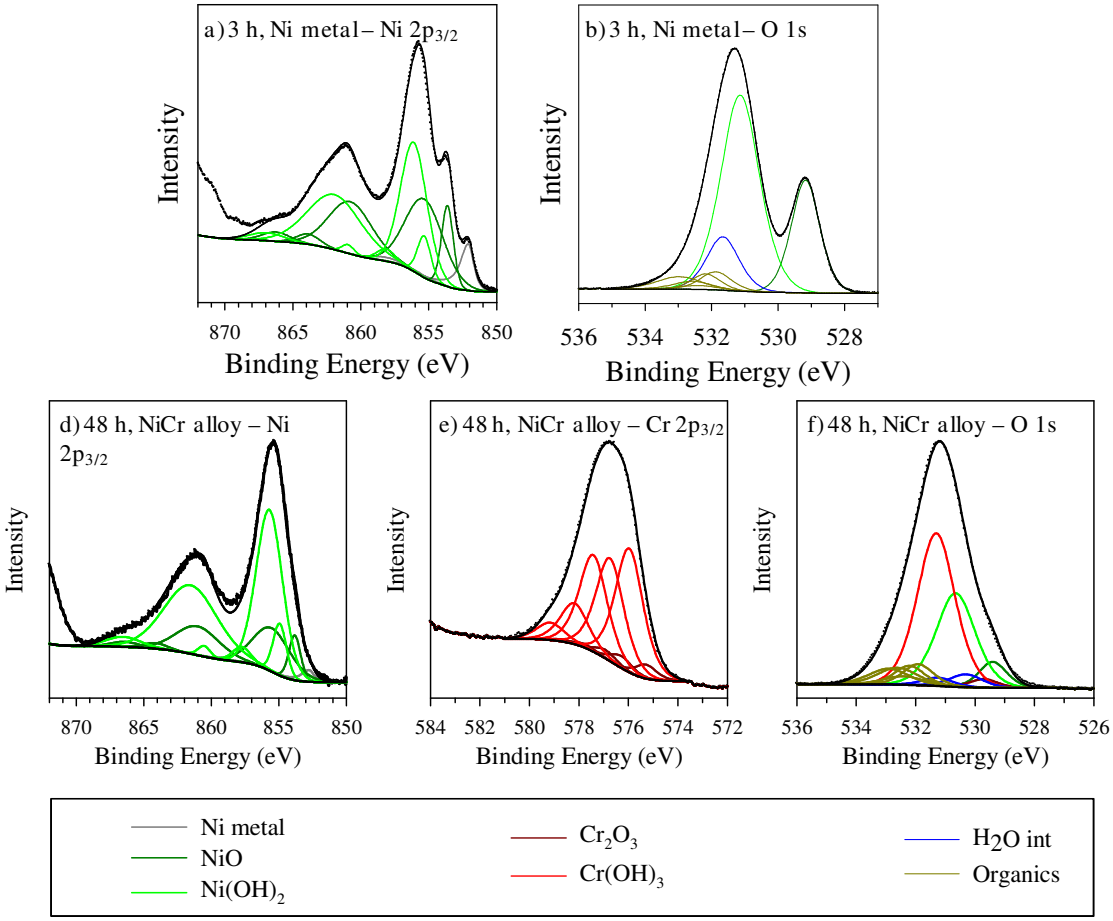

Figure 6.8: The high-resolution (a) Ni $2p_{3/2}$ and (b) O 1s spectra collected for a Ni metal surface following aqueous oxidation for 3 h at 150°C in basic solution ($pH_{150°C}$ = 7.8) at a highly oxidizing potential of 1.5 V vs. a Ag/AgCl reference electrode. The high-resolution (c) Ni $2p_{3/2}$, (d) Cr $2p_{3/2}$ and (e) O 1s spectra for a NiCr surface oxidized for 48 h under the same temperature, solution pH and potential conditions.

at these potentials [21,22]. None were observed in this work, perhaps because of the non achievement of the desired potential or perhaps because they are not formed in any case.

6.3.9 Surface reaction products under highly oxidizing conditions followed by exposure to more mildly oxidizing potential in a basic environment at 150°C

An alloy sample (NiCr-11) was oxidized at 150°C in a basic solution ($pH_{150°C}$ = 7.8) for 3 h at a highly oxidizing potential of E_{app} = 1.5 V vs. a Ag/AgCl electrode followed by 3 h at a milder potential of E_{app} = 0.0 V vs. the same electrode. The reaction produced a Ni-containing corrosion product having a similar NiO:β-$Ni(OH)_2$ ratio to the alloy sample exposed to a constant highly oxidizing potential of E_{app} = 1.6 V for 48 h at the same temperature (see Tables 6.1and 6.2). An increase in the Cr_2O_3:$Cr(OH)_3$ ratio was also observed following the 6 h reaction compared to the 48 h oxidation at the constant highly oxidizing potential. The presence of a small amount of Cr^{6+} on this surface after the 6 h exposure indicated that some Cr dissolution had occurred. These results showed that the effects of the highly oxidizing condition were not removed following a return to more mildly oxidizing potentials.

6.4 Conclusions

Exposure of Ni metal and NiCr alloy surfaces to highly reducing or mildly oxidizing conditions in basic solutions resulted in the preferential growth of a β-$Ni(OH)_2$ film at either 25° and 150°C. This oxidative process was believed to occur via the dissolution of metallic Ni followed by the deposition of β-$Ni(OH)_2$; with the thickest films being observed following reactions at the elevated temperature. The presence of β-$Ni(OH)_2$, $Cr(OH)_3$ and Cr^{6+} on the NiCr surfaces subjected to mildly oxidizing conditions

in neutral solutions at 150°C suggested the dissolution of both metallic Ni and Cr, followed by back precipitation of the corresponding corrosion products was responsible for oxide formation under these conditions. Very thin Cr-rich films containing varying amounts of $Cr(OH)_3$ were observed following alloy exposures to mildly oxidizing potentials in acidic solutions at 150°C. This indicated a dissolution/deposition mechanism for Cr oxidation in acidic solution. Small amounts of β-$Ni(OH)_2$ were also observed on these specimens suggesting that deposition of a Ni corrosion product had occurred, even under these pH conditions.

The films formed at 150°C under highly oxidizing potentials on both a Ni metal and NiCr alloy surface in basic solutions were found to be thinner and contained higher levels of NiO compared to the analogous reactions carried out at slightly oxidizing potentials. The higher NiO content of these films was attributed to an accelerated dehydration of the β-$Ni(OH)_2$ phase. In the case of the alloy surface an increase in the $Cr(OH)_3$ content was also observed following reaction at the higher potential and was ascribed to a more rapid and complete dissolution of the metallic Cr phase compared to the mildly oxidizing conditions. Finally, exposure to a highly oxidizing potential followed by a return to less oxidizing conditions had little effect on the composition of the corrosion products produced.

6.5 References

[1] L. Liu, Y. Li, F. Wang, Electrochim. Acta 52 (2007) 2392.

[2] R.S. Dutta, A. Lobo, R. Purandare, S.K. Kulkarni, G.K. Dey, Metall. Mater. Trans. A, 33A (2002) 1437.

[3] Y.Y. Andreev, E.A. Skryleva, I.A. Safonov, Prot. Met. Phys. Chem. S. 45 (2009) 181.

[4] M. Lampimäki, K. Lahtonen, P. Jussila, M. Hirsimäki, M. Valden, J. Electron Spectrosc. Relat. Phenom. 154 (2007) 69.

[5] S.E. Ziemniak, M. Hanson, Corros. Sci., 48 (2006) 498.

[6] R.S. Dutta, Jagannath, G.K. Dey, P.K. De, Corros. Sci., 48 (2006) 2711.

[7] B.A. Kobe, S. Ramamurthy, M.C. Biesinger, N.S. McIntyre, A.M. Brennenstühl, Surf. Interface Anal., 37 (2005) 478.

[8] A. Machet, A. Galtayries, S. Zanna, L. Klein, V. Maurice, P. Jolivet, M. Foucault, P. Combrade, P. Scott, P. Marcus, Electrochim. Acta 49 (2004) 3957.

[9] A. Machet, A. Galtayries, P. Marcus, P. Combrade, P. Jolivet, P. Scott, Surf. Interface Anal. 34 (2002) 197.

[10] J.T. Francis, N.S. McIntyre, R.D. Davidson, S. Ramamurthy, A.M. Brennenstühl, A. McBride, A. Roberts, Surf. Interface Anal., 33 (2002) 29.

[11] A. Rossi, B. Elsener, G. Hähner, M. Textor, N.D. Spencer, Surf. Interface Anal., 29 (2000) 460.

[12] N.S. McIntyre, R.D. Davidson, T.L. Walzak, A.M. Brennenstühl, F. Gonzalez, S. Corazza, Corros. Sci. 37 (1995) 1059.

[13] N.S. McIntyre, D.G. Zetaruk, D.Owen, J. Electrochem. Soc., Electrochm. Soc. 126 (1979) 750.

[14] B.P. Payne, A.P. Grosvenor, M.C. Biesinger, B.A. Kobe, N.S. McIntyre, Surf. Interface Anal. 39 (2007) 582.

[15] B.P. Payne, M.C. Biesinger, N.S. McIntyre, J. Electron Spectrosc. Relat. Phenom. 175 (2009) 55.

[16] M.C. Biesinger, B.P. Payne, L.W.M. Lau, A.R. Gerson, R.St.C. Smart, Surf. Interface Anal. 41 (2009) 324.

[17] M.C. Biesinger, B.P. Payne, A.P. Grosvenor, L.W.M. Lau, A.R. Gerson, R.St.C. Smart, Appl. Sur. Sci. 257 (2011) 2717.

[18] B.P. Payne, M.C. Biesinger, N.S. McIntyre, J. Electron Spectrosc. 184 (2011) 29.

[19] B.P. Payne, M.C. Biesinger, N.S. McIntyre, J. Electron Spectrosc. Submitted.

[20] B. Beverskog, I. Puigdomenech, Corros. Sci. 39 (1997) 43.

[21] B. Beverskog, I. Puigdomenech, Corros. Sci. 39 (1997) 969.

[22] B. Beverskog, I. Puigdomenech, Corros. Sci. 55 (1999) 1077.

[23] P. Jakupi, J.J. Noël, D.W. Shoesmith, Electrochem. Solid S., 13 (2010) C1.

[24] P. Jakupi, F. Wang, J.J. Noël, D.W. Shoesmith, Corros. Sci., (2011) doi: 10.1016/j.corsci.2011.01.028.

[25] E. Protopopoff, P. Marcus, in: S.D. Cramer, B.S Corvino Jr. (Eds.), Corrosion: Fundamentals, Testing, and Protection, Vol 13A, ASM Handbook, ASM International, (2003), p 17–30.

[26] S.J. Hawkes, J. Chem. Edu. 72 (1995) 799.

[27] D. Johnson, CoreWare for Windows, Version 3.2, Scribner Associates Inc. 1990-2010.

[28] N. Fairley, CasaXPS Version 2.2.15, 1999-2009.

[29] G. Beamson, D. Briggs, in: High-resolution XPS of Organic Polymers The Scienta ESCA300 Database, John Wiley and Sons, Toronto, 1992 (Appendices 1 – 3).

[30] T.A. Carlson, G.E. McGuire, J. Electron Spectrosc. Relat. Phenom. 1 (1972/1973) 161.

[31] B.R. Strohmeier, Surf. Interface Anal. 15 (1990) 51.

[32] NIST Electron Inelastic Mean Free Path Database (Version 1.1)©, U.S. Secretary of Commerce, 2000.

[33] Ion-ToF (GmbH), IONSPEC, Version 3.14.9, Ion-ToF, Münster, Germany, 1995-2000.

[34] S.V. Kagwade, C.R. Clayton, G.P. Halada, Surf. Interface Anal., 31 (2001) 442.

Chapter 7 Summary and Conclusions

7.1 General Summary

In Chapter 2 the composition and structure of the oxides formed on polycrystalline Ni metal surfaces following exposure to low pressures of ultra pure O_2 gas at both 25°C and 300°C were studied using XPS and ToF SIMS. Several Ni surfaces were subjected to doses of O_2 gas in the range of $10^7 – 10^9$ Langmuirs (L) and changes in film composition with both time and temperature were monitored.

Reactions of polycrystalline and single crystal (100) Ni metal surfaces with O_2 gas produced thin films composed predominantly of NiO (Ni^{2+}-containing) at both 25°C and 300°C . Smaller contributions from a Ni^{3+}-containing oxide were also observed in the Ni $2p_{3/2}$ spectra for all samples oxidized at 25°C, as well as following the shortest exposures at 300°C. This Ni^{3+} component was only observed at the very near surface and thought to be created during the initial stages of the reaction. Contributions from Ni^{3+} were not observed after the longest exposures at 300°C suggesting this species did not play as large a role in film growth over these periods at this temperature.

Using QUASES™-based algorithms [1-2] it was determined that oxide formation at both 25°C and 300°C proceeded via island growth on a nanometric scale. The thickest films were observed following the longest reactions at 300˚C. Modeling of the reaction kinetics showed a parabolic pathway at the elevated temperature, while a direct logarithmic mechanism was observed under ambient conditions.

The oxide growth rate on polycrystalline Ni surfaces was found to be almost four times faster than the analogous reaction on a single crystal (100) sample; attributed to the presence of grain boundaries on the polycrystalline specimens. There was no evidence to

indicate differential oxide growth based on grain orientation had occurred at 300°C using micro-XPS analysis, while some grain-specific oxidation was detected at 25°C using a combination of XPS and ToF SIMS imaging. Additionally, exposure of polycrystalline samples to multiple sputtering/annealing cycles produced highly twinned surfaces, thus reducing the number of high-angle boundaries available for cation transport, leading to a significant reduction in observed rate of oxide formation.

Chapter 3 presented an XPS and ToF SIMS study of the oxidation of polycrystalline Ni metal surfaces exposed to low pressures of H_2O vapour for doses in the range of 10^9 – 10^{10} L at 25°C and 300°C. The changes in film composition and structure as a function of dose and temperature were monitored and a possible mechanism for oxide formation was proposed.

Analyses of the Ni $2p_{3/2}$ spectra collected from Ni metal surfaces exposed to H_2O vapour at 300°C showed the formation of thin defective NiO films containing varying amounts of Ni^{2+} and Ni^{3+}. Peaks corresponding to lattice O^{2-} (bound to Ni^{2+}) and O (def) atoms (bound to Ni^{3+}) were assigned in the accompanying O 1s spectra. Contributions from organic contamination determined from the analysis of the C 1s spectra were also included in the fitting of the O 1s envelopes. As a result, there was no spectral evidence to support the presence of H_2O (ads) or OH (ads) on any of the oxidized Ni surfaces at 300°C.

In Chapter 2 the O (def) component was attributed to O (ads) atoms, but was reassigned here as the same species was observed in the O 1s spectra for a number of well characterized NiO powder samples. When the combined atomic concentrations of the O^{2-} and O (def) components were compared to the normalized Ni^{2+} intensities for the

powder samples O/Ni ratios of close to 1 were obtained. Similar ratios were obtained when the normalized concentrations of the O^{2-} and O (def) components were compared to the Ni^{2+} and Ni^{3+} intensities obtained for the Ni surfaces exposed to H_2O vapour. These results suggested that the oxides formed following exposures to H_2O vapour at 300°C were similar in structure to the powder NiO specimens. A re-examination of the data collected from the Ni surfaces exposed to extended doses of O_2 gas using the O 1s peak assignments presented in Appendix A also produced O/Ni ratios of close to 1. Other authors have presented similar assignments for defective NiO species as well [3-7]. Additional comments on the XPS spectra collected for powder NiO samples were discussed in Chapter 5.

Analysis using QUASES™ showed oxidation proceeded through island oxide growth following reaction to H_2O vapour at 300°C. The films formed on these surfaces were found to be much thinner when compared to similar doses of O_2. Modeling of the reaction kinetics showed that oxide growth following exposure to H_2O vapour was best described by a direct logarithmic mechanism. Conversely, a parabolic relationship with dose was observed for metal reactions with O_2 gas at 300°C. The initial nucleation of oxide was also found to occur almost four times slower after exposure to the vapour when compared to the onset of oxide growth following doses of the pure O_2 gas at 300°C.

The reaction of a Ni metal sample with H_2O vapour following a dose in the range of 10^9 L at 25°C showed no detectable amounts of oxide formation. As was observed following reaction at 300°C there was no O 1s spectral evidence to support the presence of H_2O (ads) following vapour exposure at this temperature. However, a small amount of OH (ads) species was detected on this surface.

Using the results obtained from both the 25° and 300°C exposures the following reaction mechanism was proposed. Reactant H_2O molecules quickly decomposed into OH (ads) and H (ads) on metallic Ni surfaces at both 25° and 300°C. This was followed by the slow place exchange of OH (ads) with metallic Ni and subsequent loss of H. This process is believed to be the rate determining step. Some of the H produced at the surface may become trapped in Ni vacancies and retard the migration of such vacancies, slowing the oxidation rate even further. The presence of H (using high-purity deuterium) was verified in the near surface region of a thin oxide formed following exposure to H_2O vapour at 300°C using ToF SIMS. Finally, the OH (ads) is only stabilized on metallic Ni and once these sites became unavailable for reactant H_2O molecules the reaction was terminated.

To this point the reactions on Ni metal surfaces following exposure to gas phase O_2 and H_2O vapour had been extensively studied. In Chapter 4 several Cr-O systems were investigated yielding additional interpretations of the Cr $2p_{3/2}$ line shapes for both Cr_2O_3 and $Cr(OH)_3$, as well as providing more details for the oxidation mechanisms occurring on Cr metal surfaces exposed to either O_2 gas or H_2O vapour.

The Cr $2p_{3/2}$ spectra collected for samples of a polycrystalline Cr_2O_3 powder were found to be very similar to the Gupta and Sen predicted line shape for the free Cr^{3+} [8-9]. The narrowest Cr $2p_{3/2}$ multiplet structures were obtained following annealing of vacuum fractured Cr_2O_3 aggregate specimens to 550°C. Other authors have shown that heating polycrystalline Cr_2O_3 surfaces near the temperatures applied here resulted in a conversion the crystal structure to the low energy (0001) orientation [10-11]. Similar reorganizations are believed to have occurred on the fractured and annealed surfaces analyzed here. The

broadening of the Cr $2p_{3/2}$ spectra collected for the polycrystalline samples was proposed to be the result of a small difference in BE between the Cr^{3+} atoms situated in the (0001) orientation and those oriented in the other major crystallographic directions.

Comparison of the atomic concentrations for the lattice O^{2-} and Cr^{3+} components for all Cr_2O_3 samples produced O/Cr ratios between 1.5 and 1.6. Based on these results there was no evidence to suggest the presence of a O (def) species as was observed for NiO. Similarly, the observed O/Cr ratios indicated that significant amounts of $Cr(OH)_3$ were not present on the polycrystalline Cr_2O_3 specimens and therefore were not responsible for the observed signal broadening of these samples. Additionally, the Cr $2p_{3/2}$ line shape and O/Cr ratio derived for a polycrystalline powder sample was used to remove the Cr_2O_3 contribution from the Cr $2p_{3/2}$ spectrum collected for a powder sample containing both Cr_2O_3 and $Cr(OH)_3$. From the remaining spectral intensity a possible Cr $2p_{3/2}$ line shape for $Cr(OH)_3$ was modeled.

Reactions of Cr metal surfaces with either gas phase O_2 or H_2O vapour at 300°C produced thin Cr^{3+} deficient films composed primarily of Cr_2O_3 along with varying contributions from a hypo-stoichiometric Cr component. The absence of model spectra did not allow for the exact chemical nature of this sub-stoichiometric oxide to be identified here. It is believed that this species was formed during the initial stages of oxidation and is analogous to the creation of Ni^{3+} on metallic Ni surfaces. In addition, the exposure of Cr metal surfaces to doses of H_2O vapour did not produce any evidence for the formation of $Cr(OH)_3$. In contrast, reaction of a NiCr alloy surface in an aqueous environment resulted in the growth of an oxide film containing contributions from both

Cr_2O_3 and $Cr(OH)_3$. There was no evidence to support the formation of a hypo-stoichiometric Cr oxide under these conditions.

The XPS spectra of a number of powder samples of NiO, β-$Ni(OH)_2$, γ-NiOOH and $NiCr_2O_4$ were examined in Chapter 5. The Ni and Cr $2p_{3/2}$ spectra for these compounds were extensively studied previously [12-14]. This work focused on separating the different O 1s intensities for lattice O^{2-}, O (def) and OH^- species from other surface components such as interstitially situated H_2O molecules and adsorbed organic contaminants. The atomic O/Ni ratios were calculated for all Ni-containing oxides using the corrected O 1s intensities for the lattice components only and were found to correspond well with the expected values for the respective compounds.

All NiO samples studied showed contributions for both lattice O^{2-} and O (def) species in the O 1s spectra; NiO was the only compound found to exhibit this defective structure. Inspection of the O/Ni ratios calculated for certain β-$Ni(OH)_2$ powders as well as for the γ-NiOOH compound indicated some sample decomposition had occurred. In addition contributions from interstitially positioned H_2O molecules were observed in the O 1s spectra for one β-$Ni(OH)_2$ and both $NiCr_2O_4$ samples. The O/Ni ratios obtained for these powder samples were then used to verify the Ni $2p_{3/2}$ assignments of mixed oxide phases formed on Ni metal and NiCr alloy surfaces following aqueous exposures in basic solutions at highly oxidizing potentials.

Chapter 6 presented an XPS and ToF SIMS study of the oxidation of Ni metal and NiCr surfaces in aqueous solutions at controlled electrochemical potentials and temperatures of 25° and 150°C. The aqueous environments were chosen to emulate possible solution conditions in the SG tubing of pressurized water reactors.

Oxide formation on metallic Ni and alloy surfaces in basic solutions under highly reducing or mildly oxidizing potentials was found to occur via the dissolution of Ni metal followed by the back deposition of β-$Ni(OH)_2$ at both 25° and 150°C. The presence of Cr in the alloy appeared to have little effect on the oxide produced, particularly at 25°C. Dissolution of Ni and Cr metal species followed by the deposition of β-$Ni(OH)_2$ and $Cr(OH)_3$ was determined to be responsible for film growth on NiCr samples exposed to neutral solutions under mildly oxidizing potentials at 150°C. In acidic solutions a much slower rate of oxide formation was observed. Under these conditions both metallic Ni and Cr species were dissolving, however the increased solubility of the Ni^{2+} corrosion product at acidic pH [15-16] limited the amount of β-$Ni(OH)_2$ deposited, leading to the growth of a $Cr(OH)_3$-rich film with increasing exposure time.

7.2 Impact of work

The work outlined in this thesis has shown that "defective" oxide films are formed on polycrystalline Ni and Cr metal surfaces during the initial stages of reaction with either O_2 gas or H_2O vapour. These "defect" structures were particularly prevalent following gas/vapour doses of up to 10^{10} L. The results presented in this thesis show that XPS provides an extremely reliable and effective means of examining the changes in oxide film chemistry following the formation of the first 0-15 monolayers of oxide on both polycrystalline Ni and Cr metal surfaces.

As discussed in the Introduction the surface sensitivity of XPS makes this technique the perfect tool to analyze the thin films formed on polycrystalline Ni metal surfaces following exposure to O_2 gas and H_2O vapour. The thickest oxides studied here were on the range of 4.5 nm. Using QUASES™-based algorithms it was determined that

oxide formation following exposure to O_2 gas and H_2O vapour resulted in "island" oxide growth on a nanometric scale (see Chapters 2 and 3). Attempts were made to verify the QUASES™ results, however the thin nature (< 5 nm) as well as the nanometer dimensions of the oxide "islands" formed did not allow for any structural information to be obtained using other surface sensitive techniques such as Scanning Electron Microscopy (SEM) and ToF SIMS. Typically, SEM cannot provide usable images of surfaces having films thinner than approximately 10 nm, due to the IMFPs of the excited secondary electrons. ToF SIMS is another extremely surface sensitive technique able to provide topographical and limited compositional information in the form of depth profiles and secondary ion images. However, the films formed following exposure to O_2 gas and H_2O vapour were composed primarily of NiO, with small contributions from a Ni^{3+}-containing oxide. Even though ToF SIMS has a much lower detection limit than XPS it cannot provide accurate chemical state analysis. ToF SIMS imaging can resolve surface structures separated by distances of 1-2 μm. Imaging of an oxidized polycrystalline Ni metal surface exposed to O_2 gas following a 6.0×10^8 L dose of O_2 at 25ºC did not show any "island" oxide growth. Thus it appears the most accurate way to monitor thin film growth is with XPS and modeling routines such as QUASES™.

Evidence for the presence of a "defective" Ni^{3+}-containing oxide in the films formed on polycrystalline Ni metal surfaces was observed following reaction with O_2 gas at 25ºC, after shorter exposures (1.0×10^7 – 2.4×10^8 L) at 300ºC, as well as on all surfaces dosed with H_2O vapour at 300ºC (see Chapters 2 and 3). In all cases the Ni $2p_{3/2}$ spectra were dominated by intense metallic Ni signals, which were removed using spectral subtraction. The resultant line shapes and peak positions of the metal subtracted

Ni $2p_{3/2}$ spectra were found to be very similar to that of NiO, however the characteristic doublet structure of NiO was obscured by the presence of an additional Ni species near 856 eV. Subsequent removal of the NiO contribution produced spectra having mainline peak shapes and positions similar to that of NiOOH, a Ni^{3+}-containing compound. The intensity of the "defective" oxide component was found to diminish with increasing O_2 exposure at 300ºC. It is believed that some Ni^{3+} is still present following these longer doses at the elevated temperature, however because significantly more non-defective NiO (Ni^{2+}-containing) was formed, the signal from Ni^{3+} could not be resolved (i.e. below the detection limit of 0.1 – 0.3 at.%). In addition, the observed decrease in the Ni^{3+}/Ni^{2+} ratio also indicated a change in the oxidation mechanism (i.e. logarithmic to parabolic growth) had occurred sometime between the 2.4×10^8 and 1.2×10^9 L of exposure at 300ºC.

Spectral subtraction techniques were also used to show that "defective" oxide films were formed following the exposure of polycrystalline Cr metal surfaces to either O_2 gas or H_2O vapour (see Chapter 4). Removal of the metallic Cr signal from all Cr $2p_{3/2}$ envelopes produced subtracted spectra having line shapes and positions similar to that of powder polycrystalline Cr_2O_3. In all cases the line shapes of the oxidized Cr components were broadened at lower BEs and this was ascribed to the formation of a hypo-stoichiometric oxide. The exact nature of this "defective" oxide could not be determined as part of this work as a suitable reference spectrum was not available. However it was clear that the observed broadening could not be attributed to the formation of $Cr(OH)_3$ or to differential surface charging. The presence of $Cr(OH)_3$ was eliminated as the observed BE shift for the "defective" component was found to be well below that expected for Cr^{3+} species bound to OH^-. Spectral broadening resulting from

differential charging was also discounted based on the thin nature of the films formed and the proximity of the metal substrate. In addition, if surface charging was an issue similar broadening of the respective O 1s and C 1s spectral lines would also be expected, however no such phenomenon was observed.

The work presented in this thesis also exploited the elemental and chemical state sensitivities of XPS to analyze the chemistry of the oxides formed on both polycrystalline Ni and Cr metal surfaces through rigorous modeling of the O 1s and M $2p_{3/2}$ line shapes (see Chapters 2-5). Of particular interest was differentiating between the O 1s peak intensities attributed to O species bound within a regular oxide, hydroxide and/or oxyhydroxide crystal from those adsorbed on the surface. The validity of the O 1s peak assignments were verified by comparing the O/M atomic ratios calculated for all oxidized surfaces with the ratios obtained for well characterized polycrystalline Ni- and Cr-containing oxide, hydroxide and oxyhydroxide powder samples.

The mechanism for polycrystalline Ni metal oxidation following exposure to doses of H_2O vapour was studied using O/Ni atomic ratios at 300ºC and a pressure of 1 Torr (see Chapter 3). The rate of the Ni-H_2O reaction was found to be much slower than the Ni-O_2 system under the same temperature and pressure conditions (see Chapter 2). The difference in the reaction rates was attributed to the formation of an OH (ads) intermediate following H_2O exposures, while the reaction of Ni with O_2 proceeded through an O (ads) surface species. In addition, it appeared that H_2O desorption was competing with H_2O dissociation reactions on the oxidized Ni metal surfaces.

The line shapes and positions of the oxidized portions of all Ni $2p_{3/2}$ and O 1s spectra collected from polycrystalline Ni surfaces exposed to H_2O vapour indicated that

the films formed were composed primarily of NiO, with smaller contributions from "defective" oxide components. The O/Ni ratios were calculated using the combined atomic concentrations of two O 1s components attributed to O^{2-} and O (def) species near 529.4 eV and 531.0 eV respectively. The remainder of the O 1s intensities for the oxidized surfaces were completely fit with contributions from organic contamination. Based on the observed O/Ni atomic ratios it was determined that significant levels of OH (ads) and H_2O (ads) species were not present on polycrystalline Ni metal surfaces exposed to H_2O vapour at 300ºC. Fitting of the O 1s spectrum collected following a 3.0 x 10^9 L dose at 25ºC however, did indicate that a small amount of OH (ads) was formed under these conditions. These results suggested that OH (ads) is not well stabilized on oxidized Ni surfaces at 300ºC nor is it as reactive as the analogous O (ads) intermediate species formed during reaction of Ni metal surfaces with O_2 gas at either 25ºC or 300ºC. The latter conclusion is based on the fact that films in the range of 1 nm were formed on polycrystalline Ni metal surfaces exposed to doses of 3.0 x 10^9 L of O_2 gas at 25ºC. The presence of OH (ads) even after a 3.0 x 10^9 L exposure at 25ºC also indicated that the loss of H is a slow process and is the rate determining step of the Ni-H_2O reaction. The absence of any $Ni(OH)_2$ formation also suggested that loss of H occurred prior to incorporation of O into the oxide lattice. The lack of evidence for H_2O suggests that desorption reactions are competing with dissociation at both 25ºC and 300ºC.

Atomic O/Cr ratios were also used to follow the reaction of polycrystalline Cr metal surfaces with both O_2 gas and H_2O vapour at 300ºC and 1 Torr. Fitting of the Cr $2p_{3/2}$ and O 1s spectra showed that Cr deficient oxide films composed primarily of Cr_2O_3 with smaller contributions from a hypo-stoichiometric component were formed. An

additional O species was observed near 531.7 eV in the O 1s spectra collected from all oxidized Cr surfaces exposed to O_2 gas and H_2O vapour. Based on the calculated O/Cr atomic ratios this O component did not represent a "defective" species (as seen for NiO), nor did it arise from the formation of $Cr(OH)_3$. From these results it appeared that adsorbed intermediate O species are stabilized on oxidized Cr surfaces even at 300ºC. At this time it is unclear if this O 1s component represents O (ads), OH (ads) or interstitial H_2O. However, the mere presence of intermediate species may explain why the films formed on polycrystalline Cr metal surfaces exposed to H_2O vapour were found to be much thicker than those grown on polycrystalline Ni metal samples exposed to similar doses of vapour.

In contrast to the gas phase exposures of O_2 and H_2O discussed above the oxidation of polycrystalline Ni metal and NiCr alloy surfaces in aqueous media produced corrosion products composed primarily of $Ni(OH)_2$, with only small contributions from NiO detected under most conditions. Using O/Ni ratios it was determined that the "defective" oxide structures associated with NiO formation following the gas phase oxidation of polycrystalline Ni metal surfaces were not observed following aqueous reactions on either the pure metal or the alloy. This suggested that NiO formation had occurred via the dehydration of $Ni(OH)_2$. Analysis of the oxidized Cr portions (where present) of the films formed on the alloy surfaces indicated that both $Cr(OH)_3$ and Cr_2O_3 were present. Again, the lack of evidence for a Cr deficient oxide component suggested that Cr_2O_3 formation occurred through the dehydration of $Cr(OH)_3$. It also appeared that interstitial H_2O molecules associated with both $Ni(OH)_2$ and $Cr(OH)_3$ were present on all surfaces.

In this work a number of XPS derived O/M atomic ratios were calculated for a collection of well characterized Ni- and Cr-containing oxide, hydroxide and oxyhyroxide powders (see Chapters 3 and 5). The ratios obtained from this work were then used to model the near surface compositions of the thin films formed on polycrystalline Ni, Cr and NiCr (20%) alloy surfaces. By applying these ratios to our surface analysis we were able to separate the contributions from overlapping oxidation products and adsorbed intermediate species formed on metallic Ni, Cr and NiCr alloy surfaces (see Chapters 3-6 and Appendix A). The use of O/Ni ratios was particularly important in monitoring the mechanism of oxide formation on Ni metal surfaces exposed to H_2O vapour. The analysis of a number of NiO powders showed that a "defective" O species was present in the O 1s spectra near 531.0 eV. This higher BE species was found to be unique to NiO. Initially the "defective" component was attributed solely to O atoms adjacent to a Ni vacancy (or bound to Ni^{3+}). However, this assignment would require O/Ni ratios of more than 1 to be observed as the powder samples would be highly Ni deficient. More recently it is believed that this higher BE component arises from the incorporation of H into the structure in the form of a hydride. A similar assignment was suggested previously by Norton et al [3]. This latter designation is more reasonable based on the observed O/Ni ratios of close to 1 for the NiO powder samples (see Chapter 5). In the case of the oxidized Ni surfaces some of the signal observed near 531.0 eV would also be attributed to O bound to Ni^{3+}. Possible "defective" $Ni(OH)_2$ structures were also inferred on the basis of O/Ni ratios. For "regular" $Ni(OH)_2$ atomic ratios of close to 2 were observed, while ratios of close to 1.5 were calculated for the "defective" hydroxide samples. The mechanism of decomposition was not explored here, however the O 1s BE of the "regular"

OH^- peak was found to be almost 0.3 eV below that observed for the "defective" hydroxide. Unlike what was observed for NiO, it appears that interstitial H_2O molecules may be stabilized on $Ni(OH)_2$ surfaces.

The atomic ratios obtained for the Ni- and Cr-containing powder samples studied here are believed to be very accurate based on the sample purities. The respective NiO and "regular" $Ni(OH)_2$ ratios of 1 and 2 were verified using EDX. It is also believed that these ratios can be used to accurately evaluate the composition of mixed oxide films formed on metallic Ni, Cr and NiCr (20%) surfaces. However, the validity of these ratios may break down when nearing the detection limit of XPS (0.1 – 0.3 at.%). If a particular oxidic component is only present in trace amounts its photoelectron signal could be partially obscured by that of another, species on the surface. This leads to a higher error in assigning intensity for the former component, thus increasing the error in the atomic ratios. Additional sources of error in the atomic ratios may occur in systems where one oxide component is buried beneath another near the photoelectron escape depth limit (~3λ, see Equation 1.5). This effect would be most amplified if the M (2p, 3p, 3d etc.) and O 1s photoelectrons are separated in KE by several hundreds of eVs. For example, if the IMFP value for the O 1s photoelectrons was longer than that of the M for a particular oxide, there is a limiting depth beyond which only the O 1s photoelectrons would be detected. Hence, if an overlayer was present with a thickness equal to or greater than this limiting depth, the O/M ratios would be skewed for the underlying oxide. This example would only arise in a very small portion of samples analyzed and should be considered as a limiting case. In general, having a buried layer system would not affect the accuracy of the atomic ratios as the RSF values derived for the M and O 1s components are meant to

account for signal attenuation based on differences in the respective IMFP values. Finally, it is unclear at this time if the presence of additional components (i.e. additional alloying elements) will affect the accuracy of the atomic ratios. As the number of contributing components increases the assignment of different chemical species in the O 1s spectrum becomes more challenging. It is our hope that others will be able to use atomic ratios to analyze three component alloy systems like NiCrFe alloys 600 and 690. This work in itself could produce another Ph.D. worthy thesis.

7.3 Future work

In this work XPS was used to monitor the oxidation of polycrystalline Ni metal surfaces following exposure to O_2 gas for doses ranging from $6.0 \times 10^7 - 6.0 \times 10^{10}$ L at a pressure of 1 Torr and temperatures of 25ºC and 300ºC. Under these reaction conditions limiting oxide thicknesses were not observed at either temperature. If this project were to be continued extended doses should be carried out at both 25ºC and 300ºC to determine if a limiting thickness would be reached. The use of a different surface analytical technique may be required to monitor the oxide films produced on polycrystalline Ni metal surfaces following larger doses of O_2 gas at 300ºC, as the thickest films observed in this work were approaching the limit of XPS analysis (~ 5 nm).

Using QUASES™ analytical routines it was determined that oxide growth on polycrystalline Ni metal surfaces following exposure to O_2 gas and H_2O vapour occurred via "island" growth on a nanometric scale. The size and distributions of these "islands" of oxide could not be confirmed using SEM or ToF SIMS. Future experiments should include surface analysis using other surface sensitive techniques such as Low Energy Electron Diffraction (LEED) to monitor the "defective" nature of the oxide films formed

and Transmission Electron Microscopy (TEM) to try and verify the presence of nanometre sized oxide "islands". However, the major limitation in studying these thin films is isolating the sample from atmospheric conditions. The XPS system used in this work was designed so that gas phase exposures could be carried out in an attached chamber followed by transfer of the sample under vacuum to the analysis chamber. To accurately study the thin films formed similar in-situ experimental setups must be applied to avoid additional oxide formation upon exposure to atmospheric or low vacuum conditions.

In addition, significant levels of a Ni^{3+}-containing ("defective") oxide component were also observed in the films formed on polycrystalline Ni metal surfaces subjected to reaction with O_2 gas at 25ºC. The change in Ni^{3+} concentration should also be monitored following extended O_2 exposures at this temperature.

The reaction of polycrystalline Ni metal surfaces with H_2O vapour was also studied using XPS following doses ranging from 1.2×10^9 – 3.0×10^{10} L at a pressure of 1 Torr and a temperature of 300ºC. From oxide thickness measurements obtained in this work it appeared that a limiting oxide thickness was approached sometime after a dose of 3.0×10^{10} L. Any future work involving the Ni-H_2O system should include exposures beyond 3.0×10^{10} L to determine if the reaction is in fact terminated, or if it continues, possibly at a different rate, due to a change in oxidation mechanism. As was observed for most of the O_2 exposures, the oxides formed on the polycrystalline Ni metal surfaces dosed with H_2O vapour at 300ºC were composed primarily of NiO, however small contributions from Ni^{3+} were also detected. The Ni^{3+} content of the films formed following extended H_2O exposures should also be monitored. Additional ToF SIMS

experiments should be completed to determine the distribution of H (if any) within the oxides formed following doses beyond 1.2 x 10^9 L. Finally, the reaction of a polycrystalline Ni metal surface with H_2O vapour following a dose of 3.0 x 10^9 L at 1 Torr and a temperature of 25ºC was also examined. In this case there were no detectable levels of oxide formed. Surfaces of polycrystalline Ni metal should be exposed to extended doses of H_2O at 25ºC in order to determine the length of time required for oxide nucleation to occur, as well as to determine if the films formed under these conditions are similar in composition to those grown at 300ºC. It is possible that both $Ni(OH)_2$ and/or NiOOH may form at the lower temperature.

The oxidation products formed on polycrystalline Cr metal surfaces were also examined with XPS following doses of O_2 gas and H_2O vapour ranging from 6.0 x 10^7 – 2.4 x 10^8 L at a pressure of 1 Torr and a temperature of 300ºC. In all cases the bulk of the oxide formed was found to be Cr_2O_3, however it was also determined that a "defective" hypo-stoichiometric oxide component was also present. The contribution from this "defective" component was also found to be much larger following exposure to H_2O vapour than when compared to similar doses of O_2 gas. Unfortunately, identification of this hypo-stoichiometric oxide was not determined here. Any future studies concerning the Cr-O_2 or Cr-H_2O systems should focus on identifying this "defective" oxide component, as well as try to determine if the presence of H within the oxide leads to an increased formation of this hypo-stoichiometric oxide. In addition, several other polycrystalline Cr metal samples should be exposed to O_2 gas and H_2O vapour over larger dosing ranges and the changes in the distribution of oxidized Cr

species and oxide thicknesses as a function of exposure should be examined using QUASES™.

The corrosion products formed on polycrystalline Ni metal and NiCr (20%) alloy surfaces were investigated using XPS. All XPS analysis involved rigorous modeling of the M $2p_{3/2}$ and O 1s spectra using O/M atomic ratios obtained from the fitting of the spectra collected from well characterized Ni- and Cr-containing oxides, hydroxides and oxyhydroxides. Using the O/M ratio method it was determined that the oxides formed on the Ni metal and NiCr alloy surfaces following aqueous exposures differed significantly from those grown on pure polycrystalline Ni and Cr metal surfaces exposed to gas phase O_2 and H_2O. Any future work in this area should include the exposure of the NiCr (20%) alloy to both O_2 and H_2O gas at both 300ºC and 25ºC and the films formed should be compared to those grown on the pure metals. This work is meant to form a base for the analysis of more complex Ni-alloy systems exposed to either gas phase or aqueous reaction conditions. It is also hoped that the data analytical techniques developed here can be applied to the study of the oxidation products formed on other transition metals (i.e. Fe, Mn, W, Ti) used in commercially available alloys.

7.4 References

[1] S. Tougaard, Surf. Interface Anal. 26 (1998) 693.

[2] S. Tougaard, QUASES™, Version 4.4, Software for Quantitative XPS/AES of Surface Nano-structures by Analysis of the Peak Shape Background, 2000.

[3] P.R. Norton, R.L. Tapping, F. Thieme, Surf. Sci. 65 (1977) 13.

[4] M.W. Roberts, R.St.C. Smart, J. Chem. Soc. Faraday Trans. 80 (1984) 2957.

[5] M.W. Roberts, Surf. Sci. 299/300 (1994) 769.

[6] A.F. Carley, S.R. Grubb, M.W. Roberts, J. Chem. Soc., Chem. Commun. (1994) 459.

[7] A.F. Carley, P.R. Chalker, M.W. Roberts, Proc. R. Soc. Lond. A399 (1985) 167.

[8] R.P. Gupta, S.K. Sen, Phys. Rev. B 10(1) (1974) 71.

[9] R.P. Gupta, S.K. Sen, Phys. Rev. B 12(1) (1975) 15.

[10] V. Maurice, S. Cadot, P. Marcus, Surf. Sci. 458 (2000) 195.

[11] C.P. Huggins, R.M. Nix, Surf. Sci. 594 (2005) 163.

[12] M.C. Biesinger, B.P. Payne, A.P. Grosvenor, L.W.M. Lau, A.R. Gerson, R.St.C. Smart, Appl. Sur. Sci. 257 (2011) 2717.

[13] M.C. Biesinger, B.P. Payne, L.W.M. Lau, A.R. Gerson, R.St.C. Smart, Surf. Interface Anal. 41 (2009) 324.

[14] M.C. Biesinger, C. Brown, J.R. Mycroft, R.D. Davidson, N.S. McIntyre, Surf. Interface Anal. 35 (2004) 1550.

[15] B. Beverskog, I. Puigdomenech, Corros. Sci. 39 (1997) 969.

[16] B. Beverskog, I. Puigdomenech, Corros. Sci. 55 (1999) 1077.

Appendix A Calculation of O/Ni ratios using the combined intensities of the O^{2-} and O (def) species for the Ni metal surfaces exposed to O_2 gas

Table A.1: The Ni and O surface concentrations in at.% for Ni metal surfaces exposed to doses of O_2 gas.

Reactant gas and temperature (^oC)	Dose of O_2 gas (L)	Oxidized Ni on surface (at.%)	O^{2-} and O (def) present (at.%)	O/Ni Ratio	Oxide thickness (nm)
O_2/25	6.0×10^8	2	2	1	0.2
	6.0×10^8	0.9	3	3	0.1
	6.0×10^8	4	5	1.2	0.2
	1.5×10^9	4	8	2	0.4
	1.5×10^9	13	22	1.7	0.8
	3.0×10^9	10	17	1.7	0.7
	3.0×10^9	17	22	1.3	0.9
	3.0×10^9	21	25	1.2	1.1
	6.0×10^9	18	24	1.3	1.3
	6.0×10^9	10	19	1.9	0.9
O_2/300	6.0×10^7	21	12	1.1	1.2
	6.0×10^7	7	10	1.4	0.6
	6.0×10^7	24	28	1.2	1.4
	6.0×10^7	25	28	1.1	1.5
	2.4×10^8	25	27	1.1	1.5
	2.4×10^8	19	20	1.1	1.0
	2.4×10^8	22	28	1.3	1.3
	2.4×10^8	33	29	0.89	1.8
	1.2×10^9	37	37	1.0	3.1
	3.6×10^9	49	40	0.81	4.7
	3.6×10^9	43	41	0.95	4.2
	3.6×10^9	44	39	0.89	4.6

The spectra for the O_2 exposed surfaces were originally collected and presented in Chapter 2. In this chapter the O (def) peak had been interpreted solely as O (ads).

Appendix B Copyright release form from Wiley Inter Science for the publication in Surface and Interface Analysis 39 (2007) 582

JOHN WILEY AND SONS LICENSE
TERMS AND CONDITIONS

Aug 01, 2011

This is a License Agreement between Brad P Payne ("You") and John Wiley and Sons ("John Wiley and Sons") provided by Copyright Clearance Center ("CCC"). The license consists of your order details, the terms and conditions provided by John Wiley and Sons, and the payment terms and conditions.

All payments must be made in full to CCC. For payment instructions, please see information listed at the bottom of this form.

License Number	2706070481604
License date	Jul 11, 2011
Licensed content publisher	John Wiley and Sons
Licensed content publication	Surface & Interface Analysis
Licensed content title	Structure and growth of oxides on polycrystalline nickel surfaces
Licensed content author	Brad P. Payne,Andrew. P. Grosvenor,Mark C. Biesinger,Brad A. Kobe,N. Stewart McIntyre
Licensed content date	Jul 1, 2007
Start page	582
End page	592
Type of use	Dissertation/Thesis
Requestor type	Author of this Wiley article
Format	Print and electronic
Portion	Full article
Will you be translating?	No
Order reference number	
Total	**0.00 USD**

Terms and Conditions

TERMS AND CONDITIONS

This copyrighted material is owned by or exclusively licensed to John Wiley & Sons, Inc. or one of its group companies (each a "Wiley Company") or a society for whom a Wiley Company has exclusive publishing rights in relation to a particular journal (collectively "WILEY"). By clicking "accept" in connection with completing this licensing transaction, you agree that the following terms and conditions apply to this transaction (along with the billing and payment terms and conditions established by the Copyright Clearance Center Inc., ("CCC□s Billing and Payment terms and conditions"), at the time that you opened your Rightslink account (these are available at any time at http://myaccount.copyright.com)

Terms and Conditions

1. The materials you have requested permission to reproduce (the "Materials") are protected by copyright.

2. You are hereby granted a personal, non-exclusive, non-sublicensable, non-transferable, worldwide, limited license to reproduce the Materials for the purpose specified in the licensing process. This license is for a one-time use only with a maximum distribution equal to the number that you identified in the licensing process. Any form of republication granted by this licence must be completed within two years of the date of the grant of this licence (although copies prepared before may be distributed thereafter). The Materials shall not be used in any other manner or for any other purpose.

Permission is granted subject to an appropriate acknowledgement given to the author, title of the material/book/journal and the publisher and on the understanding that nowhere in the text is a previously published source acknowledged for all or part of this Material. Any third party material is expressly excluded from this permission.

3. With respect to the Materials, all rights are reserved. Except as expressly granted by the terms of the license, no part of the Materials may be copied, modified, adapted (except for minor reformatting required by the new Publication), translated, reproduced, transferred or distributed, in any form or by any means, and no derivative works may be made based on the Materials without the prior permission of the respective copyright owner. You may not alter, remove or suppress in any manner any copyright, trademark or other notices displayed by the Materials. You may not license, rent, sell, loan, lease, pledge, offer as security, transfer or assign the Materials, or any of the rights granted to you hereunder to any other person.

4. The Materials and all of the intellectual property rights therein shall at all times remain the exclusive property of John Wiley & Sons Inc or one of its related companies (WILEY) or their respective licensors, and your interest therein is only that of having possession of and the right to reproduce the Materials pursuant to Section 2 herein during the continuance of this Agreement. You agree that you own no right, title or interest in or to the Materials or any of the intellectual property rights therein. You shall have no rights hereunder other than the license as provided for above in Section 2. No right, license or interest to any trademark, trade name, service mark or other branding ("Marks") of WILEY or its licensors is granted hereunder, and you agree that you shall not assert any such right, license or interest with respect thereto.

5. NEITHER WILEY NOR ITS LICENSORS MAKES ANY WARRANTY OR REPRESENTATION OF ANY KIND TO YOU OR ANY THIRD PARTY, EXPRESS, IMPLIED OR STATUTORY, WITH RESPECT TO THE MATERIALS OR THE ACCURACY OF ANY INFORMATION CONTAINED IN THE MATERIALS, INCLUDING, WITHOUT LIMITATION, ANY IMPLIED WARRANTY OF MERCHANTABILITY, ACCURACY, SATISFACTORY QUALITY, FITNESS FOR A PARTICULAR PURPOSE, USABILITY, INTEGRATION OR NON-INFRINGEMENT AND ALL SUCH WARRANTIES ARE HEREBY EXCLUDED BY WILEY AND ITS LICENSORS AND WAIVED BY YOU.

6. WILEY shall have the right to terminate this Agreement immediately upon breach of this Agreement by you.

7. You shall indemnify, defend and hold harmless WILEY, its Licensors and their respective directors, officers, agents and employees, from and against any actual or threatened claims, demands, causes of action or proceedings arising from any breach of this Agreement by you.

8. IN NO EVENT SHALL WILEY OR ITS LICENSORS BE LIABLE TO YOU OR ANY OTHER PARTY OR ANY OTHER PERSON OR ENTITY FOR ANY SPECIAL, CONSEQUENTIAL, INCIDENTAL, INDIRECT, EXEMPLARY OR PUNITIVE DAMAGES, HOWEVER CAUSED, ARISING OUT OF OR IN CONNECTION WITH THE DOWNLOADING, PROVISIONING, VIEWING OR USE OF THE MATERIALS REGARDLESS OF THE FORM OF ACTION, WHETHER FOR BREACH OF CONTRACT, BREACH OF WARRANTY, TORT, NEGLIGENCE, INFRINGEMENT OR OTHERWISE (INCLUDING, WITHOUT LIMITATION, DAMAGES BASED ON LOSS OF PROFITS, DATA, FILES, USE, BUSINESS OPPORTUNITY OR CLAIMS OF THIRD PARTIES), AND WHETHER OR NOT THE PARTY HAS BEEN ADVISED OF THE POSSIBILITY OF SUCH DAMAGES. THIS LIMITATION SHALL APPLY NOTWITHSTANDING ANY FAILURE OF ESSENTIAL PURPOSE OF ANY LIMITED REMEDY PROVIDED HEREIN.

9. Should any provision of this Agreement be held by a court of competent jurisdiction to be illegal, invalid, or unenforceable, that provision shall be deemed amended to achieve as nearly as possible the same economic effect as the original provision, and the legality, validity and enforceability of the remaining provisions of this Agreement shall not be affected or impaired thereby.

10. The failure of either party to enforce any term or condition of this Agreement shall not constitute a waiver of either party's right to enforce each and every term and condition of this Agreement. No breach under this agreement shall be deemed waived or excused by either party unless such waiver or consent is in writing signed by the party granting such waiver or consent. The waiver by or consent of a party to a breach of any provision of this Agreement shall not operate or be construed as a waiver of or consent to any other or subsequent breach by such other party.

11. This Agreement may not be assigned (including by operation of law or otherwise) by you without WILEY's prior written consent.

12. Any fee required for this permission shall be non-refundable after thirty (30) days from receipt.

13. These terms and conditions together with CCC□s Billing and Payment terms and conditions (which are incorporated herein) form the entire agreement between you and WILEY concerning this licensing transaction and (in the absence of fraud) supersedes all prior agreements and representations of the parties, oral or written. This Agreement may not be amended except in writing signed by both parties. This Agreement shall be binding upon and inure to the benefit of the parties' successors, legal representatives, and authorized assigns.

14. In the event of any conflict between your obligations established by these terms and conditions and those established by CCC□s Billing and Payment terms and conditions, these terms and conditions shall prevail.

15. WILEY expressly reserves all rights not specifically granted in the combination of (i) the license details provided by you and accepted in the course of this licensing transaction, (ii) these terms and conditions and (iii) CCC□s Billing and Payment terms and conditions.

16. This Agreement will be void if the Type of Use, Format, Circulation, or Requestor Type was misrepresented during the licensing process.

17. This Agreement shall be governed by and construed in accordance with the laws of the State of New York, USA, without regards to such state□s conflict of law rules. Any legal action, suit or proceeding arising out of or relating to these Terms and Conditions or the breach thereof shall be instituted in a court of competent jurisdiction in New York County in the State of New York in the United States of America and each party hereby consents and submits to the personal jurisdiction of such court, waives any objection to venue in such court and consents to service of process by registred or certified mail, return receipt requested, at the last known address of such party.

18. Other Terms and Conditions:

BY CLICKING ON THE "I ACCEPT" BUTTON, YOU ACKNOWLEDGE THAT YOU HAVE READ AND FULLY UNDERSTAND EACH OF THE SECTIONS OF AND PROVISIONS SET FORTH IN THIS AGREEMENT AND THAT YOU ARE IN AGREEMENT WITH AND ARE WILLING TO ACCEPT ALL OF YOUR OBLIGATIONS AS SET FORTH IN THIS AGREEMENT.

v1.4

Gratis licenses (referencing $0 in the Total field) are free. Please retain this printable license for your reference. No payment is required.

If you would like to pay for this license now, please remit this license along with your payment made payable to "COPYRIGHT CLEARANCE CENTER" otherwise you will be invoiced within 48 hours of the license date. Payment should be in the form of a check or money order referencing your account number and this invoice number RLNK0.
Once you receive your invoice for this order, you may pay your invoice by credit card. Please follow instructions provided at that time.

Make Payment To:
Copyright Clearance Center
Dept 001
P.O. Box 843006
Boston, MA 02284-3006

For suggestions or comments regarding this order, contact Rightslink Customer Support:
customercare@copyright.com or +1-877-622-5543 (toll free in the US) or +1-978-646-2777.

Appendix C Copyright release form from Elsevier for the publication in Journal of Electron Spectroscopy and Related Phenomena 175 (2009) 55

ELSEVIER LICENSE
TERMS AND CONDITIONS

Aug 01, 2011

This is a License Agreement between Brad P Payne ("You") and Elsevier ("Elsevier") provided by Copyright Clearance Center ("CCC"). The license consists of your order details, the terms and conditions provided by Elsevier, and the payment terms and conditions.

All payments must be made in full to CCC. For payment instructions, please see information listed at the bottom of this form.

Supplier	Elsevier Limited The Boulevard,Langford Lane Kidlington,Oxford,OX5 1GB,UK
Registered Company Number	1982084
Customer name	Brad P Payne
Customer address	Room 25 Department of Chemistry London, ON N6A 5B7
License number	2706061418334
License date	Jul 11, 2011
Licensed content publisher	Elsevier
Licensed content publication	Journal of Electron Spectroscopy and Related Phenomena
Licensed content title	The study of polycrystalline nickel metal oxidation by water vapour
Licensed content author	B.P. Payne, M.C. Biesinger, N.S. McIntyre
Licensed content date	December 2009
Licensed content volume number	175
Licensed content issue number	1-3
Number of pages	11
Start Page	55
End Page	65
Type of Use	reuse in a thesis/dissertation
Portion	full article
Format	both print and electronic
Are you the author of this Elsevier article?	Yes
Will you be translating?	No
Order reference number	
Title of your thesis/dissertation	X-ray Photoelectron Spectroscopy Studies on the Oxidation Processes of Nickel, Chromium and their Alloys
Expected completion date	Jul 2011

Estimated size (number of pages)	200
Elsevier VAT number	GB 494 6272 12
Permissions price	0.00 USD
VAT/Local Sales Tax	0.0 USD / 0.0 GBP
Total	**0.00 USD**

Terms and Conditions

INTRODUCTION

1. The publisher for this copyrighted material is Elsevier. By clicking "accept" in connection with completing this licensing transaction, you agree that the following terms and conditions apply to this transaction (along with the Billing and Payment terms and conditions established by Copyright Clearance Center, Inc. ("CCC"), at the time that you opened your Rightslink account and that are available at any time at http://myaccount.copyright.com).

GENERAL TERMS

2. Elsevier hereby grants you permission to reproduce the aforementioned material subject to the terms and conditions indicated.
3. Acknowledgement: If any part of the material to be used (for example, figures) has appeared in our publication with credit or acknowledgement to another source, permission must also be sought from that source. If such permission is not obtained then that material may not be included in your publication/copies. Suitable acknowledgement to the source must be made, either as a footnote or in a reference list at the end of your publication, as follows:
"Reprinted from Publication title, Vol /edition number, Author(s), Title of article / title of chapter, Pages No., Copyright (Year), with permission from Elsevier [OR APPLICABLE SOCIETY COPYRIGHT OWNER]." Also Lancet special credit - "Reprinted from The Lancet, Vol. number, Author(s), Title of article, Pages No., Copyright (Year), with permission from Elsevier."
4. Reproduction of this material is confined to the purpose and/or media for which permission is hereby given.
5. Altering/Modifying Material: Not Permitted. However figures and illustrations may be altered/adapted minimally to serve your work. Any other abbreviations, additions, deletions and/or any other alterations shall be made only with prior written authorization of Elsevier Ltd. (Please contact Elsevier at permissions@elsevier.com)
6. If the permission fee for the requested use of our material is waived in this instance, please be advised that your future requests for Elsevier materials may attract a fee.
7. Reservation of Rights: Publisher reserves all rights not specifically granted in the combination of (i) the license details provided by you and accepted in the course of this licensing transaction, (ii) these terms and conditions and (iii) CCC's Billing and Payment terms and conditions.
8. License Contingent Upon Payment: While you may exercise the rights licensed immediately upon issuance of the license at the end of the licensing process for the transaction, provided that you have disclosed complete and accurate details of your proposed use, no license is finally effective unless and until full payment is received from you (either by publisher or by CCC) as provided in CCC's Billing and Payment terms and conditions. If full payment is not received on a timely basis, then any license preliminarily granted shall be deemed automatically revoked and shall be void as if never granted. Further, in the event that you breach any of these terms and conditions or any of CCC's Billing and Payment terms and conditions, the license is automatically revoked and shall be void as if never granted. Use of materials as described in a revoked license, as well as any use of the materials beyond the scope of an unrevoked license, may constitute copyright infringement and publisher reserves the right to take any and all action to protect its copyright in the materials.
9. Warranties: Publisher makes no representations or warranties with respect to the licensed material.
10. Indemnity: You hereby indemnify and agree to hold harmless publisher and CCC, and their respective officers, directors, employees and agents, from and against any and all claims arising out of your use of the licensed material other than as specifically authorized pursuant to this license.
11. No Transfer of License: This license is personal to you and may not be sublicensed, assigned, or transferred by you to any other person without publisher's written permission.
12. No Amendment Except in Writing: This license may not be amended except in a writing signed by both parties (or, in the case of publisher, by CCC on publisher's behalf).
13. Objection to Contrary Terms: Publisher hereby objects to any terms contained in any purchase order, acknowledgment, check endorsement or other writing prepared by you, which terms are inconsistent with these terms and conditions or CCC's Billing and Payment terms and conditions. These terms and conditions, together with CCC's Billing and Payment terms and conditions (which are incorporated herein), comprise the entire agreement between you and publisher (and CCC) concerning this licensing transaction. In the event of any conflict between your obligations

established by these terms and conditions and those established by CCC's Billing and Payment terms and conditions, these terms and conditions shall control.
14. Revocation: Elsevier or Copyright Clearance Center may deny the permissions described in this License at their sole discretion, for any reason or no reason, with a full refund payable to you. Notice of such denial will be made using the contact information provided by you. Failure to receive such notice will not alter or invalidate the denial. In no event will Elsevier or Copyright Clearance Center be responsible or liable for any costs, expenses or damage incurred by you as a result of a denial of your permission request, other than a refund of the amount(s) paid by you to Elsevier and/or Copyright Clearance Center for denied permissions.

LIMITED LICENSE

The following terms and conditions apply only to specific license types:
15. **Translation**: This permission is granted for non-exclusive world **English** rights only unless your license was granted for translation rights. If you licensed translation rights you may only translate this content into the languages you requested. A professional translator must perform all translations and reproduce the content word for word preserving the integrity of the article. If this license is to re-use 1 or 2 figures then permission is granted for non-exclusive world rights in all languages.
16. **Website**: The following terms and conditions apply to electronic reserve and author websites:
Electronic reserve: If licensed material is to be posted to website, the web site is to be password-protected and made available only to bona fide students registered on a relevant course if:
This license was made in connection with a course,
This permission is granted for 1 year only. You may obtain a license for future website posting,
All content posted to the web site must maintain the copyright information line on the bottom of each image,
A hyper-text must be included to the Homepage of the journal from which you are licensing at
http://www.sciencedirect.com/science/journal/xxxxx or the Elsevier homepage for books at http://www.elsevier.com , and
Central Storage: This license does not include permission for a scanned version of the material to be stored in a central repository such as that provided by Heron/XanEdu.
17. **Author website** for journals with the following additional clauses:
All content posted to the web site must maintain the copyright information line on the bottom of each image, and
he permission granted is limited to the personal version of your paper. You are not allowed to download and post the published electronic version of your article (whether PDF or HTML, proof or final version), nor may you scan the printed edition to create an electronic version,
A hyper-text must be included to the Homepage of the journal from which you are licensing at
http://www.sciencedirect.com/science/journal/xxxxx , As part of our normal production process, you will receive an e-mail notice when your article appears on Elsevier's online service ScienceDirect (www.sciencedirect.com). That e-mail will include the article's Digital Object Identifier (DOI). This number provides the electronic link to the published article and should be included in the posting of your personal version. We ask that you wait until you receive this e-mail and have the DOI to do any posting.
Central Storage: This license does not include permission for a scanned version of the material to be stored in a central repository such as that provided by Heron/XanEdu.
18. **Author website** for books with the following additional clauses:
Authors are permitted to place a brief summary of their work online only.
A hyper-text must be included to the Elsevier homepage at http://www.elsevier.com
All content posted to the web site must maintain the copyright information line on the bottom of each image
You are not allowed to download and post the published electronic version of your chapter, nor may you scan the printed edition to create an electronic version.
Central Storage: This license does not include permission for a scanned version of the material to be stored in a central repository such as that provided by Heron/XanEdu.

19. **Website** (regular and for author): A hyper-text must be included to the Homepage of the journal from which you are licensing at http://www.sciencedirect.com/science/journal/xxxxx. or for books to the Elsevier homepage at http://www.elsevier.com
20. **Thesis/Dissertation**: If your license is for use in a thesis/dissertation your thesis may be submitted to your institution in either print or electronic form. Should your thesis be published commercially, please reapply for permission. These requirements include permission for the Library and Archives of Canada to supply single copies, on demand, of the complete thesis and include permission for UMI to supply single copies, on demand, of the complete thesis. Should your thesis be published commercially, please reapply for permission.
21. **Other Conditions**:

v1.6

Gratis licenses (referencing $0 in the Total field) are free. Please retain this printable license for your reference. No payment is required.

If you would like to pay for this license now, please remit this license along with your payment made payable to "COPYRIGHT CLEARANCE CENTER" otherwise you will be invoiced within 48 hours of the license date. Payment should be in the form of a check or money order referencing your account number and this invoice number RLNK0.
Once you receive your invoice for this order, you may pay your invoice by credit card. Please follow instructions provided at that time.

Make Payment To:
Copyright Clearance Center
Dept 001
P.O. Box 843006
Boston, MA 02284-3006

For suggestions or comments regarding this order, contact Rightslink Customer Support:
customercare@copyright.com or +1-877-622-5543 (toll free in the US) or +1-978-646-2777.

Appendix D Copyright release form from Elsevier for the publication in Journal of Electron Spectroscopy and Related Phenomena 184 (2011) 29

ELSEVIER LICENSE
TERMS AND CONDITIONS

Aug 01, 2011

This is a License Agreement between Brad P Payne ("You") and Elsevier ("Elsevier") provided by Copyright Clearance Center ("CCC"). The license consists of your order details, the terms and conditions provided by Elsevier, and the payment terms and conditions.

All payments must be made in full to CCC. For payment instructions, please see information listed at the bottom of this form.

Supplier	Elsevier Limited The Boulevard,Langford Lane Kidlington,Oxford,OX5 1GB,UK
Registered Company Number	1982084
Customer name	Brad P Payne
Customer address	Room 25 Department of Chemistry London, ON N6A 5B7
License number	2706070240906
License date	Jul 11, 2011
Licensed content publisher	Elsevier
Licensed content publication	Journal of Electron Spectroscopy and Related Phenomena
Licensed content title	X-ray photoelectron spectroscopy studies of reactions on chromium metal and chromium oxide surfaces
Licensed content author	B.P. Payne, M.C. Biesinger, N.S. McIntyre
Licensed content date	February 2011
Licensed content volume number	184
Licensed content issue number	1-2
Number of pages	9
Start Page	29
End Page	37
Type of Use	reuse in a thesis/dissertation
Intended publisher of new work	other
Portion	full article
Format	both print and electronic
Are you the author of this Elsevier article?	Yes
Will you be translating?	No
Order reference number	
Title of your thesis/dissertation	X-ray Photoelectron Spectroscopy Studies on the Oxidation Processes of Nickel, Chromium and their Alloys

Expected completion date	Jul 2011
Estimated size (number of pages)	200
Elsevier VAT number	GB 494 6272 12
Permissions price	0.00 USD
VAT/Local Sales Tax	0.0 USD / 0.0 GBP
Total	**0.00 USD**

Terms and Conditions

INTRODUCTION

1. The publisher for this copyrighted material is Elsevier. By clicking "accept" in connection with completing this licensing transaction, you agree that the following terms and conditions apply to this transaction (along with the Billing and Payment terms and conditions established by Copyright Clearance Center, Inc. ("CCC"), at the time that you opened your Rightslink account and that are available at any time at http://myaccount.copyright.com).

GENERAL TERMS

2. Elsevier hereby grants you permission to reproduce the aforementioned material subject to the terms and conditions indicated.
3. Acknowledgement: If any part of the material to be used (for example, figures) has appeared in our publication with credit or acknowledgement to another source, permission must also be sought from that source. If such permission is not obtained then that material may not be included in your publication/copies. Suitable acknowledgement to the source must be made, either as a footnote or in a reference list at the end of your publication, as follows:
"Reprinted from Publication title, Vol /edition number, Author(s), Title of article / title of chapter, Pages No., Copyright (Year), with permission from Elsevier [OR APPLICABLE SOCIETY COPYRIGHT OWNER]." Also Lancet special credit - "Reprinted from The Lancet, Vol. number, Author(s), Title of article, Pages No., Copyright (Year), with permission from Elsevier."
4. Reproduction of this material is confined to the purpose and/or media for which permission is hereby given.
5. Altering/Modifying Material: Not Permitted. However figures and illustrations may be altered/adapted minimally to serve your work. Any other abbreviations, additions, deletions and/or any other alterations shall be made only with prior written authorization of Elsevier Ltd. (Please contact Elsevier at permissions@elsevier.com)
6. If the permission fee for the requested use of our material is waived in this instance, please be advised that your future requests for Elsevier materials may attract a fee.
7. Reservation of Rights: Publisher reserves all rights not specifically granted in the combination of (i) the license details provided by you and accepted in the course of this licensing transaction, (ii) these terms and conditions and (iii) CCC's Billing and Payment terms and conditions.
8. License Contingent Upon Payment: While you may exercise the rights licensed immediately upon issuance of the license at the end of the licensing process for the transaction, provided that you have disclosed complete and accurate details of your proposed use, no license is finally effective unless and until full payment is received from you (either by publisher or by CCC) as provided in CCC's Billing and Payment terms and conditions. If full payment is not received on a timely basis, then any license preliminarily granted shall be deemed automatically revoked and shall be void as if never granted. Further, in the event that you breach any of these terms and conditions or any of CCC's Billing and Payment terms and conditions, the license is automatically revoked and shall be void as if never granted. Use of materials as described in a revoked license, as well as any use of the materials beyond the scope of an unrevoked license, may constitute copyright infringement and publisher reserves the right to take any and all action to protect its copyright in the materials.
9. Warranties: Publisher makes no representations or warranties with respect to the licensed material.
10. Indemnity: You hereby indemnify and agree to hold harmless publisher and CCC, and their respective officers, directors, employees and agents, from and against any and all claims arising out of your use of the licensed material other than as specifically authorized pursuant to this license.
11. No Transfer of License: This license is personal to you and may not be sublicensed, assigned, or transferred by you to any other person without publisher's written permission.
12. No Amendment Except in Writing: This license may not be amended except in a writing signed by both parties (or, in the case of publisher, by CCC on publisher's behalf).
13. Objection to Contrary Terms: Publisher hereby objects to any terms contained in any purchase order, acknowledgment, check endorsement or other writing prepared by you, which terms are inconsistent with these terms and conditions or CCC's Billing and Payment terms and conditions. These terms and conditions, together with CCC's

Billing and Payment terms and conditions (which are incorporated herein), comprise the entire agreement between you and publisher (and CCC) concerning this licensing transaction. In the event of any conflict between your obligations established by these terms and conditions and those established by CCC's Billing and Payment terms and conditions, these terms and conditions shall control.
14. Revocation: Elsevier or Copyright Clearance Center may deny the permissions described in this License at their sole discretion, for any reason or no reason, with a full refund payable to you. Notice of such denial will be made using the contact information provided by you. Failure to receive such notice will not alter or invalidate the denial. In no event will Elsevier or Copyright Clearance Center be responsible or liable for any costs, expenses or damage incurred by you as a result of a denial of your permission request, other than a refund of the amount(s) paid by you to Elsevier and/or Copyright Clearance Center for denied permissions.

LIMITED LICENSE

The following terms and conditions apply only to specific license types:
15. **Translation**: This permission is granted for non-exclusive world **English** rights only unless your license was granted for translation rights. If you licensed translation rights you may only translate this content into the languages you requested. A professional translator must perform all translations and reproduce the content word for word preserving the integrity of the article. If this license is to re-use 1 or 2 figures then permission is granted for non-exclusive world rights in all languages.
16. **Website**: The following terms and conditions apply to electronic reserve and author websites:
Electronic reserve: If licensed material is to be posted to website, the web site is to be password-protected and made available only to bona fide students registered on a relevant course if:
This license was made in connection with a course,
This permission is granted for 1 year only. You may obtain a license for future website posting,
All content posted to the web site must maintain the copyright information line on the bottom of each image,
A hyper-text must be included to the Homepage of the journal from which you are licensing at
http://www.sciencedirect.com/science/journal/xxxxx or the Elsevier homepage for books at http://www.elsevier.com , and
Central Storage: This license does not include permission for a scanned version of the material to be stored in a central repository such as that provided by Heron/XanEdu.
17. **Author website** for journals with the following additional clauses:
All content posted to the web site must maintain the copyright information line on the bottom of each image, and
he permission granted is limited to the personal version of your paper. You are not allowed to download and post the published electronic version of your article (whether PDF or HTML, proof or final version), nor may you scan the printed edition to create an electronic version,
A hyper-text must be included to the Homepage of the journal from which you are licensing at
http://www.sciencedirect.com/science/journal/xxxxx , As part of our normal production process, you will receive an e-mail notice when your article appears on Elsevier's online service ScienceDirect (www.sciencedirect.com). That e-mail will include the article's Digital Object Identifier (DOI). This number provides the electronic link to the published article and should be included in the posting of your personal version. We ask that you wait until you receive this e-mail and have the DOI to do any posting.
Central Storage: This license does not include permission for a scanned version of the material to be stored in a central repository such as that provided by Heron/XanEdu.
18. **Author website** for books with the following additional clauses:
Authors are permitted to place a brief summary of their work online only.
A hyper-text must be included to the Elsevier homepage at http://www.elsevier.com
All content posted to the web site must maintain the copyright information line on the bottom of each image
You are not allowed to download and post the published electronic version of your chapter, nor may you scan the printed edition to create an electronic version.
Central Storage: This license does not include permission for a scanned version of the material to be stored in a central repository such as that provided by Heron/XanEdu.

19. **Website** (regular and for author): A hyper-text must be included to the Homepage of the journal from which you are licensing at http://www.sciencedirect.com/science/journal/xxxxx. or for books to the Elsevier homepage at http://www.elsevier.com
20. **Thesis/Dissertation**: If your license is for use in a thesis/dissertation your thesis may be submitted to your institution in either print or electronic form. Should your thesis be published commercially, please reapply for permission. These requirements include permission for the Library and Archives of Canada to supply single copies, on demand, of the complete thesis and include permission for UMI to supply single copies, on demand, of the complete thesis. Should your thesis be published commercially, please reapply for permission.

21. **Other Conditions**:

v1.6

Gratis licenses (referencing $0 in the Total field) are free. Please retain this printable license for your reference. No payment is required.

If you would like to pay for this license now, please remit this license along with your payment made payable to "COPYRIGHT CLEARANCE CENTER" otherwise you will be invoiced within 48 hours of the license date. Payment should be in the form of a check or money order referencing your account number and this invoice number RLNK0.
Once you receive your invoice for this order, you may pay your invoice by credit card. Please follow instructions provided at that time.

Make Payment To:
Copyright Clearance Center
Dept 001
P.O. Box 843006
Boston, MA 02284-3006

For suggestions or comments regarding this order, contact Rightslink Customer Support: customercare@copyright.com or +1-877-622-5543 (toll free in the US) or +1-978-646-2777.

Curriculum Vitae

Bradley P. Payne
PH.D. CANDIDATE DEPARTMENT OF CHEMISTRY
THE UNIVERSITY OF WESTERN ONTARIO
LONDON ONTARIO CANADA N6A 5B7

EDUCATION

Department of Chemistry
The University of Western Ontario,
London Ontario, Canada

B.Sc. Honors Degree in Chemistry (September 1999 – April 2005)
The University of Western Ontario,
London Ontario, Canada

CONFERENCES

Surface Canada Conference (May 14-17 2006)
Queens University,
Kingston Ontario, Canada

WINS Workshop (May 19 2005)
The University of Western Ontario,
London Ontario, Canada

33rd SOUSCC – Annual Undergraduate Chemistry Conference (March 19 2005)
University of Toronto,
Toronto Ontario, Canada

AWARDS AND SCHOLARSHIPS

Christian Sivertz Scholarship – Best Overall Performance (January 2007)
in a Physical Chemistry Graduate Course
The University of Western Ontario,
London Ontario, Canada

Dean's Honor List (Undergraduate) (2005 Academic Year)
The University of Western Ontario,
London Ontario, Canada

First Place Analytical Chemistry Division at the 33rd SOUSCC (March 19 2005)
Undergraduate Chemistry Conference
The University of Toronto,
Toronto Ontario, Canada

PUBLICATIONS

B.P. Payne, M.C. Biesinger, N.S. McIntyre, "Use of oxygen/nickel ratios in the XPS characterization of oxide phases on nickel metal and nickel alloy surfaces", Journal of Electron Spectroscopy and Related Phenomena, Submitted March 2011 (ELSPEC-D-11-00017).

B.P. Payne, M.C. Biesinger, N.S. McIntyre, "X-ray photoelectron spectroscopy studies of reactions on chromium metal and chromium oxide surfaces", Journal of Electron Spectroscopy and Related Phenomena, 184, 29 (2011).

M.C. Biesinger, B.P. Payne, A.P. Grosvenor, L.W.M. Lau, A.R. Gerson, R.St.C. Smart, "Resolving surface chemical states in XPS analysis of first row transition metals, oxides and hydroxides", Applied Surface Science, 257, 2717 (2011).

B.P. Payne, M.C. Biesinger, N.S. McIntyre, "The study of polycrystalline nickel metal oxidation by water vapour", Journal of Electron Spectroscopy and Related Phenomena, 175, 55 (2009).

M.C. Biesinger, B.P. Payne, L.W.M. Lau, A. Gerson, R.St.C. Smart, "X-ray photoelectron spectroscopic chemical state quantification of mixed nickel metal, oxide and hydroxide systems", Surface and Interface Analysis, 41, 324 (2009).

M.C. Biesinger, B.P. Payne, B.R. Hart, A.P. Grosvenor, N.S. McIntyre, L.W.M. Lau, R.St.C. Smart, "Quantitative chemical state XPS analysis of first row transition metals, oxides and hydroxides", Journal of Physics: Conference Series, 100, 012025 (2008).

B.P. Payne, A.P. Grosvenor, M.C. Biesinger, B.A. Kobe, N.S. McIntyre, "Structure and growth of oxides on polycrystalline nickel surfaces", Surface and Interface Analysis, 39**,** 582 (2007).

CONFERENCES

Poster Session, "Mechanisms for Oxide Growth on Polycrystalline Nickel Surfaces", Surface Canada Conference, Kingston ON, May 2006.

Poster Session, "Structure and Growth of Oxides on Polycrystalline Nickel Surfaces", WINS Conference, London ON, May 2005.

Oral Presentation, "Structure and Growth of Oxides on Polycrystalline Nickel Surfaces", Southwestern Ontario Undergraduate Chemistry Conference, Toronto ON, March 2005.

TEACHING EXPERIENCE

Chemistry 3372G (January 2010 – April 2010)
The University of Western Ontario,
London Ontario, Canada

Chemistry 1050 Lab Section (September 2009 – December 2009)
The University of Western Ontario,
London Ontario, Canada

Chemistry 1050 Lab Section (September 2008 – April 2009)
The University of Western Ontario,
London Ontario, Canada

Chemistry 020 Lab Section (September 2007 – April 2008)
The University of Western Ontario,
London Ontario, Canada

Chemistry 020 Lab Section only (September 2006 – April 2007)
The University of Western Ontario,
London Ontario Canada

Chemistry 023 Lab Section only (September 2005 – April 2006)
The University of Western Ontario,
London Ontario, Canada

COURSE WORK

Chemistry 658y (September 2007 – April 2008)
The University of Western Ontario,
London Ontario, Canada
Grade 88%

Chemistry 541a Crystallography 1 (September 2007 – Dec 2008)
Professor N.C. Payne
The University of Western Ontario,
London Ontario, Canada
Grade 88%

Chemistry 557b Topics in Surface Science (January 2007 – April 2007)
Professor L.M.W. Lau
The University of Western Ontario,
London Ontario, Canada
Grade 93%

Chemistry 724a Materials Analysis using Synchrotron Radiation (September 2006 – January 2007)
Professors T.K. Sham and Y. Song
The University of Western Ontario,
London Ontario, Canada
Grade 91%

Chemistry 657b Scanning Probe Microscopy and Related Techniques (January 2006 - April 2006)
Professor M. Kovar
The University of Western Ontario,
London, Ontario, Canada
Grade 96%

Chemistry 534a Organic Functional Materials (September 2005- December 2005)
Professor O. Semenikhin
The University of Western Ontario,
London, Ontario, Canada
Grade 86%